THE UNIVERSITY *of* EDINBURGH

Coupled hybrid modelling for fire engineering

Benjamin Ralph

THE UNIVERSITY *of* EDINBURGH

Thesis submitted for the degree of
Doctor of Philosophy

University of Edinburgh
School of Engineering

Year of submission 2019

Abstract

Due to time and cost constraints, fire engineers typically curtail the domain of analysis when carrying out quantitative assessments using computational fluid dynamics (CFD)-based fire modelling. This could embody unquantified hazard and is especially critical when designing complex building with a shared ventilation system. Secondarily, prescriptive model solutions have been developed using engineering judgement and empirical evidence. There is a risk that under-investigated mechanisms may lead to unacceptable prescriptive solution risk levels.

The overarching thesis aim is to enable a more robust quantification of fire hazard in complex buildings with a shared ventilation system. The objectives of the study are to develop and evaluate a novel coupled hybrid model implementation and highlight potential shortcomings of existing prescriptive design solutions for shared ventilation systems.

This study develops a novel 3D-1D coupled hybrid modelling implementation within Fire Dynamics Simulator (FDS). The new implementation addresses the pre-existing limitation of time-dependent transport or storage within the 1D sub-domain and introduces a novel fan model. A new experimental rig was created comprising two $1\,m^3$ boxes interconnected with shared mechanical ventilation. A propane burner was used as a fire source, with propane flow rates ranging between $0.2\,g/s$ to $0.45\,g/s$, in one of the boxes. Variable speed controllers and dampers were used to alter the ventilation with target free flow fan velocities of $1\,m/s$ to $3\,m/s$.

The novel model implementation satisfactorily passed verification and presented generally good agreement with the experimental results. Prediction of maximum temperature in the fire and non-fire enclosures are typically within 40% and 5% respectively. Prediction of ventilation duct velocity is typically within 5 - 25%. Model correction factors of 1.0, 0.7, and 1.4 are proposed for enclosure temperature, in-duct temperatures, and duct velocities respectively.

Experimental data demonstrate that empirical methods may not be suitable for complex arrangements with shared ventilation because there is a stronger dependency of fire hazard upon the ratio of heat losses to ventilation enthalpy advection when compared to traditional arrangements. The data illustrate that remote area fire hazard is very sensitive to the balance of the energy transfer rate (i.e. power) of the fire and the ventilation system and that this relationship is non-linear; a correlation which would not be well-captured using the typical modelling paradigm nor prescriptive design solutions.

The study concludes that the new coupled hybrid modelling implementation may be used to analyse a total system with quantified uncertainties. Further development is recommended for the new model implementation (e.g. conductive heat transfer within the 1D sub-domain). Further experimentation is recommended to further inform prescriptive design solutions for complex buildings with a shared ventilation system.

Lay summary

A common tool used by engineers when developing and testing design solutions for complex buildings is computational fluid dynamics (CFD)-based fire modelling. These models are very complicated and carrying out this type of simulation takes a long time. Therefore, engineers typically reduce the size of the model so the calculation takes a shorter time to run.

The problem with this simplification is that the model can no longer account for the entirety of the building. This means that how fire and smoke may spread through the whole building is ignored. Also ignored is how part of the building far away from the fire may affect the growth and spread of fire and smoke. Therefore, this simplification limits the ability of an engineer to make robust solutions and could be dangerous to occupants of the building if there is a fire.

One way to address this limitation is the use of 'coupled hybrid modelling'. This type of model combines the originally used model (which takes a long time to run) and another model (which takes a much shorter time to run) together. Therefore, a fire engineer can increase the size of the model to include more or all of a building, but still carry out a simulation that doesn't take an unreasonable length of time to run.

This thesis first documents a critical literature review of existing coupled hybrid models and concludes that lack of collaborative working and proprietary software has led to wasted effort. Therefore, a coupled hybrid model implementation is developed in this thesis, which is based upon the open source and widely used fire model, Fire Dynamics Simulator (FDS).

A critical part of the development of a new computer model is its comparison to real experiments to ensure that it can represent the physical world within reasonable limits. Applicable experimental data were not found during an extensive search of the literature and discussions with applicable bodies. Therefore, to provide these data, a new experimental rig was specifically designed and built.

Data from the new experimental rig was first used to examine potential holes in the current typical fire safety design paradigm for complex buildings. This analysis demonstrated that there are phenomena related to the two-way coupling of a fire and a shared ventilation system that may not be captured by commonly used simple engineering methods or addressed in current design guidance documents.

Secondly, the new experimental data were compared to the predictions of the novel computer model and the qualitative and quantitative differences stated. The computer model predicts well fire hazard within the experimental set-up. Key information is provided, which is required by future model users to ensure that their analysis is robust.

The original insights into how a total building system and a fire interacts and the newly developed coupled hybrid model implementation can be used together by fire engineers to deliver solutions with more deeply understood fire life safety risk for complex buildings incorporating a mechanical ventilation system.

Declaration

I declare that this thesis is composed by myself and is my own work. I declare that this work has not been submitted for any other degree or professional qualification.

Signed:

Benjamin Ralph, October 18, 2019
[Word count: 64 965 words]

For Jamba. Meow.

Acknowledgements

- Major thanks go to my supervisor, Dr Ricky Carvel (University of Edinburgh), for his pragmatic help, guidance, and thoughts throughout the course of the project.
- I am deeply grateful for the support and friendship given to me by Dr Randy McDermott (NIST). He is a true inspiration and made me feel so welcome during my time at NIST.
- Massive gratitude goes to Dr Jason Floyd (Jensen Hughes), who has helped me so much navigating my way through the code.
- Thanks to my family; especially mum and dad, who have never stopped being my biggest fans.
- Thank you to Ge for all the care and food provided during those 18 hour writing stints that will be some of the most joyous memories of my life.
- Thanks to: Chris for the pints, Daryan for the homebrew, Eric for the gigs/gifs, Farian for Farian, Ieuan for the techno, Juan for the welcome, Marc for the tie, Moss for the Division, Nikolai for the White Russians, Paul for the voice clips, Simón for the coffees, and Tim for the dancing.
- Big cheers to everyone who has been in John Muir during my time there. A great place and a great group.
- I have nothing but appreciation for the lab support I got from Michal and Mark.
- I'd like to acknowledge the Engineering and Physical Sciences Research Council (EPSRC) and BRE for funding my research.
- Last and by no means least, thank you to all the inspirational leaders I have met during my PhD: Prof Luke Bisby (University of Edinburgh), Prof Grunde Jomaas (University of Edinburgh), Dr Kevin McGrattan (NIST), Prof Guillermo Rein (Imperial College London), Prof Albert Simeoni (Worcester Polytechnic Institute), and Prof José Torero (University College London).

Contents

List of Figures

List of Tables

Nomenclature

Greek Symbols

ϵ	Absolute roughness	m
Γ	Boundary	
Ω	Domain	
ϕ	Conserved variable	
ϕ_P	Fire to fan power ratio	
ρ	Gas density	$\mathrm{kg/m^3}$

Roman Symbols

$\bar{p}$	Background pressure	Pa
$\dot{Q}$	Heat release rate	kJ/s
$\dot{Q}_c$	Convective heat release rate	kJ/s
A	Cross sectional area	$\mathrm{m^2}$
c_p	Specific heat capacity	$\mathrm{kJ/(kg\,K)}$
D	Diameter	m
$D*$	Characteristic fire diameter	m
D_α	Diffusion coefficient	$\mathrm{m^2/s}$
F	Fan set	
f	Friction factor	
g	Acceleration due to gravity	$\mathrm{m/s^2}$
H	Height	m
h	Specific enthalpy	kJ/kg
h_k	Effective heat transfer coefficient	$\mathrm{kJ/(m^2\,K\,s)}$
K	Loss coefficient	
k	Conductivity	$\mathrm{kJ/(m\,K\,s)}$

k	Turbulent kinetic energy	kJ
L	Length	m
L_f	Flame length	m
m	Mass	kg
p	Pressure	Pa
p_L	Pressure loss	Pa
q	Volume flow rate	m^3/s
R	Universal gas constant	kJ/(K mol)
r	Radius from fire	m
T	Temperature	K
t	Time	s
u	Gas velocity	m/s
V	Volume	m^3
W	Molecular weight	kg/mol
x	First dimension of space	m
Y	Species concentration	
z	Elevation	m

Superscripts

$''$	Per unit area	$1/m^2$
k	Iteration index	
n	Time step index	

Subscripts

α	Species index
∞	Ambient value
c	Duct cell index
f	Fan index
g	Gas cell (where used on a domain)
g	Gas field cell index
i	Upstream duct node index
j	Duct index

k	Downstream duct node index
p	Propane
V	Vent index
V	Vent-adjacent cell set (where used on a domain)
w	Wall cell index

Other Symbols

$\bar{}$	Cell centred value
δn	Normal unit vector
$\dot{}$	First derivative of time
$\tilde{}$	Extrapolated value or cell face value

Chapter 1

Introduction

1.1 Aim

The overarching aim of this thesis is to facilitate the reduction of unquantified fire hazard within complex elements of the built environment, such that fire safety designs can be more robustly developed to provide societally acceptable levels of safety. The specific aims of this thesis are: (1) to develop an evaluated quantitative analysis method to enable fire engineers to practicably consider more of a complex system; and (2) to investigate potential unaddressed hazards embodied within current model solutions.

1.2 Objectives

The objectives of the thesis are presented in the following list.

1. Develop and numerically verify a new coupled hybrid model implementation.
2. Design and carry out novel experiments and hence elucidate potential hazards embodied in the current fire safety design and analysis paradigm.
3. Experimentally benchmark the new model implementation and output relevant correction factors.

1.3 Background

1.3.1 'Fire engineering' yesterday

One of the first examples of the regulation of building fire safety was a proclamation made by King Charles II, after the Great Fire of London, in September 1666 [3]. The proclamation stated that all new buildings were to be made of brick or stone and that main roads should be widened to inhibit fire spread. This decree, made over 350 years ago, was a cornerstone of prescriptive fire safety design of the built environment. Over the following 300 or so years, prescriptive fire safety policy, law, guidance, and codes proliferated internationally.

However, during the 1990s, enabled by an increasing understanding of fire science and the development of analysis methodologies and driven by financial benefits, the built environment saw the rise of performance-based design in the field of fire engineering [4].

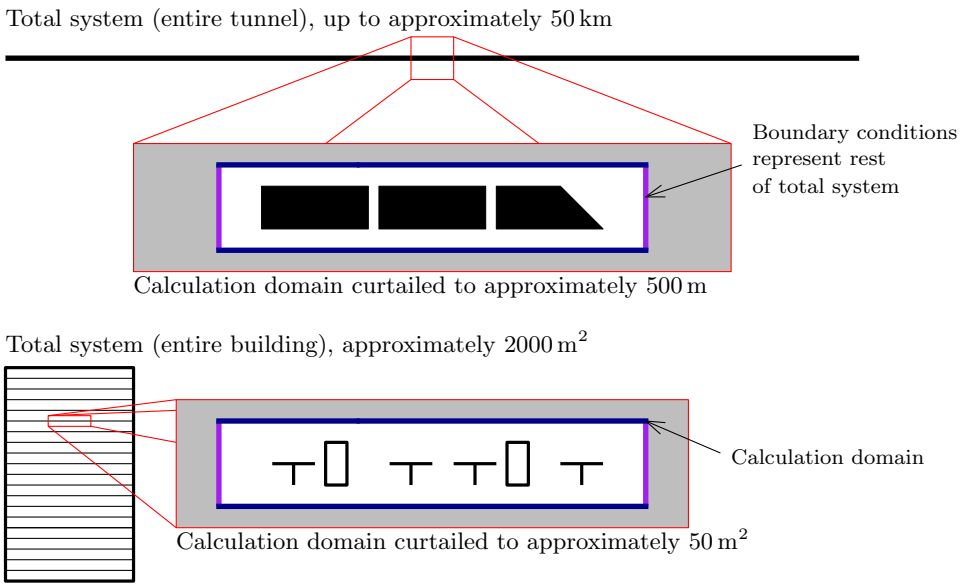

Figure 1.1: Typical fire engineering modelling paradigm.

1.3.2 Fire engineering today

Performance-based or outcome-based design is becoming more common internationally in fire engineering and fire safety design [5]. Especially for more complex or unusual elements of the built environment, it is replacing more traditional codified implicit safety or prescriptive design methods [6]. Performance-based design requires the explicit examination and measurement, either qualitatively or quantitatively, of fire hazard - to enable a risk-based analysis to be carried out. To fulfil this requirement, fire engineers often use fire models to predict how fire and smoke may spread through a building [7]. These predictions of fire hazard are then used to assess the consequence on occupants, structural stability, and fire spread.

Use of complex fire models, for example computational fluid dynamics (CFD)-based fire modelling tools (also called field models), as a means to predict fire hazard as part of performance-based design is customary. Employment of CFD-based fire models is becoming more commonplace as buildings get taller [8] and more complicated [9]. Simultaneously, the construction industry is becoming ever more driven by time constraints [10] and these constraints can lead to compromises in engineered safety [11]. Fire engineers and modellers are motivated to reduce the time required for analysis to take place [12]. One limitation of CFD-based fire modelling is the very long real elapsed times (wall-clock times) required to carry out a typical calculation on an element of the built environment (for example, a long tunnel, a tall building, or a large ship). Wall-clock times of weeks, months, or years are not practical for the construction industry, where design solutions often need to be assessed rapidly to enable design or construction to proceed [13].

Therefore, to deliver output within reasonable and expected timeframes, modellers curtail the domain (as shown in Figure 1.1) to keep simulation runtimes low [14, 12]. Modellers explicitly consider a small part of a total system (e.g. a single room in a building or a short section of a tunnel) and expand conclusions to the entire system [15]. Examples of the conclusions that may be incorporated into the fire safety design are: material choice, number of stairs, arrangement of egress routes, and smoke hazard management system requirements.

Based upon this spatially piecemeal design methodology, when a performance-based design incorporates sub-systems related to total system behaviour, reliance is (by necessity) often placed back upon prescriptive guidance or 'model solutions'. Examples of such total system-related design solutions are: interaction of elevator travel and system-wide pressurisation systems, building-wide pre-fire temperature differentials, effect on the near field of firefighting operations in the far field, and centralised ventilation systems. Given the large and complex spatial domain of these system, the typical performance-based design methodology (based upon the use of CFD-based fire modelling) cannot be practicably used. The analysis of systems involving a shared centralised ventilation system is explicitly pursued further in this thesis - though the method developed as part of this work could be used to carry out analysis of other applications.

1.3.3 Design of spaces connected with a shared ventilation system

Typical prescriptive design strategy

An archetypal mechanical ventilation and smoke hazard management strategy is the use of a centralised plant room. This plant room, which may incorporate multiple supply and return/exhaust air handling units, is shared between smoke control zones. The smoke control zones may also be different fire compartments, depending on the fire safety strategy of the building. The general intent of most national guidance with respect to shared mechanical ventilation systems used in smoke management upon fire detection is described in Figure 1.2 and the following list:

1. Turn the return air handling unit to smoke-spill mode for the fire-affected zone. Continue exhaust fans running to the fire-affected zone until failure of the system or operation of fire dampers.

2. Close return system air dampers to non-fire-affected zones. Open return air dampers to fire-affected zone.

3. Reduce supply air handling unit to make-up air mode and change to 100 % outside air. Continue operation to the fire-affected zone to prevent pressure increases that may preclude doors opening.

4. Increase supply air handling unit to adjacent non-fire-affected zones to provide a positive pressure differential between these zones and the fire-affected zone.

5. Shut down the supply air handling unit if smoke is detected within the air handling unit in the shared air handling plant room.

6. Provide fire and smoke dampers on exhaust system ductwork where it passes through construction bounding fire or smoke compartments.

7. Provide fire and smoke dampers or fire-resisting ductwork to supply ductwork where it passes through construction bounding fire or smoke compartments.

The assumption behind the provisions of point number 5 is that hot gases and/or smoke may leak out of the exhaust air handling unit or ductwork within the shared plant room and be drawn into the supply air handling unit. In this case, hot gas or smoke would be blown into both the fire-affected and the non-fire-affected zones. To preclude this, the supply air handling unit is shut down. As previously discussed, quantitative

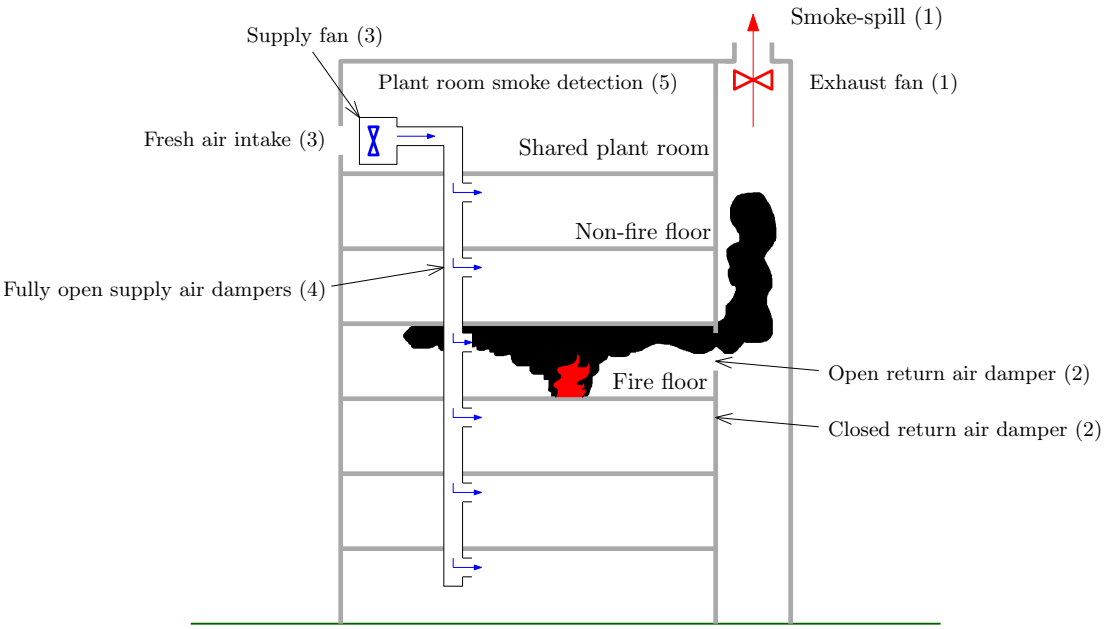

Figure 1.2: Typical fire mode mechanical ventilation operation implementing a shared air handling plant room.

consideration of a total system is often impracticable. Therefore, this 'model solution' has most likely been empirically developed using qualitative engineering consideration and experience.

National guidance for shared ventilation systems

Examples of the fire safety measures within specific 'model solutions' from the relevant guidance documents and Standards of the United Kingdom, Australia, and the United States are examined to establish, what could be described as, international good practice.

British Standard 9999: 2017 - 'Fire safety in the design, management and use of buildings. Code of practice' [16] gives guidance on safety provisions for mechanical ventilation systems. The guidance recommends that fire and smoke dampers be provided where exhaust ducts pass through fire-resisting construction. The guidance does not recommend the same for supply systems and protecting the duct externally is sufficient. The risk is considered to be the compromise of the fire-resisting construction and not spread via the supply system. The Standard recommends that smoke detection should be provided in a shared air handling plant room and in exhaust ducts. No smoke detection is recommended within the supply system. The assumption being that no smoke will enter or spread via the supply system. The provision of smoke detection within the plant room does not address the risk of smoke spreading via the downstream supply system - not entering the plant room - and spreading to other downstream areas via the supply system network. Upon fire mode exhaust systems are recommended to be kept on and run to destruction. Supply systems are recommended to be stopped. This further increases the risk of smoke and fire spread via the downstream supply system duct network.

Australian/New Zealand Standard 1668.1: 2015 - 'The use of ventilation and air conditioning in buildings. Fire and smoke control in buildings' [17] gives guidance on the use of mechanical ventilation systems with respect to fire safety. The Standard

recommends air dampers only on supply systems to enable the control of make up air for smoke exhaust systems. Fire and smoke dampers are not required on penetrations in smoke control zones if hot smoke is not drawn through that duct by design in fire mode. No consideration is given to the possibility that hot gas and fire could spread via the downstream supply system, against the flow of the fans.

NFPA 92: Standard for Smoke Control Systems [18] gives recommendations for the provision of mechanical systems used to control smoke. The Standard recommends that smoke detection be provided in a shared plant room containing air handling units, including specifically in the inlet of supply systems air handling units. The addressed risk is smoke entering the plant room, being drawn into the supply system and hence being actively blown to other parts of the building. There is no protection recommended to the downstream parts of the supply system network however. This means that there is a risk that smoke can enter the downstream supply system and spread to other connected spaces via the supply system without entering the plant room and activating the smoke detectors. The recommendation is that supply air handling units are turned off in fire mode. This would increase the risk that fire and smoke can spread up a downstream supply duct, against the 'normal' direction of air flow.

1.3.4 Importance of experimental data within fire engineering

For development of prescriptive solutions

Prescriptive solutions, especially ones for large and/or complex systems, are often based on engineering judgement and/or a posteriori knowledge. For example, guidance for the provision of lobbies to stairs in residential developments in the UK was developed using a qualitative engineering consideration of likely means of smoke spread (engineering judgement) and guidance for the provision of compartmentation following the large fire at Summerland in 1974 (a posteriori knowledge). The latter of these solutions are sometimes called 'design by disaster' and often apply to low probability, high consequence catastrophes.

The potential problem with using these two methods to generate prescriptive solutions is that engineering judgements may miss important parts of a system (especially for complex systems) and a posteriori knowledge requires an unwanted event to occur.

A third route to develop prescriptive solutions is experimentation. This route involves carrying out a range of experiments, with the aim of representing typical arrangements, and creating model solutions to address the hazards witnessed in the experiments. An example of this method is the codification of the fire safety design of mass timber buildings in the International Building Code 2022 based upon a series of large scale experiments. One of the motivations of the data generated as part of this thesis, is to assist in the formation of more robust model solutions which are based upon experimental data of total systems.

For validation of models

The modelling of buildings is inherently prone to error [19]. Model developers must translate a real system into a conceptual model and then to a numerical model. Verification and validation (sometimes called V&V) has been developed to quantify and minimise errors within this process. V&V can help deliver useful models which have been designed to meet a purpose. Verification is checking the implementation of the mathematics, i.e. the linking of the numerical model to the conceptual model. Validation is checking that the conceptual model predicts the real system accurately enough

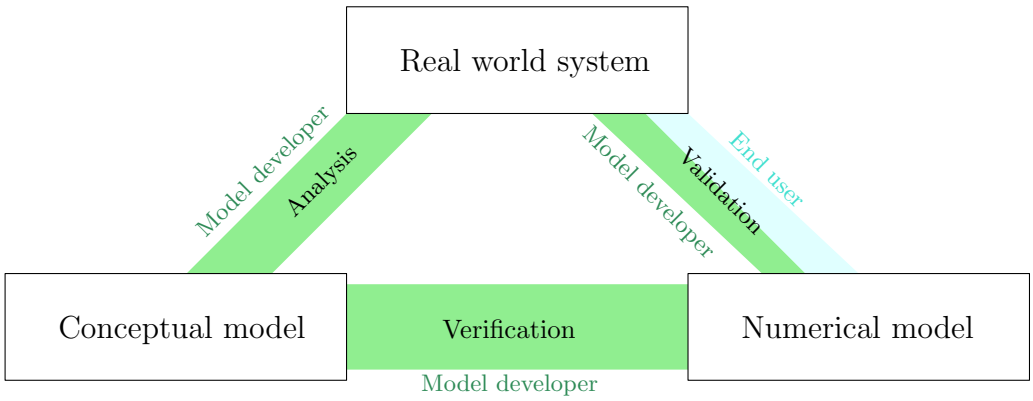

Figure 1.3: The connection between the real world, conceptual model, and numerical model. Input from the developer and the user is shown.

for a given purpose. This is described in Figure 1.3. In this way, validation is inherently linked to purpose [20].

Why is the quantification of accuracy important? Numerical models are used to make decisions as part of a design process or an investigation process [21]. Model users need to understand how accurate the predictions by the numerical model are when predicting the real world. This enables the designer to understand and accept the risk embodied in the prediction uncertainty of a real system. For example, if a simple empirical model for smoke filling time is used to define limitations on the maximum occupancy of a room and the designer knows that the model typically under-predicts the smoke filling time they may be more confident in safely relying upon the output of the model when forming their design. Validation is the process by which this crucial knowledge is gained.

Validation involves three stages. Comparing model predictions with experimental measurements, quantifying differences and uncertainties of measurements and model inputs and deciding if the model is suitable for the application. These first two stages can be referred to as benchmarking. Benchmarking is defined as the process of determining how accurately a numerical model predicted the real-world physical phenomena [22]. The third and final step cannot typically be carried out by the model developer and must be carried out by the user of the model. This is because it is case-specific and a model developer, especially within an open source environment, can never control to what cases users choose to apply the numerical model.

1.4 Problem

1.4.1 Fire engineering modelling methodologies

Current modelling paradigm

Over half of fire fatalities in the built environment in the US, UK and Australia occur outside of the room of fire origin [23, 24, 25]. Over 65 % of UK fire fatalities are due to smoke inhalation [26]. The entire building system and its ventilation have significant influence on how fire behaves and how smoke is generated and spreads throughout the system [27]. Considering the total building system when carrying out fire engineering analysis is imperative [28].

The current typical fire engineering modelling paradigm, described in Section 1.3.2, ignores this two-way interaction of the total system and the fire. The potential for the

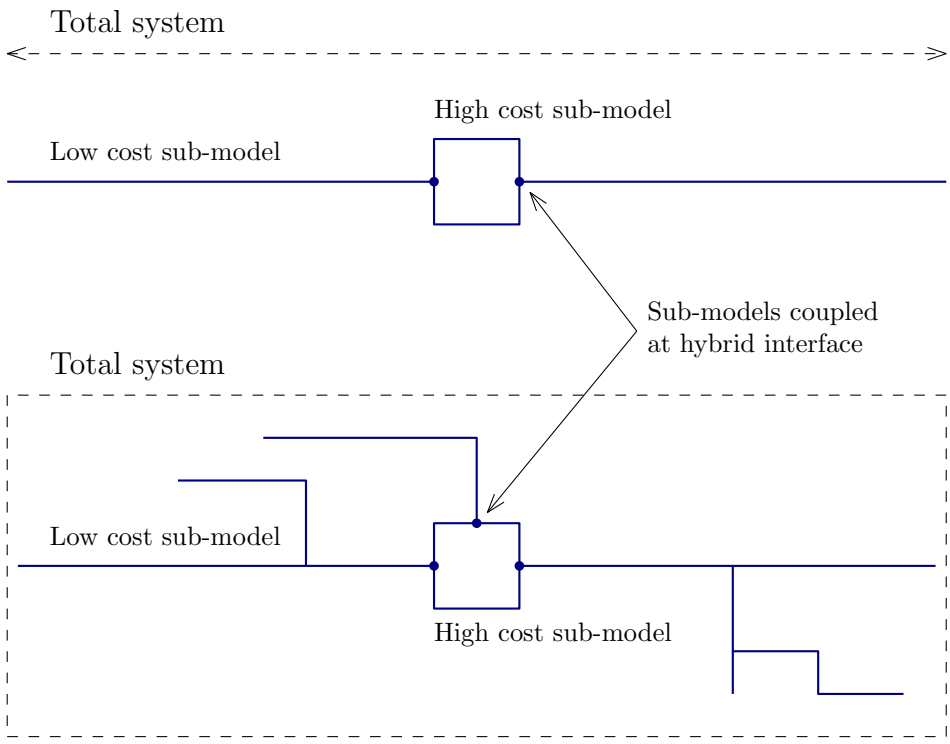

Figure 1.4: Schematic of coupled hybrid modelling for tunnels (upper) and buildings (lower).

total system affecting the fire, for example the operation of a shared ventilation system or remote doors opening and closing, is ignored. The potential for the fire to affect the total system, for example smoke spread via a mechanical exhaust system or fire spread to the level above, is also ignored.

A real world exemplar of this risk is that, within the current modelling paradigm, the potential for smoke from a fire at level 3 of a multi-storey hospital building spreading to an intensive care unit (ICU) at level 5 via the stairs or ventilation system is ignored - as the latter level is outside of the calculation domain. The designer and stakeholders would have no data to inform them that the ICU occupants could be at risk. The acuteness of this risk is increasing, as buildings are getting larger and more complex [8, 9], tunnels are getting longer [29], and the whole built environment is becoming more reliant upon performance-based design [5].

Innovative methods and limitations

There are multiple areas of contemporary research that aim to address the risk embodied in the requirement to curtail the domain within the current fire modelling paradigm that may be leading to buildings that do not meet the relevant fire safety objectives. These include adaptive meshing [30], the use of lower fidelity models within a risk or reliability-based model [31], and coupled hybrid fire models. The latter of these methods, which is described in Figure 1.4, is the topic of this thesis.

Coupled hybrid fire models constitute the coupling of two or more fire models to one another, such that the benefits of the constituent sub-models are experienced for the hybridised model. Coupled hybrid modelling can be used to expand the domain of a fire calculation using a very computationally cheap model. This method enables modellers to expand the calculation domain and explicitly examine more, or all, of a total system [32, 33]. In this way, more or all of the total system can be included (albeit

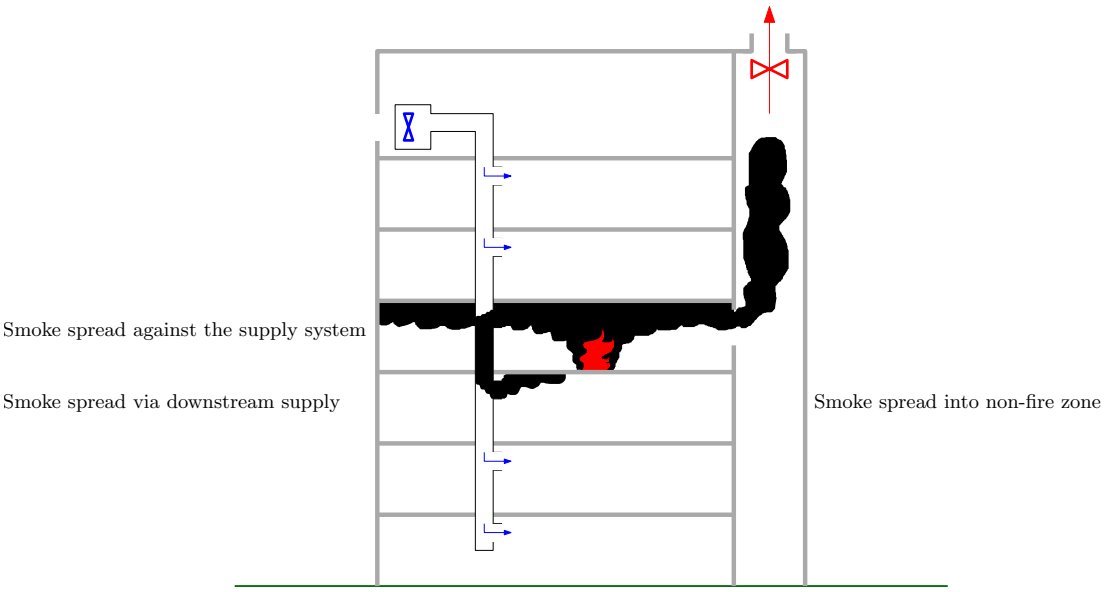

Figure 1.5: Potential smoke spread from the fire floor to non-fire floor via the supply system of a shared ventilation system.

in a simple manner) in the computation. Therefore, a fire engineer can quantitatively estimate hazard within a system, accounting for the two-way coupling of the total system and the fire. However, development and evaluation of coupled hybrid models has been limited and sporadic.

Fire Dynamics Simulator (FDS) version 5.5 introduced a 1D network sub-model (called 'HVAC') which could be coupled to the field domain at vents. Prior to FDS version 6.5.3 (the version that first included the novel developments documented in this thesis), this 1D network sub-model instantaneously moved energy and matter from the inlet vent to the outlet vent within the field domain. There was no unsteady motion of mass or energy through the HVAC network subdomain. This meant that for calculations where time-dependent phenomena were important, for example evacuation assessments, the use of FDS as a coupled hybrid model may not have given accurate predictions.

Furthermore, there are no experimental datasets to be used as validation cases to enable the quantification of output uncertainty for a coupled hybrid model implementation. Such case-specific validation requires suitable benchmarking experimental data and is required as part of a robust fire engineering analysis.

1.4.2 Holes in guidance, model solutions, and residual risk

Recognising that, given the current limitations on the use of CFD-based fire models and the time constraints of the industry, typically used performance-based analysis methods are not practicable for holistic analysis of shared ventilation systems, then the risk contained within the 'model solutions' should be examined.

There is no recognition within standard practice or national guidance documents of the United Kingdom, Australia, or the United States that hot gases, smoke, or fire may spread against the flow of the supply system within the downstream supply system network. This phenomena is described in Figure 1.5. There is agreement within the guidance documents that smoke within the shared plant room should be detected as soon as possible to ensure that supply air handling systems do not push smoke to unaffected parts of the building.

There is a complex interplay between a total building system and a fire. A total building system may affect the growth and spread of a fire, for example by the operation of a mechanical ventilation system. A fire may affect a total building system, for example by spreading far beyond the room of fire origin. There is the potential for there to be phenomena that could have a high hazard to life but which are not examined by existing experimental set ups.

Guidance documents, Standards, and best practice (being implicit safety level design documents) are based partially upon experiential evidence. There is a risk that under-examined mechanisms that pose a life safety risk are not addressed in current guidance. This is becoming more important as elements of the built environment are becoming more complex, more interlinked, and more reliant upon mechanical systems. For example, underground facilities and supertall buildings.

1.5 Solution

1.5.1 Enabling coupled hybrid modelling

Model development

To address the risk embodied within the typical fire engineering modelling paradigm and unlock the potential of FDS to be used as a robust coupled hybrid model, the unsteady transport of mass and energy through the HVAC sub-model has been developed and implemented into the release version of FDS as part of this thesis. This addition enables designers to use the coupled hybrid modelling method to effectively expand the domain of their calculation whilst still being able to deliver results to the stakeholder team within a reasonable and expected time frame.

Model benchmarking

Providing benchmarking information for numerical models is a key stage in model evaluation. Specifically, model validation. New experimental data are required to act as benchmarking cases, enabling model users to carry out case-specific validation exercises.

It is unrealistic to expect a model to be validated for all potential uses by the model developers. Instead, the model developers (or other collaborators) can provide suitable benchmarking data so that a user may validate the model for their use. The benchmarking exercises should belong in the parameter space expected for the typical application. This ensures the usefulness of the benchmarking exercises.

A new experimental rig provides quantitative data with known uncertainties. These data can then be used as benchmarking data and also to investigate phenomena of enclosures connected with a shared mechanical ventilation system. The data that the experimental rig provides reflect the quantities that are typically used within the fire safety and building design industry. That is, primarily, temperatures and velocities.

Within the literature of numerical models for fire, there is a tendency to concentrate on a single benchmarking method. For example, the comparison of quantities through time, maximum heat release rate, or flame spread speed. In this work, a gamut of benchmarking methods are utilised to provide a fuller picture of the uncertainties between the numerical set up data and the experimental apparatus data. The more information that is provided to a model end user, the more robustly they can utilise the novel model implementation as part of a competently executed fire engineering analysis.

1.5.2 Towards more robust design guidance

The limitations within the current typical design and assessment framework are at least partially due to limited investigatory experimental data and the current CFD-based fire modelling-driven assessment paradigm of considering only the domain immediately surrounding the room of fire origin.

Therefore, in addition to the development and evaluation of a novel coupled hybrid modelling implementation, a new experimental rig has been developed, which features spaces connected only with a shared ventilation system. This ventilation system is broadly representative of a typical mechanical ventilation system. That is, it incorporates a recycle mode, representing the normal use of a space, and also a smoke-spill mode. The intent of the experimental rig is not to provide a scale model of a real building. Instead, it is to be paradigmatic of the built environment and exhibit the same functionality, mechanisms, and phenomena. The experimental rig is located within the same parameter space as that of the built environment for which an assessment method will be developed.

Due to time, money, and scope limitations the new experimental data is not proposed to be used as the single source of information to review and modify standard guidance and model solutions. However, it can be used as an initial investigation and also to signpost where further investigatory research could be directed.

1.6 Value

This thesis documents the development and evaluation of a novel coupled hybrid modelling implementation within the most widely used, open source, and freely available fire model in the world. The application of the conceptual model has been verified to be coded correctly. A specifically designed experimental campaign has been used to generate data which have been used to quantify uncertainties and provide model correction factors for typically used output quantities. The novel model implementation can therefore be used by fire engineers to quantitatively analyse a larger proportion of a total system when compared to the current typical modelling paradigm. The implication of this is that the unknown hazard embodied in large and complex buildings can be reduced. The fire safety design can be adapted as required to address the quantified hazard and the information passed to the project team, stakeholders, occupants and users, and society can be relied upon as being more robust.

Furthermore, data from the novel experimental rig can be used to inform the development of international guidance and good practice with respect to the design of buildings with a shared ventilation system.

1.7 Roadmap

The structure and content of the thesis is described in the following list.

- Chapter 2 critically reviews literature of coupled hybrid modelling, primarily in fire engineering.
- Chapter 3 documents the creation and numerical verification of the novel coupled hybrid model implementation and a novel fan model.
- Chapter 4 presents the experimental design and methodology for the novel experimental rig.

- Chapter 5 gives the numerical case design and methodology, which was built for the benchmarking exercises.
- Chapter 6 presents and describes the experimental results.
- Chapter 7 analyses the experimental data.
- Chapter 8 compares the experimental and numerical data, as part of a benchmarking exercise.
- Chapter 9 discusses the major findings of the thesis, their implications, and limitations.
- Chapter 10 concludes the thesis.
- Appendix A provides laboratory notes to provide more description and images of the experimental apparatus and to document hopefully useful 'lessons learnt' during the development of the rig.
- Appendix B provides the new source code produced by the author.
- Appendix C provides the FDS input file used for the benchmarking exercise.

Chapter 2

Literature review

2.1 Preface and statement

This literature review has been published within Fire Safety Journal [34]. The second author was Dr Ricky Carvel, the first supervisor for this thesis. Dr Carvel provided editorial input to the journal article. The work presented in the article and this chapter is that of the author of this thesis.

The existing coupled hybrid models within the field are examined. This critical review concentrates on model capabilities and evaluation, methodologies adopted, and performance and success. The aim is to learn from past work and increase project impact.

2.1.1 What's in a name?

Coupled fluid modelling has been investigated in a wide range of fields of study (haemodynamics [35], indoor air quality [36], building ventilation [37], including fire [38], tunnel ventilation [39], including fire [40], wildland fire [41], and climatology [42]). Each field has slightly differing terminology for this method, including coupled, hybrid, integrated, multiscale, two-scale, multi-dimensional, 3D-1D, field-zone, field-network, and others. In this review we adopt the catch all term 'coupled hybrid' to describe the coupling of two or more sub-models, which have the same overarching function, into a single hybrid model. It is acknowledged that some coupled hybrid models may also be multiscale (work at multiple scales of time and space), 3D-1D (couple 3D and 1D fluid solvers), field-zone (couple a field model and a zone model), etc.

2.1.2 Modelling methods for fire and smoke

A short description of the model types discussed in this review is presented in the text and in Figure 2.1. The definitions are not designed to be comprehensive explanations, but instead to give a broad overview and to point those interested to further reading. The models are presented in order of increasing complexity and computational cost.

Network models

1D network models represent a system as a one-dimensional network of nodes (compartments or junctions) and node connections (ducts, tunnels, corridors, or leakage paths). Nodes contain a single set of variables such as temperature, density, mass and are treated as homogeneous. Node connections represent 1D transfer conduits between

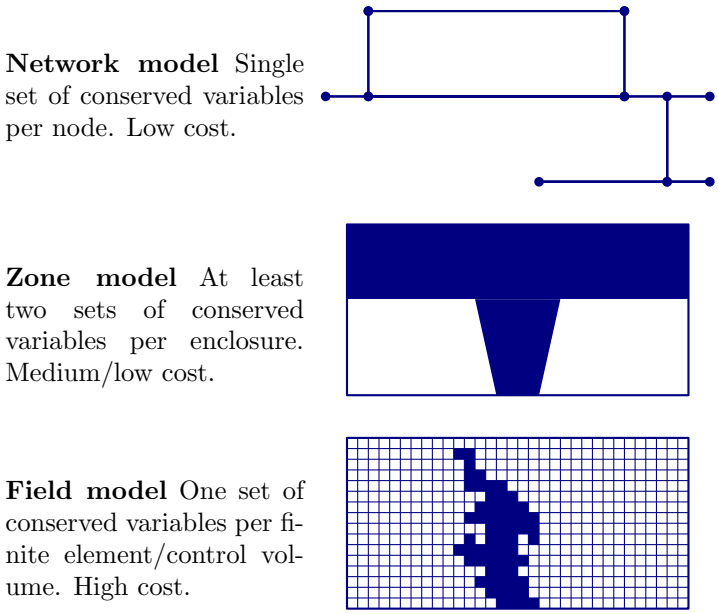

Figure 2.1: Hierarchy of typical fire engineering simulation models.

nodes. Network models contain relatively simple forms of conservation equations (such as the use of Bernoulli's equation for the conservation of momentum) and hence enable a large domain to be analysed with low computational cost [43]. Examples of network models include the Subway Environmental Simulator (SES) [44] and Fire and Smoke Simulator (FSSIM) [43].

Zone models

Zone models represent a compartment as multiple uniform zones (typically two zones: a hot upper layer and a cooler lower layer) with the inclusion of vents to represent doors and windows [45]. Zone models solve conservation equations between the uniform zones and typically include empirical relationships for phenomena such as fires, plume flow and corridor jets. Zone models are limited by the geometry they can represent (simple, cuboidal compartments), but are solved relatively quickly. Examples of zone models include CFAST [46] and BRANZFIRE [47].

Field models

Field models, also called computational fluid dynamics (CFD) models, divide a domain into finite elements or volumes for which conservation equations are solved. Each finite element holds a set of conserved variables. Field models can be used to examine complex geometry but require large storage space, high computation requirements and have a high computational cost. Due to typical meshing strategies, field models are not well-suited to studying leakage through small gaps in a relatively large enclosure [48]. Examples of field models include FDS [49], SMARTFIRE [50], and FireFOAM [51].

Alternative 'coupled models'

The term "coupled modelling" is sometimes also used in fire science to describe the coupling of field models and solid-phase heat transfer and structural response models

[52, 53]. These are not considered to be "hybrid" models (the sub-models do not perform essentially the same function) and are outside of the scope of this review.

2.2 Coupled hybrid modelling in other fields

The haemodynamics industry has employed coupled 3D-1D hybrid fluid models to simulate multiscale blood flow through vessels [54, 55, 56, 57, 58, 59, 60]. Coupled hybrid modelling in haemodynamics also incorporates unsteady geometric deformation of the vessel; typically via the use of FEM [61].

The automotive industry use coupled 3D-1D hybrid fluid and combustion models to simulate internal combustion engines [62, 63, 64, 65]. Coupled hybrid methods enable the entire system, including combustion chamber, fuel injection, exhaust, intake, and filters to be efficiently modelled. The method is used especially during engine development stage. 1D models typically used to simulate whole engine behaviour are phenomenological and require fitting to experimental data. To address the lack of validation data, 3D fluid models are used to capture complex combustion processes and pollutant generation [66].

Tunnel ventilation researchers and practitioners have developed and used coupled 3D-1D hybrid models for the 'multi-dimension' design and assessment of ventilation systems and passenger comfort and safety [39, 67, 68, 69]. In this industry the use of 1D network models to design ventilation systems is typical [39, 70]. However, calculation of 1D junction loss factors is slow and labour intensive [71] and the required oversimplification of complex geometries at stations could introduce passenger comfort and safety risks [72].

The field of building simulation (the study of ventilation and air quality in buildings) uses coupled hybrid modelling; these instances involve the coupling of a 'multizone model' (a 1D network model) and a field model [37, 73, 74, 75, 76, 77, 78, 79]. In building simulation, the field sub-model is typically used to simulate external wind conditions around the building and not features inside the building.

Wildland fire researchers use coupled hybrid methods, typically called atmosphere-fire coupling, to examine the interaction of wildfire and atmospheric systems [41, 80, 81, 82]. Studies couple a field model (used to simulate mass and enthalpy flow in the atmosphere above a wildfire) and an empirical 2D fire spread model. The fire spread model provides a source of enthalpy to the atmosphere field model which then models large scale atmospheric flow and turbulence with a grid cell size of typically 20 m to 100 m.

2.3 Coupled hybrid modelling in fire engineering

In fire engineering, coupled hybrid modelling can be broken into three categories based on the selection of sub-models. The categories are coupled field-zone, field-network and zone-network hybrid models. The following sub-sections provide a critical literature review of each category in turn.

2.3.1 Coupled field-zone hybrid models

The earliest of the coupled hybrid model categories to emerge in the 90s. These models are used to examine building and ship fires. These coupled hybrid models simulate the

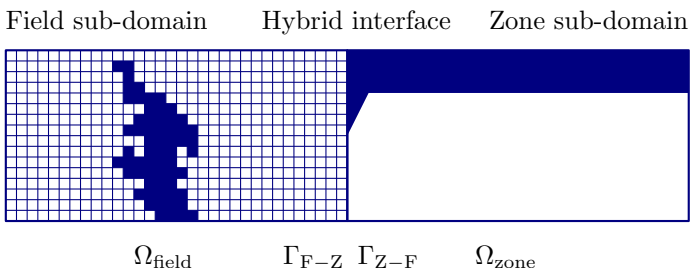

Figure 2.2: Coupled field-zone hybrid model schematic.

fire, the enclosure of fire origin and proximal enclosures in the field sub-domain and simulate medium to far field spaces in the zone sub-model. Refer to Figure 2.2.

Xu et al. [83] developed a coupled field-zone hybrid model and documented the results of a numerical demonstration case on a single storey, multi-room building. The field sub-model was 2D and was coupled to a bespoke zone sub-model. No validation of the coupled hybrid model was presented. Wang et al. [84] later extended the field sub-model to enable the consideration of 3D cases - the article is not scientifically thorough and presents a short summary of the extended model with no verification or validation.

Fan et al. [85], from State Key Laboratory of Fire Science of China, presented a field-zone hybrid method, coupling proprietary unnamed sub-models to create a new model called F-Z model. The field model used k-ε turbulence modelling. In the field sub-domain, the hybrid interface is a zero gradient Neumann boundary condition for all variables except the perpendicular velocity component which is output based upon mass conservation. In the zone sub-domain, the hybrid interface is a mass and enthalpy flux boundary condition - computed using relevant summations of variables (velocity, temperature, specific heat, species concentration, and density) taken from the adjacent field sub-model grid cells. Heat losses to the bounding construction are ignored.

The authors validated the F-Z Model against medium-scale fire test data of a two-room arrangement with generally good agreement. The hybrid model over-predicts the peak gas temperatures in both the fire room and the connected room by approximately 3 °C to 10 °C. The author states that this may be due to the omission of heat loss to the bounding walls. The validation case heat source was an electric heater; this limits the conclusions that can be drawn as phenomena such as changes to density and pressure due to mass flux from a fire, soot disposition, and spatial variability of burning (due to low equivalence ratio) are neglected.

Fan & Wang [86] further developed the F-Z Model, describing an enhanced coupled field-zone-network hybrid model called FZN Ver. 3. Fan et al. [85] and Fan & Wang [86] contain disagreement in the model descriptions, with the latter publication describing the original F-Z Model as including a network sub-model. It is presumed that an unpublished version 2 of the FZN model introduced a network sub-model. Fan & Wang replaced the network sub-model with a single control volume zone sub-model and altered the zone sub-model pressure modification method. The former change is self-explanatory and the authors state that this optimises the code. There is no discussion of the effect of removing node connections, and hence axial velocity, from the network sub-model. The second change is that the zone sub-model of FZN Ver. 3 computes pressure modifications using energy and volume conservation - in contrast to the original model which used mass conservation. The authors state that this method converges faster and more reliably. The article describes the original method as unstable as compartment mass is an implicit parameter, whereas volume is constant and therefore less likely to

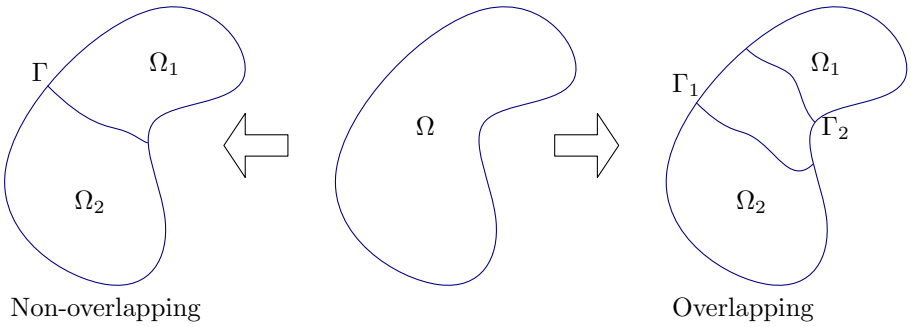

Figure 2.3: Differing domain decomposition methods.

lead to divergence. This is in contrast to CFAST 6's solution, which is based upon conservation of mass and energy [87]. The article presents no validation of the updated FZN Ver. 3. Similarly to the 1992 F-Z model, the fire is modelled as a source of mass flow at a certain temperature. There is no discussion of heat loss and this is assumed to be absent in the FZN Ver. 3 model.

Yao et al. [88] continues the coupled hybrid modelling work carried out by Fan and colleagues [85, 86]. The FZN model involves the coupling of the FAC3 (Fire And Combustion in three dimensions) field model with the two zone model and the one zone model from the previous FZN Ver. 3 model. FAC3 uses k-ε turbulence modelling and the two zone model uses the multi-cell method presented by Chow [89]. The field sub-domain is extended into the two zone sub-model domain (an overlapping domain decomposition, refer to Figure 2.3). The authors state that it would be difficult to model the field-zone interface boundary condition otherwise – this is in contradiction to later work by Burton [90], see below. A hybrid interface vent in the zone sub-domain is covered by the field sub-domain; the vent flows can be obtained directly from the field sub-model velocity data (in contrast to mass conservation adopted by Fan et al. [85]). For these hybrid interface vents, entrainment mixing is computed using an empirical relationship. In the one zone sub-domain, the two zone sub-model provides a velocity boundary condition computed using the pressure difference across the vent; entrainment mixing from the lower layer is ignored.

Yao et al. validated the FZN model using a half-scale experimental room and corridor arrangement with a 9.7 kW fire source in the room. No data are compared for the field-modelled fire room. The authors compare temperatures in the upper layer in the corridor for the experiment and the FZN model (i.e. two zone sub-domain). The FZN model predicts the general trend, but over-predicts temperatures by 10 °C. The authors do not discuss how they define a layer height from the test results. The authors present a FZN model demonstration case of a five-storey building. As in the precursory FZN Ver. 3 model, heat losses to the bounding construction are ignored and the fire is modelled simply as a source of heated mass.

Hua et al. [91] present the development and testing of a coupled field-zone hybrid model called Hybrid Field and Zone Model (HFAZM). HFAZM couples a bespoke k-ε turbulence based field model and a bespoke zone model, which uses a mass and energy conservation pressure correction algorithm. This method is similar to CFAST [46] but is in contrast to Fan & Wang [86], who used energy and volume conservation. HFAZM models the fire as a source of heat and ignores heat loss to the boundary. In the field sub-domain, the hybrid interface is a pressure boundary condition, using zero gradient variables from the zone sub-model plus a hydrostatic distribution. In the zone sub-domain, the hybrid interface is a mass and enthalpy flux source, which is computed

using adjacent field sub-domain density, velocity, specific heat and temperature data.

The authors compare HFAZM to the output of alternative numerical methods for a room and corridor arrangement (with the multicell method being used in the zone sub-model simulated corridor). Comparison is against a full zone model (CFAST) and a full field model (Fluent). There is good agreement between HFAZM and the full field model for steady state smoke layer height in the corridor, with maximum deviations at the end of the modelling period of approximately 40 mm. Transient conditions in far field of the modelling domain are predicted less consistently with maximum deviations of approximately 300 mm. The authors attribute this to lateral spread of smoke in the zone sub-model being ignored; though the multicell method is proposed specifically to address this limitation. HFAZM predicts corridor smoke layer heights closer to the field model results than the zone model results. There is no comparison of temperature. For this case, HFAZM reduced runtime by 83 % when compared to full field calculations for a 70 % reduction in the field domain (over unity). The case featured a small fire size (100 kW) and a short runtime of 200 s. The article presents a demonstration case for a room/corridor/shaft/corridor arrangement over two levels; but does not compare to alternative simulation methods. The authors present no validation against experimental results.

Hua et al. use 'critical temperature' to reduce the approximately continuous variability of the field data into the two-zone assumption required for input into the zone sub-model. This method incorporates the prescription of a temperature, above which all mass and energy flows into the upper zone and below which all mass and energy flows into the lower zone. This is a simplistic methodology and is heavily sensitive to the prescribed critical temperature. This method also introduces the possibility of the creation of potential energy at the hybrid interfaces.

Jie et al. [92], from State Key Laboratory of Fire Sciences of China, present a coupled field-zone hybrid model, called LFZ, based upon a large eddy simulation (LES) field solver (specifically Fire Dynamics Simulator (FDS)). The article does not state the version of FDS or the zone model used. It is reasonable to assume that Jie's work is the continuation of that of others at the State Key Laboratory of Fire Sciences of China [85, 86, 88]. The proprietary FAC3 field code used previously appears to have been dropped in favour of the open source FDS code. The authors present the basic formation of the constituent solvers and state that the field sub-domain is extended over the zone sub-model vent consistent with Yao et al. [88]. Boundary conditions for the hybrid interface in the zone domain can be 'obtained directly from the field modelling simulation results'. The article does not discuss hybrid interfaces in the field sub-domain.

The authors present the results of a full-scale fire test of a room and corridor arrangement and provide numerical output from two zone models (CFAST and BR12), full field results from FDS, and results from the LFZ hybrid model. The peak fire size is not stated. All the numerical methods over-predict the maximum upper layer temperature by 10 °C to 40 °C with BR12 being the worst performing and CFAST, FDS and LFZ being very similar. Except for LFZ, all numerical methods predict the reduction in temperature following the removal of the fire source. LFZ under-predicts the enclosure cooling and over-predicts final temperature at 360 s by 20 °C. This is assumed to be primarily because LFZ does not model heat loss at bounding construction. FDS predicts the commencement of lowering of the layer height more accurately than all other models, which under-predict by 90 s. Both FDS and LFZ predict well the reduction of layer height to its minimum and the value of this minimum, with final layer height

being within 100 mm.

Ren et al. [93] developed a training software targeted at firefighting in ships. The software incorporates a virtual reality (VR) interface, 3D visual representation of the sea, ship, flames and smoke, and a coupled field-zone-network hybrid model which is stated to include fire spread modelling. The article is short and presents very little information on the coupled hybrid model; it is unclear how it interfaces with the 3D visual simulation used for the VR training. The authors state that the field sub-model uses LES turbulence modelling and incorporates manual and automatic water suppression modelling. The article neither presents the theoretical or computational basis nor verification or validation of the coupled hybrid model. The authors state that 'the network model ignores fume flow and air flow'. It is assumed that this means the network model contains no mass and ignores transient species transport. The article states that the enclosure of fire origin is modelled using the field sub-model, the immediately adjacent enclosures by the zone sub-model and the rest of the ship by the network sub-model. This appears to have been arrived at by anecdotal evaluation and not analysis of conditions in these spaces and the suitability of the sub-model. The article is too sparse to allow any useful comment on the use of a coupled hybrid model. The article was presented at a software engineering conference and does not prioritise fire safety science.

Research carried out by Burton and colleagues [90, 38, 94] represents a comprehensive work package on coupled field-zone hybrid modelling and concentrates on ships and buildings. Burton developed and presented validation of a coupled field-zone hybrid model based upon the SMARTFIRE field solver package and two different zone models. Initially the coupled zone model was CFAST; however, due to pressure solution convergence issues, a novel zone model, called FSEG-ZONE, was embedded in SMARTFIRE. The problem with the use of CFAST was due to the differing scale time step used in the solving methods of the two sub-models: SMARTFIRE is an implicit solver, whereas CFAST is explicit, with much smaller time steps. This led to SMARTFIRE outputting large fluxes to CFAST at large intervals and caused convergence problems. Burton therefore developed a bespoke 'semi-implicit' zone sub-model, called FSEG-ZONE. The new zone sub-model is iteratively called until convergence for each field sub-model iteration; only then is the global time step advanced.

Interface boundaries in the field sub-model are pressure and temperature boundary conditions. The pressure consists of the zone room pressure, hydrostatic pressure distribution, dynamic pressure due to vent velocity and a 'normalisation pressure' used to correct the treatments of pressure in the two sub-models. The computation adopts upstream values of temperature and density. In the zone sub-model domain, the interface boundaries are mass and enthalpy flux source or sink terms; output using upstream values of density, velocity, specific heat and temperature.

The authors chose to pass fluxes from the field sub-model to the zone sub-model as this empowers the less empirical and higher definition sub-field model to calculate interface fluxes. Conservation is ensured by passing fluxes in one direction only; this would be uncertain if fluxes were passed in both directions (due to the differing numerical method employed by the sub-models). This method agrees with work by Hua et al. [91] and Floyd [95] but in contrast to Fan et al. [85] who pass fluxes in both directions and Wang et al. [96] who pass pressures in both directions.

Burton draws two separate case types; which are defined as 'open' and 'closed' cases. Open cases are those in which the zone sub-domain has a connection directly to the open atmosphere - pressure in the zone sub-model can equalise rapidly with the outside. Closed cases are those in which pressure relief is only available via the field sub-domain.

The latter case leads to pressure solution divergence when using the explicit zone model solver CFAST.

The author presents test cases comparing the FSEG-ZONE based coupled hybrid model with a SMARTFIRE-only model with the zone sub-domain replaced with a simple vent to ambient. In all cases the coupled hybrid model presented better agreement of results with full field simulations when compared to the simplified arrangement. Unsurprisingly, but importantly, the coupled hybrid model performs better than simply ignoring the extended domain.

Burton documents six numerical comparison cases against full field results and one validation case against full field and experimental results. Numerical cases are 3 to 11 room arrangements, fire sizes between 100 kW to 500 kW and include the heat source being removed during simulation. The CFAST coupled hybrid model over-predicts upper layer temperature by 2 % to 20 %, under-predicts lower layer temperature by 10 % to 20 %, over and under-predicts layer height by −300 mm to 200 mm (with disagreement increasing into the zone domain), as shown in Figure 1.1 and predicts a leaning plume when the hybrid interface is near the fire (towards zone domain). The FSEG-ZONE based coupled hybrid model without 1D conduction predicts well upper layer temperature and layer height (being bound by data reduction methods) and under-predicts lower layer temperature by 5 % to 50 %. When 1D conduction is implemented, upper layer is under-predicted by 20 % during cooling and lower layer is under-predicted by 30 % during heating. The coupled hybrid model agrees with experimental and full field results more than coarse grid field for layer temperatures and height. Burton postulates that the variance in coupled hybrid predictions is due to the zone sub-model uniform layer variable assumption - which leads to gas with a higher temperature venting from the compartment and uniform conduction.

In their short article, Jiao et al. [97] document a new coupled field-zone-network hybrid model, aimed at assessment of fire in ships. The article is not from a peer-reviewed resource, has limited content, and is poorly translated, which reduces its usefulness - it is presented here for completeness. FDS, CFAST and a bespoke model are used for the field, zone, and network sub-models respectively. There is no validation. The author omits discussion of the coupling methodology and uses a simple method to define the zone/network interface location (where hot layer height is 80 % or greater the network solver). It is impossible to say whether this simplistic method yields acceptable results due to the lack of validation. The article discusses and defines a scale model of a ship fire test rig; however, no reference is made to tests being carried out and no results are presented.

2.3.2 Coupled field-network hybrid models

These coupled hybrid models have been mainly used for the examination of tunnel fires, where the total system may have a length of tens or hundreds of kilometres. This may be due to the prevalence of 1D network models in tunnel ventilation engineering. More recently, this category has been applied to buildings and ships for the modelling of ventilation systems. Refer to Figure 2.4.

Li et al. [98] developed a coupled field-network hybrid model called Tunnel Network FIRE version 3 (TNFIRE3), which builds on the previous non-hybrid TNFIRE models. The coupled model hybrid is based upon an unnamed field sub-model, which uses k-ε turbulence modelling, the Semi-Implicit Method for Pressure-Linked Equations (SIMPLE) solver, and a bespoke network sub-model based on the Multidimensional Multiple-choice Knapsack Problem (MMKP) method. No information is given regard-

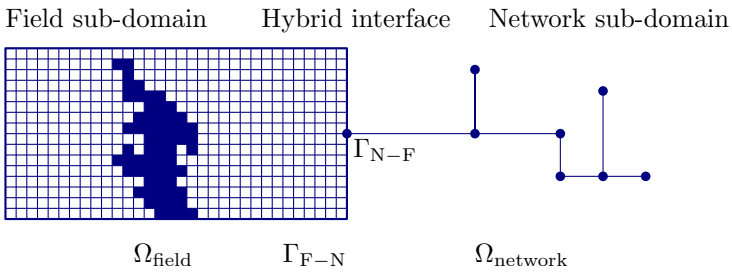

Figure 2.4: Coupled field-network hybrid model schematic

ing hybrid interface boundary condition treatment. The network sub-model includes heat losses to boundaries. The sub-models are solved sequentially for each time step. The field sub-model output at time step t_n, solved using network sub-model data from time step t_{n-1}, provides boundary condition data to the network sub-model for the solution at time step t_n. The authors define a smoke concentration and a temperature field to model the fire. The authors present a test case of Tehran Subway Line 1, but no validation.

Jiang et al. [99] presented the preliminary description of a coupled field-network hybrid model, based on bespoke sub-models, which was aimed at examining fires in mine networks. The article is based on a brief discussion of the mathematical basis of the coupled hybrid model and omits any example test cases, verification, or validation of the model. The nonlinear PDEs of the network sub-model are solved using the difference method of characteristic curves and the field sub-model (which uses k-ε turbulence modelling) is solved using SIMPLE.

The model features unsteady two-way fluid flow and asynchronously solves the constituent sub-models at each time step. The solution of the network sub-model at time step t_{n-1} provides the boundary conditions of the field sub-model at time step t_n, which is then solved to provide the boundary conditions for the network sub-model at time step t_n. In the field sub-model domain, at the hybrid interface, all variables (velocity, enthalpy, concentration, and k and ε) are adopted based upon the network sub-model parameters. It is unclear how this could be the case, as some parameters (e.g. y and z velocity component, and k and ε) would not be tracked in the network sub-model. This highlights an important point regarding how to track turbulence within the 1D sub-domain. In the network sub-model domain, at the hybrid interface, the sums of each parameter from the field sub-model grid cells adjacent to the interface are used to define an equivalent ghost node which is inserted into the network model. Jiang & Wang's hybrid model does not model any chemical reactions in the network sub-model, therefore any combusting of unburnt fuel or further oxidisation of CO is ignored. Heat loss to the bounding walls of the mine is ignored.

Deng et al. [100] present the further development of TNFIRE3, first published in Li et al. [98], a coupled field-network hybrid model for the assessment of tunnels. The coupled hybrid model is based upon the field code Phoenics, implementing k-ε turbulence modelling and a proprietary network model that is directly embedded in the field solver code. TNFIRE3 includes heat loss at the bounding walls of the domain. Deng states that, to 'save cost and time', radiation modelling and combustion modelling have both been removed from the Phoenics solver. The article documents the broad mathematical basis of the coupled hybrid model and presents a demonstration case using TNFIRE3.

In the field sub-domain, the hybrid interface is a mass flux boundary condition at

the field sub-domain inlet (with fluid properties being adopted from the network data) and a Neumann pressure boundary condition at the field domain outlet. In the network sub-model domain, the hybrid interface is a momentum source boundary condition at the inlet and a mass sink boundary conditions at the outlet. There is no discussion of the locating of the hybrid interface. This is a key item for coupled field-network models in tunnels as the cross-section properties (flow field, temperature, pressure, etc.) are required to be approximately homogeneous for the network model assumptions to be valid. There is no validation of the coupled hybrid model.

Jung et al. [101] examined coupled field-network hybrid modelling for ventilation of tunnel rescue stations. They used the commercial codes STAR-CD [102] and SES [44] for the field and network sub-models respectively. The article presents a numerical demonstration case in which the rescue station is within the field sub-domain and the remainder of the tunnel network is in the network sub-domain. Indirect coupling is used with the steady state network sub-model being solved initially and the output being used as constant boundary conditions for the unsteady field model solution (Dirichlet velocity and mass flux boundary conditions).

Work carried out by Colella and colleagues [103, 104, 105, 106, 107, 108, 109, 110, 40] is a comprehensive examination of coupled field-network hybrid modelling in tunnels. Colella developed a coupled field-network hybrid model for the examination of tunnels based upon Fluent, using k-ε turbulence modelling, and a bespoke 1D network model. Fires are modelled as sources of heat and mass. The coupled hybrid model can use either indirect or direct coupling. Indirect coupling entails the initial running of the field sub-model to obtain characteristic pressure-velocity curves for ventilation devices (such as fans) and fires and the subsequent use of these curves as boundary conditions for the network sub-model. Direct coupling involves the feedback of data between the two sub-models until convergence within a simulation time step.

The sub-models provide spatially averaged integral pressure, temperature, velocity and mass flow rate to one another, depending on the direction of flow. The hybrid interface assumes that area, mean pressure, mean velocity and mean temperature are identical on either side of the hybrid interface. The sub-model domains are coupled by way of a Dirichlet-Neumann boundary condition (Dirichlet and Neumann in the network and field sub-model respectively) and are based on non-overlapping domain decomposition. This method is similar to Li et al. and Jiang et al. [98, 99] but in contrast to Fan et al. [85]. Colella provides comprehensive grid size and interface location sensitivity analysis for all test cases and concludes that the interface should be located approximately 20 times the hydraulic diameter of the tunnel away from a fire or jet fan. The is no discussion of boundary layer effects and velocity profiles when moving from the sparse network sub-model to the field sub-model (i.e. at defective boundary conditions).

The coupled hybrid model is validated against full-scale steady state ambient (non-fire) conditions in a 1.2 km tunnel in Dartford, UK [107]. 80 % of the tunnel's length is modelled in the network sub-model. The coupled hybrid results are in very good agreement with the experimental results having a maximum velocity deviation of 1 m/s and a general velocity deviation of 0 m/s to 0.5 m/s. Output from the coupled hybrid model is compared to the output of a series of full field steady state fire condition cases for the same tunnel. Fire sizes of 10 MW to 100 MW are adopted in various ventilation conditions. The coupled hybrid results are in very good agreement with the full field results with maximum bulk velocity deviations of approximately 7 % (favourably compared to approximately 70 % deviations for full network model output). The use of the

coupled hybrid model reduced runtimes from approximately 50 h to 70 h for full field simulations to approximately 2 h to 4 h; a 95 % reduction in time for an 80 % reduction in field domain. Colella presents an unsteady fire condition demonstration case for the same tunnel; this was not compared to full field results as the predicted runtime was three months.

Floyd [95] presents the verification and validation of the coupling of a network model to the field model FDS (version 5.5) produced by NIST. This article is the precursory work to the network model that is included in FDS version 5.5 onwards ('HVAC'). The network sub-model is based upon the MELCOR solver [111], which was used in the Fire and Smoke Simulator (FSSIM) network model [43] (a propriety code produced by JENSEN HUGHES). The network sub-model incorporates an explicit solver for conservation of mass and energy and an implicit solver for conservation of momentum (Bernoulli equation with wall and minor losses). The network sub-model is designed for HVAC systems, and nodes do not have volume. There is no unsteady transport of species or energy or heat loss in the network sub-model.

The sub-models are asynchronously coupled or loosely coupled. The network sub-model solution at time step t_n uses field sub-model data from time step t_{n-1} as boundary conditions, is solved for a 'temporary steady state' (within that time step) and hence outputs boundary conditions for the field sub-model at time step t_n. This is similar to Li et al., Jiang et al. and Deng et al. [98, 99, 100] but in contrast to Burton and Colella [90, 103]. In the network sub-model the hybrid interface are pressure, temperature, and species concentration boundary conditions. For inflows from the field sub-model, variables are the density weighted average temperature and species concentration and the area weighted total pressure (background pressure and dynamic pressure) from the field model. In the field sub-model domain, inflows from the network sub-model are represented by mass flux and temperature boundary conditions. The temperature is adopted directly from the network sub-model. The mass flux is calculated from the species concentration, velocity, duct area, and gas density from the network model.

The article presents three numerical verification cases for flow losses, species concentration and mass conservation at non-uniform temperatures. The coupled hybrid model passes all verification tests. Floyd provides three validation cases, one against a canonical HVAC system solution from the ASHRAE Fundamentals handbook [112] and two against an enclosed space experimental test facility containing 23 compartments, four levels, 20 openings and three HVAC systems. There is very good agreement between the coupled hybrid model and the ASHRAE solution, with a maximum error in pressure drops of approximately 2 %. In the enclosed space experimental facility, two tests were carried out with a diesel pool fire. The first having no HVAC operating and the second with HVAC operating normally and then moving to smoke exhaust mode after one minute. There is very good agreement between visibility and velocity data for both tests, typically approximately 10 % maximum deviation. Floyd states that errors are expected to be primarily due to the lack of modelling of fan spin up/down times, differences in actual and reference table duct friction coefficients (one of the main drivers behind the work of Prince et al. [39] for tunnel ventilation modelling) and fan performances and heat release rate errors.

The network sub-model does not account for mass storage or transient mass, energy and species transport time, chemical reactions, or heat loss. Floyd states that as the pressure solutions of the sub-models are not tightly coupled an error may be introduced in the overall solution, however stating that this error will be small as, in typical fire scenarios, pressure changes slowly.

Vermesi [113] provides the opening for a stream of work from the Technical University of Denmark (DTU) and Imperial College London on the use of FDS+HVAC for tunnels. This workstream builds on the work of Colella but instead uses FDS 6 and the coupled network sub-model HVAC, in lieu of Fluent and a bespoke network sub-model. The fire is modelled as a source of heat and mass, in line with the methodology adopted by Colella. Vermesi carries out sensitivity studies of mesh sizing and location of field-network coupling location with respect to fire location across three numerical test cases.

Vermesi carries out numerical comparison cases against the full field and coupled hybrid model output data published in Colella. There is a general agreement although a reliance on visual results make it hard to make absolute comment on the veracity of agreement for temperature and velocity predictions. The modelling method does not account for heat loss at bounding construction or any environmental factors at the portals (they are zero-friction Neumann boundary condition vents).

Tao et al. [114] present a coupled field-network hybrid model for the examination of urban traffic link tunnel (large tunnel network) fires. The field sub-model, which uses k-ε turbulence modelling, is not stated and the network sub-model is a bespoke solver. Analysis is steady state and the sub-models are iteratively run until coupled hybrid model convergence. The output of one sub-model is used as boundary conditions for the next step in the iteration of the other sub-model. The fire is modelled as a source of mass and heat and heat loss to the boundary is not considered. Tao et al. present a numerical demonstration. There is no verification or validation presented.

Ang et al. [115] continue work on FDS+HVAC for tunnels and present validation of the coupled hybrid model for the steady state non-fire tunnel experiments given in Colella. They carried out a sensitivity analysis to investigate the effect of the limitations of the rectilinear meshing strategy in FDS 6.1.1 in representing a curved tunnel section. A rectangular and a stepped tunnel cross section is examined and the mass flow is shown to be within 2 % of each other. FDS+HVAC gives very good agreement with steady state experimental measurements of velocity for a range of jet fan arrangements, with predictions being bound by experimental error estimates. The results were shown to be sensitive to the geometric jet fan modelling method and the skin friction of the tunnel. The 1D network sub-model used less than 1 % of the total CPU time and the use of the coupled hybrid model reduced runtimes by ∼50 % for a ∼50 % reduction in field domain. Heat losses in the network sub-domain are not accounted for.

Vermesi et al. [116] further build on the FDS+HVAC for tunnels work and investigate the potential for combining coupled hybrid modelling with parallel processing. The article compares the steady state results from FDS+HVAC to that of the coupled hybrid model developed in Colella for the 1.2 km long tunnel fire scenario documented in Colella et al. The temperature is in good agreement with differences of approximately 2 %. The velocity, however, is not in good agreement, especially near the fire, though only visual output is shown of this metric. The authors state that this is due to the way the fan was modelled within the network sub-model and if a quadratic fan curve had been used, the throttling effect of the fire would have been captured (refer to Vaitkevicius et al. [117] for further discussion). The combined use of coupled hybrid modelling and parallel processing is shown to decrease runtime by approximately 90 % for an approximately 66 % reduction in field domain. Similarly to Ang [118, 119], heat losses in the network sub-domain are not modelled and the coupled hybrid model presents false/numerical oscillations of mass flow.

Given the continuous development and integration cycle used in the FDS project,

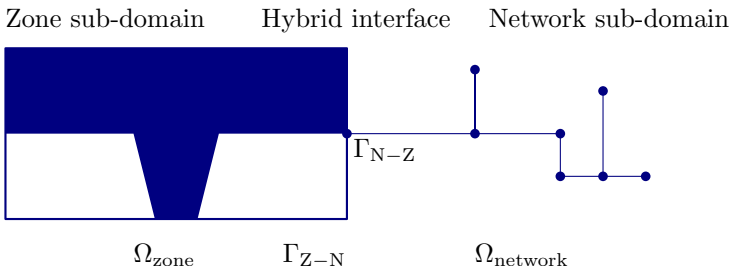

Figure 2.5: Coupled zone-network hybrid model schematic

there have been incremental improvements in the coupled hybrid model capability. The author of this review has expanded the coupled 1D network model HVAC in FDS 6.5.3 [49] to compute the unsteady transport of species and energy through the network sub-domain using an explicit Euler method. The FDS Verification Guide [120] presents various numerical verification cases of the transient coupled hybrid model against canonical solutions and first principles, which are passed with very low or nil tolerances. The network sub-model does not account for heat losses, allow for nodes with a volume and the unsteady conservation equations are based on pure advection. The FDS Validation Guide [121] presents the validation of FDS+HVAC (non-transient network sub-model) using experimental data from the PRISME Project [122] and the Lawrence Livermore National Laboratory (LLNL) enclosure experiments [123]. Upper layer and surface temperatures are predicted well (maximum deviations of 20 °C and 10 °C respectively), gas species concentrations are predicted reasonably well (maximum oxygen volume fraction deviations of 0.05), pressure is predicted very well (maximum deviations of 10 Pa) and heat flux is predicted reasonably (maximum deviations of 1 kW/m^2). Validation is not provided for the coupled hybrid model using the transient network sub-model.

2.3.3 Coupled zone-network hybrid models

The last of the three coupled hybrid model categories is the sparsest. Aimed primarily at building and ship ventilation, there is an emphasis on the development of the network sub-model. The fire is located within the zone sub-model and vertical shafts are simulated using the network sub-model. Coupling is invariably one-way. Refer to Figure 2.5.

Zhu [124], from Carleton University, presents the development and testing of a coupled zone-network hybrid model for buildings. The work centres primarily on the development of the network sub-model and there is little discussion of the zone sub-model or the coupling methodology. Zhu evaluates many nonlinear ordinary differential equation (ODE) solvers to justify the chosen solvers adopted in the network sub-model pressure equation. He concludes that the Newton-GMRES solver with the Krykov subspace method is the best suited solution method. The temperature equation is solved using the DLSODE solver. The pressure component of the network sub-model solves substantially quicker than the temperature component. Therefore, the pressure and temperature solver are uncoupled and are batch solved in series assuming the other parameter remains steady in the given time step. Zhu states that this avoids stiff ODEs in the pressure and temperature equations. This uncoupled method could reduce predictive validity, due to the assumption of lack of feedback within a time step, however the author claims that errors are within acceptable limits due to the small time steps.

The author presents numerical comparisons of the constituent zone and network models with CFAST and CONTAM respectively for a small single-storey building,

a multi-room single storey building and a ten-storey apartment block. The analysis demonstrates generally good agreement with the comparison methods. A demonstration case of the coupled hybrid model is presented for a ten-storey building. No validation is presented.

One-way coupling between the zone and network sub-models is completed manually by running the zone model, outputting vent mass flow rates and temperatures and inputting these data into the network model as mass sources. Zhu uses ceiling vents and does not discuss the method by which two zone data would be reduced in the case of a wall vent (e.g. door) to enable it to be passed to the network sub-model. The coupled hybrid model ignores heat loss to the boundaries and the fire is modelled as a source of mass at a temperature.

The ASHRAE Research Project RP-1328 [125, 126] is a continuation of the work carried out at Carleton University by Zhu. RP-1328 involved the development of a zone-network hybrid model based upon bespoke zone and network sub-models. Kashef et al. [125] contains the theoretical background and development of the two sub-models. As per Zhu, Kashef's coupled hybrid model incorporates only one-way coupling (mass fluxes from the zone model are passed to the network model). This is justified with the assumption that mass fluxes will always be from the zone sub-domain (room of fire origin) to the network sub-domain (far field). This makes it difficult to state that the model would be valid for large complex buildings where unsteady changes in ventilation could lead to reversing mass fluxes. In contrast to Floyd [95], the network sub-model tracks mass storage in the network sub-domain. At the hybrid interface, the network sub-model mass flux boundary condition simply adopts the temperature of the upper layer in the zone sub-model irrespective of the location of the hot layer. The coupling and solution methodology employed by Kashef is relatively simplistic and incorporates the steady state solution of the zone sub-model and the subsequent one-way coupling of these results to a separately-solved network model.

Hadjisophocleous et al. [126] present further numerical comparison cases and optimisation of the RP-1328 coupled zone-network model developed in Zhu and Kashef et al. The article presents numerical comparison cases for the constituent sub-models; the zone model against CFAST and the network model against CONTAM. The article notes that the solving of the network sub-model takes longer than the solving of the zone sub-model component. Although the network sub-model is substantially less complex than the zone sub-model, there are many more instances of the former. Hadjisophocleous introduces an adaptive time step that, for an undefined test case, is claimed to reduce the network sub-model run time by an order of magnitude whilst giving the same results.

Hadjisophocleous et al. compare the results from the zone sub-model to that of CFAST for a two storey, four room test building using a 1 MW fire. The zone models are in general agreement, however the coupled hybrid model's network sub-model predicts a 40 °C greater temperature in the room of fire origin at the end of the simulation (300 seconds). The second comparison case is that of the network sub-model to a CONTAM network model. Due to the limitations of the models, the fire is modelled as a mass flow source with a temperature of 77 °C; this temperature is considered too low to represent a typical building fire. The general agreement between the models is good; however, there are some nodes for which the results are orders of magnitude apart. For both comparison cases, it is impossible to state which model is the most valid due to lack of experimental data and the author provides no evaluation of the differences. One-way manual coupling of the zone and network sub-models and lack of coupled hybrid model testing or validation presented in Zhu continue.

Zhang et al. [48] document a coupled zone-network hybrid model aimed at the examination of smoke spread in stair and elevator shafts and smoke control in tall buildings. The zone sub-model domain only comprises a portion of the fire floor and is manually one-way coupled to the network sub-model very simply. The hybrid interface is represented by a temperature boundary condition with the temperature computed by the spatial averaging of the upper and lower layer of the zone sub-model. This is simplistic and could lead to erroneously high or low boundary condition temperatures in the network sub-model. Heat losses are accounted for in the network sub-domain; as per TNFIRE3 and Colella, and unlike the F-Z/FZN/LFZ model and FDS+HVAC.

Validation is carried out against a medium scale experiment of a 1.5 m shaft and connected room that contained an ethanol fire. There is good agreement between the network sub-model and the experimental results with a maximum difference of 20 °C. The article presents a demonstration case for a 30 storey single shaft building and investigates the effect of different door opening/closing arrangements.

2.4 Summary of fundamental coupled hybrid components

The following section is a summary of the treatment of poignant pieces of the coupled hybrid modelling paradigm in fire engineering. It serves to highlight where the literature contains agreement and where it does not.

2.4.1 Sub-models used and coupled hybrid model purpose

Different coupled hybrid model types are possible; based upon the constituent sub-models adopted. The choice of which sub-model type to adopt is based upon what element of the built environment is being examined and the type and extent of output required to perform the desired analysis.

Where tunnels are the subject of analysis, all authors have adopted a field-network modelling methodology [105, 100, 98, 114, 113]. Some authors have also taken advantage of primarily unidirectional flow in tunnels to model only one directional coupling between sub-models. The lack of adoption of a zone sub-model is because this model type, at least in its typical state, is not useful for a tunnel. A zone model does not typically account for lateral variation in parameters or lateral movement of mass. Therefore, information related to smoke spread, back-layering and critical velocity in a longitudinally ventilated tunnel is not resolved. Authors have attempted to use zone models in a 'multicell' arrangement for tunnels [127, 128, 129] although this is not discussed here. Network models lend themselves to tunnels as they are able to output the variation of variables of interest, such as pressure, enthalpy, velocity or temperature, through the length of the network [44].

In buildings and ships the choice of constituent sub-model has been less unanimous with all three options being adopted. Early examples were based upon a field-zone methodology and this continues to the majority of contemporary models (F-Z/FZN/LFZ model [85, 84], HFAZM [91], and SMARTFIRE/FSEG-ZONE [90]). Zone sub-models are more suitable for buildings and ships as the complete mixing assumption of network models is not realistic for a room enclosure near to a room of fire origin. Zone sub-models can be used to more realistically represent the behaviour of the proximal enclosures that are not the room of fire origin when compared to a network sub-model. A zone sub-model is able to output vertically variable enclosure conditions (within the limits of the two-zone assumption) and this can be used to test relevant acceptance

criteria (e.g. clear height or temperature at head height [130]). A limitation of this method is the representation of enclosures suitability far away from the fire origin such that the two-layer assumption is not true and/or homogeneous conditions have been reached. The representation of an HVAC system cannot be validly modelled in a two-zone model due to strong and variable bulk flow characteristics in the duct parallel to the direction of the duct.

One logical conclusion of the above discussion of the limitations of using only a zone sub-model is to also include a network sub-model. This field-zone-network method has been adopted by a small number of authors (F-Z/FZN/LFZ model [86, 88], Ren et al. and Jiao et al. [97, 93]). The rationale of this method is the modelling of the very far field enclosures and air-handling systems (that is, parts of the domain where the homogeneous assumption is valid) in the network sub-model.

FDS+HVAC [95, 131] adopts a field-network methodology. It should be noted that this coupled hybrid model was aimed specifically at air-handling infrastructure (hence it is named HVAC) and therefore the assumptions embedded in the network model (homogeneous parameters across a cross section) are relatively valid. An interesting development of this method is the work from DTU and Imperial College London [118, 115, 113, 116], who use this coupled hybrid model with full height vents to simulate a tunnel. Although the network sub-model was not initially intended for this purpose, documented results look promising.

The remaining published model, RP-1328 - developed at Carleton University, disavows use of a field sub-model and adopts a more simplistic coupled zone-network hybrid method. This coupled hybrid model type would not be able to capture the 3D flow field surrounding complex geometry. Combustion modelling is more simplistic and would not account for the propagation of unburnt fuel in underventilated fires. This model type is more susceptible to inaccuracies outside of the relevant validation range due to the empirical nature of the primary solver (the zone sub-model). Runtimes would be substantially quicker than a coupled hybrid model that contains a field sub-model.

To summarise, there is a unanimous choice for the examination of tunnels to use a coupled field-network hybrid method; however, no such choice has been made for buildings and ships. Most authors adopt a coupled field-zone hybrid model for this application although coupled field-network hybrid models have been developed also. One body of work adopts a coupled zone-network hybrid method. It cannot be stated that one choice of sub-model(s) is any more correct than any other; instead, it is important to define what the required output and end user expectations of the coupled hybrid model are and verify that these requirements are met by the adopted sub-model choices [132].

2.4.2 Coupled hybrid interface boundary conditions

A major element of any coupled hybrid model is the treatment of the boundary conditions in the sub-models that represent the hybrid interface. Valid and sensible boundary conditions ensure that the problem is mathematically well-posed [133] and that conservation is ensured. Boundary conditions are also affected by the choice of domain decomposition used (overlapping or non-overlapping). Table 2.1 summarises the choice of boundary conditions in the reviewed literature.

Table 2.1: Summary of hybrid interface boundary condition type.

Flow from field sub-domain	
To zone sub-model	Fan et al. 1992; Hua et al. 2005; Burton 2011: Dirichlet mass and enthalpy flux.
	Yao et al. 1999; Jie et al. 2006: fluxes adopted directly from cells of overlapping sub-domain.
To network sub-model	Jiang & Wang 1997: area sum of all variables inserted into ghost cell.
	Deng et al. 2007: Dirichlet momentum source.
	Colella 2010: Dirichlet velocity.
	McGrattan et al. 2017: Dirichlet pressure, temperature and species concentration.
Flow from zone sub-domain	
To field sub-model	Fan et al. 1992; Yao et al. 1999; Jie et al. 2006: zero gradient for all variables except velocity which is Dirichlet and computed based on mass conservation.
	Hua et al. 2005: zero gradient for all variables except pressure which is computed based on empirical pressure distributions.
	Burton 2011: Dirichlet pressure and temperature.
To network sub-model	Yao et al. 1999: Dirichlet velocity computed from vent pressure drop.
	Zhu 2009: Dirichlet mass and temperature.
	Zhang et al. 2014: Dirichlet temperature.
Flow from network sub-domain	
To field sub-model	Jiang & Wang 1997: zero gradient for all variables.
	Deng et al. 2007: Dirichlet mass flux.
	Jung et al. 2010: Dirichlet velocity and mass flux.
	Colella 2010: Neumann pressure.
	McGrattan et al. 2017: Dirichlet mass flux and temperature.
To zone sub-model	Not applicable (relevant work used one-way coupling).

2.4.3 Numerical coupling procedure

There is a wide range of coupling procedures. They are all based on assumptions, model requirements and application. This is a major issue for all coupled hybrid models. It affects code stability and convergence, and computational cost. Many authors omit any relevant discussion (Xu et al. [83], the F-Z/FZN/LFZ project [85, 86, 92, 88], HFAZM [91] and Ren et al. [93]). In Table 2.2 the different numerical coupling methods are summarised.

2.4.4 Extent and results of validation and comparison studies

There is a vast range in the volume, quality and applicability of validation work that has been carried out on coupled hybrid models. Approximately 50 % of the published works are related only to the mathematical development of the constituent sub-models, the coupling methods and/or presentation of numerical demonstration cases [100, 86, 97, 98, 114]. Although these works are useful in enlightening the reader and serve to demonstrate that a coupled hybrid model is able to produce outputs that give realistic results, they are critically limited in their validity and safe usability.

There is a body of validation work of varying soundness. Authors have presented both numerical comparisons and experimental validation [90, 38, 106, 107, 85, 95, 94, 92, 88] and others only numerical comparisons are provided [126, 91, 125, 124].

The advantage of numerical comparisons is that they are easier, cheaper and quicker to carry out when compared with experimental validation. This means that many comparison cases can be completed. Statements related to the output of a coupled hybrid model compared to an alternative numerical method (which is widely used and societally trusted) can be made. It can be said that the output of a coupled hybrid model is similar to an established numerical model which is used within a certain set of limitations to model the real world. The disadvantage of carrying out only numerical comparisons is that no statement can, per se, be made on the ability of the coupled hybrid model to represent the real world [134]. Depending on the level of validation of the numerical model used to provide the comparison case and the extent of the test case it may only be concluded that the tested coupled hybrid model provides similar output to an existing model. Care should be taken to not make statements such as 'therefore the coupled hybrid model is at least as good as the comparison model'. Variation between the coupled hybrid model and the unimodal comparison model could indicate that the coupled hybrid model is either predicting real behaviour more, or less, accurately than the unimodal model. Without experimental data, it is typically impossible to conclude which statement is true.

When comparing subject model output with the output of other numerical methods and/or experimental data, there is a distinction to draw between: (1) literature that contains numerical comparisons and experimental validation for different test cases; and (2) those that, in a single case, involve numerical and experimental comparison. The former does not, ipso facto, increase the absolute real world validity of the numerical comparison cases. The latter provides richer validation and the opportunity to make statements regarding the representation of real behaviour. The advantage of comparison with both numerical and experimental data in a single test case is that if the separately validated unimodal model agrees with the limited experimental data then the richer unimodal model data can be used for further validation in the test case. For fire tests, one constraint is limited instrumentation. However McGrattan et al. [134] argue that 'quantity [of experiments] makes up for lack of quality [of individual experiments]' and

Table 2.2: Summary of numerical coupling method and procedure.

Steady state one-way, 'indirect coupling'	Jung et al. 2010: Solve network sub-model to steady state convergence. Use output as boundary conditions for unsteady field sub-model solution.
	Colella 2010 (one of two options): Solve field sub-model to steady state convergence. Output characteristic curves for ventilation elements. Use curves as boundary conditions for steady state network sub-model.
Steady state iterative	Tao et al. 2014: Iteratively run network and field sub-models to steady state convergence, exchanging boundary condition data at the end of each iteration. Iterate until steady state global convergence.
Unsteady one-way	Zhu 2009 and Zhang et al. 2014: Solve zone sub-model to t_{end} and store unsteady boundary conditions. Apply these boundary conditions to the network sub-model.
Unsteady asynchronous, 'loose coupling'	Li et al. 1995 (TNFIRE3), Jiang & Wang 1997, Deng et al. 2007 and McGrattan et al. 2017 (FDS+HVAC): Solve field sub-model at time step t_n using boundary conditions from network sub-model at time step t_{n-1}. Apply field sub-model boundary conditions for solution of network sub-model at time step t_n.
Unsteady direct, 'fully coupled'	Burton 2011 (SMARTFIRE/FSEG-ZONE): Iterate field sub-model, apply boundary conditions to zone sub-model and iterate until solution fully converges for that field sub-model iteration. Advance field sub-model iteration and re-solve. Iterate process until field sub-model convergence, then advance time step.
	Colella 2010 (one of two options): Solve network sub-model to end of t_n, apply boundary conditions from network sub-model to solve field sub-model until end of time step t_n and apply boundary conditions to network sub-model. Iterate process until global convergence, then advance time step to t_{n+1}.

that many more data points can overcome the limitations of experiments of lower quality when used with a statistical validation analysis.

The problem with much of the experimental validation cases [85, 92, 88] is that the test case has a small domain. They comprise two or three directly connected enclosures. They are not representative of the probable end use of a coupled hybrid model and the applicability of these cases as useful validation is compromised. The simpler constituent sub-models, being zone or network models, lend themselves to enclosures remote from the fire origin. In a two or three room test case, this is not the case and the validation may not be 'fair' to the coupled hybrid model as it is being tested outside of its planned remit. Moreover, benchmarking cases should be designed to reside in the probable use parameter space. The prototypical use of a coupled hybrid model is to explicitly model more, or all, of a total system. Poor performance in these low enclosure cases is not a failure of the coupled hybrid model for the intended use.

2.5 Potential experimental data usable for validation

Following a thorough literature review, discussions with experimental experts and communication with multiple experimental facilities and institutes, no suitable datasets were found that could be used to benchmark the new coupled hybrid model implementation.

One could ask the question: 'Why is there no suitable validation data?' To answer this, the history of experiments used to validate fire models has to be examined. Early CFD-based fire models, which relied upon the Boussinesq approximation, were benchmarked against fire plumes [135, 136]. Following the general abandonment of the Boussinesq approximation in the late 1990s, and the development of simulation of more fire-specific phenomena, CFD-based fire models were more frequently validated using prototypical arrangements such as 'the enclosure fire' [137]. Since this time, the vast majority of fire dynamics validation experiments have been within the compartment fire sphere - being carried out within a single enclosure or a low number of directly connected enclosures [138, 139]. This reflects a historic trend within fire safety, fire science and fire engineering to consider experimental and numerical enclosure fires [140, 141]. An early simulation of an enclosure fire and window spill plume is presented in Figure 2.6.

These types of fire would not be analysed using a coupled hybrid model, whose strength and utility comes from the quantitative examination of the two-way coupling between a total building system and a fire. The domain of the typical experimental enclosure fire is small enough that it is reasonably practicable to simulate the entire domain within the field domain. These experiments do not provide applicable validation data to quantify the uncertainties embedded within a coupled hybrid model and hence do not advance the safe use of these models. The lack of applicable validation data further demonstrates the novel nature of the new coupled hybrid modelling implementation.

The PRISME project experiments [142, 122], which were conducted at the Institut de Radioprotection et de Sûreté Nucléaire (IRSN), and the FOA and Aalto experiments, carried out by Aalto University [143, 144], initially appeared to be a suitable set of experiments to use to benchmark the new coupled hybrid model implementation. Indeed, these three sets of data have been used for validation cases for previous versions of FDS using the coupled HVAC network sub-model prior to the introduction of transient species and energy transfer. Data from part of the PRISME project were used to provide pressure, temperature and duct volume flow validation data for FDS version 6.0.0 (released in 2012) [142]. Data from the FOA experiments were used to provide pressure validation data for FDS version 6.3.2 (released in 2015) [143]. Data from the Aalto

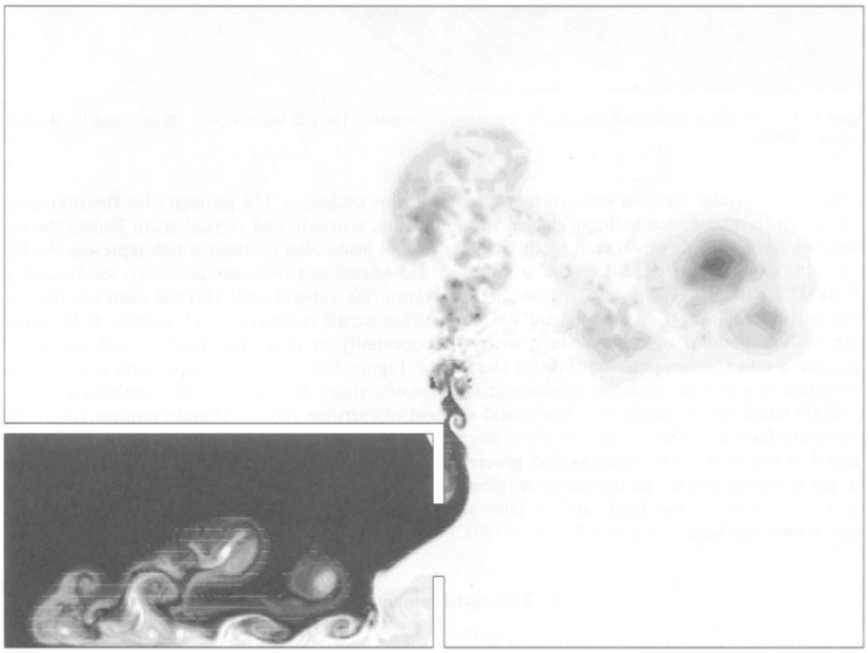

Figure 2.6: Numerical simulation of a plume of hot gas escaping from an enclosure opening. This work is emblematic of experimental and numerical work in CFD-based fire modelling in the 1990s [1].

experiments were used to provide pressure, temperature, duct velocity, and oxygen and CO concentration validation data for FDS version 6.3.2 (released in 2015) [144]. However, these experimental data sets are not suitable for a trenchant benchmarking exercise for the new coupled hybrid implementation released in FDS version 6.5.3 as explained in the following paragraphs.

The PRISME experiments comprised a range of fire experiments in a four room, one corridor test facility. The facility incorporated a mechanical ventilation system consisting of a supply system and an exhaust system. The mechanical ventilation system was well-defined within the literature [142] and well-instrumented. The aim of the project was generation of data for use within the nuclear industry. In the nuclear industry, supply and exhaust ventilation systems are typically fresh air and spill systems respectively. Therefore, the supply and exhaust systems within the PRISME experiments were isolated from one another.

The FOA experiments were a set of 14 fire experiments in a single enclosure facility. In three of these experiments the facility was served by a supply and exhaust ventilation system. These ventilation systems were not connected to one another via a return system.

The Aalto experiments were a set of four experiments in a 1970s apartment with four enclosures. The apartment was provided with a well-defined mechanical supply and exhaust ventilation system. Again, these ventilation systems were not connected to one another by a return system.

The presence of a mechanical supply and exhaust ventilation system made these three sets of experiments suitable validation cases for the original HVAC network sub-model within FDS version 5.5 onwards. However, these experiments would not be strongly affected by transient transport of gaseous species through the ventilation system nor mass and energy stored within the ventilation system at the start of the experiments. The original HVAC network sub-model did not account for transient transport or storage

within its domain. Therefore, its weaknesses were not significant to the prediction of phenomena and measured quantities in the three sets of experiments.

The new coupled hybrid implementation introduced in FDS version 6.5.3 accounts for transitory phenomena (e.g. transport of hot smoke through a duct) and storage of mass and energy within its subdomain. Suitable benchmarking cases used for validation must incorporate these phenomena to validate whether the real-world physics are being suitably simulated by the numerical model and hence fulfil objective three of this thesis.

2.6 Closing remarks

Coupled hybrid modelling for fire engineering applications is numerically realisable. Verification shows technical soundness and demonstration cases present very promising computational cost reductions at or above field domain reduction ratio unity. Numerical comparison cases and limited experimental validation show generally good agreement. Coupled hybrid modelling has exciting promise for the future of fire engineering analysis of buildings, ships, mines, and tunnels. The capability of coupled hybrid models to provide a computationally efficient method of high level risk analysis of elements of infrastructure (using the lower order sub-models), whilst offering the ability to scale up the fidelity of output in areas of highlighted risk within the same simulation framework (using the higher order sub-models), lends the method to risk analysis of existing and new infrastructure. The same model can be scaled over a range of levels of required output resolution to further investigate cases highlighted during a higher level initial risk analysis exercise.

Like any under-developed and disparately investigated avenue of research, there are fractured opinions regarding the various sub-problems and little agreement as to the correct solution method [145]. Unresolved questions include: which sub-models to include, how to represent the hybrid interface boundary conditions, how to decompose the domain, and the numerical solution method for coupling the sub-models.

Then there are the gaps. Relevant experimental benchmarking data to be used within validation is critically lacking. Before a coupled hybrid model moves from being a research topic to being utilised by practitioners, this deficiency needs to be addressed. Validation experiments need to be specifically designed (or chosen) to test a coupled hybrid model's capabilities and as it would be used in a real-world application. This dataset would enable the more thorough investigation of the most effective hybrid interface boundary conditions treatment and sub-model choices.

Lack of communication, structure and agreement leads to obsolete models and wasted work [146]. There are at least 168 different computer modelling programs for fire and smoke simulation, including 17 field models and 50 zone models [45]. Considering just coupled field-zone hybrid models, this gives 850 hypothetical coupled hybrid models; though a small fraction of these models are realistically available or actively maintained and used. Finite project-centric and non-collaborative model development has led to these demises. If there is no communication and collaboration, then these potential research silos could swallow even more resource, require parallel re-working and produce soon-to-die coupled hybrid models. For the development of coupled hybrid models to be efficient and effective, there needs to be communication between research parties and community-led signposted collaboration. This impetus for collaboration is a motivation for the use of open source software as part of coupled hybrid model development. The nature of open source software focuses collaboration, increases quality, and gives users and developers freedom of customisability [147]. There is hope in this

regard. Jie et al. [92] removed the closed source FAC3 from the State Key Laboratory of Fire Sciences of China coupled hybrid model and replaced it with the open source FDS. Work following on from Colella [106] replaced the proprietary Fluent with FDS [118, 115, 113, 116]. In tunnel ventilation, Prince [39] used the open source FireFOAM field model and an embedded network sub-model, eschewing the proprietary SES. This trend should be continued, to decrease the number of dead coupled hybrid models and maximum knowledge exchange.

The positioning of the hybrid interface and the treatment of homogeneous and heterogenous data at this location is an unresolved question. In tunnels, estimations have been made as to the distance away from a turbulence source where the homogeneous assumption of the network sub-model becomes valid. (20 times the hydraulic diameter away from a fire or jet fan [110]. However, there is limited agreement with this value [115]). This is important if using coupled hybrid models to study loss of stratification in tunnels. To capture the heterogeneity of the smoke density, the 3D field sub-model domain should be extended to at least the extent of the continuation of stratification. Otherwise, there is potential to introduce mixing sub-models into the network sub-model to empirically study the loss of stratification within the 1D domain. In buildings, there has been no study of the sensitivity of results due to the proximity of the hybrid interface to the fire or ventilation elements. The acknowledgement that variables may well not be homogenous at hybrid interfaces and the treatment of communicating sparse data steer us to the consideration of defective boundary conditions [148]. Much work has been done on the treatment of defective boundary conditions when coupling 1D and 3D models in haemodynamics [149, 133]. The conclusions made, and solutions formulated, by Formaggia and colleagues has informed the treatment of defective boundary conditions in non-fire tunnel ventilation via the use of the Lagrange multiplier method [72]. For coupled hybrid modelling in fire engineering, this remains an unanswered question.

There are limitations of the simulation methods. These may be (1) established weaknesses of the sub-models; (2) limitations due to the early stage of a sub-model; or (3) novel problems due to the coupled hybrid model implementation. A full discussion of (1) is outside of the scope of this review but could include, for example, the uncertainties in prediction of heat release rate in a compartment fire using a field model [150], conductive heat loss and vent enthalpy flux errors due to the homogeneous variable assumption of a zone model [151], or inaccurate loss coefficients for duct fittings in network models [152]. (2) has a relationship with the previous discussion regarding collaboration. Researchers have generated multiple new models to use as a sub-model in a coupled hybrid model (e.g. the new zone sub-models of Hua et al. [91] and Burton [90] and the new 1D network sub-model of Colella [40]). Duplication of models has led to a patchwork of capability spread across a multitude of codes. The piecemeal capability profile should be collated into a consolidated number of sub-models. This applies mainly to the 'add in' lower order sub-models (i.e. zone and network models). (3) is specific to the implementation of coupled hybrid models so is discussed in more detail in the following paragraph.

Zone models do not account for lateral spread of species or lateral velocities (except for at vents). This makes them unsuitable for the simulation of long corridors. If zone sub-models are to be used in a coupled field-zone hybrid model, this needs to be addressed by implementing conservation of lateral momentum. Earlier versions of CFAST empirically accounted for lateral spread in corridors using a corridor flow delay sub-model. This was removed in version 7.0.1 and replaced with a Heskestad correlation

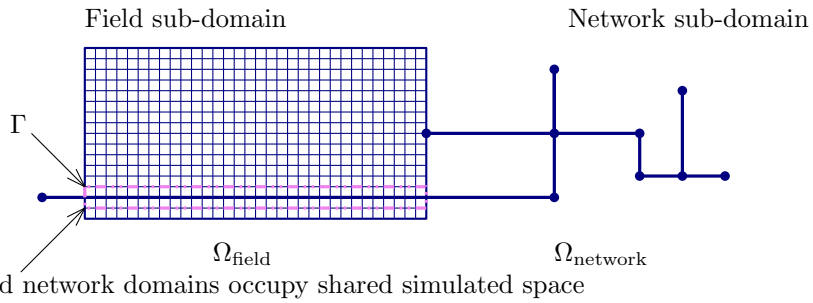

Figure 2.7: Schematic of domain overlap for a HVAC duct passing through an enclosure.

model for ceiling jet velocity (no spread or delay). No coupled hybrid model accounts for heat transfer between sub-domains where these sub-domains coexist in space. For example, an HVAC duct (modelled in a network sub-model) passing through a room (modelled in a field sub-model), refer to Figure 2.7. This HVAC duct may be transporting hot fire products and would heat the room, potentially leading to secondary ignition. This would be ignored by all current coupled hybrid models. Network sub-models should be expanded to account for obstructions in their domain (e.g. a carriage in a tunnel or objects in a corridor), more complex heat transfer (e.g. to simulate different wall boundary conditions of a corridor) and reacting flow.

In closing, coupled hybrid modelling offers a method for fire safety designers to efficiently model more of a domain of interest. Two-way coupling between a total system and a fire can be practicably investigated and the effect of this coupling understood within reasonable timeframes. Coupled hybrid modelling for fire engineering has application in any big, long or complex element of the built environment; for example, tunnels, supertall buildings and large complexes. The industry should consolidate the work already completed and fill the gaps in knowledge, understanding, and application, which have been highlighted in this review.

Chapter 3

Model development

3.1 Existing numerical model and its limitations

3.1.1 General description

The new transient transport subroutine builds upon the existing HVAC sub-model. The coupled hybrid model, being formed of the coupling of the FDS 3D field solver and the HVAC 1D network solver, can be used to solve the boundary value problem posed by a user-defined total domain incorporating various 3D and 1D geometries and boundary conditions. A non-overlapping domain decomposition method is used to form the subdomains of the two coupled sub-models as shown in Figure 3.1.

The 1D network sub-model exchanges information with the FDS field domain at special vent-connected HVAC nodes. Figure 3.2 presents a sketch of the coupled hybrid model.

Nodes have no volume and the sub-model solves the following nodal conservation equations of mass and energy:

$$\sum_j \rho_j u_j A_j = 0 \tag{3.1}$$

$$\sum_j \rho_j u_j A_j h_j = 0 \tag{3.2}$$

and the conservation equation of momentum in a duct:

$$\rho_j L_j \frac{\mathrm{d}u_j}{\mathrm{d}t} = \left(p_i - p_k\right) + \left(\rho g \Delta z\right)_j + \Delta p_j - \frac{1}{2} K_j \rho_j |u_j| u_j \tag{3.3}$$

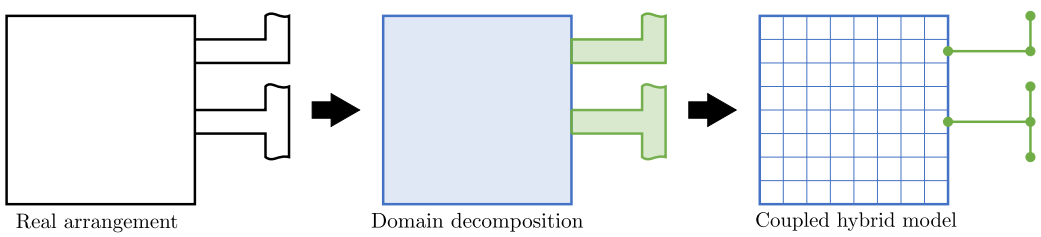

Figure 3.1: Domain decomposition.

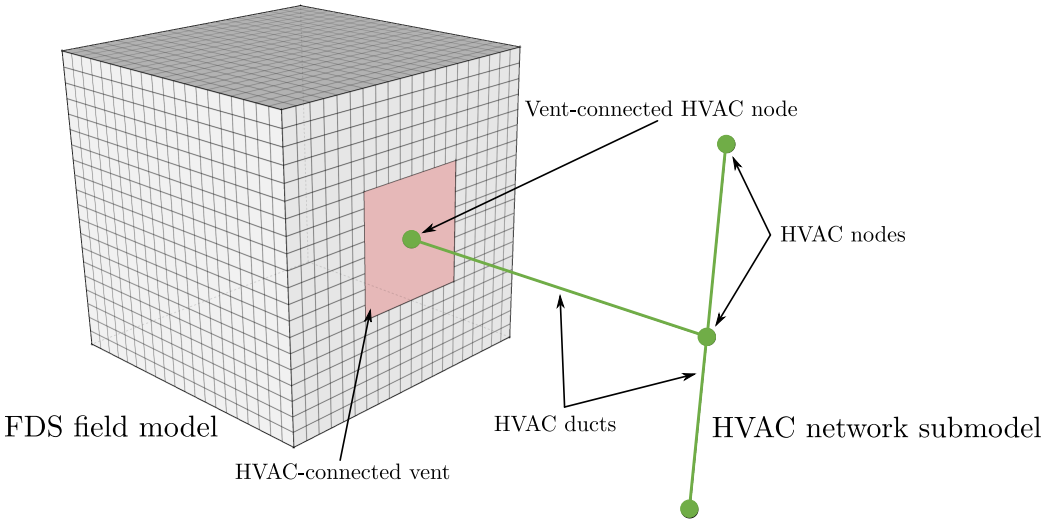

Figure 3.2: Primary components of coupled hybrid model within FDS.

The subscripts i, k, and j denote upstream node, downstream node and duct respectively. The first term on the right-hand side of the momentum equation is the pressure difference between the upstream and downstream nodes, the second term is the hydrostatic pressure head, the third term is a pressure increase source (e.g. a fan), and the fourth term is the pressure losses due to wall friction and minor losses (e.g. bends and fittings).

The following discretisation is used for the solution of the momentum equation, which is non-linear with respect to velocity:

$$u_j^{n+1} = u_j^n \frac{\Delta t^n}{\rho_j L_j}\Big(\big(\tilde{p}_i^n - \tilde{p}_k^n\big) + \big(\rho g \Delta z\big)_j^n - \Delta p_j^n - \frac{1}{2} K_j \rho_j \big(|u_j^{n-} + u_j^{n+}| u_j^n - |u_j^{n+}| u_j^{n-} \big) \Big) \quad (3.4)$$

The $n+$ and $n-$ superscripts denote, respectively, the prior iteration value and either the prior iteration value or zero if flow reversal has occurred. This is carried out to linearise the flow losses in a duct by avoiding large changes in K during flow reversal if the forward and backward losses are very different.

Node pressures are expressed as $\tilde{p}_i$ (not p_i) because they are extrapolated pressures based upon the rate of pressure change during the previous time step. This is because the pressure solution of vent-connected nodes is based upon mass and energy flows predicted by the HVAC sub-model and the FDS hydrodynamic solver. If the node is an internal node then the solution for the actual pressure is closed.

If convergence checks of mass conservation or velocity change fail, the solution for the momentum is re-iterated with a new extrapolated node pressure.

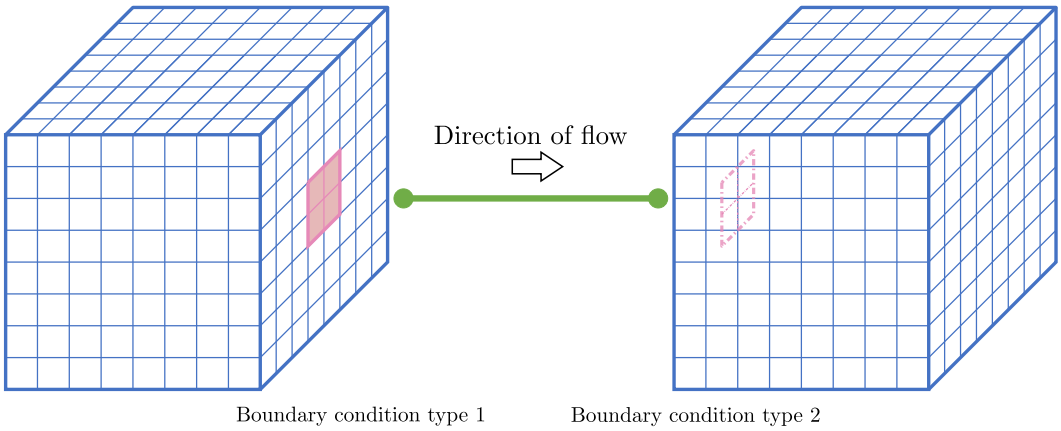

Figure 3.3: Two different types of coupling boundary condition within model.

3.1.2 Boundary conditions at coupling location

Boundary conditions within the HVAC subdomain

There are two types of boundary condition required to solve the boundary value problem on the HVAC subdomain. Flow into the HVAC subdomain and flow out of the HVAC subdomain. Where the two types of boundary condition occur are represented in Figure 3.3.

The upstream quantities are used when updating the duct nodes. For flow into the HVAC subdomain (boundary condition type 1 in Figure 3.3) quantities are populated using data collected from the FDS domain and for flows out of the HVAC subdomain (boundary condition type 2 in Figure 3.3) quantities are populated using 1D data from the connected HVAC ducts.

For flow into the HVAC subdomain (boundary condition type 1 in Figure 3.3) information is required to be transferred from the FDS domain to the HVAC subdomain. This is a reverse 'defective boundary condition' [148] and hence the 2D vent data from FDS that is connected to the vent-connected HVAC node must be reduced to 1D data. The density, species, enthalpy (based upon adjacent gas phase temperatures and species concentration), and temperatures are summed and averaged from gas cells adjacent to the HVAC-connected vent.

$$\rho_i = \frac{\sum_{g \in V} \rho_g A_g}{\sum_{g \in V} A_g} \tag{3.5}$$

$$Y_{\alpha,i} = \frac{\sum_{g \in V} Y_{\alpha,g} A_g}{\sum_{g \in V} A_g} \tag{3.6}$$

$$p_i = \frac{\sum_{g \in V} p_g A_g}{\sum_{g \in V} A_g} \tag{3.7}$$

$$h_i = \frac{\sum_{g \in V} c_p(T_g, Y_g) T_g A_g}{\sum_{g \in V} A_g} \tag{3.8}$$

$$T_i = \frac{\sum_{g \in V} T_g A_g}{\sum_{g \in V} A_g} \tag{3.9}$$

The subscript i denotes duct nodes, g gas cells and V is the set of gas cells adjacent to the FDS vent which is connected to the vent-connected HVAC node (i). The summed and averaged temperature (T_i) may not correspond to the summed and averaged enthalpy (h_i) as there may be a variation in specific heat due to temperature and species across the gas cells adjacent to the FDS vent ($g \in V$) which is connected to the vent-connected HVAC node (i). The initial average temperature is therefore iterated to converge with the temperature equating to the average enthalpy, using the following Newton-Raphson root finding loop:

$$T_i^{k+1} = T_i^k + \frac{\left(h_i - h\left(T_i^k, Y_{\alpha,i}^k\right)\right)}{\left(c_p\left(T_i^k, Y_{\alpha,i}^k\right) + T_i^k \frac{\Delta c_p\left(T_i^k, Y_{\alpha,i}^k\right)}{\Delta T_i^k}\right)} \tag{3.10}$$

where $h\left(T_i^k, Y_{\alpha,i}^k\right)$ is the enthalpy as output by the averaged temperature and the area-averaged species concentrations in the vent-connected HVAC node at that iteration. The density, species, and pressure of the vent-connected HVAC node is adopted as the averaged quantities in Equation 3.5 to 3.7, the temperature is adopted as the converged solution from Equation 3.10, and the specific heat of the vent-connected HVAC node is populated as:

$$c_{p_i} = \frac{h\left(T_i, Y_{\alpha,i}\right)}{T_i} \tag{3.11}$$

For flow from the HVAC subdomain to the FDS domain (boundary condition type 2), the population of vent-connected duct node values is a trivial population using 1D duct quantities.

Boundary conditions within the FDS field domain

Again there are two types of boundary condition within the FDS field domain. When the flow is from the FDS field domain (boundary condition type 1 in Figure 3.3) and when flow is into the FDS field domain (boundary condition type 2 in Figure 3.3). The coupling boundary conditions within the FDS field domain are represented by 2D wall vents which are connected to vent-connected HVAC nodes. Vent wall cell quantities are adopted based upon upstream data (i.e. from the FDS field domain for coupling boundary condition type 1 and from the HVAC subdomain for coupling boundary condition type 2).

For coupling boundary condition type 1 (flow out of the FDS field domain) the wall vent cell quantities are generally populated using the adjacent gas cell quantities and the perpendicular velocity is output using the mass flux in the connected HVAC duct.

$$T_w = T_g \tag{3.12}$$

$$Y_{\alpha,w} = Y_g \tag{3.13}$$

$$\rho_w = \rho_g \tag{3.14}$$

$$u_w = \frac{\dot{m}'_j}{\rho_w} \tag{3.15}$$

where the mass flux in the duct $\dot{m}'_j$ is output:

$$\dot{m}'_j = \frac{u_j A_j \rho_j}{A_v} \tag{3.16}$$

For coupling boundary condition type 2 (flow into the FDS field domain) the wall vent cell quantities are populated using the spatially averaged quantities from the vent-connected HVAC node within the HVAC subdomain. Coupling boundary condition type 2 within the FDS field domain is a defective boundary condition. The problem is mathematically ill-posed and the input data (single dimensional averaged velocity) is scarce compared to the required output data (three-dimensional spatially resolved velocity). An interpolation method must be used to address these defective boundary conditions.

For other applications of a coupled hybrid fluid solver the coupling boundary conditions span two entire dimensions of the subdomains. For example, Blanco et al. [153] and Colella et al. [40] use coupled hybrid fluid models for simulation of blood vessel networks and tunnel networks respectively. In these cases the coupling boundary conditions span both the y and z dimensions. In these cases it is reasonable to assume that the spatial distribution of quantities such as the velocity and the density on the coupling boundary condition could affect the overall solution. For these applications, the treatment of the defective boundary condition may be critical to the meaningful solution of the boundary value problem being solved on the decomposed hybrid domain. In these cases advanced interpolation methods such as the Lagrange multiplier method, Nitsche's method [154], and Schur's method [155] have been adopted within the literature.

The coupling boundary conditions within the FDS field model (being the HVAC-connected vents) will typically occupy only a fraction of the overall dimensions of the

domain. Within the parameter space that is the subject of this work, these interpolation methods are concluded to be too expensive to justify their use. The speed reduction is not seen as justifiable for the majority of code users. If the coupled hybrid model is further expanded to another parameter space then the treatment of the defective boundary conditions will be addressed. The wall vent cell quantities are populated using a linear distribution model based upon quantities from the upstream HVAC subdomain.

$$T_w = T_i \tag{3.17}$$

$$\dot{m}'_{\alpha,w} = \dot{m}'_j Y_{\alpha,i} \tag{3.18}$$

$$u_w = \frac{\dot{m}'_j}{\rho_w} \tag{3.19}$$

$$Y_{\alpha,w} = \frac{\dot{m}'_{\alpha,w} + \frac{2\rho_w D_\alpha Y_{\alpha,g}}{\delta n}}{u_w \rho_w + \frac{2\rho_w D_\alpha}{\delta n}} \tag{3.20}$$

$$\rho_w = \frac{\bar{p}\bar{W}_w}{RT_w} \tag{3.21}$$

where mass flux in the duct $\dot{m}'_j$ is per Equation 3.16. To ensure consistency between the species mass fraction, density, and velocity, Equations 3.19 to 3.21 are solved iteratively using the iterating method given in Equations 3.22 to 3.25.

$$u_w^{k+1} = \frac{\dot{m}'_j}{\rho_w^k} \tag{3.22}$$

$$\left(\rho_w D_\alpha\right)^{k+1} = \left(\rho_w D_\alpha\right)^k \frac{\rho_w^k}{\rho_w^{(k-1)^*}} \tag{3.23}$$

$$Y_{\alpha,w}^{k+1} = \frac{\dot{m}'_{\alpha,w} + \frac{2\left(\rho_w D_\alpha\right)^{k+1} Y_{\alpha,g}}{\delta n}}{u_w^{k+1}\rho_w^k + \frac{2\left(\rho_w D_\alpha\right)^{k+1}}{\delta n}} \tag{3.24}$$

$$\rho_w^{k+1} = \frac{\bar{p}\bar{W}\left(Y_{\alpha,w}^{k+1}\right)}{RT_w} \tag{3.25}$$

where $(k-1)^*$ is data either from the previous iteration or the previous time step if it is the first iteration.

3.1.3 Pertinent limitations of the pre-existing HVAC sub-model

The pre-existing HVAC network sub-model (i.e. prior to FDS version 6.5.3) did not account for transient transport of mass, species, or energy. This omission had two main implications for its use as part of a coupled hybrid model. Firstly, there was no mass, species, or energy storage within the HVAC network subdomain. Thus any mass, species, or energy within the portion of the total domain being simulated using the HVAC network sub-model was ignored and did not form part of the total domain calculation. Secondly, the coupled hybrid model implementation did not account for the time taken for mass, species and energy to be transported through the HVAC network

subdomain. Any mass, species or energy passing into the HVAC network subdomain was instantaneously moved to the connected FDS field domain(s).

3.2 New unsteady transport subroutine

3.2.1 Conservation equations and numerical solution

A new transient transport subroutine has been developed which is an augmentation to the existing HVAC network sub-model and addresses the limitations described in Section 3.1.3. The new subroutine uses the existing nodal conservation equations for mass and energy, and the duct conservation equation for momentum. The HVAC transient transport subroutine is an explicit Runge-Kutta method [156] conservation of species and energy using a finite difference Euler method [157] with a Godunov upwinding scheme [158]. In a typical HVAC system, as velocities in the ducts are relatively high, transport due to advection is expected to greatly outweigh that due to diffusion. Based upon this assumption of a high Péclet number the subroutine accounts for advective transport only (i.e. no diffusive transport). The analytical form of the conservation equation solved:

$$\frac{\rho\partial\phi}{\partial t} = -u\frac{\rho\partial\phi}{\partial x} \tag{3.26}$$

The ducts are discretized into cells with conserved variables (species mixture, specific heat, temperature, and density) being located at cell centres. The numerical discretization used to solve the partial differential equation is:

$$\left(\widetilde{\rho\phi}\right)_c^{n+1} = \left(\widetilde{\rho\phi}\right)_c^{n} - \frac{\Delta t}{\Delta x}\left(\rho u\right)_j^n\left(\bar{\phi}^n_{c+\frac{1}{2}} - \bar{\phi}^n_{c-\frac{1}{2}}\right) \tag{3.27}$$

where $\left(\rho u\right)_j^k$ is the mass flow within the duct and tilde and bar represent cell centred and cell face quantities respectively. A Godunov pure upwinding scheme is used to define the cell face values (for positive velocity):

$$\left(\widetilde{\rho\phi}\right)_c^{n+1} = \left(\widetilde{\rho\phi}\right)_c^{n} - \frac{\Delta t}{\Delta x}\left(\rho u\right)_j^n\left(\tilde{\phi}^n_{c} - \tilde{\phi}^n_{c-1}\right) \tag{3.28}$$

The Courant-Friedrichs-Lewy (CFL) condition for the Godunov scheme is $\Delta t \leq \frac{\Delta x}{2u}$. To ensure stability for the HVAC transient transport subroutine, the time step used in the subroutine could drop lower than the FDS time step. To maintain the CFL condition, the subroutine takes sub-steps of the FDS time step via the least integer of the FDS time step divided by the CFL time step.

A second CFL condition on the solver is:

$$\Delta t \leq \frac{\sum\limits_{c\in j} m_c}{\dot{m}'_j A_j} \tag{3.29}$$

where Δt is the solver time step, the term in the numerator is the sum of the masses within all cells in a duct, $\dot{m}'_j$ is the mass flow rate in the duct, and A_j is the area of the duct. The physical meaning of this limit is to ensure that the mass flowing out of

a duct within a transient solver time step is not greater than the content of mass in the duct. If this CFL is breached then a sub-step time step is created for the transient solver (which is less than the global time step).

Energy is conserved as a single variable. To separate the specific heat and the temperature, and hence be able to update the cell centred variables, the Newton-Raphson method, as described in Equation 3.30, is used to iterate on the cell temperature T_c. A maximum iteration number of ten or a variation in T_c^{k+1} and T_c^k of less than 0.05 % is used.

$$T_c^{k+1} = T_c^k + \frac{\left(c_p T\right)_c^0 - h_c^{k+1}\left(T_c^k, Y_c\right)}{{c_p}_c^{k+1}\left(T_c^k, Y_c\right) + T^k \cdot \left[\frac{\delta c_p}{\delta T}\left(Y_c\right)\right]_c^{k+1}} \tag{3.30}$$

where $\left(c_p T\right)_c^0$ is the initial enthalpy estimate from the solution of Equation 3.28 and $\left[\frac{\delta c_p}{\delta T}\left(Y_c\right)\right]_c^{k+1}$ is an estimate of the species-dependent variation in specific heat due to temperature. This estimated gradient is output using a discrete interpolation across a 1 K temperature range at the current time step temperature using a species-specific pre-populated $c_p\left(T\right)$ lookup table. Following the iteration on cell temperature, the cell specific heat is:

$$c_{p_c} = \frac{h\left(T_c, Y_c\right)}{T_c} \tag{3.31}$$

3.2.2 Checking flow through an HVAC node

With the exception of the updating of the conservation equations within the transient solver, the HVAC network sub-model time step matches the FDS field model time step. There is potential for a non-integer number of cells' content to flow through a node from connected ducts within a time step. This is not acceptable as the HVAC sub-model uses total flows of mass, energy and species passing through HVAC nodes for velocity and mass convergence checks, and for separating quantities from conserved variables. For example, if duct cells had a length of 0.1 m, the velocity in the duct was 3.5 m/s and the global time step was 0.1 s then the variable advected within a time step would be contained in 3.5 cells. When computing the total flow passing through a node, this non-integer amount of cell content should be calculated.

The spatial end of the volume of mass that will be advected within a time step is first located. This is carried out by summing the cumulative mass passing through duct cells in that time step (m'_{sum}), from the end cell backwards, and comparing this to the total mass passing through the duct in that time step output from the steady state HVAC solver (m'^n_j).

The duct cell within which the end of the advected mass falls within is defined as cell $r-1$. Hence, a new temporary cell size (Δx_{tmp}) is output. This temporary cell size is dimensioned such that the contents of all the previously backward-summed cells (from the final cell to the r^{th} cell) and the temporary cell is equal to the total duct mass flux in that time step (m'^n_j). This is described in Equation 3.32 and Figure 3.4.

$$\Delta x_{\text{tmp}} = \frac{m'^n_j - \sum_{r \le c \le \text{end}} m'^n_c}{\rho_c} \tag{3.32}$$

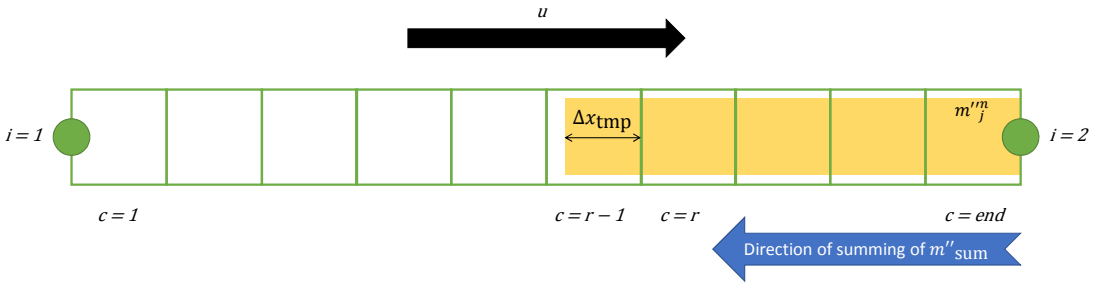

Figure 3.4: Backward summing of mass to locate and dimension temporary duct cell.

This temporary cell size is then used to compute the total variable flowing from a duct through a node. For example, Equation 3.33 gives the computation of enthalpy flowing through a node i from all connected ducts j within a time step n.

$$h_i^n = \sum_j \Big(\sum_{r \le c \le \text{end}} \left(\rho c_p T \Delta x\right)_c + \rho_c c_{p_c} T_c \Delta x_{\text{tmp}} \Big) A_j \tag{3.33}$$

3.2.3 Initialisation

A duct in the HVAC subdomain is defined by a pair of nodes. Duct runs are sets of ducts and nodes that are connected to one another directly by way of the HVAC network subdomain. When initialising the conditions in a duct run, with transient transport enabled, the user has two options: use the conditions of the lowest numbered node in the duct run (`DUCT_INTERP_TYPE=NODE1`) or use the conditions of the highest numbered node in the duct run (`DUCT_INTERP_TYPE=NODE2`). There is a third developer option (linear interpolation) which is used only for verification cases.

Before initialisation of the HVAC network model, a bespoke network clustering algorithm is used to group connected ducts and duct nodes into individual duct runs. The original clustering algorithm starts at the first node, loops through all connected ducts and tags all numerically downstream nodes as connected to the initial node. This process is looped over all nodes until all nodes and ducts are assigned to a duct run. With duct runs known, the initialising can then proceed to propagate the quantities of the relevant vent-connected HVAC node through all elements of the duct run set (j ducts, i nodes, and c cells) according to the user selected initialisation option.

An example is given in Figure 3.5, which presents a coupled hybrid decomposed domain comprising three FDS field domains (A, B and C) and two HVAC subdomain duct runs ($d = 1$ and $d = 2$). The three FDS field domains A, B and C are filled with quantities ϕ_A, ϕ_B, and ϕ_C respectively. The user has selected (`DUCT_INTERP_TYPE=NODE1`) for duct run $d = 1$ and (`DUCT_INTERP_TYPE=NODE2`) for duct run $d = 2$. The lowest numbered node in duct run $d = 1$ is $i = 1$ which is connected to FDS field domain A. Therefore the entire duct run $d = 1$ is initialised with quantities ϕ_A (orange). The highest numbered node in duct run $d = 2$ is $i = 9$ which is connected to FDS field domain C. Hence the duct run $d = 2$ is initialised with quantities ϕ_C (yellow).

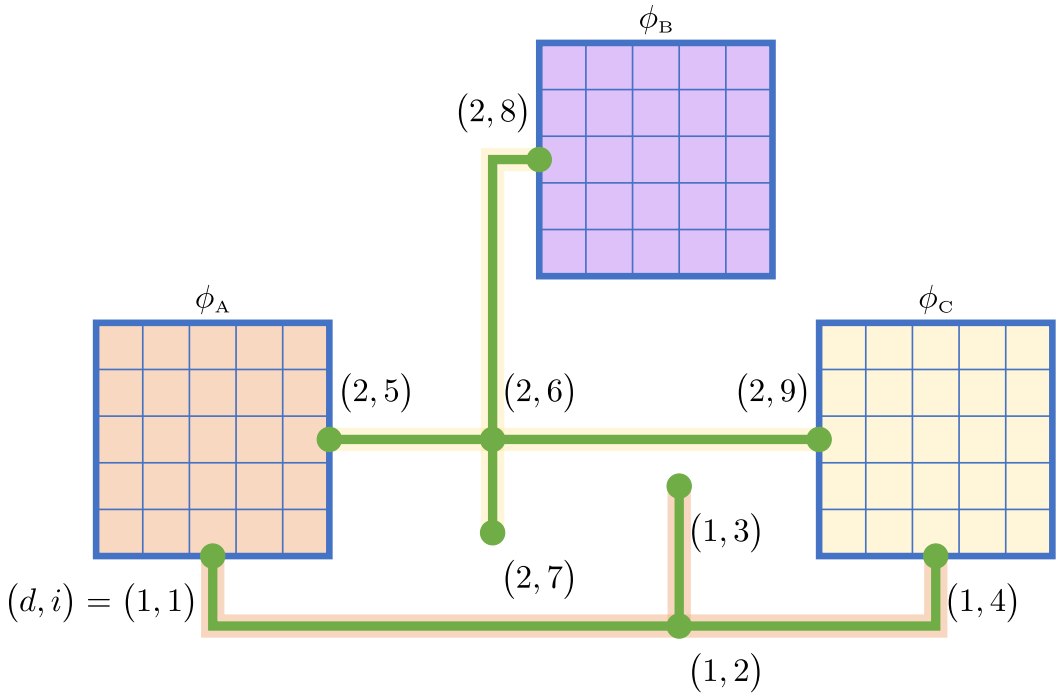

Figure 3.5: Two methods of interpolation for duct runs. Duct run $d = 1$ and $d = 2$ are initialised with quantities ϕ_A (orange) and ϕ_C (yellow) respectively

3.3 Verification of new subroutine

Numerical verification of the HVAC unsteady transport subroutine in accordance with ASTM E 1355 [22] has been carried out. Verification is carried out across nine cases, using FDS release version 6.7.0. All cases are available on the FDS GitHub repository. The HVAC unsteady transport subroutine is enabled by setting `HVAC_MASS_TRANSPORT=.TRUE.` on the `&MISC` line in the input file.

Unless otherwise stated, the general verification test case comprises two $0.5\,\mathrm{m}^3$ FDS field model compartments connected, in some manner, by an HVAC network subdomain. The general arrangement is described in Figure 3.6. The left and right compartments are initialised with species 1 and species 2 respectively which have identical transport and thermophysical properties. Both species have an initial density of $1\,\mathrm{kg/m}^3$. The duct(s) have a cross sectional area of $0.01\,\mathrm{m}^2$ and a flow rate of $0.01\,\mathrm{m}^3/\mathrm{s}$ (an ideal velocity of $1\,\mathrm{m/s}$).

3.3.1 Numerical convergence study

The HVAC transient transport subroutine is an Euler method with Godunov upwinding scheme. This method is formally first-order accurate in space and should exhibit l_1-norm error decay rates of $\mathcal{O}(\Delta x)$ for a continuous solution. A convergence study is undertaken to demonstrate that the adopted numerical method exhibits the expected spatial error decay.

The two FDS field model compartments are connected with a single 1 m long HVAC sub-model duct which is initialised using linear interpolation between the upstream and downstream duct node. In this manner, the mass fraction of species 1 linearly decreases from 1 to 0 kg/kg along the duct. When the species 1 mass fraction at the downstream node is examined, its value is expected to increase linearly from 0 kg/kg to 1 kg/kg

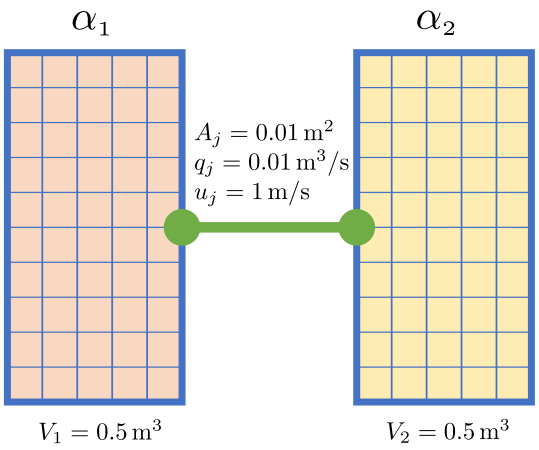

Figure 3.6: General verification case. Two FDS field model compartments, initialised with species 1 and 2, connected by an HVAC subdomain.

between 0 s and 1 s and then to remain at 1 kg/kg until the end of the simulation. The mass fraction of species 1 at the downstream duct node is examined and compared to the analytical result for a range of duct cell numbers (20, 40, 80, 160 and 320). The time step is fixed to satisfy the CFL of the case cell size; this ensures that the $\frac{\Delta x}{\Delta t}$ ratio is fixed for each case.

Figure 3.7 shows the mass fraction of species 1 at the downstream duct node for all cases and the analytical solution. The figure illustrates the mass fraction of species 1 starting at zero and then linearly increasing due to the initial conditions in the duct. At 1 s the mass fraction reaches its maximum and remains at this value until the end of the simulation. The figure illustrates that at lower cell counts (blue line) there is increased numerical diffusivity and that, for higher cell counts (cyan line), the numerical solution converges towards the analytical solution (black dashed line). Figure 3.8 presents the L1-norm error decay and demonstrates the numerical solution decays at $\mathcal{O}(\Delta x)$ towards the exact solution for decreasing cell size Δx as expected.

3.3.2 Duct definition sensitivity

A sensitivity analysis is carried out to verify that results are not sensitive to differing methods of defining the same duct network. The solution should not be sensitive to the method of definition of a duct j and the number of HVAC nodes i that are used along the length of a duct j. The set of cases that are used for this verification case have a general arrangement that is identical to that of the previous section but with the single duct being represented by a number of connected node-duct-node sets. The duct is initialised as species 2. Test cases 1 to 4 incorporate the use of increasing numbers of ducts (one, two, four, and five respectively) and affiliated duct nodes but the number of cells in the overall discretized duct (and hence the cell size) remains identical. Figure 3.9 describes the set of four cases used in this verification case.

Species 1 mass fraction at the downstream duct node is expected to show no variation in the solution for the differing number of ducts. The exact solution and numerical solution are presented in Figure 3.10 and show species 1 mass fraction in the downstream duct node for different duct definitions. Although different numbers of ducts are used, the number of cells is identical for all cases and therefore the output for all cases should also be identical. The plot demonstrates that the solution is not sensitive to differing

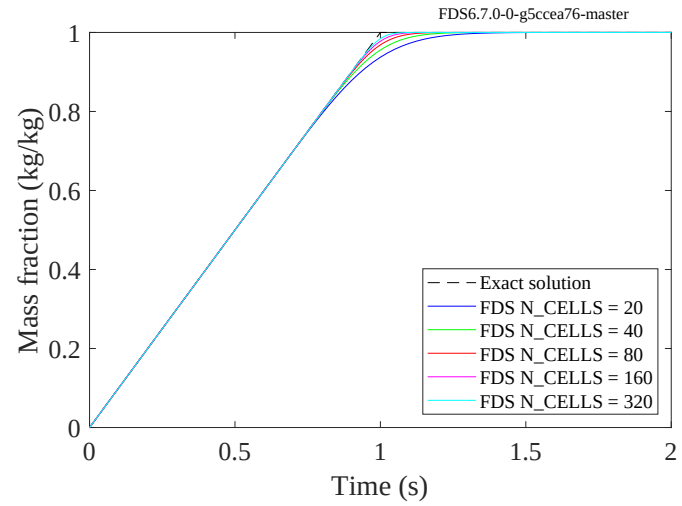

(a) Full range output.

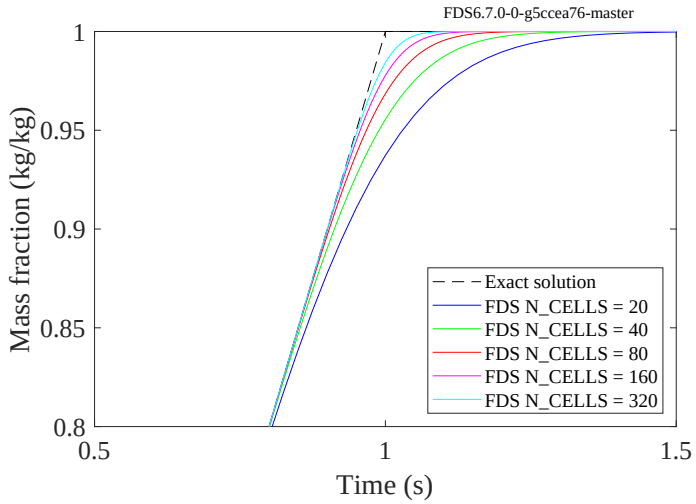

(b) Partial range output.

Figure 3.7: Exact and numerical solutions for node 2 mass fraction, showing convergence towards exact solution.

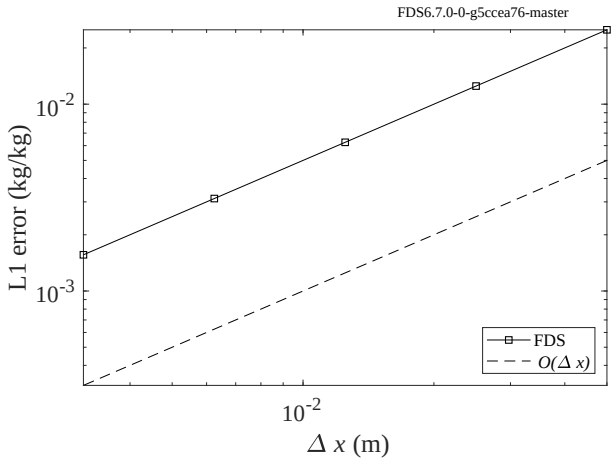

Figure 3.8: l_1-norm error between the numerical solutions and the exact solution, showing $\mathcal{O}(\Delta x)$ error decay.

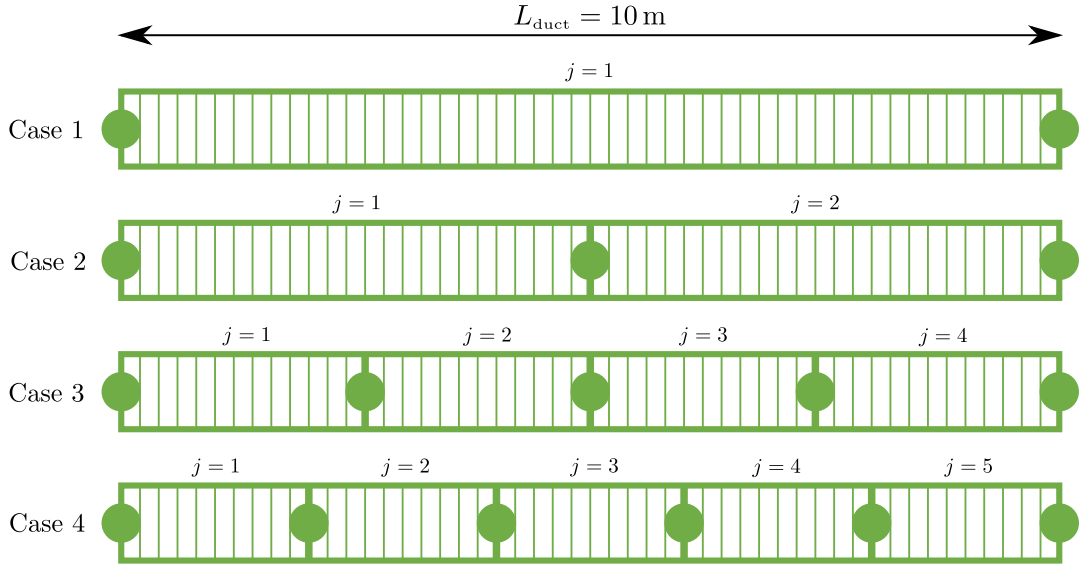

Figure 3.9: HVAC subdomains used for the set of four cases used for duct sensitivity verification case. Duct cell size shown is purely indicative. FDS field domains are omitted for clarity.

duct definitions.

3.3.3 Species transport time

A single 10 m long HVAC sub-model duct connects the two FDS field model compartments. The duct is initialised using data from the right duct node (i.e. species 2). Species 1 mass fraction at the downstream duct node is expected to start and remain at 0 kg/kg until 10 s and then instantaneously increase to 1 kg/kg as the content of the left FDS field model compartment has passed through the duct and reached the left node. The exact solution and the numerical solution are presented in Figure 3.11. The figure demonstrates that the expected transport time for species 1 is observed. The slightly smooth solution for species concentration (i.e. not a step function at $t = 10\,\text{s}$) is due to numerical diffusion.

3.3.4 Mass conservation 1

The two FDS field model compartments are connected by two HVAC sub-model ducts, A and B, each being 10 m long. Duct A is initialised with species 1 and has a flow from left to right and duct B is initialised with species 2 and has a flow from right to left. The total mass in the FDS field domain and in each compartment is expected to remain the same. Figure 3.12 shows mass in the left compartment, right compartment and in the whole FDS field domain. The figure demonstrates that the masses remain constant and that mass is conserved.

The two species are expected to mix to a species mass fraction equilibrium throughout the total hybrid domain (the FDS domain and the HVAC subdomain). There is the same mass of species 1 and 2 in the total hybrid domain ($0.7\,\text{m}^3$). The mass of species 1 in the left compartment is expected to decrease from 0.5 kg to 0.25 kg and in the right compartment it is expected to increase from 0 kg to 0.25 kg. The spatially mirrored behaviour is expected of species 2. Figure 3.13 presents the species 1 and 2 masses in the left and right compartments. The figure illustrates the species masses decreasing and

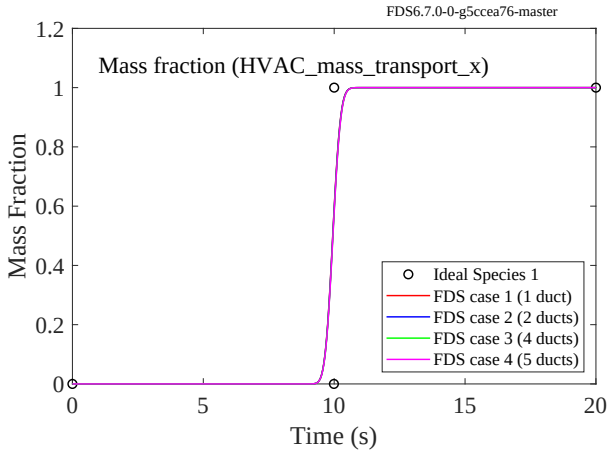

Figure 3.10: Mass fraction of species 1 at downstream node for duct sensitivity verification case. The four numerical solutions completely overlap as expected.

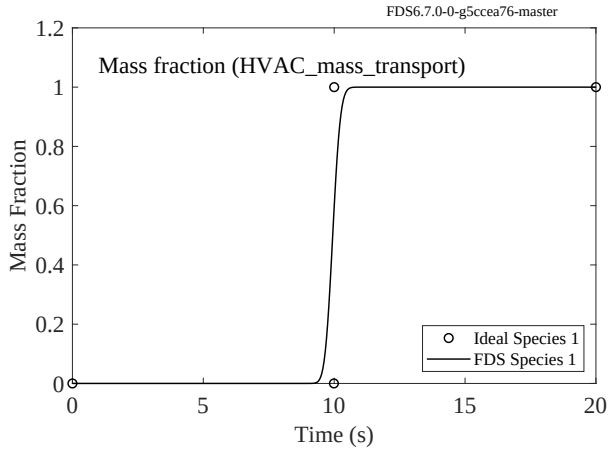

Figure 3.11: Mass fraction of species 1 at the downstream node 2 for transport time verification case.

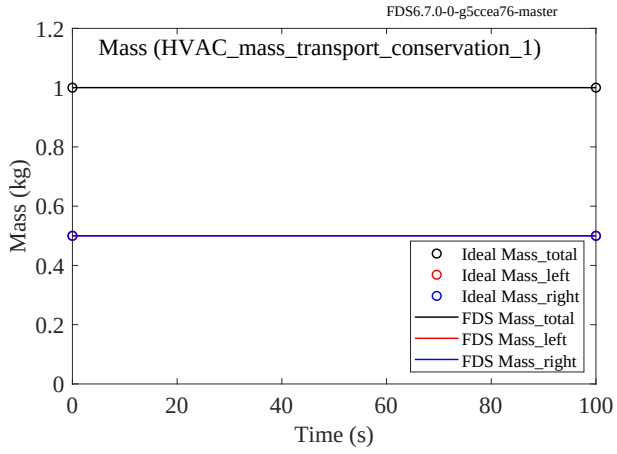

Figure 3.12: Volume integrated masses in the FDS field domain and in each compartment for the mass conservation 1 verification case.

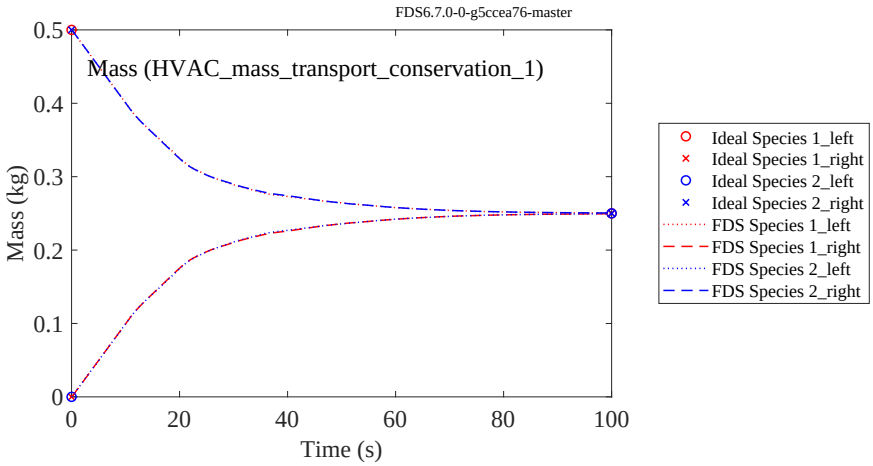

Figure 3.13: Masses of species 1 and 2 in the left and right FDS field domain compartments for the mass conservation 1 verification case.

increasing from their initial values as the two gases mix within the hybrid domain. At 100 s the masses come to equilibrium at their total hybrid domain mass ratio (50 : 50).

3.3.5 Mass conservation 2

The case set up is identical to that of Section 3.3.4 with the exception of the length of duct A being reduced to 5 m and the length of duct B being increased to 20 m. The mass of species 1 and 2 in the total hybrid domain are:

$$\sum_{\Omega_{\text{hybrid}}} m_1 = m_{1,\text{left}} + m_{1,\text{duct A}} = 0.5\,\text{kg} + 0.05\,\text{kg} = 0.55\,\text{kg} \tag{3.34}$$

$$\sum_{\Omega_{\text{hybrid}}} m_2 = m_{2,\text{right}} + m_{2,\text{duct B}} = 0.5\,\text{kg} + 0.2\,\text{kg} = 0.7\,\text{kg} \tag{3.35}$$

0.05 kg (0.022 kg of species 1 and 0.028 kg of species 2) and 0.2 kg (0.088 kg of species 1 and 0.112 kg of species 2) of gas mixture is expected to be stored within the HVAC subdomain in ducts A and B respectively. Therefore the remaining 1 kg of gas mixture (0.44 kg of species 1 and 0.56 kg of species 2) is expected to be within the FDS field domain at equilibrium.

Figure 3.14 shows the total masses of species 1 and 2 within the FDS field domain for the verification case. The figure illustrates the two species each starting at the initial conditions of 0.5 kg, gas phase mixing and establishment of equilibrium. As expected, species 1 and 2 come to equilibrium at 0.44 kg and 0.56 kg respectively (their total hybrid domain mass ratio of 0.44 : 0.56).

3.3.6 Mass conservation 3

The case set up is identical to that of Section 3.3.4 except that both ducts A and B have a length of 12.5 m and are initialised with species 2. This gives a total hybrid domain species 1 : species 2 mass ratio of 0.4 : 0.6. The species 1 and 2 masses within the FDS field domain is expected to come to equilibrium at this ratio. Figure 3.15 presents the exact and numerical solutions for the total masses of species 1 and 2. The figure shows

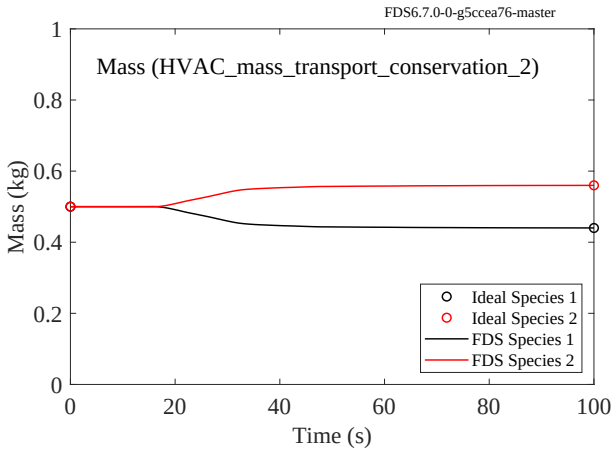

Figure 3.14: Total masses of species 1 and 2 in the FDS field domain for the mass conservation 2 verification case.

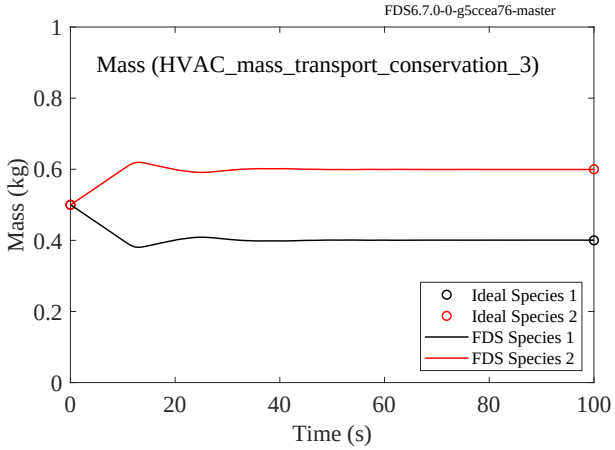

Figure 3.15: Total masses of species 1 and 2 in the FDS field domain for the mass conservation 3 verification case.

the mixing of the two species and the establishment of equilibrium at a mass ratio of $0.4 : 0.6$ as expected.

3.3.7 Branching ducts

This verification case checks that the transient transport solution is correct for an HVAC subdomain that incorporates a bifurcating duct run. The schematic of the case is presented in Figure 3.16. The two FDS field compartments are connected by an HVAC network subdomain comprising a single 5 m feed duct (duct 0) which branches into two ducts (ducts A and B) at a tee with both ducts A and B discharging to the right compartment. Ducts A and B each have a cross-sectional area of $0.005\,\mathrm{m}^2$, half that of the feed duct 0. Both ducts A and B will therefore both have a velocity of 1 m/s. Duct A has a length of 5 m and duct B has a length of 10 m. The HVAC subdomain is initialised using data from the right FDS field compartment (species 2).

Based on the duct lengths and a constant velocity of 1 m/s the species 1 mass fraction at outlet A and B is expected to increase from 0 kg/kg to 1 kg/kg at 10 s and 15 s respectively. Exact and numerical solutions are presented in Figure 3.17. The figure

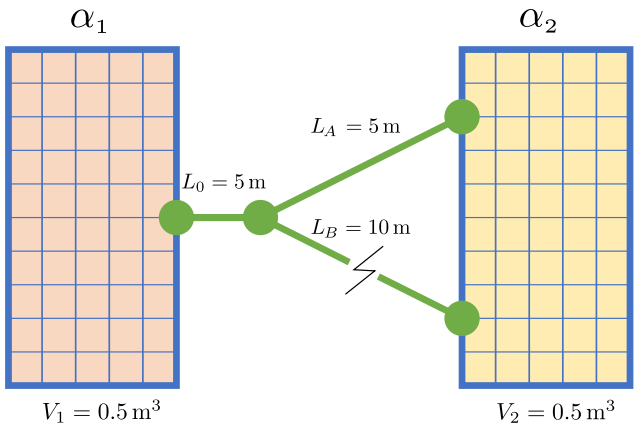

Figure 3.16: Branching ducts verification case. Velocity through HVAC subdomain is constant as ducts A and B have a cross-sectional area half that of duct 0.

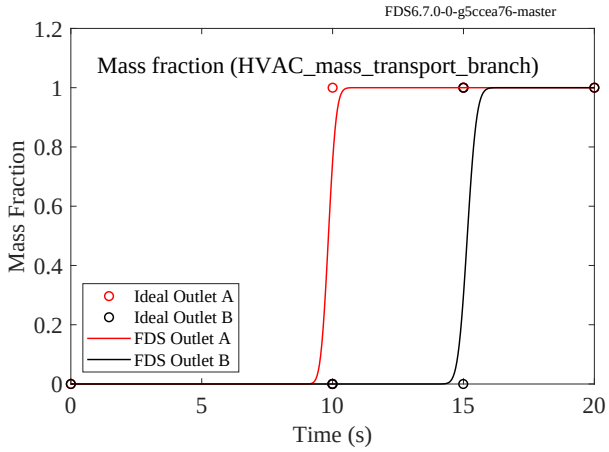

Figure 3.17: Mass of species 1 at the downstream nodes A and B. Transport time to the discharge node of duct A and B is expected to be 10 s and 15 s respectively.

illustrates that it takes 10 s for the upstream species 1 to reach the discharge node of duct A and 15 s for the upstream species 1 to reach the discharge node of duct B as expected. The slight variation is related to numerical diffusion inherent in the first-order scheme.

3.3.8 Combining ducts

This verification case checks the combining of HVAC ducts at nodes and the correct mixing of gas species. The schematic of the case is presented in Figure 3.18. The left FDS field compartment is separated into two sub-compartments, A and B. FDS field sub-compartments A and B are initialised with species 1 and 2 respectively. An inlet vent is located in both sub-compartments A and B. The inlet vents in sub-compartments A and B are connected to two separate HVAC ducts (duct A and B), of lengths 1 m and 2 m respectively, which combine at an internal tee. A single HVAC duct (duct 0), with a length of 1 m, connects this tee to the right FDS field compartment where it discharges to a single outlet vent. Ducts A and B each have a cross-sectional area of $0.005\,\mathrm{m}^2$, half that of the feed duct 0. Both ducts A and B will therefore both have a velocity of 1 m/s. The right compartment and the duct network is initialised with species 3.

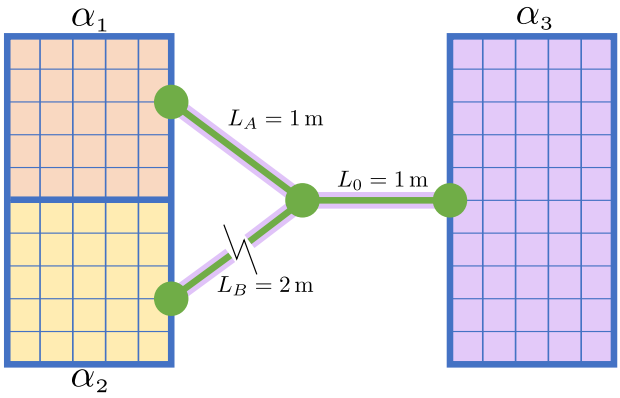

Figure 3.18: Combining ducts verification case. Velocity through HVAC subdomain is constant as ducts A and B have a cross-sectional area half that of duct 0.

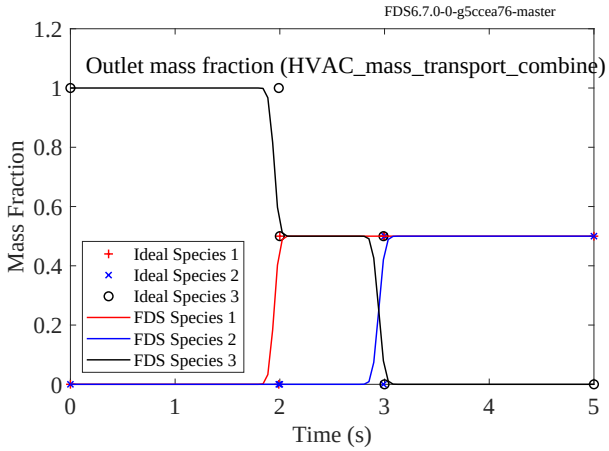

Figure 3.19: Species 1, 2 and 3 mass fraction at the outlet node into the right FDS field compartment. Initially flow contains only species 3, then a 50 : 50 mix of species 1 and 3 and finally a 50 : 50 mix of species 1 and 2.

The species mass fractions at the downstream outlet duct node are expected to be a species 3 mass fraction of 1 kg/kg for 2 s, a species 1 and 3 mass fraction of 0.5 kg/kg each from 2 s to 3 s and a species 1 and 2 mass fraction of 0.5 kg/kg each from 3 s until the end of the simulation. The exact solution and the numerical solution is presented in Figure 3.19. The figure shows that species 3 starts and remains at 1 kg/kg for 2 s as the initial contents of the HVAC subdomain flow out of the outlet node. At 2 s the species from FDS field sub-compartment A and the remaining initial species from the longer HVAC subdomain duct B flows out of the outlet node. At 3 s the species from FDS field sub-compartment B reaches the outlet node and the mass fraction is split between the species from the two upstream FDS field sub-compartments (no initial species remains in the ducts).

3.3.9 Energy conservation and pressure

This verification case checks that gas phase energy is conserved within the total hybrid domain and that pressure drop down an HVAC duct is correctly computed. The left FDS field compartment is initialised with a temperature of 100 °C, the right FDS field compartment is initialised at ambient (20 °C). The total hybrid domain is initialised

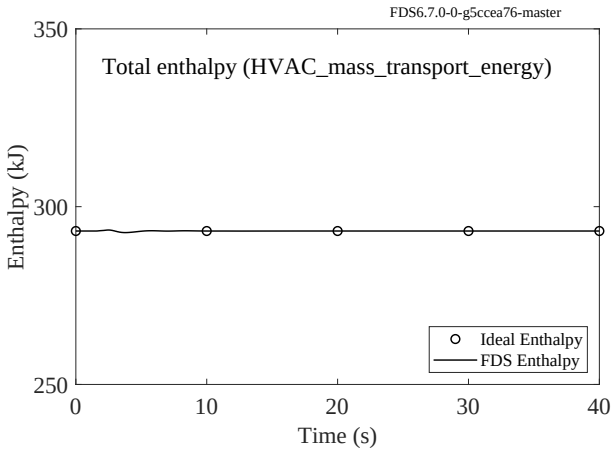

Figure 3.20: Enthalpy within the FDS field domain for the energy conservation and pressure verification case. Enthalpy is conserved for the gases at different temperatures mixing.

with a single species. The species has a specific heat of $1\,\mathrm{kJ/(kg\,K)}$. The pressure in both FDS field compartments is ambient ($101\,325\,\mathrm{Pa}$). All surfaces are set as adiabatic. The FDS field compartments are connected by two separate HVAC ducts, ducts A and B), both with a length of $1\,\mathrm{m}$. Duct A has a specified flow from left to right with a velocity of $1\,\mathrm{m/s}$, duct B has no defined flow and a minor losses coefficient $K_{\mathrm{minor}} = 2$. HVAC ducts A and B are initialised using gas data from the left and right FDS field compartments respectively (i.e. duct A has a gas temperature of $100\,^{\circ}\mathrm{C}$ and duct B of ambient).

The enthalpy in the FDS field domain is expected to be $293.15\,\mathrm{kJ}$ in Equations 3.37 to 3.38. This value should remain constant. Figure 3.20 presents the exact and numerical solution for the enthalpy within the FDS field domain. The figure demonstrates that energy is conserved within the coupled hybrid model incorporating gases at different temperatures, with different enthalpies, mixing within the total domain.

$$h_{\mathrm{field}} = c_p \frac{V_{\mathrm{field}}}{2} \left(T_{\mathrm{left}} \rho_{\mathrm{left}} + T_{\mathrm{right}} \rho_{\mathrm{right}} \right) \tag{3.36}$$

$$h_{\mathrm{field}} = 1\,\mathrm{kJ/(kg\,K)} \cdot \frac{1\,\mathrm{m}^3}{2} \left(373.15\,\mathrm{K} \cdot 0.786\,\mathrm{kg/m}^3 + 293.15\,\mathrm{K} \cdot 1\,\mathrm{kg/m}^3 \right) \tag{3.37}$$

$$h_{\mathrm{field}} = 293.15\,\mathrm{kJ} \tag{3.38}$$

To check the pressure drop along the length of duct B, first the enthalpy within the total hybrid domain in Equations 3.40 to 3.42 is calculated to enable the output of the steady state temperature and density at equilibrium.

$$h_{\mathrm{total}} = h_{\mathrm{field}} + h_{\mathrm{network}} \tag{3.39}$$

$$h_{\mathrm{total}} = h_{\mathrm{field}} + c_p \frac{V_{\mathrm{network}}}{2} \left(T_{\mathrm{A}} \rho_{\mathrm{A}} + T_{\mathrm{B}} \rho_{\mathrm{B}} \right) \tag{3.40}$$

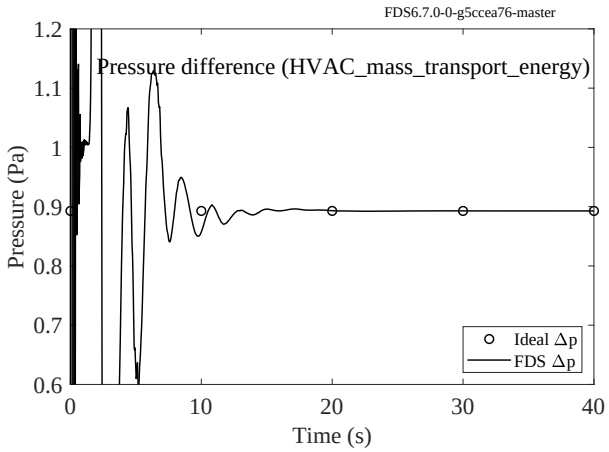

Figure 3.21: Pressure drop between the upstream and downstream HVAC nodes of duct B for the energy conservation and pressure verification case. After an initial transient stage, prior to equilibrium gas temperature and duct flow rate, the pressure drop down duct B is as expected.

$$h_{\text{total}} = 293.15\,\text{kJ} +$$

$$1\,\text{kJ/(kg K)} \cdot \frac{0.2\,\text{m}^3}{2}\left(373.15\,\text{K} \cdot 0.786\,\text{kg/m}^3 + 293.15\,\text{K} \cdot 1\,\text{kg/m}^3\right) \tag{3.41}$$

$$h_{\text{total}} = 351.78\,\text{kJ} \tag{3.42}$$

Next the equilibrium temperature is calculated. Finally the expected steady state pressure drop between the inlet and outlet node of duct B is calculated in Equation 3.46.

$$T_{\text{SS}} = \frac{h_{\text{total}}}{c_p m_{\text{total}}} \tag{3.43}$$

$$T_{\text{SS}} = \frac{351.78\,\text{kJ}}{1\,\text{kJ/(kg K)} \cdot 1.2\,\text{kg}} = 328.35\,\text{K} \tag{3.44}$$

$$\Delta p_{\text{B}} = \frac{K_{\text{minor}} \rho_{\text{SS}} u^2}{2} \tag{3.45}$$

$$\Delta p_{\text{B}} = \frac{2 \cdot 0.8928\,\text{kg/m}^3 \cdot 1\,\text{m/s}^2}{2} = 0.8928\,\text{Pa} \tag{3.46}$$

where the subscript SS denotes steady state values. Figure 3.21 presents the pressure drop calculated by the HVAC network sub-model down the length of duct B from the upstream node to the downstream node. The figure describes the initial transitory unsteady state wherein the gases at two temperatures and densities are mixing within the total hybrid domain. After this transitory state, steady state is established, wherein the gas temperature, density and duct velocity are at equilibrium, and the expected duct pressure drop is predicted.

3.4 Fire engineering test case example

To demonstrate the advantages of the new unsteady coupled hybrid modelling method implemented into FDS from version 6.5.3 onward a test case is presented representing

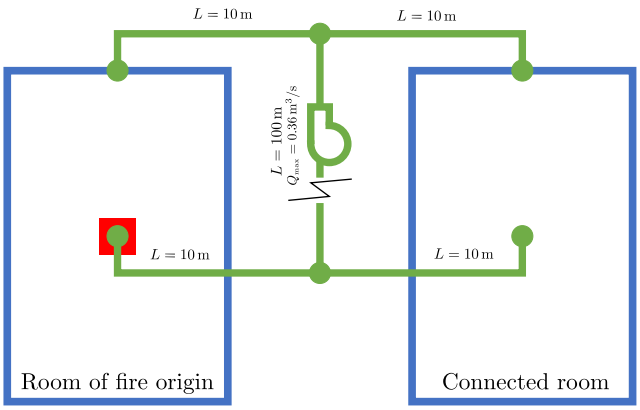

Figure 3.22: Plan of two room test case. The left room contains the fire and is connected to a non-fire room through a shared ventilation system.

a typical fire engineering assessment. The test case is designed to represent a two room arrangement where the rooms are connected only with a shared ventilation system. This is typical of an office building or hospital wards.

A fire will be modelled in the left room. The evolution of hot layer height, head height temperature, and head height visibility in proximity to the exit doors will be examined. These output quantities are typical of a fire engineering assessment for occupant evacuation. The calculation will be carried out for two cases; case 1, where `HVAC_MASS_TRANSPORT=.FALSE.`, and case 2, where `HVAC_MASS_TRANSPORT=.TRUE.`.

The rooms will be modelled within the FDS field domain and the ventilation system will be within the HVAC network subdomain.

3.4.1 Description of general arrangement of test case

Both rooms are 6 m wide, 9 m deep and 3 m high. Both rooms are provided with leakage to ambient at door locations at the back of the rooms. The leakage is located at the door sills and below the lintels and totals $0.02\,\mathrm{m}^2$ per door. The walls are modelled as `INERT` (a Dirichlet boundary condition at a constant temperature of 20 °C). The steady state heat release rate of the fire is 500 kW and starts at $t = 50\,\mathrm{s}$.

All ventilation ducts are circular. The exhaust and supply ducts serving each room have a diameter of 0.2 m. The shared return duct has a diameter of 0.3 m. Duct cross-sectional areas are adopted to achieve duct velocities typical for office buildings (5 m/s to 10 m/s [159]). The set of two exhaust ducts and two supply ducts each have a length of 10 m. The shared return duct, which contains the mechanical ventilation fan, has a length of 100 m. Duct wall roughnesses are taken as 0.003 m, typical for aluminium ducts [160]. Minor loss coefficients for fittings and junctions are taken from the literature [161]. The ventilation fan has a maximum flow rate of $0.36\,\mathrm{m}^3/\mathrm{s}$ which approximately equates to an air change per hour of 4 (typical for office accommodation [162]). The exhaust vent in each room is orientated horizontally and located on the ceiling in the centre of the room. The supply vent in each room is orientated vertically and located on the rear wall of the room.

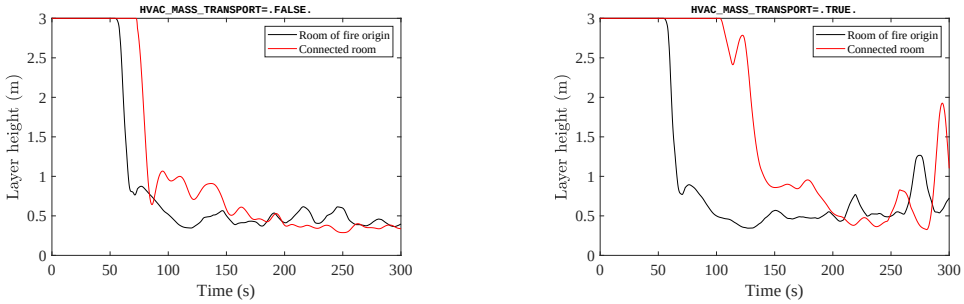

(a) Case 1. (b) Case 2.

Figure 3.23: Hot layer height in proximity to the exit for the two cases.

3.4.2 Simulation and numerical parameters

The Deardorff turbulent viscosity model is used. A single-step, mixing-controlled combustion model is used. The adopted fuel is polyurethane with a soot yield of 0.1 kg/kg. A cell size of 0.1 m is adopted for this comparative analysis. A visibility factor of 3 is used.

3.4.3 Results

Key life safety quantities have been output in the vicinity of the exit doors in each of the two rooms. The exit doors have been nominally placed at the centre front of each room. The conditions are those expected to be experienced by occupants entering or queuing at the exit doors. This is a typical fire engineering methodology used to output the available safe egress time (ASET).

Hot layer height

The hot layer height in the vicinity of the exit doors is examined. To output hot layer height a data reduction method must be used to reduce the three-dimensional field data to a single parameter called layer height (the interface between the hot upper layer and the cooler lower layer). Here the method proposed by Janssens [163] is used which has shown good agreement with experimental results.

Figure 3.23 presents the output for the two cases. Figure 3.23a illustrates that in case 1 the layer height in the connected room is predicted to drop very rapidly following that of the room of fire origin. This is because, with `HVAC_MASS_TRANSPORT=.FALSE.`, FDS does not predict the transport time required for gas phase quantities to move through the HVAC network domain. Whatever mass and energy is removed from the FDS field domain at the upstream vent is instantly transported to the downstream vent. The slight delay in the dropping of the hot layer (approximately 15 s is due to the requirement for smoke to flow out of the low level supply vent, rise to the ceiling, and start forming a hot layer. Figure 3.23b demonstrates that for case 2 the layer height in the connected room starts to drop approximately 50 s after that of the fire room. This is because case 2, with `HVAC_MASS_TRANSPORT=.TRUE.`, predicts the transient transport of mass and energy through the HVAC network subdomain.

The near-instantaneous dropping of the layer height in the connected room for case 1 would have a drastic impact upon the fire engineering analysis, conclusions and requirements. For example, provisions related to occupant notification and evacuation (sizing of horizontal and vertical exits, and use of phased or simultaneous evacuation). The

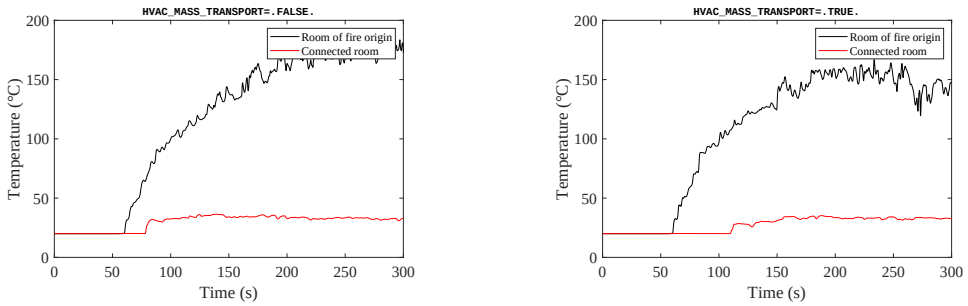

(a) Case 1. (b) Case 2.

Figure 3.24: Head height temperature in proximity to the exit for the two cases.

use of the coupled hybrid model within FDS version 6.5.2 or earlier (i.e. case 1) could lead to over-onerous and under-optimised fire engineering requirements.

Head height temperature at exit

Figure 3.24 presents the head height temperature predictions within the fire and connected room for the two cases. It shows that the temperature at head height in the connected room in both cases does not rise greatly above ambient. For this assessment, temperature may not be the critical life safety criterion for occupants egressing the connected room (a value of 60 °C is typically used [164]). However, Figure 3.24 does show two interesting and important differences between cases 1 and 2.

Firstly, Figure 3.24a illustrates that, for case 1, the increase in the predicted temperature at head height in the connected room occurs soon after the predicted increase in temperature in the fire room. This is because there is no simulated transport time and all energy and mass is instantly moved from the fire room to the connected room. In comparison, Figure 3.24b demonstrates that for case 2 the expected delay in the increase in predicted head height temperature is predicted. This is because case 2 simulates the gas transport time through the ventilation system.

Secondly, Figure 3.24 shows a higher predicted head height temperature in the fire room for case 1 when compared to case 2. This is because case 1 ignores the presence of ambient temperature air within the ventilation system. Case 2 accounts for the volume of ambient gas within the ventilation system (which is initially within the HVAC network subdomain). In case 2, there is a volume of ambient air continuing to flow into the fire room from the ventilation system after a hot layer has formed within the connected room. This cooler air will mix with the hot gas layer in the fire room and reduce the predicted head height temperature in the fire room. Furthermore, if heat losses were modelled with the duct, temperatures for case 2 would be reduced further.

These differences would have an important effect on a fire engineering assessment and any conclusions and requirements from such an assessment. For example, without the FDS calculation accounting for a mass of air within the ventilation system, oxygen availability-related phenomena may be over-predicted. These include extinction, incomplete combustion, reductions in tenability, and cooling by ambient air - all of which may be under-predicted.

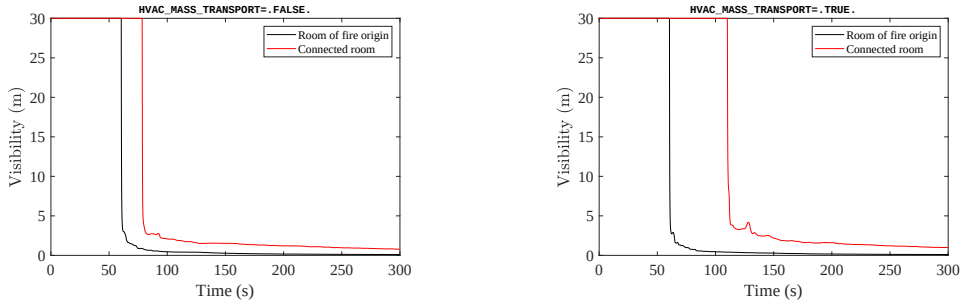

(a) Case 1. (b) Case 2.

Figure 3.25: Head height visibility in proximity to the exit for the two cases.

Head height visibility at exit

Figure 3.25 presents the predicted head height visibility at the exits for the two cases. Figure 3.25a demonstrates a very rapid drop in predicted visibility in the connected room, shortly after that in the fire room. This is because case 1 does not account for transient transport of gaseous products through the HVAC network subdomain. All mass and energy entering the ventilation system in the fire room is instantly transported into the connected room. Figure 3.25b illustrates that the reduction in predicted visibility in the room of fire is similar to that of case 1 but there is a difference in the predicted visibility in the connected room. The predicted visibility at head height in the connected room decreases at approximately 110 s. This result is due to the ability of the case 2 calculation to account for transient transport of gas phase products through the ventilation system modelled within the HVAC network sub-model. Compared to case 1 whereby all products are instantly transported to the connected room from the fire room.

Again the calculations from case 1 and case 2 would lead to a different fire engineering analysis and conclusions. For example, if relying upon the output of case 1, the analysis would under-predict the ASET within the connected room and lead to an over-specified automatic detection system.

3.5 Problems with the existing fan model

The existing HVAC sub-model within FDS version 5.5 has three fan models. The fan models are: a simple volume flow and two characteristic fan curve-based models. The two characteristic fan curve-based models are one with a user defined fan curve, specified using a `&RAMP` line, and one is a quadratic fan curve model. The quadratic fan curve model requires the user to input a maximum operating flow rate and a maximum operating pressure. FDS then computes a simple quadratic fan curve, suitable for centrifugal fans, based upon Equation 3.47 [165].

$$q_{\text{fan}} = q_{\text{max}} \operatorname{sgn}(\Delta p_{\text{max}} - \Delta p) \sqrt{\frac{|\Delta p - \Delta p_{\text{max}}|}{\Delta p_{\text{max}}}} \tag{3.47}$$

Where q_{fan} is the predicted fan flow rate, q_{max} is the maximum fan flow rate, Δp_{max} is the maximum operating pressure and Δp is the pressure at the fan. The implementation of this within the code is to find a solution of Δp. A rearranged form of Equation 3.47,

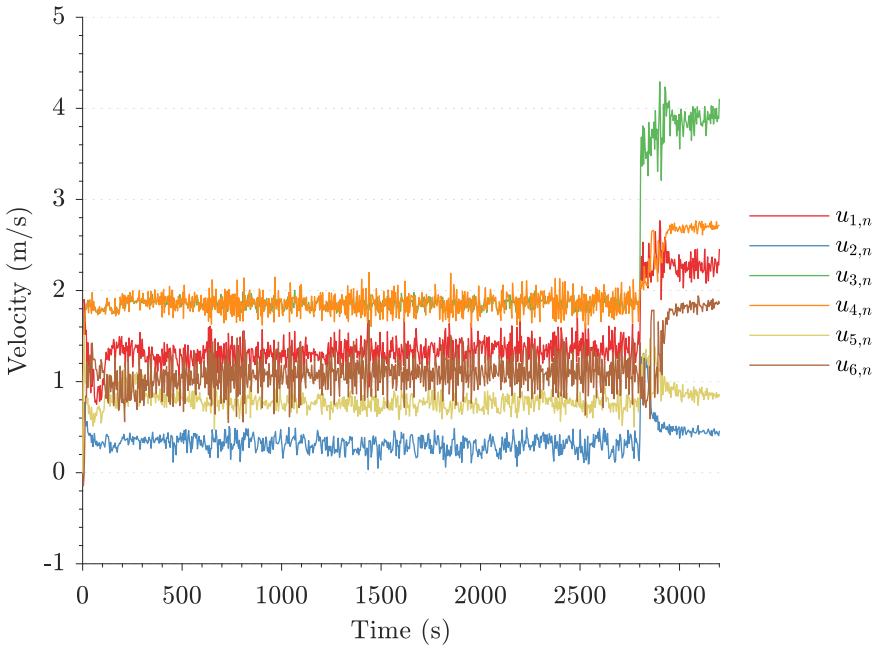

Figure 3.26: Velocities in the shared ventilation system for case `P30_F2` using the existing fan model.

given in Equation 3.48, is solved. This value of pressure is the added into the momentum equation of the duct within which the fan is located.

$$\Delta p = \Delta p_{\max} - \Delta p_{\max}\left(\frac{q_{\text{fan}}}{q_{\max}}\right)^2 \tag{3.48}$$

The fan flow rate at that time, q_{fan}, is output based upon the velocity within the duct and the area of the duct. In this manner, if the flow within the duct is low (i.e. below the operation point of the fan) the pressure drop provided by the fan is high. As the flow within the fan approaches the maximum flow rate of the fan, the pressure drop tends to zero. This is the same approach as CONTAM [166].

The problem comes when q_{fan} increases above $q_{\max}$. In this case the existing fan model code set a ceiling of q_{fan} equal to $q_{\max}$. In this way the fan could never provide a negative pressure.

This solution leads to the fan not providing a pressure drop if the flow rate through it increases over the maximum flow rate of the fan. However, this had the undesired effect of the fan pressure not being correctly predicted when the upstream pressure in the field domain connected to the network subdomain increased to a value substantially higher than the downstream field domain. In this case the fan model would throttle the flow passing through the fan. Reducing it below both the maximum fan flow rate and the flow rate expected if the fan wasn't present.

This phenomenon proved a major problem for the numerical set up. The hot box field domain of the numerical set up increases in pressure due to the presence of the fire. This was causing the existing quadratic fan model to throttle the flow passing through the shared ventilation system. This phenomenon is demonstrated in Figure 3.26. The figure is from a run of the numerical set up for case `P30_F2` using the existing fan model.

The data from the numerical set up given in Figure 3.26 shows an initial decrease in the velocities in u_1, u_3 and u_4. The opposite of what is expected to happen and what

was witnessed in the experimental data. Following the initial decrease, the velocity in the numerical set up's shared exhaust duct and the shared supply duct (u_3 and u_4 respectively) remains constant. The velocity in these ducts is expected to rise as the gases within the hot box increase in temperature and the fire-induced pressure in the hot box increases. Upon spill-mode the numerical set up's exhaust duct velocity quickly increases in magnitude substantially. Nearly doubling from approximately 2 m/s to almost 4 m/s. The shared supply duct velocity also increases in magnitude, from approximately 2 m/s to just below 2.7 m/s. The reason this increase in velocity within the shared smoke-spill and fresh air supply systems of the numerical set up occurs may be attributed to the opening of nodes connected to ambient within the network subdomain. These are the nodes at the outlet of the numerical set up's smoke-spill duct and the inlet of its fresh air supply duct. This changes the pressure solution within the network subdomain. The downstream boundary condition of the smoke-spill system is fixed. The upstream boundary condition of the fresh air supply system is fixed.

The reduction in flow rate witnessed within the numerical set up's shared ventilation system was not seen in any experimental data and is considered non-physical. A new fan model was developed to enable the correct running of the numerical set up and provide a more robust coupled hybrid model implementation.

3.6 New fan model solution adopted

3.6.1 Approach

An original method based upon finding the 'operation point' (the intersection of the system curve and the characteristic fan curve) of the fan is adopted - as described in the following paragraphs.

System curves

At any time a system (consisting of ducts, nodes, inlets and outlets) will have a 'system curve' or a 'system head'. This curve is, as the name suggests, a characteristic of the system or network. The system curve represents the pressure developed when a certain flow rate is forced through it or, considered conversely, the flow rate developed when a certain pressure is provided within the system. It is known from the fan laws, given in Equation 4.2, that pressure varies as the square of the flow rate. Therefore, when plotted on a two dimensional axis of flow rate against pressure, the system curve is a quadratic. The system curve can be thought of as the 'required pressure'. Indeed, some authors [161, 167] call the plot of the system curve 'required head' or H_{REQ}.

The simplest system curve is that for a single duct and is essentially the energy equation of that duct taken between the inlet and outlet. This is presented in Equation 3.49.

$$p_{\mathrm{sys}} = \big(p_2 - p_1\big) + \frac{1}{2}\rho\big(\alpha_2 u_2^2 - \alpha_1 u_1^2\big) + \rho g\big(z_2 - z_1\big) + p_{\mathrm{loss}} \tag{3.49}$$

Where p_{sys} is the system curve, subscripts 1 and 2 are the upstream and downstream values, p is the pressure, α is the kinematic energy correlation factor, u is the velocity, z is the elevation and p_{loss} is the pressure loss. For turbulent flow, α is assumed to be 1.0 [167]. The losses are known to be as given in Equation 3.50.

$$p_{\mathrm{loss}} = \frac{1}{2}\rho u^2\Big(\sum \frac{fl}{D} + \sum K_{\mathrm{minor}}\Big) \tag{3.50}$$

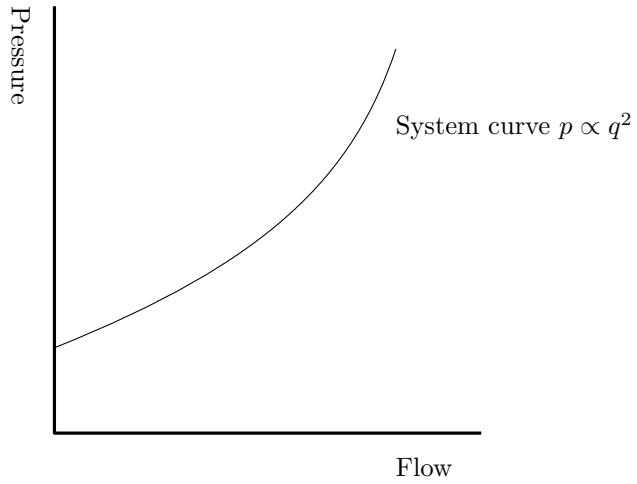

Figure 3.27: Example system curve.

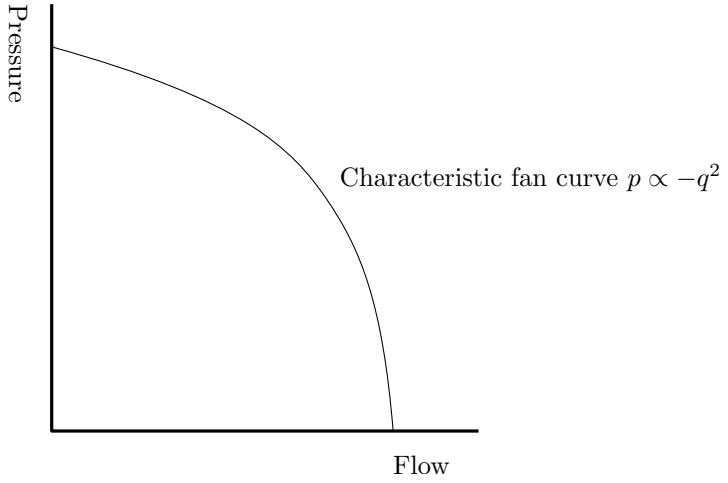

Figure 3.28: Example centrifugal fan curve.

Therefore, using Equations 3.49 and 3.50, calculating the system curve for a simple duct or a length of ducts is relatively trivial. For a complex system, in reality, final system curves are typically output using commissioning testing. An example of a system curve is presented in Figure 3.27.

From an examination of Equations 3.49 and 3.50 it is evident that this system curve will move if the conditions at the upstream and downstream nodes change. For example, if the downstream pressure increases the system curve will increase. The physical meaning of this is intuitive. If the pressure at the discharge location increases, the pressure required to develop the same flow rate will increase.

Characteristic fan curve

A characteristic fan curve is the pressure/flow rate relationship of a fan. A fan curve is set for a given blade revolution rate. A fan curve has a minimum value of flow rate ($0\,m^3/s$) at the stall pressure or 'cut-off head' of the fan and a maximum value of flow rate at the free flow condition (and hence a pressure of $0\,Pa$). An example fan curve, for a simplified centrifugal fan, is presented in Figure 3.28.

The equation for a simplified quadratic fan curve, suitable for centrifugal fans, has been presented in Equation 3.48.

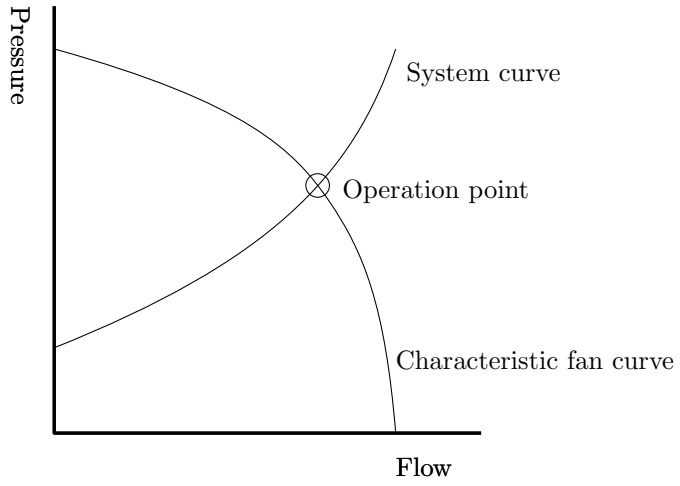

Figure 3.29: Example operation point of a fan within a system.

Finding the operation point

The operation point of a fan within a system is the intersection of the characteristic fan curve and the system curve. This is where the pressure provided by the fan matches the required system pressure. A graphical representation of this is presented in Figure 3.29.

The algebraic representation of the intersect of the fan curve and the system curve for a simple duct or run of ducts is established by equating Equations 3.48 and 3.49. In this way, the unwieldy Equation 3.51 is output.

$$\left(\Delta p_{\max} - \Delta p_{\max}\left(\frac{\rho u}{q_{\max}}\right)^2\right) - \left((p_2 - p_1) + \frac{1}{2}\rho\left(u_2^2 - u_1^2\right) + \rho g\left(z_2 - z_1\right) + \frac{1}{2}\rho u^2\left(\sum \frac{fl}{D} + \sum K_{\text{minor}}\right)\right) = 0 \quad (3.51)$$

If a solution to this equation is found, the value of pressure provided by the fan can be output. A method to assemble and solve Equation 3.51, then, is what must be implemented into FDS.

3.6.2 Implementation

Equation 3.51 is put in the form given in Equation 3.52. Where $S(q)$ is the system and $F(q)$ is the fan curve, both in terms of the flow rate. The root to this equality is then found using direct solve.

$$N(q_{\text{fan}}) = S(q_{\text{fan}}) - F(q_{\text{fan}}) = 0 \quad (3.52)$$

Outputting the fan curve

The form of the fan curve, Equation 3.48, is simply implemented within FDS. $F(q_{\text{fan}})$ is made equal to the right hand side of Equation 3.48.

Outputting the system curve

The second of the groups of terms on the left hand side of Equation 3.51 is the system curve $S(q_{\text{fan}})$. This system curve must be computed. The computation of a system curve, based upon the energy equation of Equation 3.49, is all well and good for a simple duct or run of ducts. The difficulty arises when a duct network, featuring multiple inlets and outlets, is concerned. Where are the upstream and downstream values of the quantities taken? Which pressure loss is taken? The form of Equation 3.51 breaks down. An alternative method to output $S(q_{\text{fan}})$ is required.

In reality the final commissioning of a fan within a system is carried out on site using testing. The system curve of the complex system is determined by plotting known pressures against flow rates or vice versa. The shape of this tested system curve is not expected to change beyond estimated bounds (e.g. a range of external temperatures, a range of external wind conditions).

The numerical equivalent would be to run 'tests' before a fire calculation started to characterise the system curve. A second difficulty is then encountered. The system curve can change substantially during a fire and during the fire-mode operation of the ventilation system. For example, pressure in enclosures can increase or decrease considerably and dampers can open and close. Therefore a pre-calculated system curve is not viable.

The original and innovative fan model is instead based upon the development of a system curve $S(q_{\text{fan}})$ at each time step. Based upon the fan laws and the known relationship between pressure and flow rate, the equation of a system curve can be re-written as given in Equation 3.53.

$$p_{\text{sys}} = \frac{\Delta p_{\max}}{\left(q_b - q_a\right)^2}\left(q_{\text{fan}} - q_a\right)^2 \tag{3.53}$$

Where q_a and q_b are two known flow rates which lie on the system fan curve at known locations. The location of q_a is the root of the system curve (i.e. the point of zero pressure). The location of q_b is at the maximum fan operating pressure. The problem then becomes determining q_a and q_b.

At each time step the new fan model algorithm computes the steady state solution of the duct network for an imposed pressure of zero and an imposed pressure equal to the maximum operating pressure difference of the fan. The overall steady state solutions are formed from the simultaneous solving of energy equations for each duct in the duct run (Equation 3.3) and mass conservation at each node of the duct run (Equation 3.1). Boundary conditions are set by gathering data from the relevant network-field or field-network coupling boundary condition (refer to Section 3.1.2). The solutions include pressure solutions at each node but these data are dropped as they are not required. The solution to the two steady state solves of the duct run is the values of q_a and q_b. Now the system curve at that time step is known.

Outputting the operation point

Based upon the dropping of the simplified form of the solution of the operation point (Equation 3.51), a new equality is established based upon Equation 3.53. The new equality to be solved is given in Equation 3.54.

$$N(q_{\text{fan}}) = S(q_{\text{fan}}) - F(q_{\text{fan}}) =$$

$$\left(\frac{\Delta p_{\max}}{\left(q_b - q_a\right)^2}\left(q_{\text{fan}} - q_a\right)^2\right) - \left(\Delta p_{\max} - \Delta p_{\max}\left(\frac{\rho u}{q_{\max}}\right)^2\right) = 0 \quad (3.54)$$

Equation 3.54 can be simplified to Equation 3.55 which can be directly solved using a second degree equation solution.

$$N(q_{\text{fan}}) = \left(q_{\text{fan}}^2 + q_{\max}^2\right)\left(q_a - q_b\right)^2 - q_{\max}^2\left(q_{\text{fan}} - q_a\right)^2 = 0 \quad (3.55)$$

Hence q_{fan} is output, from which Δp_{fan} is computed. The pressure provided by the fan at that time step, Δp_{fan}, can then be added to the relevant duct momentum equation to be solved as part of the overall system solve of the coupled hybrid model implementation.

3.7 Verification of the new fan model

3.7.1 Description of verification case

Two compartments (defined as pressure zones 1 and 2) share a common wall and are connected via two ducts. Both ducts have an area of 0.04 m and a length of 1 m. Duct 1 contains a fan (modelled using the new fan model) and has a loss coefficient of 5. Duct 2 has a loss coefficient of 10. The fan has a maximum volumetric flow rate of $0.16\,\text{m}^3/\text{s}$ and a stall pressure of 10 Pa. The unknown quantities to be predicted are the two compartment pressures p_1 and p_2, the velocity in the ducts u (related by the duct area to the flow rate of the fan q_{fan}), and the pressure increase from the fan p_{fan}.

Collecting the simplified energy equations for both ducts (Equations 3.56 and 3.57), the fan operation pressure equation, and acknowledging that the pressures in the two compartments will be equal and opposite - a suitable equation set is assembled.

$$\frac{p_2}{\rho} + \frac{\Delta p_{\text{fan}}}{\rho} = \frac{p_1}{\rho} + \frac{K_1 u^2}{2} \quad (3.56)$$

$$\frac{p_1}{\rho} + = \frac{p_2}{\rho} + \frac{K_2 u^2}{2} \quad (3.57)$$

Solving this equation set for the unknown quantities, the following analytical values are output: $p_1 = -p_2 = 3.12\,\text{Pa}$, $q_{\text{fan}} = 0.0408\,\text{m}^3/\text{s}$, and $p_{\text{fan}} = 9.35\,\text{Pa}$. Figure 3.30 presents a comparison between the ideal quantities established above and the predicted values. The verfication analysis demonstrates very good agreement.

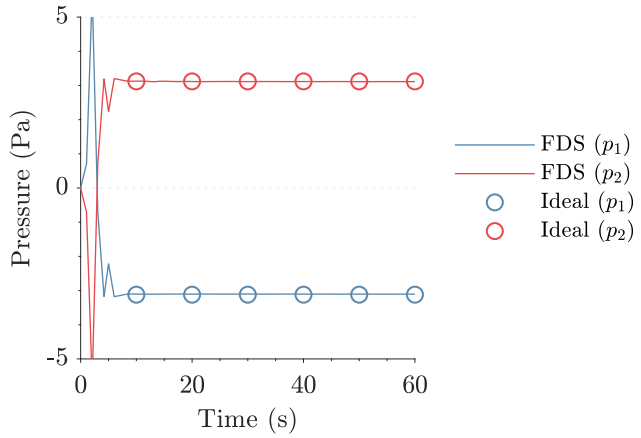

(a) Compartment pressures.

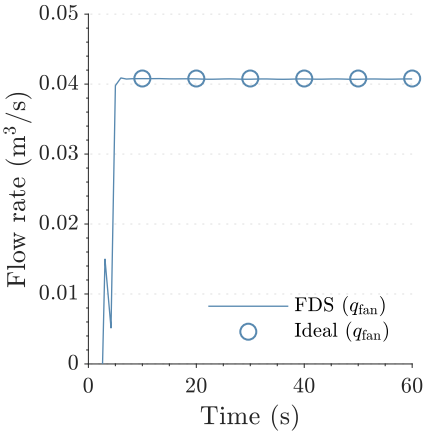

(b) Flow rate through the fan.

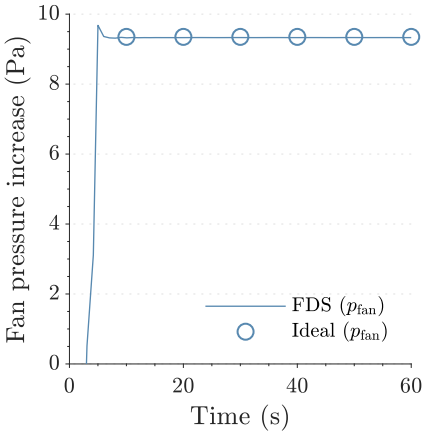

(c) Pressure increase from the fan.

Figure 3.30: Verification of new fan model. Predicted and ideal analytical values for the examined quantities. Demonstrates very good agreement between the model and the ideal values.

3.8 Closing remarks

It is known that deaths are caused by the spread of fire and smoke outside of the room of fire origin [168]. FDS version 5.5 introduced a computationally efficient way of modelling a ventilation system by way of the coupled HVAC network sub-model. However, until version 6.5.3 and the introduction of the ability to predict the transient transport of mass, species and energy though the 1D network domain the HVAC subdomain held to mass or energy and transport time was not simulated.

The original HVAC sub-model and the new addition of the transient transport of mass, species and energy (`HVAC_MASS_TRANSPORT`) have been described. Numerical verification of the new coupled hybrid model implementation has been presented and is shown to be satisfactory. Objective one of this thesis has been completed.

To illuminate the impact and usefulness of the new coupled hybrid model method, including the transient transport of gas phase quantities, a test case has been presented typical for a fire engineering analysis. The test case illustrates that the omission of transient transport through the HVAC network subdomain could have a drastic effect on the fire engineering assessment and affiliated conclusions and recommendations. The introduction of transient transport within the HVAC network sub-model will enable fire engineers to better quantify their designs when analysing a total building system.

The new coupled hybrid method implemented with FDS version 6.5.3 onward continues to have limitations. Currently, no heat loss is modelled within the HVAC network subdomain. This is expected to lead to higher predicted temperatures at HVAC-connected vents. Although the HVAC ducts have a volume and contain a mass of gas, HVAC are zero dimensional with zero volume. This functionality could be expanded to enable rooms, larger spaces, or corridors to be simply modelled within the HVAC network subdomain. There is potential for a two zone model to be introduced within the HVAC nodes for further expansion of the coupled hybrid model's capability.

The existing fan model within the network subdomain was found to lead to predictions of non-physical flow rates within the numerical set up. After investigation the problem was found to be related to how the fan reacted to pressure at the upstream and downstream connections to the field domain. An original and innovative method, based upon the computing of the fan operating point, was developed and implemented. To verify that the new fan model is addressing the problems of the existing fan model the same the numerical set up case is examined again, this time using the new fan model. Figure 3.31 presents the output of case `P30_F2` for the numerical set up with the new fan model enabled.

The data clearly illustrate that the fan is no longer throttling the flow passing through the network subdomain. The fan starts at an initial value pre-ignition. After ignition the velocity in the shared exhaust and supply system rapidly increase. The velocities continues to experience an increase through the duration of recycle mode. The new fan model also captures well the smoke-spill mode operation of the numerical set up. The shared exhaust duct velocity u_3 remains approximately at the recycle magnitude. The shared supply duct velocity u_4 drops to near to the pre-ignition magnitude.

The new fan model is currently in beta. The new fan model has been pulled into the release base build of FDS from FDS6.7.0-443-b24cf8d5-master. The new fan model is activated by setting `QFAN_BETA=.TRUE.` on the relevant fan `&HVAC` line.

As with all numerical models, benchmarking and validation are key stages in the safe and conscientious adoption and use of the simulation tool. To address this, a campaign of medium-scale experiments has been designed and carried out. The novel

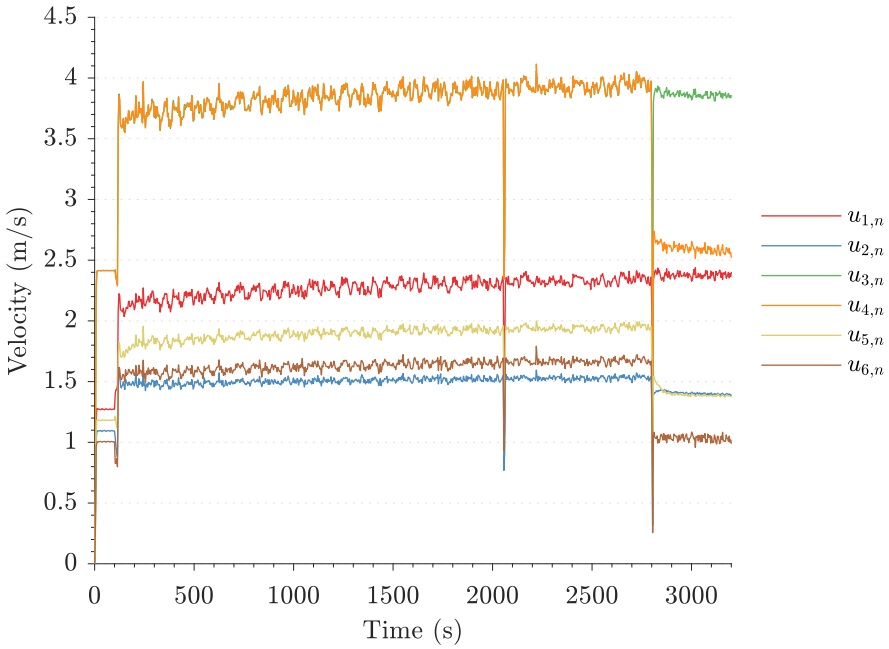

Figure 3.31: Velocity in the shared exhaust duct for case `P30_F1` using the new fan model.

experimental rig's creation is the topic of the Chapter 4. The data generated from the experimental apparatus will be used in this thesis to benchmark the new coupled hybrid model implementation in Chapter 8 and hence fulfil objective three of this thesis. This benchmarking will be able to be used by a competent fire engineer to quantify model uncertainty and safely use the newly expanded model to analyse elements of the built environment.

Chapter 4

Experimental design and methodology

4.1 Experimental design intent

The aims of the novel experimental rig can be separated into:

1. To provide good quality data to use to benchmark the new coupled hybrid model.
2. To investigate phenomena that may currently be being ignored or missed within the fire safety building design paradigm or model solutions.

Aim one of the experiments will give the model users some of the tools they require to carry out their own validation exercise of the model for their specific need. This will enable them to quantify the uncertainty of calculation output and inform their solution.

Aim two of the experiments addresses limitations within the current typical design and assessment framework, being both a limited-domain quantitative analysis and/or model solutions. These lackings are at least partially due to the current CFD-based fire modelling-driven assessment paradigm of considering only the domain immediately surrounding the room of fire origin.

With these aims in mind, the requirements of the experimental rig can be defined. The experimental rig should feature spaces connected only with a shared ventilation system. This ventilation system should be broadly representative of a typical mechanical ventilation system. That is it should incorporate a recycle mode, representing the normal use of a space, and also a smoke-spill mode. The intent of the experimental rig is not to provide a scale model of a real building. Instead it is to be paradigmatic of the built environment and exhibit the same functionality, mechanisms, and phenomena. The experimental rig should be located within the same parameter space as the built environment that it seeks to inform assessment methods of.

4.2 The mind of a modeller

Aim one of the experimental rig is to provide high quality, reliable data for validation of numerical models. These data should aim to minimise uncertainties to increase the confidence in validation conclusions made. For this reason, during the planning, design, and construction of the experimental rig, the requirements for model input were constantly considered.

The choice of materials and substances was directly affected by the acknowledgement that the data would be used to benchmark a numerical model. Therefore, materials and substances with well-characterised properties were adopted. Propane has been studied within combustion and fire science for almost one hundred years [169] and its properties, such as soot yield and CO yield, are well-characterised with small uncertainties. Vermiculite, quartz, and steel are an often-used construction materials and are similarly well-characterised with respect to density, conductivity, and specific heat. The use of the adopted fuel and construction materials increases the confidence in the data and therefore in the conclusions made during the benchmarking process.

The geometry of the experimental rig was designed to be suitable for the benchmarking of FDS and HVAC. Due to the choice of linear solver and use of the immersed boundary method, the FDS domain is (currently, though work is well underway to introduce complex geometry) constricted to a rectilinear geometry. Of course FDS can be used to model flows in non-rectilinear geometries. The use of sawtooth obstructions to represent angled geometry is commonplace in industry. However this sawtoothing of obstructions causes complications with the solution of the wall model. The default of the HVAC submodel is circular cross section ducts. For these reasons, the boxes of the experimental rig were designed as cubes and the ducting adopted had a circular cross section.

The choice of method of modelling of pyrolysis and combustion is of prime importance to the simulation of fire physics. Neither the objectives of this thesis nor the aims of the subject experimental programme encompass a fundamental examination of pyrolysis and combustion. Therefore, it is desirable to use the default pyrolysis and combustion submodels within FDS. These submodels embody lower uncertainties when compared with more advanced methods. The experimental rig should be designed so that the case falls within the limits of applicability of these default submodels. The basic 'pyrolysis' submodel within FDS is the prescribed release of a quantity of gas phase fuel into the field domain. This can be specified as a mass flow rate or a heat release rate per area. The default combustion submodel within FDS is a single-step, mixing-controlled approximation. This submodel considers a single fuel species with a prescribed soot and CO yield. Stoichiometric coefficients are calculated based on the fuel specified. Heat release rate is calculated upon known values of enthalpies of formation. The combustion mechanics within the experimental rig should be designed such that combustion occurs at or near the burner and the mixing-controlled approximation holds.

Gas phase extinction is an area of active and ongoing fire science research [170, 171]. One of the primary difficulties with this area of research is that the physics occurs at a sub-grid scale [172]. Neither the objectives of this thesis nor the aims of the subject experiment include the investigation of the modelling of extinction. Therefore, the default FDS flame extinction submodel is desirable. This submodel is based upon oxygen availability and critical flame temperature [173]. The experimental rig should be designed such that sufficient oxygen is provided to the burning gas phase fuel to remain at or near stoichiometric levels. This ensures that the adopted FDS submodel is within limits of validity.

The final primary consideration in the design of the experimental rig driven by a modeller's perspective is inflow boundary conditions of the calculations. The main inflow boundary conditions for the numerical cases are the fuel source and the air co-flow. The perfect inflow boundary condition for a modeller is an equally distributed release of a well defined volume or mass flow of a gas over a two dimensional surface.

This can be approximated for the fuel source by a sand burner. Sand burners have been developed, inter alia, to provide a well distributed and characterisable flow of gas at their surface [174]. The use of a sand diffusion media is not suitable for the air co-flow. The air co-flow is required to be directed into the gas fuel flow to ensure sufficient mixing and continued burning near the sand burner surface. Therefore, the use of a mixing-inducing apparatus is more suitable for the air co-flow. If the air co-flow is sufficiently mixed during its introduction into the experimental rig, it may be reasonably approximated by a two dimensional mass flow boundary condition within the numerical simulation.

4.3 Experimental apparatus

4.3.1 General experimental arrangement

The experimental apparatus consists of two enclosures connected to one another only with a shared ventilation system. Figures 4.1 and 4.2 present the front and left view of the experimental apparatus respectively. Figure 4.3 gives an isometric of the experimental apparatus and Figures 4.4 and 4.5 give plan and front views respectively. Appendix A presents additional photos of the rig during and after construction.

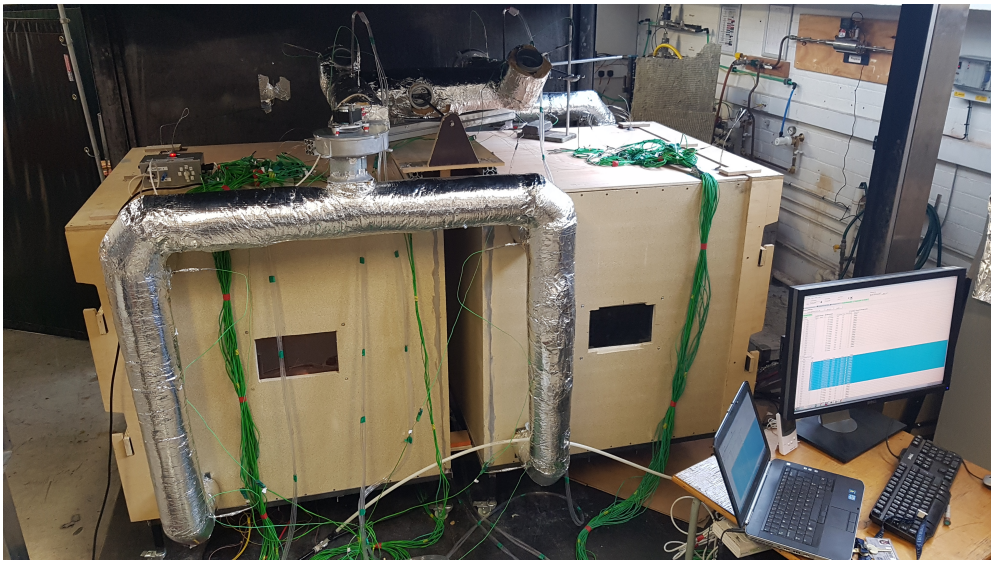

Figure 4.1: Front view of the experimental apparatus. The hot box is on the left and the cool box is on the right.

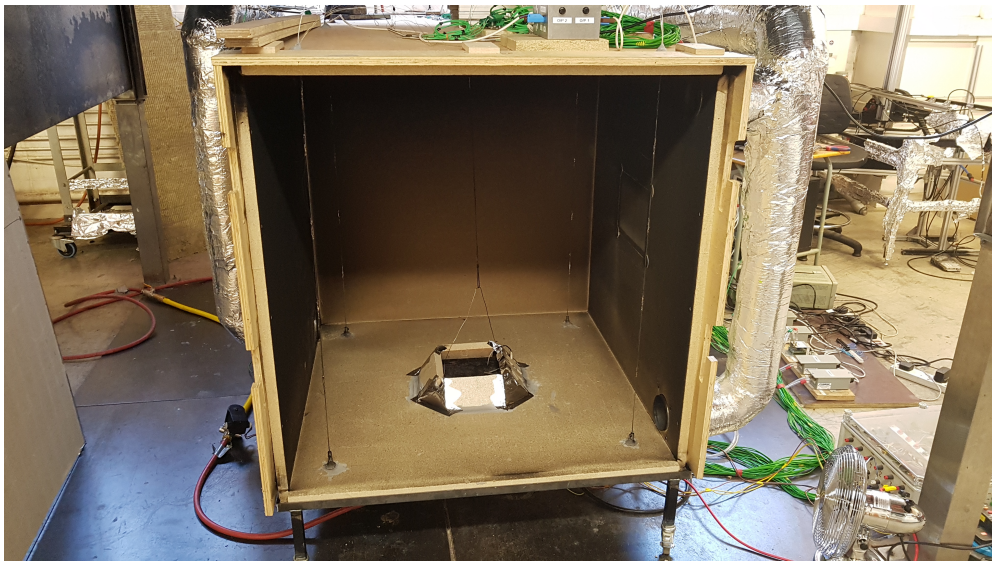

Figure 4.2: Left view of the experimental apparatus. The door to the hot box is removed and the burner can be seen at the bottom of the box.

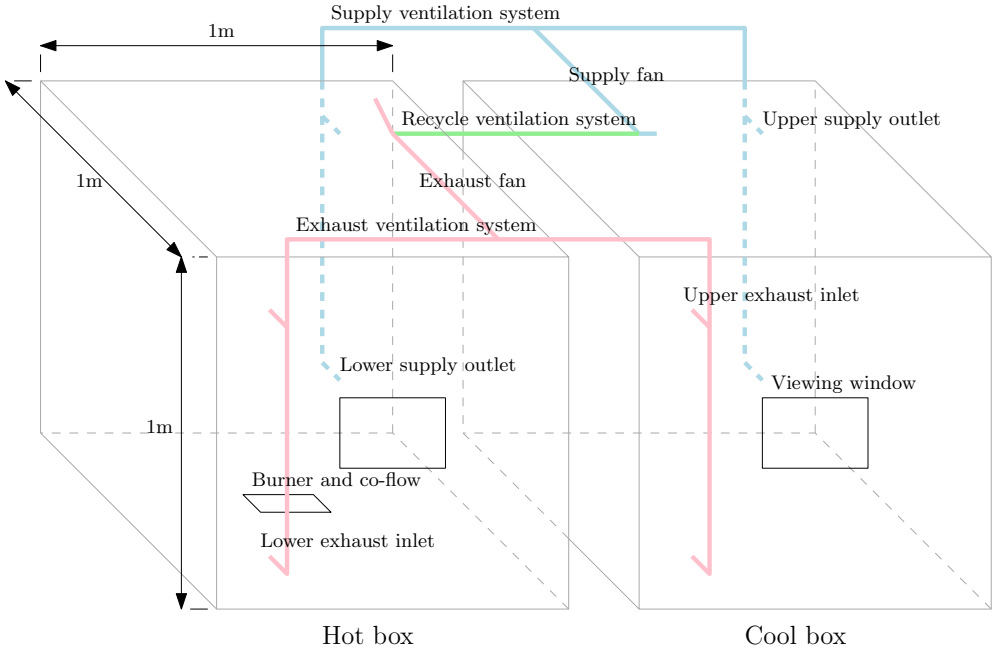

Figure 4.3: Isometric of the experimental apparatus, showing ventilation system, location of fans, viewing windows, burner, and in/outlets.

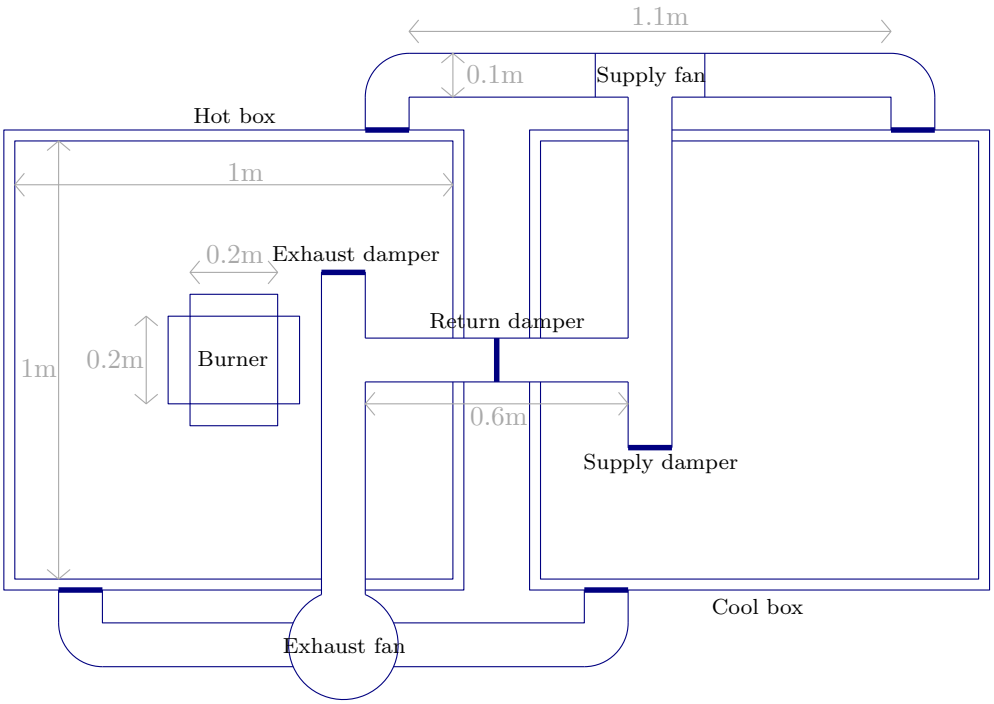

Figure 4.4: Plan view of the experimental apparatus. Hot box on left, cool box on right. Burner in centre of the hot box. Dampers shown in closed position. Internal dimensions shown.

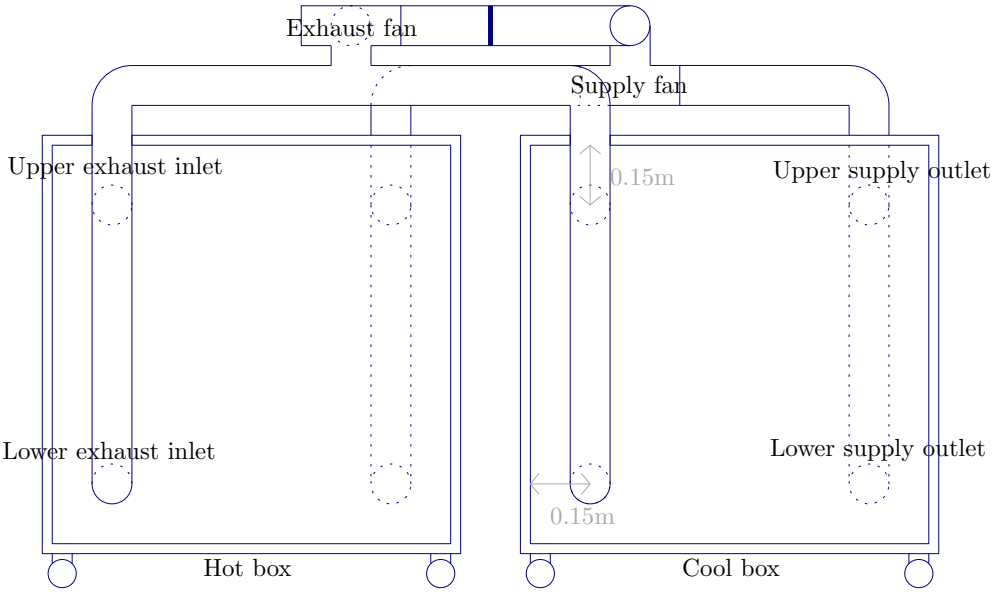

Figure 4.5: Front view of the experimental apparatus. Hot box on left, cool box on right. Exhaust ventilation system is in foreground, supply is in background/hidden.

4.3.2 The boxes

Both boxes had one wall that was removable; this served as a door to access instrumentation, seal joints, and maintain the propane sand burner and air co-flow. The walls, doors, floor, and ceiling of the boxes were each made from a single sheet of 30 mm thick vermiculite board. Edges of the boards were sealed with fire cement. Lateral and torsional restraint was provided to the boxes by an external timber frame. The timber frame was constructed of 20 mm five ply plywood. The external timber frame also held the two boxes together. The timber frame was fitted with wheels to enable the experimental apparatus to be moved within the fire laboratory. The doors were secured by two horizontal bars, which were slid into place and tightly secured the door to the box. The door was lined internally on its perimeter with ceramic paper; however, fire cement was not used on the joints of the door.

4.3.3 The burner

A propane sand burner was used for the fire source within the hot box. The sand burner had a square top surface with side dimension 200 mm. The depth of sand in the burner was 250 mm. The burner framing was constructed of welded steel. The frame comprised a main body which held the sand and meshes, a set of four legs and a propane inflow valve at the bottom of the main body. Sand and steel meshes were installed within the main body. The propane inlet at the bottom of the main body was connected to the laboratory propane supply. The connecting pipe between the propane sand burner and the laboratory propane supply was installed with a local valve. This valve was controlled electronically by the EP6 control box discussed below. The laboratory propane flow was controllable by an electronic flow control valve.

4.3.4 Ignition and gas flow control

A Caledonian EP6 control box was used to control the local propane shutoff valve and the sand burner ignitor. The EP6 has an output for a high tension (i.e. high voltage) ignitor. This ignitor was used to ignite the propane flow at the surface of the sand burner. The EP6 incorporates an ionising-based flame detector which, upon operation, turns off the ignitor.

As a safety precaution, the EP6 was arranged to close the local propane valve if no flame was detected and the ignitor was on for a period of 15 s. The remote ignition nature of the system enabled by the use of the EP6 meant that the door to the hot box could be closed prior to the start of the experiment.

4.3.5 The co-flow

To ensure that continued burning occurred at the burning surface, an air co-flow system was used. The co-flow system was connected via a control apparatus to the compressed air system within the fire laboratory. This control apparatus enables the user to specify a volume flow rate of air. The air co-flow system has multiple benefits. (1) Combustion would occur at and near the sand burner surface. This meets the requirements for reproducible benchmarking data with minimised uncertainties (default combustion and extinction submodels applicable). (2) The experiment could be run for an extended period of time without extinction. Experiments could be run to or near to steady state conditions. (3) There is a greatly reduced risk of unburnt propane being released into the experimental apparatus and hence into the fire laboratory.

Baffles were installed at the edges of the air outlets to direct air into the propane flow and to increase mixing and spreading of the air flow.

4.3.6 The viewing windows

A quartz viewing window was provided in the front of both the hot box and the cool box. The viewing windows allowed visual verification of burning at the propane burner. If burning stopped or moved from the surface of the burner, the propane flow could be quickly stopped.

Each viewing window was 250 mm wide and 200 mm high. The quartz was 3 mm thick. Quartz was selected, instead of fire-rated glass, due to its good thermal performance and visual clarity. The quartz plates were screwed into a recess in the vermiculite walls of the experimental apparatus. A gasket made of ceramic paper was used to hermetically seal the penetration in the vermiculite.

4.3.7 The shared ventilation system

The ventilation system consisted of an exhaust system and a supply system, connected by a recycle duct. All ducts were 100 mm internal diameter circular steel sections. All ducts were wrapped in aluminium lined fibre glass insulation of thickness 50 mm. The insulation was of type Climcover Roll Alu2 and provided by Isover.

The exhaust system had two inlets in each box - one low and one high. The supply system had two outlets in each box - one low and one high. For the work presented here, only the high exhaust inlet and the low supply outlet were open. This reflects typical building ventilation design [162].

The exhaust inlets from each box combined into a shared exhaust duct within which the exhaust fan was installed. From the shared exhaust duct the exhaust system either spilled to ambient or recycled into the supply system. This was achieved by opening and closing the relevant dampers. The supply system consisted of a shared fresh air inlet duct within which the supply fan was installed. This shared supply duct bifurcated into two ducts which were connected to the two boxes.

The ventilation system had operable air dampers installed in the following locations: the inlets and outlets of the exhaust and supply system for both boxes; the smoke-spill outlet to ambient; the recycle cross over duct; and the fresh air supply inlet. Figure 4.6 provides a schematic of the shared ventilation system of the experimental apparatus.

Dampers were required to control the ventilation arrangement within the experimental apparatus. Dampers were located as described in Figure 4.7.

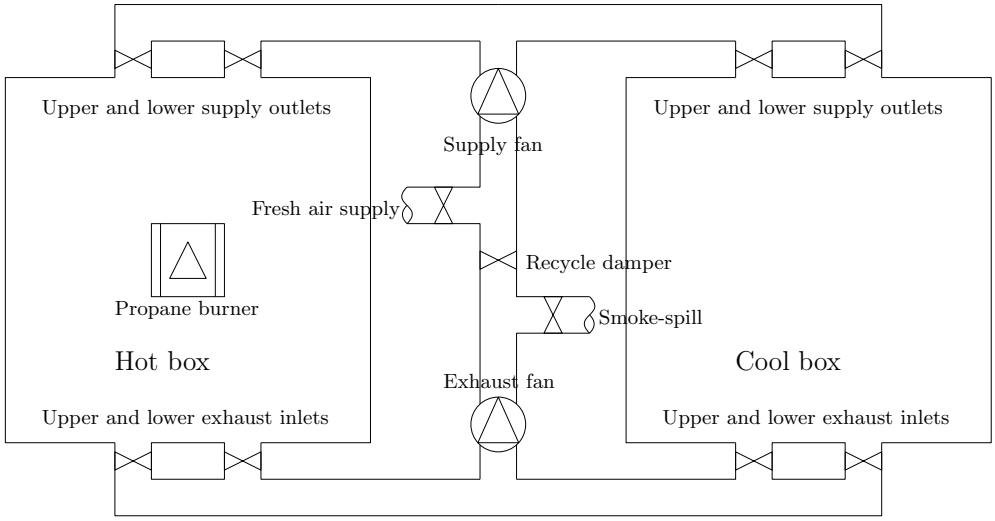

Figure 4.6: Schematic of the experimental apparatus ventilation system. The hot box is on the left, the cool box is on the right. Each box has two exhaust inlets and two supply outlets.

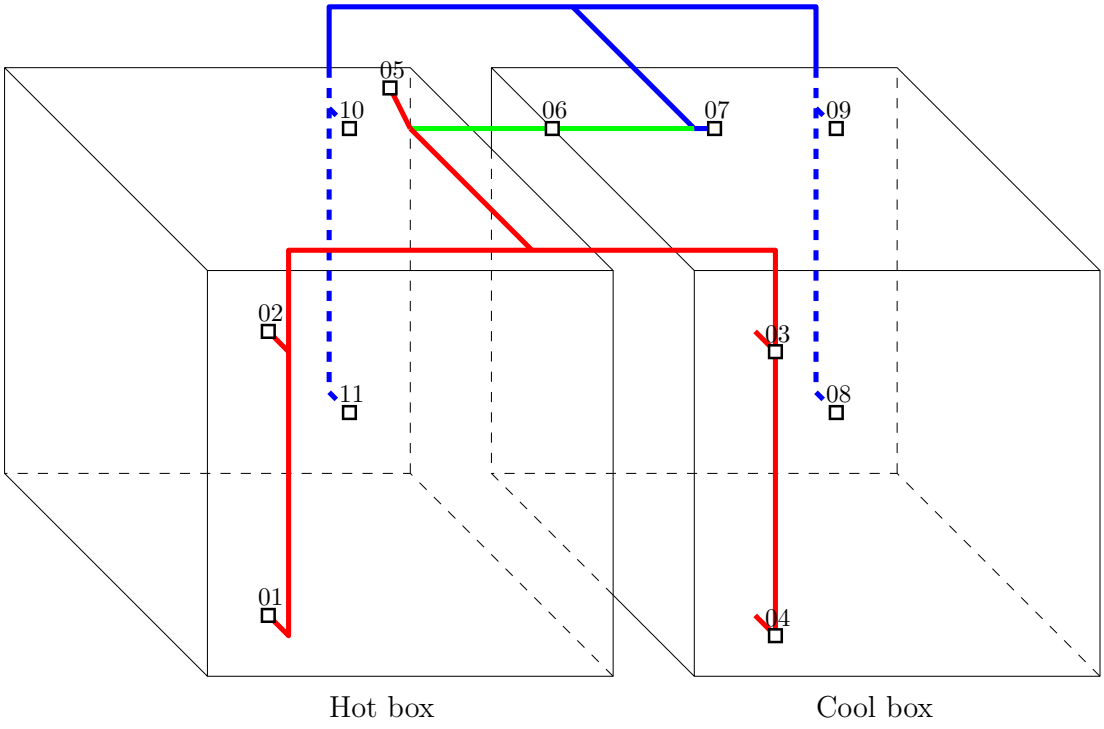

Figure 4.7: Air control dampers located within the experimental apparatus.

4.3.8 The fans

Two alternating current centrifugal fans were installed in the experimental apparatus; an exhaust fan and a supply fan. The fans were both FE-T150 fans manufactured and supplied by MMotors JSC. The fans had a free flow capacity of 145 m^3/h and a stall pressure of 280 Pa. The potential difference across the fan motors (and hence the target fan blade speed and shape of characteristic fan curve) was controlled using a potentiometer.

Characterising the fans

Cool flow experiments were carried out to characterise the relationship between the free flow fan velocity and potential difference across the fan motors. The potential difference across each fan motor was varied with a potentiometer.

Experiments were carried out with two different air velocity measuring devices: a vane type anemometer and a hot wire type anemometer. The results from the cool flow experiments were used to output a relationship between potentiometer position and free flow fan velocity for both fans. This relationship was not the same for the different combinations of fans and potentiometers (i.e. fan one had two different response curves when connected to the two potentiometers and fan two had two further different response curves when connected to the two potentiometers). Therefore, one fan was 'paired' with one potentiometer throughout the experimental campaign. The output of these cool flow tests are presented in Figures 4.8 and 4.9. The tests show good agreement between the two measurement methods. Uncertainty data for the vane and hot wire anemometers were taken from Popiolek et al. [175] and Hoff et al. [176] respectively.

These velocity data can be used to output volume flow rate using Equation 4.1. Using one of the fan laws (also known as the affinity laws or the pump laws and presented in Equation 4.2), the ratio of maximum flow rate to subject flow rate can be used to relate maximum pressure and subject pressure.

$$q = uA \tag{4.1}$$

$$\frac{{q_1}^2}{{q_2}^2} = \frac{p_1}{p_2} \tag{4.2}$$

where q is the fan flow rate, u is the free flow air velocity, A is the fan outlet area, p is fan pressure and the subscripts 1 and 2 are two points on the characteristic fan curve. These data can be used to generate the characteristic pressure-flow fan curve for the fan at the subject potential difference. The maximum duty fan curve and the fan curves for the adopted fan levels (`F1`, `F2` and `F3`) are presented in Figure 4.10.

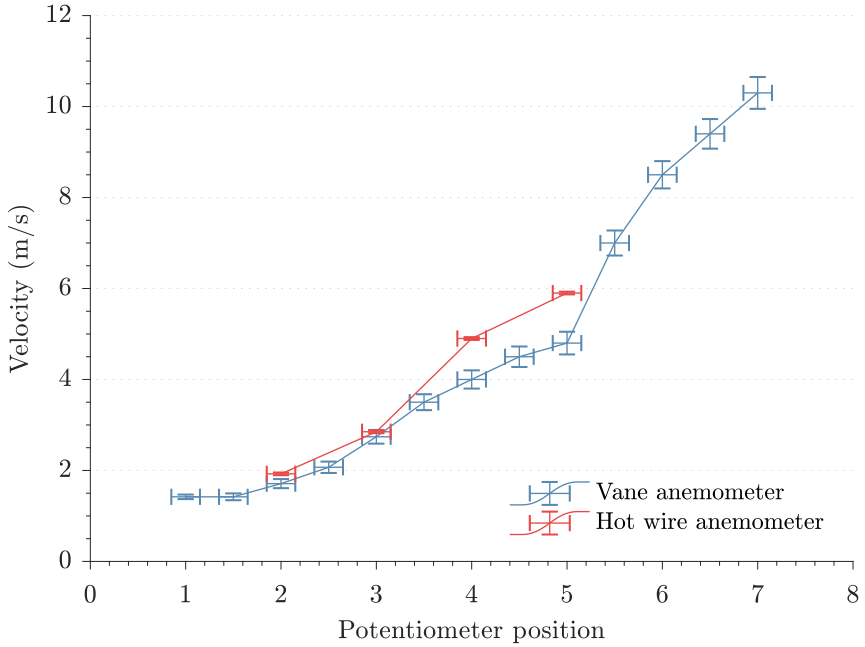

Figure 4.8: Free flow test of fan 1 (exhaust).

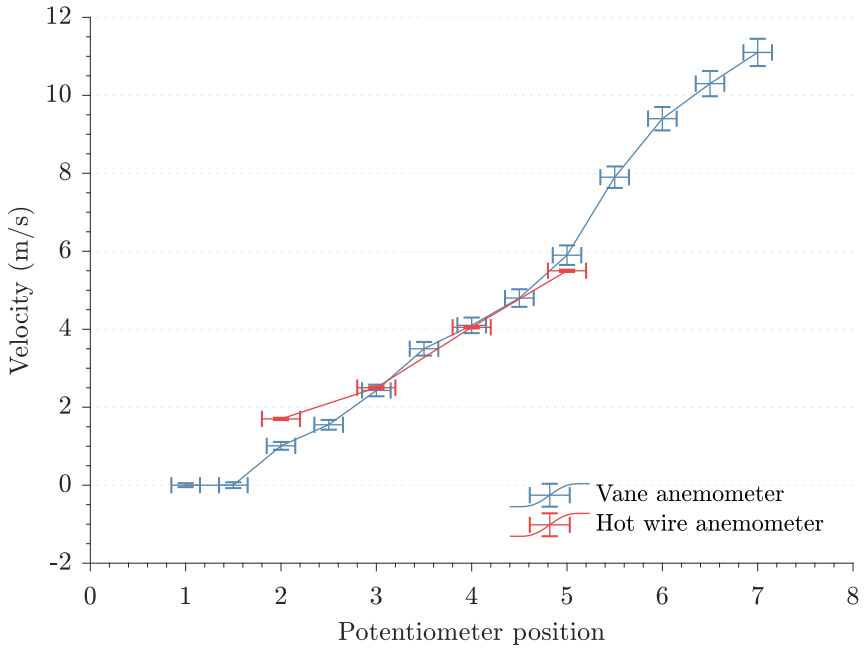

Figure 4.9: Free flow test of fan 2 (supply).

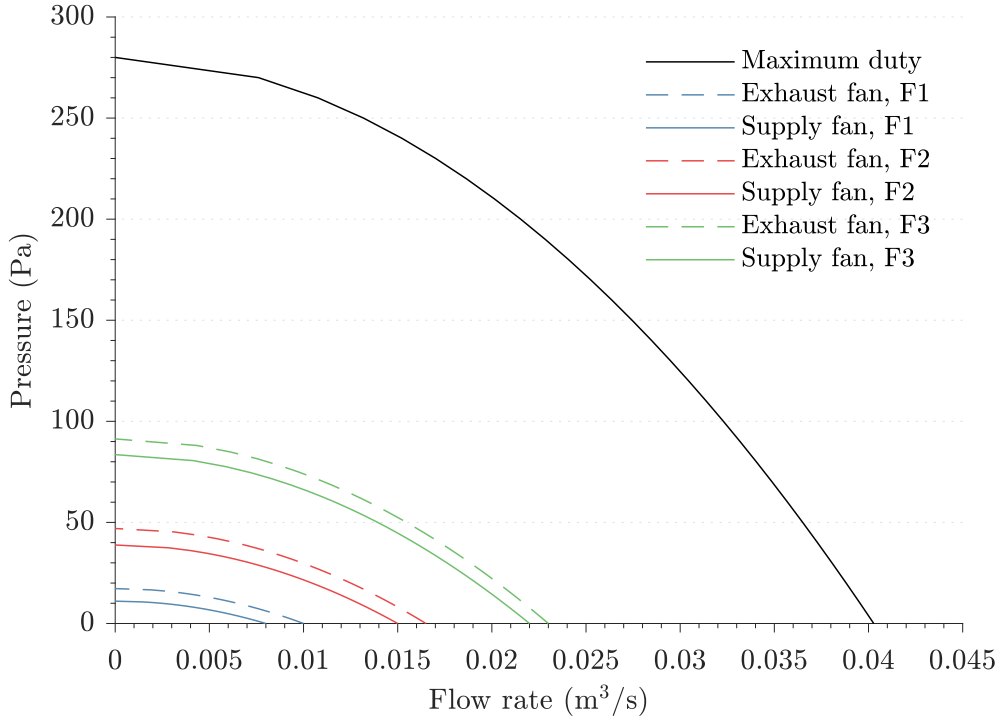

Figure 4.10: Computed characteristic fan curves.

4.4 Description of experimental procedure

The procedure for each experiment is:

- 0 s: hot box and cool box doors are closed and sealed.
- 0 s: exhaust and supply fans are set to relevant potentiometer setting.
- 0 s: all upper exhaust inlet air dampers are opened.
- 0 s: all lower exhaust inlet air dampers are closed.
- 0 s: all upper supply air dampers are closed.
- 0 s: all lower supply air dampers are opened.
- 0 s: smoke-spill and fresh air supply air dampers are closed.
- 0 s: return air damper is opened.
- 200 s: propane flow rate set to relevant setting and burner is ignited.
- 2600 s: smoke-spill and fresh air supply air dampers are opened.
- 2600 s: return air damper is closed.
- 3200 s: propane flow stopped and experiment terminated.

4.5 Independent variables

4.5.1 Adopted independent variables

The amount of variables able to be chosen as independent variables is finite. Therefore, the variables considered the most important or critical to the examined problem should be adopted. Based upon the examination of standard guidance and the typical fire engineering assessment methods the adopted independent variables are:

- **Propane mass flow.** This is a method of controlling the heat release rate of the fire within the fire enclosure. The adopted propane flow rates are presented in Table 4.1.
- **Potential difference across fan motor.** This is a method of controlling the pressure-flow behaviour of a fan. This could also be thought of as controlling of the free flow volume flow rate or velocity, the maximum stall pressure of the fan, or the shape of the characteristic fan curve. The adopted potentiometer levels (and target free flow fan velocities, refer to Section 4.3.8) are presented in Table 4.2.

Table 4.1: Propane flow rates and case sub-name identifier.

Sub-name	Propane flow rate (g/s)
P20	0.20
P25	0.25
P30	0.30
P35	0.35
P40	0.40
P45	0.45

Table 4.2: Potentiometer level, target fan velocity and case sub-name identifier.

Sub-name	Potentiometer level	Target free flow velocity (m/s)
F1	2	1.0
F2	3	2.0
F3	4	3.0

Propane mass flow is adopted because heat release rate is generally considered to be the single most important input parameter within fire engineering [177]. The sizing of mechanical ventilation systems is a typical output of a fire engineering assessment [178]. Including these independent variables, and hence providing data across a range of heat release rates and fan performances, gives model users more applicable benchmarking data to be used to inform their validation exercise.

Propane mass flow and fan potential difference were also adopted because it is considered likely that, when examining a total building system and hence the two-way coupling between a fire and a building that there is an envelope of mechanisms informed by the interplay between the fire power and the ventilation system power. This helps fulfil aim two of the experimental rig.

The principle experimental campaign case matrix is presented in Table 4.3.

Table 4.3: Experimental programme case matrix.

Case	Propane flow rate (g/s)	Target free flow velocity (m/s)
P20_F1	0.20	1.0
P20_F2	0.20	2.0
P20_F3	0.20	3.0
P25_F1	0.25	1.0
P25_F2	0.25	2.0
P25_F3	0.25	3.0
P30_F1	0.30	1.0
P30_F2	0.30	2.0
P30_F3	0.30	3.0
P35_F1	0.35	1.0
P35_F2	0.35	2.0
P35_F3	0.35	3.0
P40_F1	0.40	1.0
P40_F2	0.40	2.0
P40_F3	0.40	3.0
P45_F1	0.45	1.0
P45_F2	0.45	2.0
P45_F3	0.45	3.0

4.6 Dependent variables

4.6.1 Adopted dependent variables

As with the choice of independent variables, dependent variable choice is also infinite. The experiment designer is forced to choose dependent variables that are the most critical to the aims of the investigation as framed within the context of the application. This occurs in parallel with practicability considerations of time, buildability, and cost. The dependent variables were chosen based upon the application space of fire engineering analysis and their methods:

- Temperatures within the enclosures.
- Temperatures within the shared ventilation system.
- Velocities within the shared ventilation system.

Elevated temperatures due to fire are a prime safety consideration within the field of fire science and fire safety [130]. Quantification of this metric, both within the enclosure of fire, connected enclosure, and the shared ventilation system is of paramount importance.

Temperatures and velocities (and the subsequently calculable volume and mass flow rates) within the ventilation system and within the connected enclosure can provide valuable benchmarking data for the coupled hybrid model.

4.7 Physical parameter space

The experimental apparatus is not a scale model of a real building. There are widely acknowledged problems with attempting to scale fire phenomena [179]. Instead the apparatus serves to produce a benchmarking dataset which may be used by model users to inform their validation exercise. For this reason, the experiment should share parameter space with the specific applications for which the coupled hybrid model may be used. This is primarily elements of the built environment such as buildings and ships.

The important experimental parameters considered are based primarily upon the FDS Validation Guide [131] and NFPA 92 [18]. These are: non-dimensionalised heat release rate ($\dot{Q}^*$); the ratio of flame height to enclosure height (L_f/D); air changes per hour (ACH); and leakage flux (q'_{leak}).

The non-dimensional heat release rate, being the square root of a Froude number, is relevant to conditions where turbulence is more important than viscous forces. In this scenario, the overall behaviour is dominated by the effect of the relationship between the momentum and the buoyancy. This scenario is true of a typical natural or building fire where the flow field is turbulent. This is the most likely application of the subject coupled hybrid model. The typical form of the non-dimensional heat release rate is:

$$\dot{Q}^* = \frac{\dot{Q}_c}{\rho_\infty c_p T_\infty \sqrt{gD} D^2} \tag{4.3}$$

where Q_c is the convective [28] (or chemical [180]) heat release rate, ρ_∞ is the ambient density, c_p is the specific heat capacity of air, T_∞ is the ambient temperature and D is the diameter of the fire.

The ratio of the flame height to the enclosure height is also considered an important dimensionless group within enclosure fires. This dimensionless group can describe whether there is direct flame impingement upon the ceiling, radiative heat transfer from the flame, and entrainment. The use of flame height can also address deficiencies in the assumptions of $\dot{Q}^*$ regarding the ignoring of fuel type-related effects. Dimensionless flame height can capture fuel-dependent convective fraction [181].

Air changes per hour is a measure of the through flow of air delivered by a ventilation system. It is calculated by dividing the total serviced volume by the combined ventilation duty:

$$\text{ACH} = \frac{\sum\limits_{f \in F} q_f}{V} \tag{4.4}$$

where ACH is the air changes per hour, V is the volume of the enclosure(s), q is the fan flow rate, the subscript f denotes a fan and F is the complete set of fans. ACH characterises the total ventilation system duty relative to the volume of the conditioned space and is often used in air-conditioning design and fire safety design to prescribe mechanical ventilation system requirements.

Table 4.4 presents the important experimental parameters for the experimental apparatus and those of typical fire safety applications (office, healthcare, and marine vehicles).

Table 4.4: Experimental parameter space of the experimental apparatus.

Parameter	Experimental apparatus	Typical application
$\dot{Q}^*$	0.42 to 0.84	0.30 to 1.00 [182]
L_f/H	0.31 to 0.47	0.3 to 1.0 [131]
ACH	13 to 30	10 to 15 [112]

4.8 Instrumentation of the experiment

4.8.1 Description of measurements

Box temperature

Thermocouples were installed within both boxes of the experimental apparatus. A matrix containing twenty five thermocouples was installed in each box. The thermocouples were arranged in trees of five thermocouples. There were five thermocouple trees per box. On each tree the thermocouples were spaced at 200 mm, 400 mm, 600 mm, 800 mm and 900 mm from the floor of the box. The density of thermocouples was slightly increased at the ceiling as this is where the steepest temperature gradients are expected. The trees were located in the centre and the four corners of the boxes. The trees in the corners were located 100 mm away from the two adjacent walls of the boxes. The layout of the thermocouples in the boxes is presented in Figure 4.11.

The thermocouples within the boxes were chosen to be more durable than the thermocouples in the ducts. For this reason a bead size of 0.5 mm was chosen. Based upon the predicted temperature range, Type K thermocouples were chosen. To increase response time exposed junction type thermocouples were chosen.

Duct temperature

Sixteen thermocouples were installed within the ducts. The thermocouples were installed such that their bead was in the centre of the duct cross section. Thermocouples were installed at each inlet and outlet, on the exhaust and supply branch of each box, in the shared exhaust and the shared supply ducts and in the smoke-spill outlet and fresh air inlet. The location of thermocouples within the ventilation system is described in Figure 4.12.

It was acknowledged that the in-duct thermocouples did not need to be as robust as the in box thermocouples as they were not readily accessible. Finer thermocouples, with a bead size of 0.25 mm were used for the in-duct thermocouples. In line with the box thermocouples, the in-duct thermocouples were Type K with exposed junction.

Duct velocity

To measure velocity within the ducts, McCaffrey bidirectional low-velocity probes [2] were installed in six locations in the ventilation system. Figure 4.13 reproduces the general design of the adopted velocity probe. The velocity probes were installed in the centre of the duct cross section. McCaffrey velocity probes were chosen because they have reasonable performance at low velocities, good performance at high temperatures, and are low cost. The up and downstream tubes of the velocity probes were connected to Omega PX277-0.1D5V differential pressure transducers. These pressure transducers produce an analogue VDC output between 0 V and 10 V. The pressure transducers have a range of −12.5 Pa to 12.5 Pa in bidirectional mode or 0 Pa to 25 Pa in unidirectional

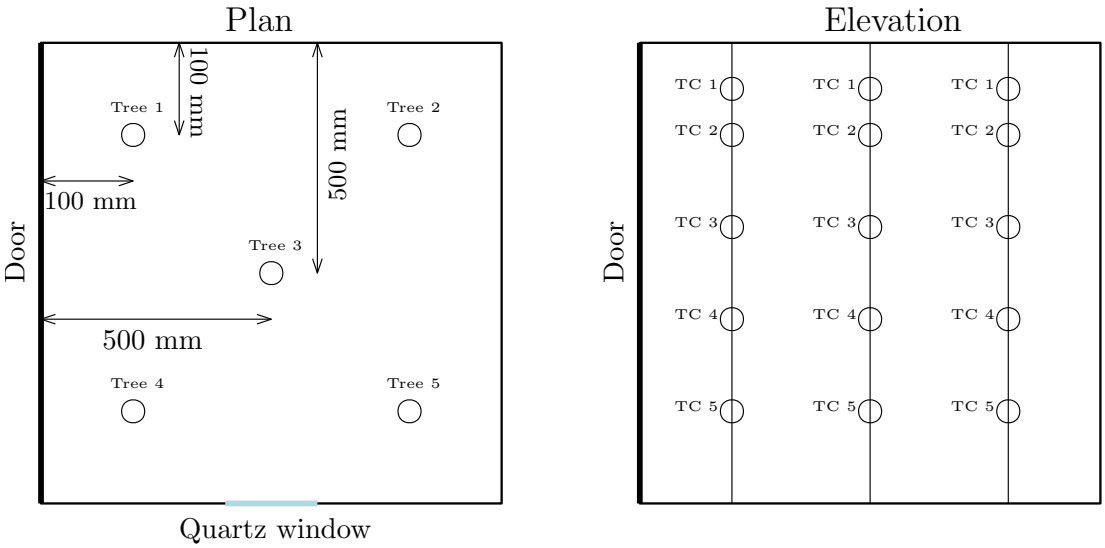

Figure 4.11: Location of thermocouples in each box (hot box). Individual naming of thermocouples is omitted for clarity. Designation of thermocouple is: TC_A_B_C where A is the box number, B is the tree number and C is the thermocouple number. For example, the middle thermocouple for the centre tree in the cool box is TC_2_3_3.

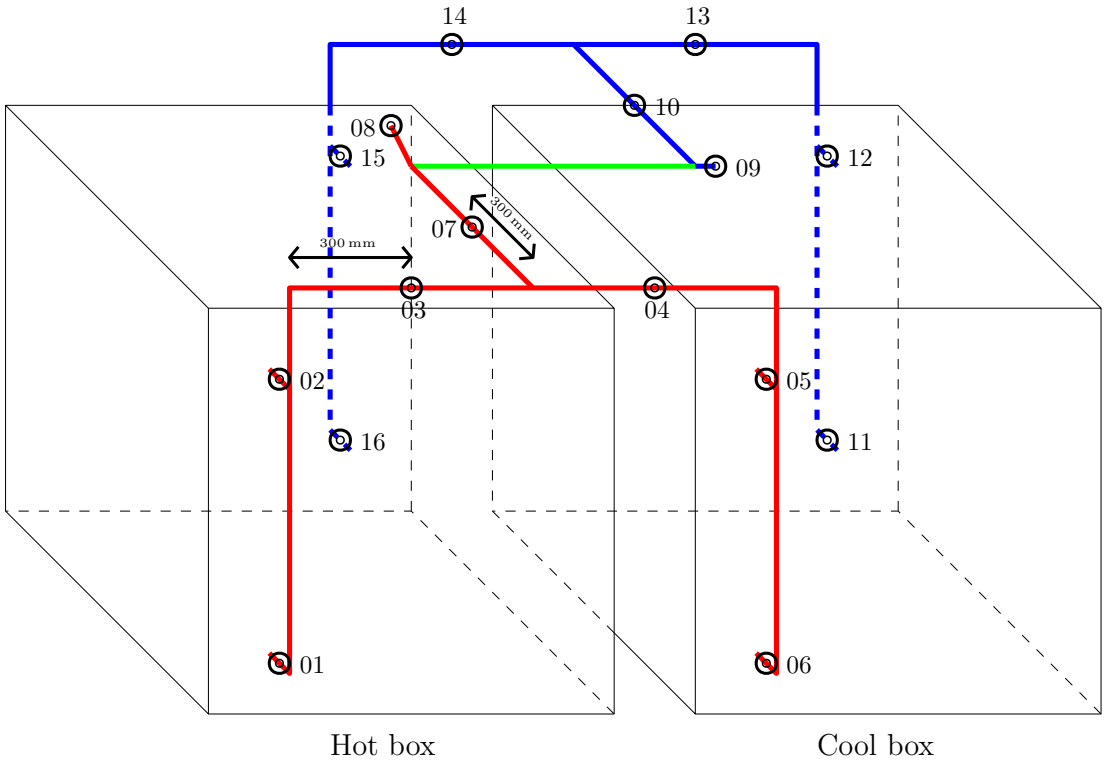

Figure 4.12: Location of in-duct thermocouples in the experimental apparatus. The exhaust, supply and return system are shown in red, blue and green respectively.

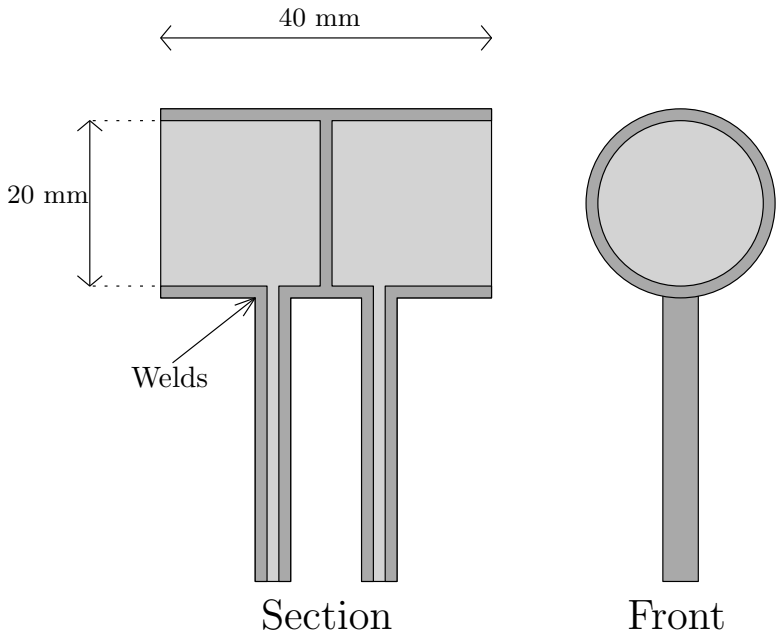

Figure 4.13: General design of McCaffrey bidirectional velocity probe used in the experimental apparatus.

mode. These pressure transducers were chosen because they have a suitable output, a range of differential pressures that span the velocities that were expected within the experimental apparatus and a reasonable cost per unit. It is acknowledged that these pressure transducers, being based upon piezoresistivity, are known to experience long term drift of measurement [183].

0.25 mm Type K exposed junction thermocouples were installed in close proximity to the velocity probes. The data from these thermocouples were used to estimate temperature-dependent density at the velocity probe. These data are needed to estimate velocity from the pressure difference data recorded by the connected pressure transducer.

To obtain a measurement of velocity from the recorded VDC output, the data must be post-processed. A linear relationship between VDC and differential pressure is adopted between the span of the voltage output and the pressure measurement. A linear coefficient of $\gamma_{\text{tran}} = 2.49\,\text{Pa/V}$ is adopted based upon calibration data from the University of Edinburgh. Estimated differential pressure is output according to Equation 4.5 for unidirectional mode and Equation 4.6 for bidirectional mode. The relationship between measured VDC and pressure for the subject pressure transducers is presented in Figure 4.15.

$$\Delta p = \gamma_{\text{tran}} V \tag{4.5}$$

$$\Delta p = \gamma_{\text{tran}} V - 12.5 \tag{4.6}$$

where Δp is the measurement of differential pressure, γ_{tran} is the transducer calibration factor and V is the VDC from the device.

To estimate the velocity from the differential pressure data a probe-specific calibration factor is required. This is typically defined as the square root of the ratio of the measured pressure and the velocity head. This is rearranged for convenience to give the velocity:

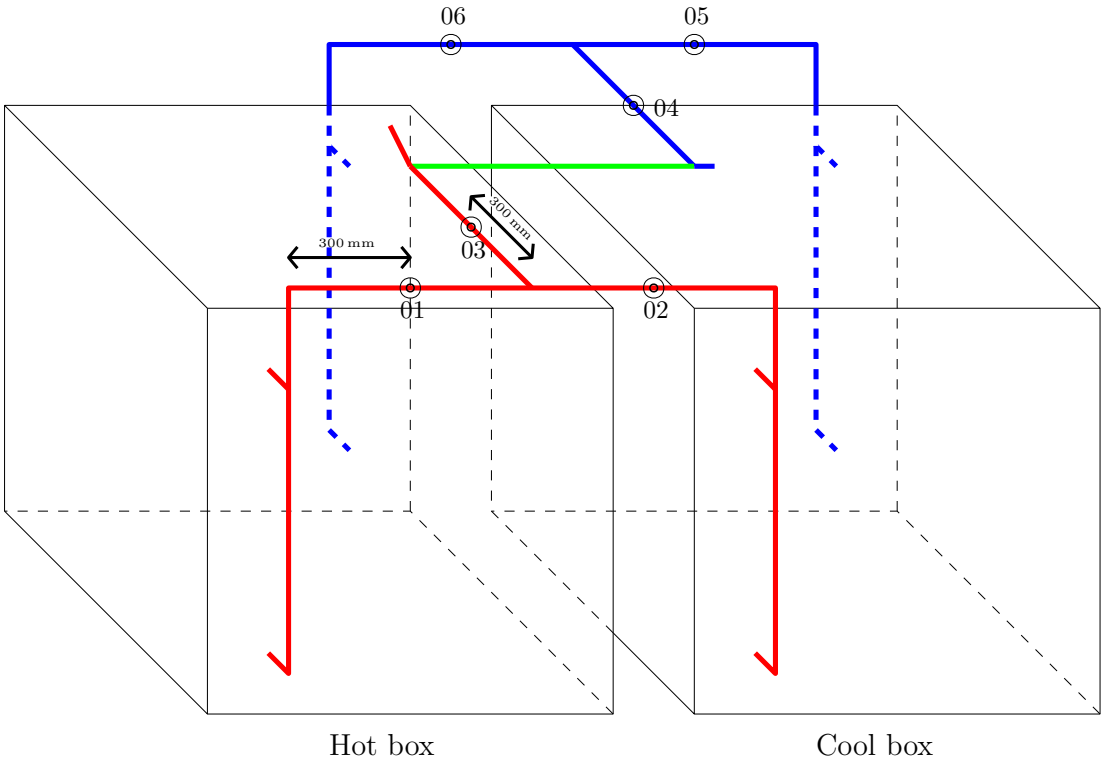

Figure 4.14: Location of in-duct velocity probes in the experimental apparatus. The exhaust, supply and return system are shown in red, blue and green respectively.

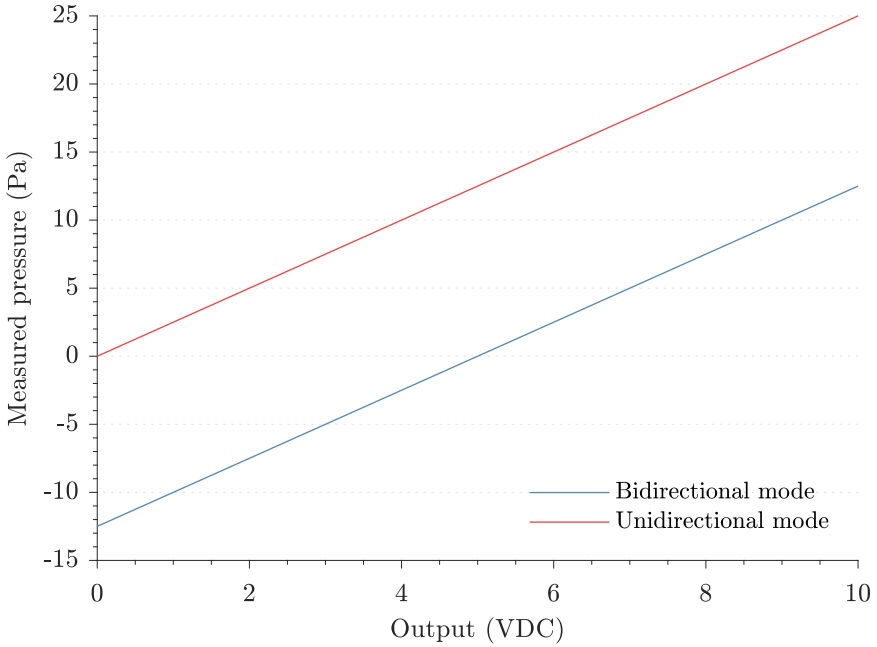

Figure 4.15: Omega PX277-0.1D5V differential pressure transducer calibration.

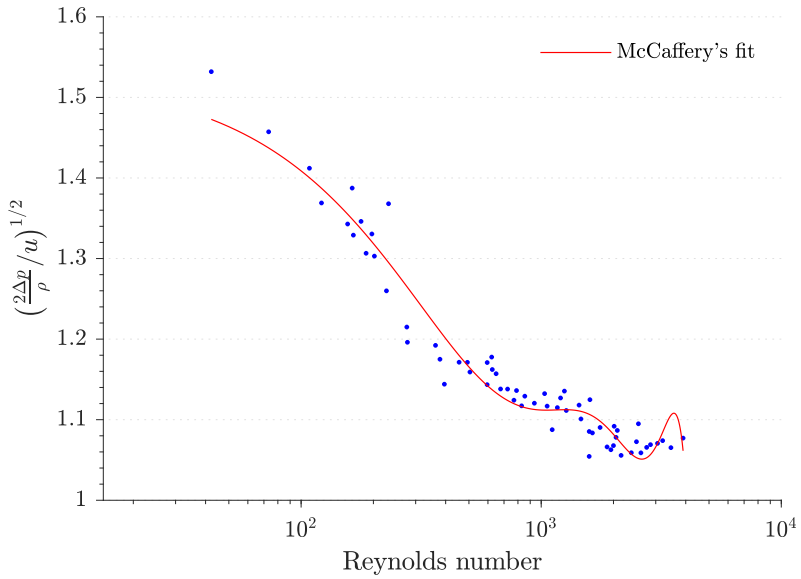

Figure 4.16: Relationship between ratio of pressure head and velocity head and Reynolds number. Data from McCaffrey and Heskestad (1976) [2]. Proposed fit was $f(x) = 1.533 - 1.366 \times 10^{-3}\ \mathrm{Re} + 1.688 \times 10^{-6}\ \mathrm{Re}^2 - 9.706 \times 10^{-10}\ \mathrm{Re}^3 + 2.555 \times 10^{-13}\ \mathrm{Re}^4 - 2.484 \times 10^{-17}\ \mathrm{Re}^5$.

$$u = \gamma_{\text{probe}} \sqrt{\frac{2\Delta p}{\rho(T)}} \tag{4.7}$$

where u is the estimate of velocity, γ_{probe} is the probe calibration factor, Δp is the measured differential pressure and $\rho(T)$ is the temperature-dependent gas density. Density is shown as a function of temperature to reinforce the fact that this pressure is the pressure at the probe, not ambient. In McCaffrey's work the probe-specific (and pressure transducer-specific) calibration factor was found to be non-linear with respect to velocity, refer to Figure 4.16.

Typically however, a constant calibration factor is used across all velocities. The historic value of 0.94 is often used for the probes manufactured at the University of Edinburgh. However, for the experiments carried out in the experimental apparatus, a velocity (in fact VDC was used as a primary)-dependent calibration factor $\gamma(V)$ was used. The VDC-dependent calibration factor was developed based upon wind tunnel experiments carried out at the University of Queensland. These experiments included two Omega PX277-0.1D5V pressure transducers and probes manufactured at the University of Edinburgh across three tests. The voltage above mid-point (i.e. above 5 V) is plotted against the computed calibration factor in Figure 4.17. A logarithmic fit is used for the data to output a voltage-dependent calibration factor. The estimated velocity becomes Equation 4.8.

$$u = \gamma_{\text{probe}}(V) \sqrt{\frac{2\Delta p}{\rho(T)}} \tag{4.8}$$

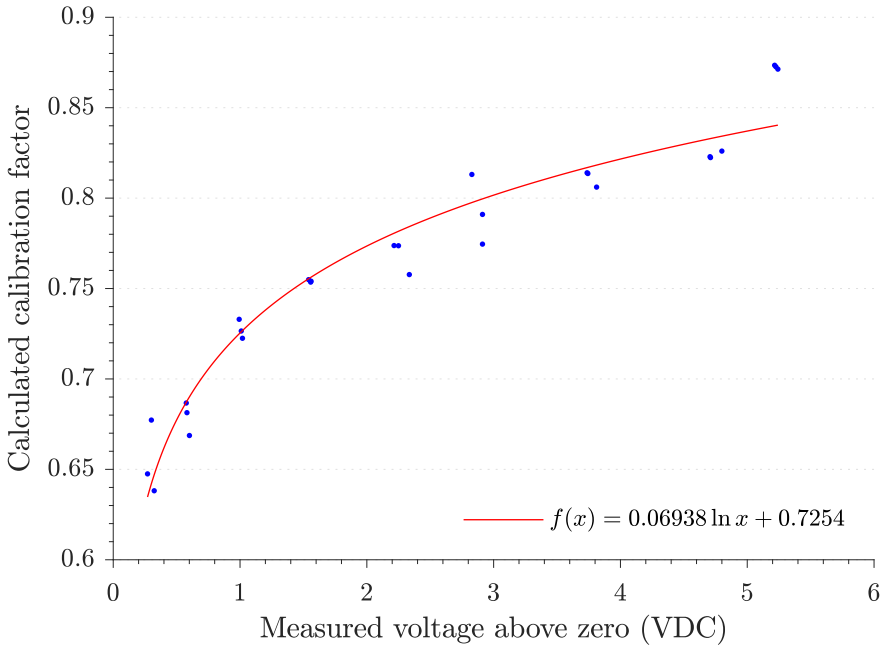

Figure 4.17: Calibration data for Omega PX277-0.1D5V pressure transducers and probes. Equation of regression: $\gamma_{\text{probe}} = f(x) = 0.0694 \ln x + 0.725$. Goodness of fit: R-square of 0.938.

4.8.2 Data acquisition

A Keysight Technologies 34980A Multifunction Measure Mainframe was used for data acquisition. The two primary choices of multiplexer and terminal block pairings for this mainframe are the 34925A/T and the 34921A/T. The 34921A multiplexer and 34921T terminal block pairing has the advantage that the terminal block is fitted with an on card reference temperature. The reference temperature is provided by an isothermal resistance thermometer (RTD). However, the recording of data from an RTD within the mainframe requires switching a slow armature relay. This massively reduces sample rate. During testing of data acquisition using the 34921A/T pairing, sample frequency was inconsistent and low. Therefore, the 34925A/T multiplexer and terminal block pairing was adopted. The disadvantage of this pairing is that a reference temperature has to be recorded at a known temperature. For example, 0 °C in an ice bath. The advantage is that sample frequency can be greatly increased and remains reliable. Sample frequency for the experimental apparatus experiments was a respectable 40 Hz. High frequency temperature readings were desirable, especially within the ducts, to be able to capture the very transient behaviour of flow within the ducts.

4.8.3 Uncertainty of measurements

Uncertainty within the measurements comes from two primary sources. The first is from the measurement device itself. The second source is propagation of uncertainty in input parameters. These uncertainties can be combined via quadrature (i.e. their integrals) into a single uncertainty for the measurement quantity of interest [184].

Temperature measurements

The uncertainty in thermocouple readings has been measured for a variety of arrangements to be between 2.5 % to 7 % [185]. For this work, a mid-value of 5 % is adopted. This is in line with best practice documented in the FDS Validation Guide [131]. The measurement of temperature also encompasses a propagated uncertainty from the experiment input parameters. Most critical to temperature is the heat release rate. An uncertainty in the experimental heat release rate propagates as an uncertainty in the thermocouple measurement. Here a simple empirical relationship can be used to relate a difference in heat release rate to a difference in temperature. The McCaffrey, Quintiere and Harkleroad correlation [186], presented in Equation 4.9, can be used to express a change in temperature (measurement uncertainty) with respect to a change in heat release rate (a propagated uncertainty).

$$T - T_0 = C\dot{Q}^{2/3} \tag{4.9}$$

where T is the gas layer temperature, T_0 is the ambient temperature, C is a constant which incorporates geometric and thermophysical parameters of the subject case, and $\dot{Q}$ is the heat release rate. If Equation 4.9 is differentiated a relationship between uncertainty in heat release rate and uncertainty in temperature can be derived:

$$\frac{\Delta T}{T - T_0} \approx \frac{2}{3}\frac{\Delta \dot{Q}}{\dot{Q}} \tag{4.10}$$

Based upon the flow switch controller, the uncertainty in the propane flow used for the experimental apparatus experiments is estimated to be 3 % [187]. Therefore, the propagated uncertainty to temperature is 6 %. In lay terms, there is an uncertainty in the real temperatures in the experimental apparatus because there is an uncertainty in the propane flow and hence the heat release rate.

Velocity measurements

The uncertainty of velocity measurements made using McCaffrey bidirectional probes has been estimated in the literature to be 7 % [188]. There is also a propagated uncertainty from the measurement of heat release rate (propane flow). Alpert provides empirical relationships between fire-induced velocities and heat release rate [189]:

$$u = 0.947\left(\frac{\dot{Q}}{H}\right)^{1/3} \text{ for } r/H \leqslant 0.18 \tag{4.11}$$

$$u = 0.197\frac{\left(\dot{Q}/H\right)^{1/3}}{\left(r/H\right)^{5/6}} \text{ for } r/H > 0.18 \tag{4.12}$$

where u is horizontal ceiling jet velocity, $\dot{Q}$ is heat release rate, H is enclosure height, and r is radial distance away from the fire plume. Both equations give velocity as being proportional to heat release rate to the power 1/3. If the differential is taken, Equation 4.13 informs that a difference (i.e. uncertainty) in velocity is proportional to one third of a difference (i.e. uncertainty) in heat release rate.

Table 4.5: Experimental uncertainties.

Quantity	Measurement uncertainty	Measurement uncertainty	Combined uncertainty
Temperature	0.05	0.02	0.05
Velocity	0.07	0.02	0.07

$$\frac{\Delta u}{u} \propto \frac{1}{3}\frac{\Delta \dot{Q}}{\dot{Q}} \tag{4.13}$$

Based upon an uncertainty in propane flow of 5 %, a propagated uncertainty in velocity due to heat release rate of 1.7 % is output (2 % is adopted).

Combined experimental uncertainty

The overall experimental uncertainty $\tilde{\sigma}_E$ is the integration of the measurement uncertainty $\tilde{\sigma}_M$ and propagated uncertainty $\tilde{\sigma}_P$. This is output using Equation 4.14. Final experimental uncertainties are presented in Table 4.5.

$$\tilde{\sigma}_E = \sqrt{\tilde{\sigma}_M^2 + \tilde{\sigma}_P^2} \tag{4.14}$$

4.9 Filtering of experimental data

4.9.1 Sources of noise

Before an examination of the experimental data, the signal itself must be considered. All data is made up of true signal and noise. This noise can come from many different places. The noise does not reflect the real quantity that is desired to be measured. It is of paramount importance to keep sources of electromagnetic interference away from low voltage input/output cabling and signal wiring. Some noise is unavoidable. This noise should, as far as is possible, be removed.

The sources of noise that could affect the data collected from the experimental apparatus are electromagnetic interference and induction, background signal noise, and miscellaneous noise sources. Signal interference can be especially dominant when the true signal is very low voltage. For example, the output of Type K thermocouples (with an unamplified output signal of 10 mV).

The main sources of electromagnetic interference within the experimental apparatus are the laboratory grounding, the adjustable fan speed drives, the AC power cables, and the high tension ignitor cable. The ground loops, which the instrumentation and apparatus were connected to, may introduce noise into the captured low voltage data signal [190]. Adjustable speed drives cause rapid voltage swings, which generate electromagnetic interference [191]. The AC power cables providing power to the fans and the ignition control box, where they pass near data acquisition cables, will lead to capacitive coupling between the low voltage data signal and the relatively high voltage, high frequency, power signal. This noise will be at a frequency of the power signal, i.e. 50 Hz. The intensity of the signal-to-noise ratio can be estimated using a modified

Table 4.6: Estimate of signal-to-noise ratio for raw VDC output for P20 propane flow cases. The signal-to-noise ratio increases with increase potential different across the fans.

Case	Signal-to-noise ratio
P20_F1_1	−13.9
P20_F2_1	−16.8
P20_F3_1	−20.8

periodogram of the same length as the signal [192]. For this application, the modified periodogram is produced using a Kaiser window with $\beta = 38$. This size of Kaiser window is deemed suitable to maximise the energy within the main signal lobe. The signal-to-noise ratio is output for cases P20_F1_1, P20_F2_1 and P20_F3_1 in Table 4.6. Where data acquisition cables run close to the high tension ignitor cable, capacative coupling will also occur. Noise is proportional to the current. This means that the high voltage, high current power signal within the high tension ignitor cable running from the control box will induce higher noise when compared to a normal power line.

The mechanical operation of the fans may also have caused noise to be added to the true signal. Fan blade rotation causes vibration of the fan unit, which is transferred to the surrounding environment, including thermocouple wires and signal cabling. This vibration motion, when occurring within an electromagnetic field, will cause an induced current in the signal wire. This will add noise to the true signal. The vibration of the fans may also cause thermocouple connections to be rapidly disconnected and reconnected at wiring junctions. These wiring junctions invariably occur outside of the enclosures of the experimental apparatus. If the thermocouple wires join outside of the experimental apparatus enclosures, the temperature at this location will, by virtue of the Seebeck effect, induce a voltage gradient proportional to the temperature at this location. In other words, the data acquisition system will record a near ambient temperature. This phenomenon can be witnessed in the unpost-processed in-duct temperatures for case P20_F1_3 presented in Figure 4.18.

4.9.2 Managing noise generation

All AC power cables and the high tension ignitor cable were kept as physically far as possible from the signal cables and thermocouple cables. As far as is practicable, amplification of thermocouple signal should be done as near to the thermocouple reading location as possible. An amplified thermocouple signal changes the effective response from 50 µV to 25 mV. Based upon a constant electromagnetic interference this increase in signal within the thermocouple cabling can reduce the noise error from 5 °C to 10 °C down to less than 0.1 °C. For this reason, thermocouple lengths were kept to a practicable minimum and the data acquisition mainframe was located as close to the experimental apparatus as safely as possible. The fans were mounted on retort stands to minimise the vibration transferred from the spinning blades to the rest of the experimental apparatus.

4.9.3 Noise removal

Noise can, to some degree, be removed from the data. The type of noise removal method or signal processing method used, depends on the nature of the noise signal. A first step to investigating the nature of any noise signal is to examine the data in time-frequency space. When viewed in time-frequency the presence of certain frequencies

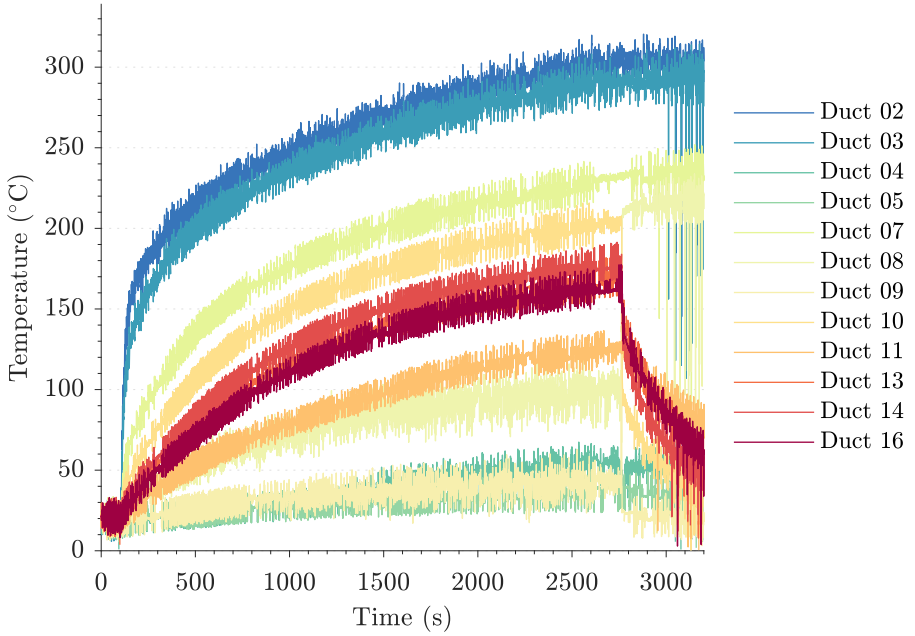

Figure 4.18: Unprocessed in-duct temperature measurements for case `P20_F1_3`. Note the temporary sharp decreases in measured temperature beyond 3000 s. This noise may be caused by the vibration of fan motors leading to undesired joining of bimetallic thermocouple wires. For the purpose of this figure, legibility of the actual temperatures of each thermocouple is not required.

that may be noise can be found in the data. One method of examining a signal in time-frequency space is the use of persistence spectrum analysis. This method is based upon a typical Fast Fourier transform but also encapsulates heat mapping. The heat mapping describes the percentage of time that the signal is at that frequency. This adds another level of information to enable the analysis of the signal and to identify noise signals. An example of a persistence spectrum analysis is presented in Figures 4.19 and 4.20. The two experiments are repeats of the same case (`P20_F1`).

Experiments `P20_F1_1` and `P20_F1_4` were carried out at different times. In the period between the carrying out of the two experiments, the experimental apparatus was moved out of the active fire laboratory and all instrumentation was disconnected. At a later date, the experimental apparatus and all instrumentation was then re-established. Evidently, something, with respect to electromagnetic interference, has changed between the two experiments. Most likely a change in cabling arrangement or apparatus.

Noise can be removed from a signal to leave behind the true signal. This involves the careful selection of various types of filter that target the noise. Based upon the spectral analysis in time-frequency space, a gamut of filters was selected and implemented for the temperature and pressure probe data signal.

An algorithm was developed to address the functioning problem encountered in thermocouple data due to fan vibration. A low pass filter was used to clean the very high frequency signal that was assumed to be noise. The parameters of the low pass filter (i.e. steepness and stop band attenuation) were based upon spectral analysis of the data signal. A multi-pass moving mean filter was used on the data signal. A moving mean filter is appropriate for reducing periodic noise in data. The filter width was based upon time-frequency signal analysis. The filter width varied between 5 to 30

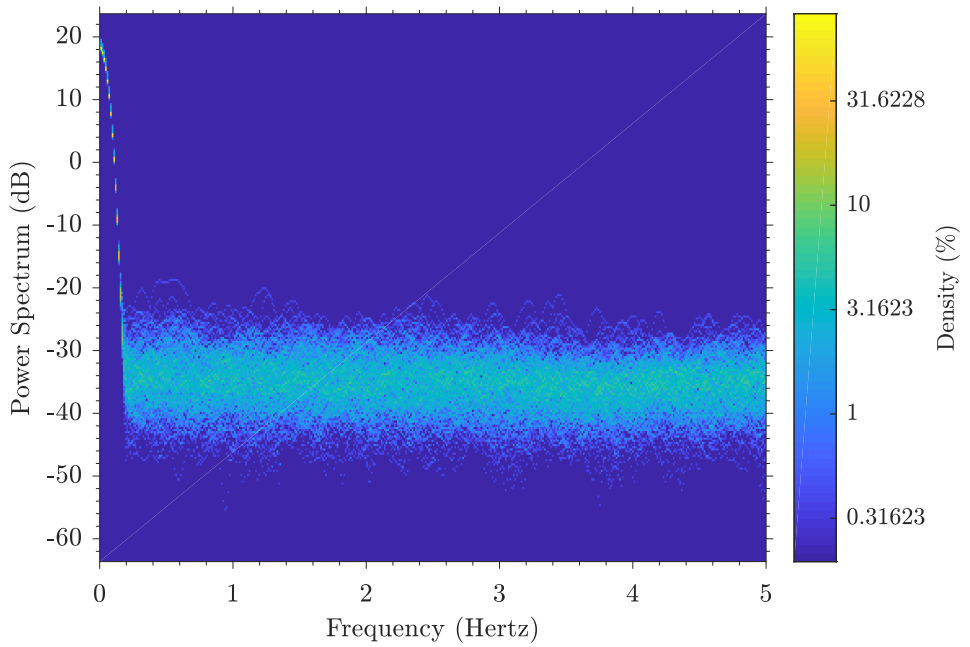

Figure 4.19: Persistence spectrum analysis of channel 1 pressure transducer data for case `P20_F1_1`. The analysis shows a high and frequent power spectrum at low frequencies. This is expected to be, at least in the majority, the true signal. There is a spread of other, high frequencies for which the power spectrum is relatively constant.

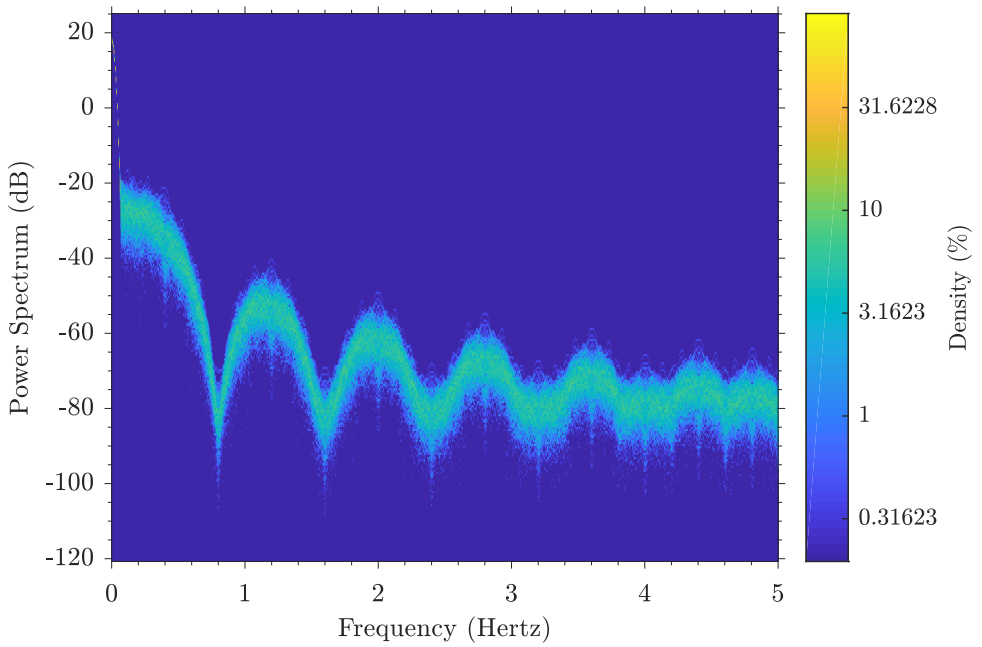

Figure 4.20: Persistence spectrum analysis of channel 1 pressure transducer data for case `P20_F1_4`. Note the marked difference in shape of the spectrum when compared to that of `P20_F1_1`. The same high power spectrum is seen in the lowest frequencies. This is the true signal. There are also periodic increases and decreases in signal at a frequency gap of about 0.5 Hz. This is considered noise and should be eliminated.

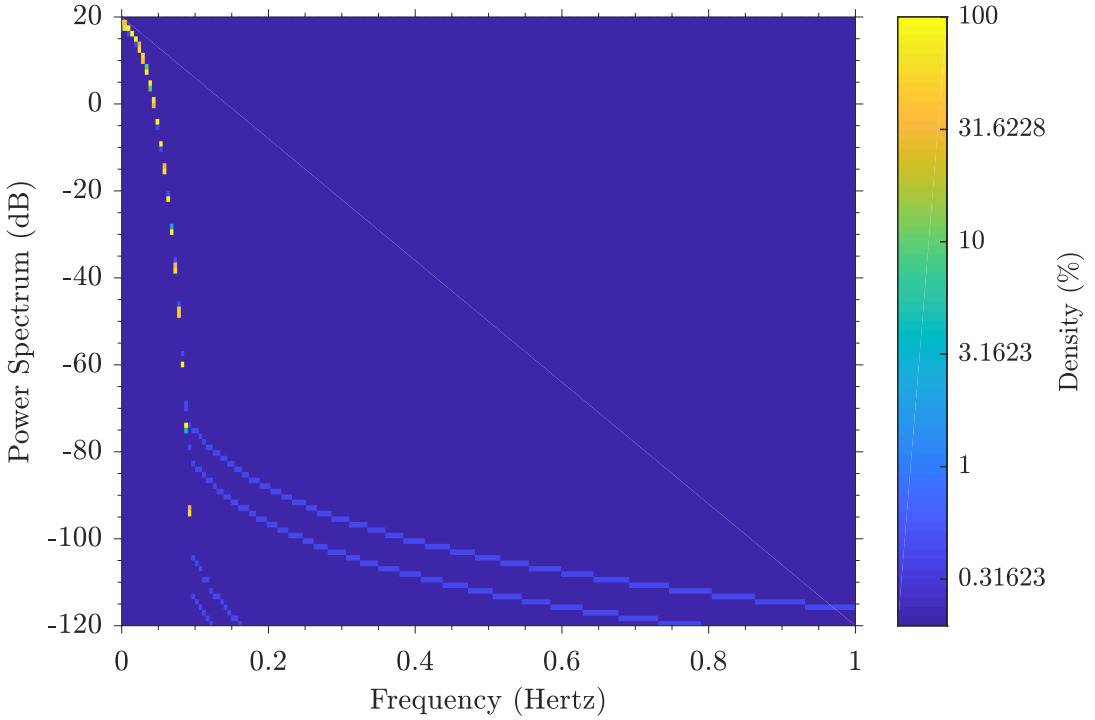

Figure 4.21: Persistence spectrum analysis of channel 1 pressure transducer data for case P20_F1_4 following signal processing to remove noise. The frequency-oscillating noise has been removed. The frequency axis has been re-scaled for clarity.

sample periods. To verify that the noise removal is successful and that the true data is retained within the signal, the persistent spectrum analysis is carried out again on the new signal. This analysis is presented in Figure 4.21.

4.10 Closing remarks

One may ask: why create *another* experimental rig? Cannot existing data be used? The answer is: not really. Objectives one and three of this thesis are to create a novel verified and benchmarked method to enable fire engineers and designers to expand the domain of their calculation. This expanded domain will enable the quantification of risk-impact of the two-way coupling between a total system and a fire. Within this new space, there is very limited (or no) experimental data available. Therefore, a new experimental rig must be specifically designed to provide the benchmarking data required to deliver a model that can be validated for a specific use.

Secondarily the creation of a new experimental rig enables the critical review of the current guidance framework and model solutions regarding the design of buildings, specifically with shared air handling plant. The data from the new rig can be used to examine potential limitations or omissions within the current design methodology.

This chapter has described the overall form and function of the experimental apparatus. This includes its construction, independent and dependent variables, instrumentation, and experimental matrix. The measurement uncertainty has been quantified. This is part of the information that enables model users to carry out validation exercises of the novel implementation for their specific purpose. Obviously a model designer cannot be oblivious to the probable uses of a model. Therefore, benchmarking experiments

should fall within the predicted usage parameter space - this has been examined and the experimental apparatus designed accordingly.

It is recognised that the new experimental rig aims to provide benchmarking data for a general coupled hybrid model. The experiments do not exhaustively address time-dependent network submodel-enabled coupled hybrid models. The rational for this is (in line with the Measurement and Computation of Fire Phenomena (MaCFP) working group methodology) the adoption of a 'building block' approach to benchmarking and validation. This building block approach demands that models must be validated 'from the ground up' - using a methodical culmination of physics and mechanisms. That is, in the absence of *any* suitable benchmarking experimental data for coupled hybrid models, a foundational benchmarking process must be developed (i.e. compartments to be modelled in the field model connected by conduits to be modelled in the network submodel) - prior to the specific and more widened benchmarking of strongly time-dependent phenomena.

Chapter 5

Numerical design and methodology

5.1 Numerical apparatus

A numerical case has been created of the experimental apparatus and is described in this chapter. The numerical case set up was set up to reflect the experimental apparatus as closely as possible. The plan and elevation of the numerical set up is given in Figures 5.1 and 5.2. Appendix C contains the .fds input file.

5.1.1 Primary geometric assumptions

Some simplifications and assumptions are unavoidable. The co-flow inflows of the numerical set up are rectangular obstructions with one surface being a Neumann volume flow rate boundary condition. See Figures 5.3 and 5.4. The vents within the field domain that represent the inlets to the ventilation system are modelled as square boundary conditions with a dimension of 100 mm.

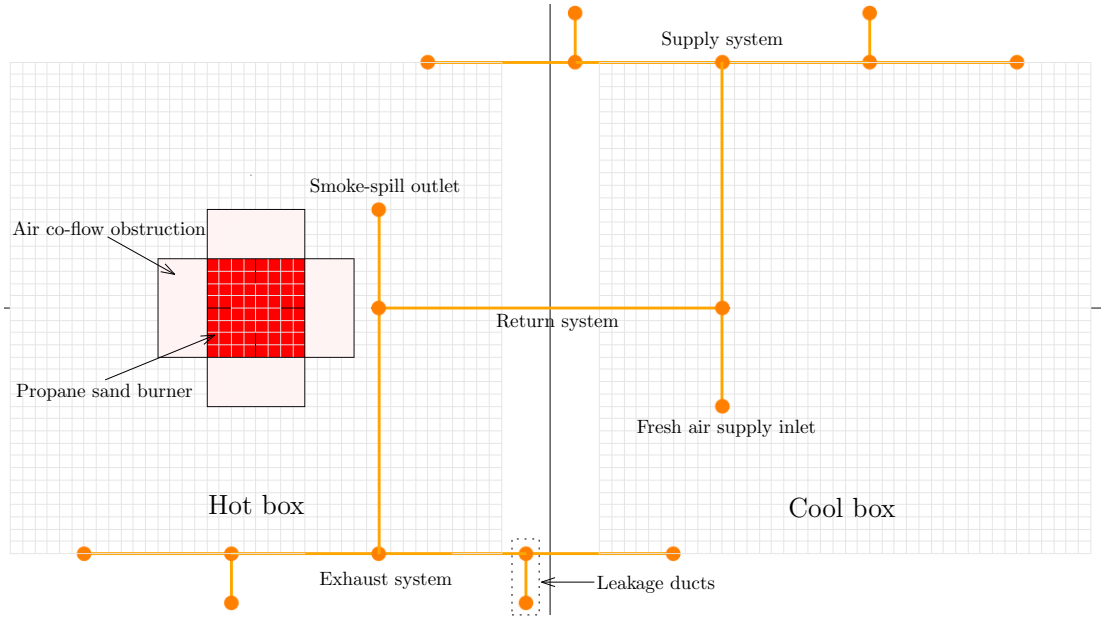

Figure 5.1: Plan of the numerical set up. Field domain is shown by the visible meshing. Network subdomain is coloured orange.

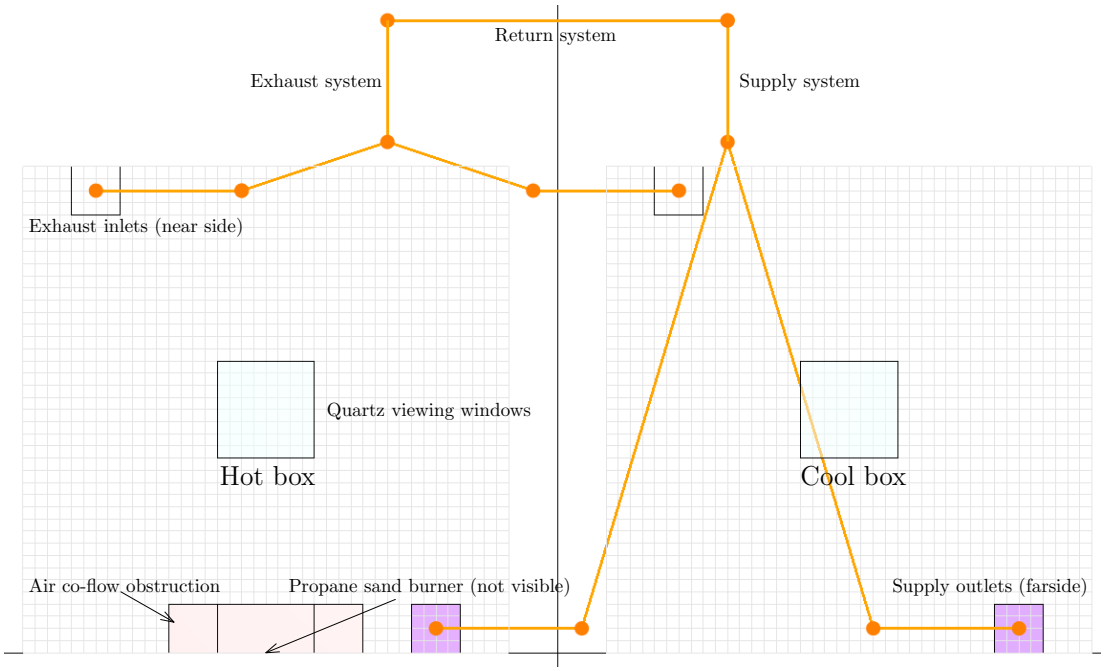

Figure 5.2: Elevation of the numerical set up (front). Field domain is shown by the visible meshing. Network subdomain is coloured orange.

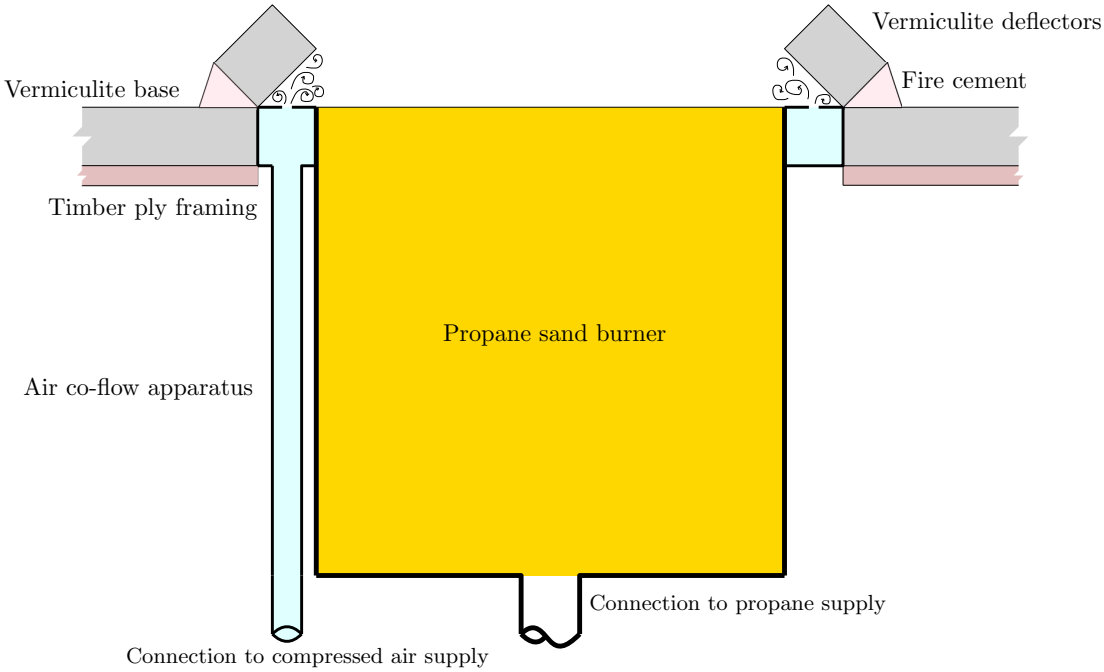

Figure 5.3: Section through the sand burner and co-flow of the experiment.

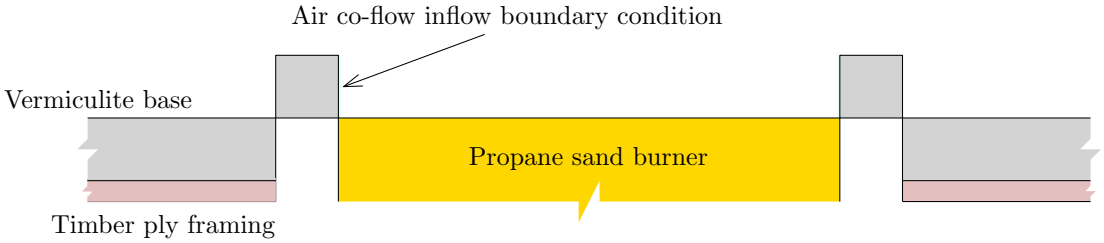

Figure 5.4: Section through the sand burner and co-flow of the numerical set up.

5.2 Sub-models and parameters

5.2.1 Solution of flow and pressure

Where possible, to ensure that the benchmarking exercise is zeroing in on the performance of the coupled hybrid implementation, the default sub-models and affiliated parameters of FDS were used. The `SIMULATION_MODE` adopted was very large eddy simulation (VLES) [193]. The flux limiter used was Superbee [194]. Default numerical stability parameters were used (minimum and maximum CFL of 0.8 and 1.0 and minimum and maximum Von Neumann Constraint of 0.8 and 1.0). The default pressure solver (CrayFishpak FFT) [195] was used with a maximum number of iterations of 10. A new quadratic fan model, discussed in Section 3.6, was used for the AC fans in the HVAC subdomain.

5.2.2 Simulation of fire phenomena

One dimensional condensed phase heat conduction was used. The simple pyrolysis sub-model was used for the specified propane mass flow rate. The single-step, mixing-controlled combustion sub-model was used for the combustion of propane. A soot yield of 0.01 and a CO yield of 0.012 were adopted; based upon available experimental data for propane from the literature [131, 196, 197, 198]. The radiative fraction radiation transport equation model was used with a radiative fraction of 0.3 [199] and a number of angles of 100. The default value of radiation angles was adopted based upon the case not being considered as radiation-dominated. This assertion is based upon the case incorporating a well-ventilated efficiently burning fire (due to the air co-flow), a relatively small flame height, and the lack of a dense sooty hot layer [200].

5.3 Material properties

Material properties used for the numerical set up are presented in Table 5.1 [201].

Table 5.1: Material properties used for numerical case.

Material	Density (kg/m^3)	Specific heat ($kJ/(kg\,K)$)	Conductivity ($W/(m\,K)$)
Quartz	2200	0.70	1.25
Timber ply	650	1.22	0.12
Vermiculite	700	1.15	0.20

5.4 Boundary conditions

Boundary conditions related to the coupling of the field model and the network sub-model are as described in Section 3.1.2.

Boundary conditions for the (assumed chemically inert) enclosure of the numerical set up (i.e. walls, floor and ceiling) are Neumann heat flux boundary conditions coupled to the one dimensional solid phase heat transfer model. A backing Dirichlet boundary condition of 20 °C is used for the one dimensional solid phase heat transfer model. The walls of the numerical set up are 25 mm thick vermiculite. The top and bottom of the

numerical set up are 25 mm thick vermiculite with a 10 mm thick timber ply backing. The numerical set up quartz viewing windows are 3 mm thick quartz.

Boundary conditions for the propane burner and the air co-flow are Neumann mass and volume flux boundary conditions respectively. The value of the boundary conditions for the propane burner and air co-flow are set based upon the case being simulated. Thermal boundary conditions for the propane burner and the air co-flow are Neumann heat flux boundary conditions with a value of $0\,\mathrm{W/m^2}$ (i.e. adiabatic).

Boundary conditions for the smoke-spill outlet and the fresh air inlet of the ventilation system, within the network sub-model, are Dirichlet boundary conditions of pressure, temperature, and density at ambient conditions.

5.5 Duct major and minor losses

Major losses occur in a duct experiencing fully developed flow, due to wall roughness. For fully developed turbulent flow in a duct there is a thin viscous sublayer at the interface between the fluid and the duct. If micro or macro elements of the duct wall protrude into or penetrate through this viscous sublayer, the layer's properties will be altered. This alteration of properties means that pressure drop in fully developed duct flow is affected by absolute wall roughness ε. The duct flow of the numerical set up is expected to be fully turbulent and major losses should be accounted for.

Major pressure losses ($p_{L,major}$) are proportional to the product of the velocity head and a dimensionless loss coefficient (K_{major}); as given in Equation 5.1. This is the Darcy-Weisbach equation [202]. K_{major} is a function of the duct length, diameter and the friction factor (f); as given in Equation 5.2.

$$p_{L,major} = K_{major}\frac{\rho u^2}{2} \tag{5.1}$$

$$K_{major} = \frac{fL}{D} \tag{5.2}$$

The friction factor is a function of the Reynolds number and the ratio of the absolute roughness (ε) to the diameter of the duct. The friction factor is determined using the Colebrook formula (Equation 5.3) or the Moody chart.

$$\frac{1}{\sqrt{f}} = -2\log_{10}\left(\frac{\varepsilon/D}{3.7} + \frac{2.51}{\mathrm{Re}_D\sqrt{f}}\right) \tag{5.3}$$

There is no analytical solution for the Colebrook formula. Within the subject coupled hybrid model implementation the Colebrook formula is solved using an approximation given in Equation 5.4. This approximation was developed by Zigrang and Sylvester [203].

$$\frac{1}{\sqrt{f}} = -2\log_{10}\left(\frac{\varepsilon/D}{3.7} - \frac{4.518}{\mathrm{Re}_D}\log_{10}\left(\frac{6.9}{\mathrm{Re}_D} + \left(\frac{\varepsilon/D}{3.7}\right)^{1.11}\right)\right) \tag{5.4}$$

To output the friction factor, and hence the dimensionless major loss coefficient, the only additional input parameter is the absolute roughness of the duct. Based upon

welded and jointed steel duct construction, the value of absolute roughness adopted for the numerical set up is 1×10^{-4} mm [201].

Minor losses in ducts occur due to bends and fittings. Theoretical analysis of minor losses is not yet practicably feasible [161]. Minor losses for standard bends, fittings, components, tees, and the like are empirically determined using experimentation. These minor losses, given as dimensionless loss coefficients (K_{minor}) are then tabulated. It is recognised in the literature that tabulated loss coefficients have wide uncertainties [43]. The pressure drop due to minor losses ($p_{L,minor}$) is then calculated as the product of the velocity head and the loss coefficient; as given in Equation 5.5.

$$p_{L,minor} = K_{minor} \frac{\rho u^2}{2} \tag{5.5}$$

$$\tag{5.6}$$

The minor loss coefficients used for the numerical set up are presented in Table 5.2 [161].

Table 5.2: Minor loss coefficients used within the ventilation system of the numerical set up.

Component	K_{minor}
Entrance flow, sharp edged	0.5
Exit flow, sharp edged	1.0
90° flanged elbow	0.3
Flanged tee, line flow	0.2
Flanged tee, branch flow	1.0
Damper, fully opened	0.1
Centrifugal fan	15.0

5.6 Grid sensitivity study

5.6.1 Importance of grid sensitivity studies

A grid sensitivity study is a key stage in any numerical work based upon finite difference, finite element or finite volume solvers. FDS is a finite difference-based solver which is second-order accurate in time and space. FDS solves approximations to various partial differential equations. When making the approximation of a partial differential equation, terms of $\mathcal{O}(\delta x^2)$ and higher are dropped from the solution. The argument is that as the cell size δx approaches zero the terms dropped from the Taylor series expansion, collectively called the discretisation error, tend to zero. The truncating of the terms of $\mathcal{O}(\delta x^2)$ and greater is also addressed by the implementation of various sub-grid scale models. For example, the aim of turbulence models is to capture the physics related to turbulence that are not captured by the basic flow solver at grid resolution levels.

The aim of a grid sensitivity study is to ensure and demonstrate that the solution is not dependent upon the grid sizing (δx). If this occurs the solution is called 'grid independent'. There is an argument that there may be a 'sweet spot' where the balance of dynamics resolved on grid and the physics modelled using sub-grid scale models is

just right to find a local solution convergence point. If the grid size was reduced further the solution may diverge once again as physics are attempted to be solved on grid and not by various sub-grid scale models. Further discussion of the issue is beyond the scope of this work but the interested reader is referred to numerical method work within the literature [204, 205, 206].

5.6.2 Output quantities to consider

When carrying out a grid sensitivity analysis the application is of crucial importance. The study must examine the output quantities that are of interest to the user and the conclusions to be drawn using the model. An example is given (which has been deliberately contrived to differ to the subject application, in order to give the reader a broader appreciation of the issue).

FDS is to be used to carry out an analysis of the potential for ignition of a wall material due to radiation from a flame. The incoming radiant heat at the material is the most important output quantity based upon the conclusions that will be drawn from the analysis. This output quantity should be the considered quantity when carrying out the grid sensitivity study. It would not be sensical to consider other output quantities like heat release rate, visibility or plume temperature. Other parameters will affect the incoming radiant heat at the considered material; but their solution is not of *primary* importance to the example analysis case.

The experiments carried out in the numerical set up are broadly speaking within the sphere of built environment fire safety. Specifically how the two-way coupling between a fire and a total system may, inter alia, lead to increased hazard within the enclosure of fire and connected enclosures. Temperature is a key fire hazard and safety parameter. Therefore, the data from the centre thermocouple tree in the hot box and in the cool box are used for the grid sensitivity study.

5.6.3 Relative errors

Temperature data

The grid sizes used for the study are 0.1 m, 0.05 m, 0.03 m, 0.025 m, 0.02 m, 0.017 m, 0.014 m and 0.0125 m. The 'worst case' of `P20_F3` is chosen for the grid sensitivity analysis. This case is the most challenging for a finite difference code such as FDS. This case has the smallest propane release rate, and hence the smallest characteristic fire diameter, and it has the highest fan potentiometer setting, and hence the largest expected ventilation velocities.

The temperatures from the central thermocouple tree of each box were used for the study. In the hot box the highest predicted temperatures occurs at thermocouple B1_3_5 (the lowest). This thermocouple is within the flame. As thermocouple B1_3_5 is within the flame it is recognised that the flame sheet will be under-resolved [207]. An additional, more reliably predicted, thermocouple should be analysed also. The thermocouple at ceiling level directly above the sand burner, B1_3_1, was used. In the cool box the highest predicted temperature was at thermocouple B2_3_1 (the highest). This thermocouple is the most affected by the hot layer that forms at the ceiling of the cool box.

$\mathbf{L}^p$ space norm relative errors

To quantitatively measure the quality of the predictions relative errors are used. The analytical or 'true solution' of the set of equations is not known. Therefore, relative errors are taken with respect to the most resolved case. When comparing scalar values, absolute errors and relative errors are both useful. This is also the case for vectors. However, a norm must be taken of the absolute error or, for relative errors, both the numerator and the denominator to apply error theory to vectors. p-norms (or l_p-norms) are a type of norm within L^p space and are related to generalised means (e.g. minimum, geometric mean, arithmetic mean, quadratic mean, and maximum). The general form of an l_p-norm is given in Equation 5.7.

$$\|\boldsymbol{x}\|_p := \big(\sum_{i=1}^{n} |x_i|^p\big)^{1/p} \tag{5.7}$$

Where $\boldsymbol{x}$ is a vector and x_i its elements. For the purposes here, the l_1, l_2 and l_∞-norms are used to output relative errors. The l_1-norm, sometimes called the taxi-cab norm, is related to the arithmetic mean. The l_1-norm relative error therefore is a measure of the arithmetic average distance between the prediction vector and the 'solution' vector. The l_2-norm is related to the quadratic mean. The l_2-norm relative error is a measure of the quadratic average distance between the prediction vector and the 'solution' vector. The l_∞-norm is related to the maximum as p tends to infinity in Equation 5.7. The l_∞-norm relative error is a measure of the distance between the maximums of the prediction vector and the 'solution' vector. The use of multiple metrics can elucidate different conclusions when carrying out a grid sensitivity analysis.

The l_1, l_2 and l_∞-norm relative errors are given in Equations 5.8, 5.9 and 5.10 respectively.

$$\delta_{l_1} = \frac{\|\hat{\boldsymbol{x}} - \boldsymbol{x}\|_1}{\|\boldsymbol{x}\|_1} \tag{5.8}$$

$$\delta_{l_2} = \frac{\|\hat{\boldsymbol{x}} - \boldsymbol{x}\|_2}{\|\boldsymbol{x}\|_2} \tag{5.9}$$

$$\delta_{l_\infty} = \frac{\|\hat{\boldsymbol{x}} - \boldsymbol{x}\|_\infty}{\|\boldsymbol{x}\|_\infty} \tag{5.10}$$

Where $\boldsymbol{x}$ is the real solution vector and $\hat{\boldsymbol{x}}$ is the prediction vector. The norm relative errors are output for each one of the examined data for each grid size. A plot of norm relative errors and grid sizes is generated for each thermocouple prediction. These data are given in Figures 5.5 through 5.7.

Errors outside of the flame region

The l_1, l_2 and l_∞-norm relative errors in Figures 5.5a, 5.5c, 5.6a, 5.6c, 5.7a and 5.7c illustrate similar behaviour for both the hot box and the cool box outside of the flame. Interesting and initially unexpected behaviour is presented. The naïve expectation is that errors monotonically decrease with decreasing cell size. This reduction is, broadly speaking, expected to reduce like the order of the solution scheme. Things become less straightforward within fire modelling. There are multiple coupled solvers, sub-models,

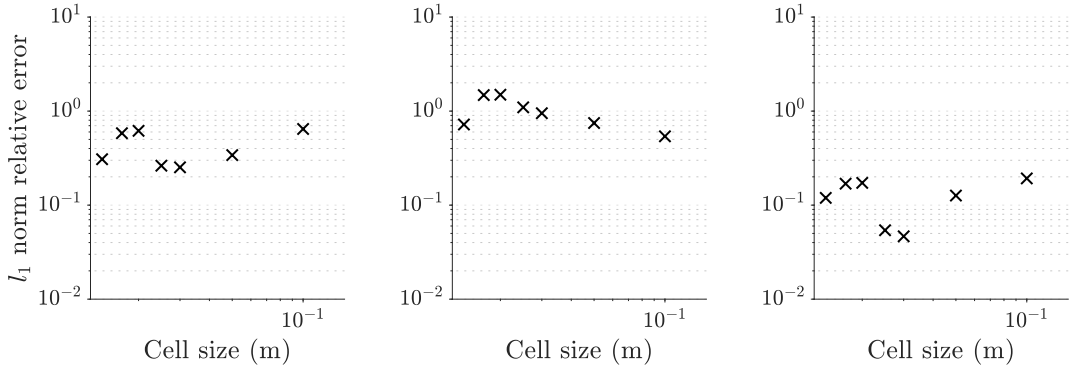

(a) B1_3_1. (b) B1_3_5. (c) B2_3_1.

Figure 5.5: l_1-norm relative errors.

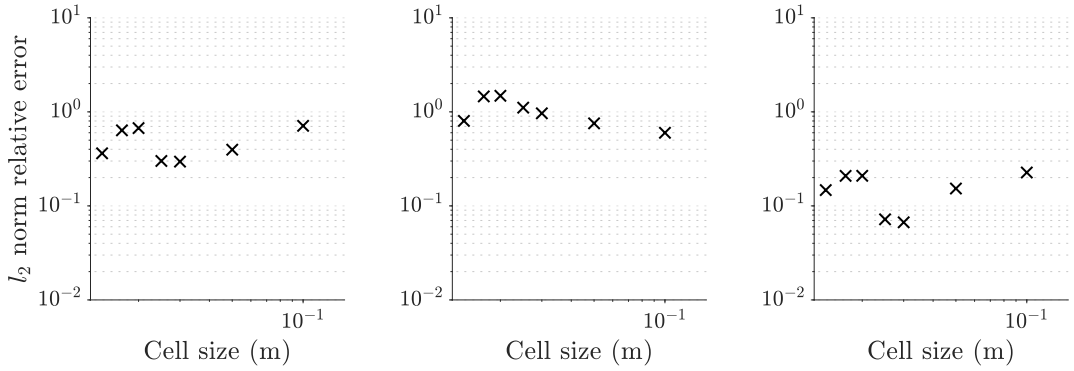

(a) B1_3_1. (b) B1_3_5. (c) B2_3_1.

Figure 5.6: l_2-norm relative errors.

and subgrid scale models all feeding into the solution. Furthermore, FDS automatically updates the time step based upon the CFL and therefore $\frac{\Delta x}{\Delta t}$ has two degrees of freedom. Even if the central hydrodynamic solver is formally second-order accurate in space and time, as is FDS's, the solution may not converge at this rate. This is in fact why grid convergence metrics, such as the Grid Convergence Index (GCI) [208], may not be suitable for fire modelling.

The monotonic decrease in errors is not presented in Figures 5.5a, 5.5c, 5.6a, 5.6c, 5.7a and 5.7c. The errors decrease through the first three decreasing cell sizes (four cell sizes for maximum flame temperatures), and then increase once again. The highest error of this second peak in the errors is almost as high as the coarsest cell size. These phenomena may have more than one explanation. One explanation is related to the modelling of turbulence, one is related to the modelling of combustion, and one is related to the modelling of radiative heat transfer. The modelling of turbulence is most likely responsible for the behaviour witnessed outside of the flame region and the modelling of the latter two is most likely responsible for the behaviour witnessed within the flame region (this is discussed later).

LES-based solvers aim to spatially resolve the large eddies on the grid. Eddies smaller than the characteristic length of the mesh are modelled using a subgrid scale turbulence model. The theory is that as the grid size tends to infinity, the solution tends towards a direct numerical resolution (DNS) where all eddies are resolved on the mesh [209]. The issue is that the path to convergence to a DNS solution might have some bumps in it. At certain lower resolutions the modelling of eddies of a certain, and important to the solution, characteristic length may be carried out by the subgrid scale model. The subgrid scale model may be simulating the effect of the eddies in a suitable way for the overall solution. If the resolution is increased these eddies may fall outside of the filter length of the subgrid scale model. The eddies may now be modelled on the mesh. This 'unrefined refined' grid size may have poorer capabilities of modelling these eddies which are on the cusp of the filter length. In this way, a large cell size can deliver a solution with lower errors than a smaller cell size. A local mesh convergence point has been found. In other words, the subgrid scale model of turbulence is performing well at this resolution.

Inside the flame region

Figures 5.5b, 5.6b and 5.7b present error data for thermocouples within the flame region. Different error behaviour is witnessed when compared to that of thermocouples outside of the flame region. The relative errors increase through the first four or five cell sizes for the l_1/l_2-norms and l_∞-norm respectively.

The simple 'mixed is burnt' combustion model was utilised for the numerical set up. If the conditions within a grid cell are suitable for combustion (based upon oxygen content and a critical flame temperature), combustion occurs within that cell. Evidently these criteria, and the heat output by the meeting of these criteria, will be different for differently sized grid cells. It may be that the 'bulk modelling' of the flame region, as carried out at coarser meshes, better predicts the propensity of oxygen to be available to the combustion zone and hence the propane to combust. A slightly more well-resolved case may lead to oxygen not being able to reach the inner combustion zone (i.e. a poorer result), but at a further resolved case oxygen could find a route into the inner combustion zone (i.e. a better result).

Flames are under-resolved in most typical LES calculations, therefore special treatment of the radiative source term within cells in which combustion is occurring is re-

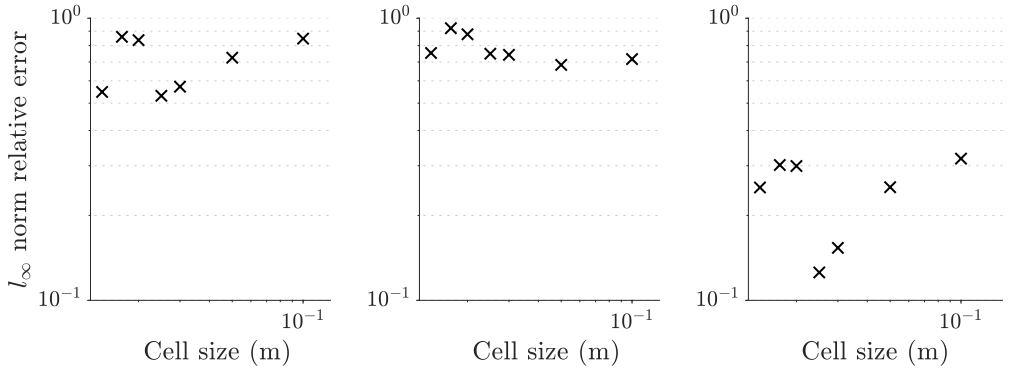

(a) B1_3_1. (b) B1_3_5. (c) B2_3_1.

Figure 5.7: l_∞-norm relative errors.

quired in FDS. The source term is set as a function of the global radiative fraction, which is a user input. Outside of the flame region the homogeneous cell temperature assumption holds better and the radiative source term can be computed directly. A radiative fraction for propane of 0.3 was adopted for the numerical set up. At larger grid sizes the three dimensional volume within which combustion is occurring is larger. Therefore, the application of the simplified radiation fraction model is over a large volume. It may be that this simple empirical relationship better predicts the overall solution when compared to a more spatially resolved solution (for this specific case).

5.6.4 Conclusion of grid sensitivity study

The question remains: which cell size to use? It is impractical to expect to have a solution that has fully converged to the DNS solution. Least of all this will not provide useful benchmarking data for end users. FDS is specifically designed to carryout typical fire safety calculations at reasonable mesh sizes with reasonable wall times [49]. Therefore, reliance is placed upon the balance of on-mesh solvers and subgrid scale models.

The error response for maximum temperatures within the flame region are relatively flat for each cell size. Within close proximity to the flame a cell size of 0.014 m is adopted; the l_∞-norm relative errors are amongst the lowest. Outside of the flame region a cell size of 0.025 m is adopted; the l_1 and l_2-norm relative errors are amongst the lowest and the l_∞-norm relative errors are the lowest.

5.7 Numerical parameter space

In addition to the physical parameter space of the experiment, discussed in Section 4.7, the numerical parameter space of the numerical set up needs to be defined. Definition of the numerical parameter space is a crucial part of model validation. Stating of key numerical parameters gives future model users the tools they need to confidently validate a model for their specific use.

The presented numerical parameters are based upon guidance in the FDS Validation Guide [131]. These are: the characteristic fire diameter D^*, the plume resolution index $D^*/\delta x$, and the ceiling height to fire diameter ratio H/D^*. Table 5.3 presents the values of the parameters for the numerical set up.

Table 5.3: Numerical parameter space of the numerical set up. Note that values are chosen to

Parameter	Value
D^*	0.14 to 0.20
$D^*/\delta x$	5.7 to 7.9
H/D^*	5.1 to 7.1

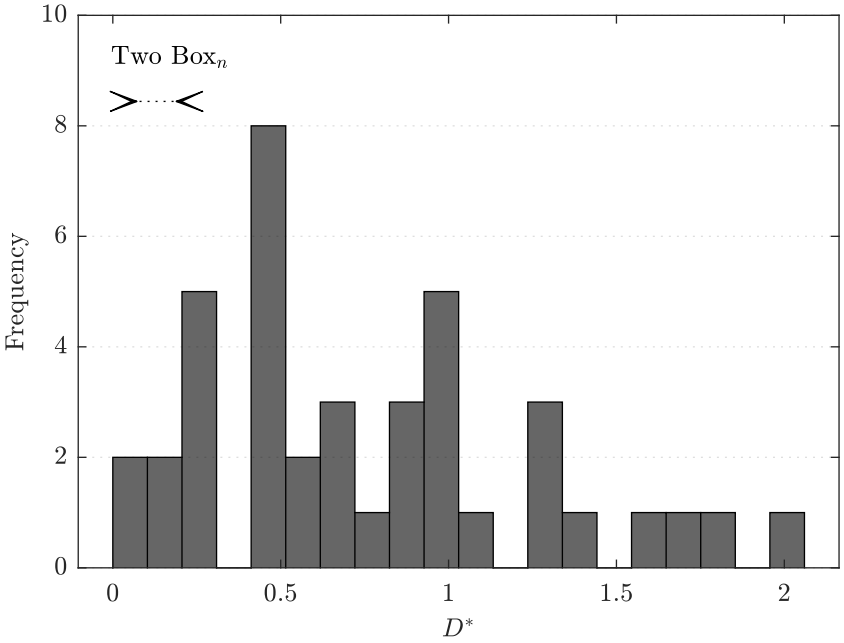

Figure 5.8: Distribution of the characteristic fire diameter for numerical cases documented in the FDS Validation Guide. The numerical set up occupies the lower end of the distribution. For clarity an outlier of $D^* = 22$ has been omitted (Heskestad experiments).

The characteristic fire diameter, measured in metres, is a length scale that encapsulates the heat release rate of the fire. The length scale is a measure of the relative importance of momentum and buoyancy forces. Referred to by some as the 'effective fire diameter'. The characteristic fire diameter is output as given in Equation 5.11.

$$D^* = \left(\frac{\dot{Q}}{\rho_\infty c_p T_\infty \sqrt{g}} \right)^{2/5} \tag{5.11}$$

The plume resolution index is a non-dimensional parameter that quantifies how well resolved the fire dynamics are. It is a measure of the number of grid cells that span the characteristic fire diameter and is output as $D^*/\delta x$.

The ceiling height to characteristic fire diameter is a non-dimensional parameter which quantifies the effect of the fire plume with respect to the enclosure height. This numerical parameter is output as H/D^*.

For information and comparison, data of numerical parameters for the experiments in the FDS Validation Guide is provided in Figures 5.8 through 5.10. Where experiments have a range of values the mean of the range is taken.

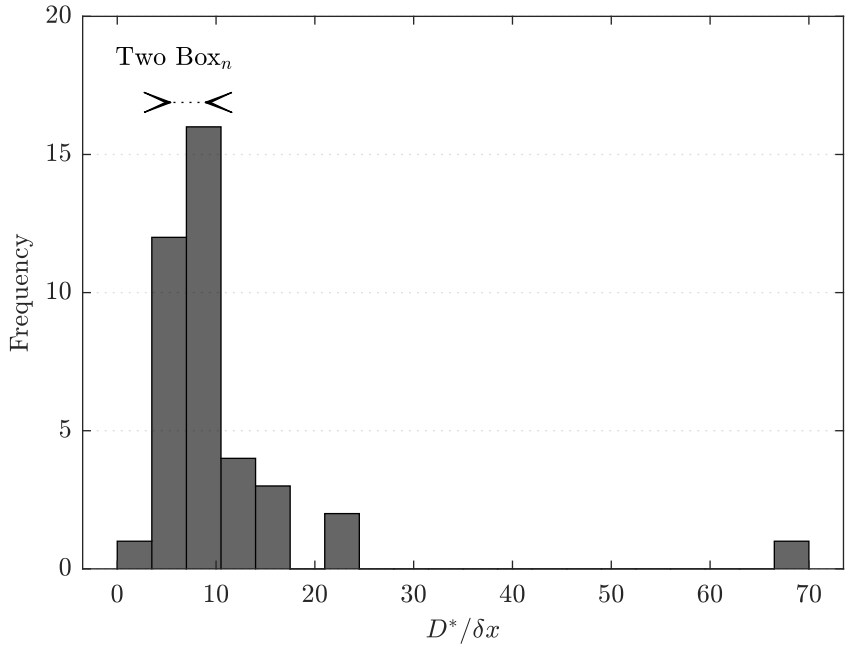

Figure 5.9: Distribution of the plume resolution index for numerical cases documented in the FDS Validation Guide.

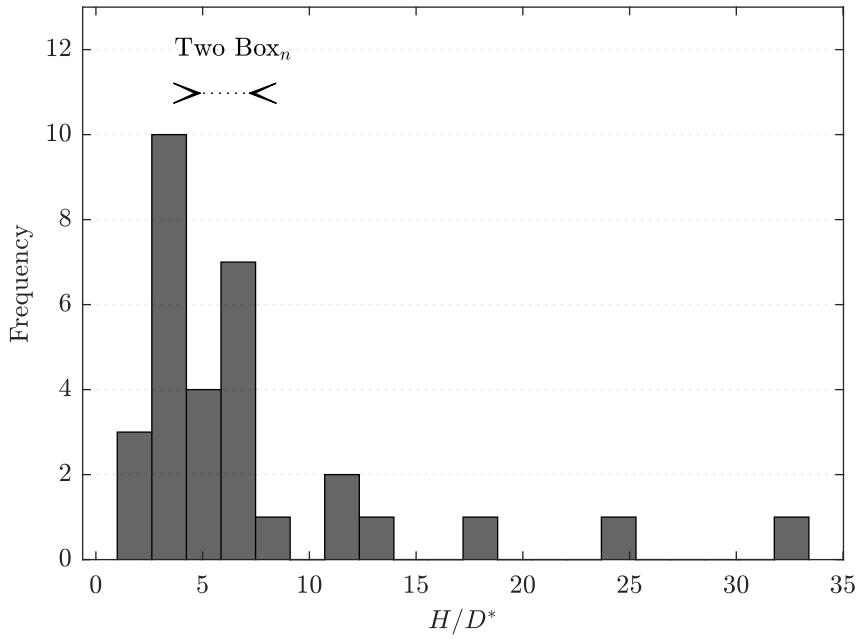

Figure 5.10: Distribution of the enclosure height to fire diameter ratio for numerical cases documented in the FDS Validation Guide.

5.8 Modelling of leakage in the numerical set up

5.8.1 Experimental procedure to measure leakages

A number of cool flow experiments were carried out in the experimental apparatus. Some of these cool flow experiments had the objective of, inter alia, providing data to calibrate the leakages in the numerical set up. An example is given here for experiment `leakage_1`.

`leakage_1` comprised the testing of both the supply and exhaust systems in fresh air and spill mode respectively. The doors to both boxes were opened. Initially all dampers with the exception of the upper exhaust damper to the hot box and the spill damper were closed. The potentiometer controlling the exhaust fan was steadily increased from zero to near to its maximum span. This was, broadly speaking, carried out twice in a row. Following this all dampers were closed with the exception of the lower supply damper to the hot box and the fresh air damper. The potentiometer controlling the supply fan was steadily increased from zero to near maximum span. This was carried out twice. The two damper and fan arrangements for `leakage_1` are described in Figure 5.11a.

The processed velocity data for `leakage_1` is presented in Figure 5.12. During `leakage_1`, the velocity in the main exhaust duct (u_3) can be seen steadily increasing as the potentiometer is increased in steps. The velocity in the hot box exhaust duct (u_1) can also be seen steadily increasing. The difference between the velocity in the main exhaust duct and that of the hot box exhaust duct can be used to quantify leakage in the hot box side exhaust system. At higher potentiometer levels, there is also a velocity in the cool box exhaust duct (u_2). This can be used to quantify leakage in the overall exhaust side ventilation system.

The testing of the supply ventilation system takes place from approximately 2400 s. The velocity in the main supply duct (u_4) can be seen steadily increasing as the potentiometer is stepped up. The velocity in the hot box supply duct (u_6) can also be seen increasing. Note that the difference between the velocity main supply system duct and the hot box supply duct is greater than that between the main exhaust system duct and the hot box exhaust duct. This indicates that there is more leakage from the supply side ventilation system than the exhaust side ventilation system.

The velocity and temperature data can be used to estimate mass flow. The mass flow data can be used to carry out mass conservation calculations on the experimental apparatus. The conservation control volumes available are presented in Figure 5.13.

For the current purposes control volumes 3 and 5 are useful and can quantify the leakage in the exhaust and supply side ventilation system respectively. The output of the mass conservation for control volumes 3 and 5 are presented in Figures 5.14 and

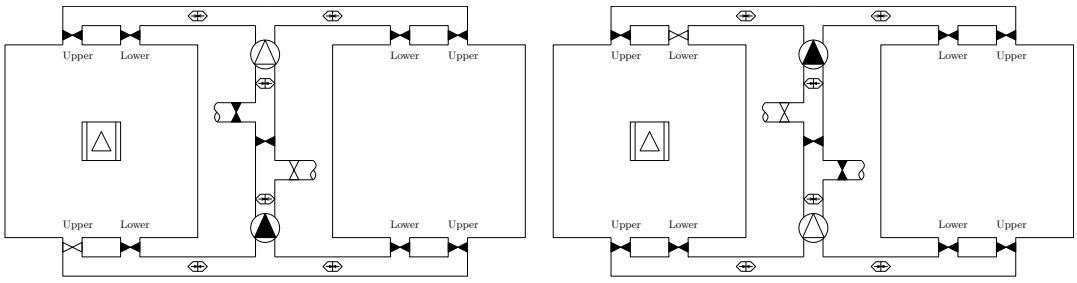

(a) `leakage_1` exhaust system testing. (b) `leakage_1` supply system testing.

Figure 5.11: `leakage_1` damper and fan arrangement for the two stages of the experiment.

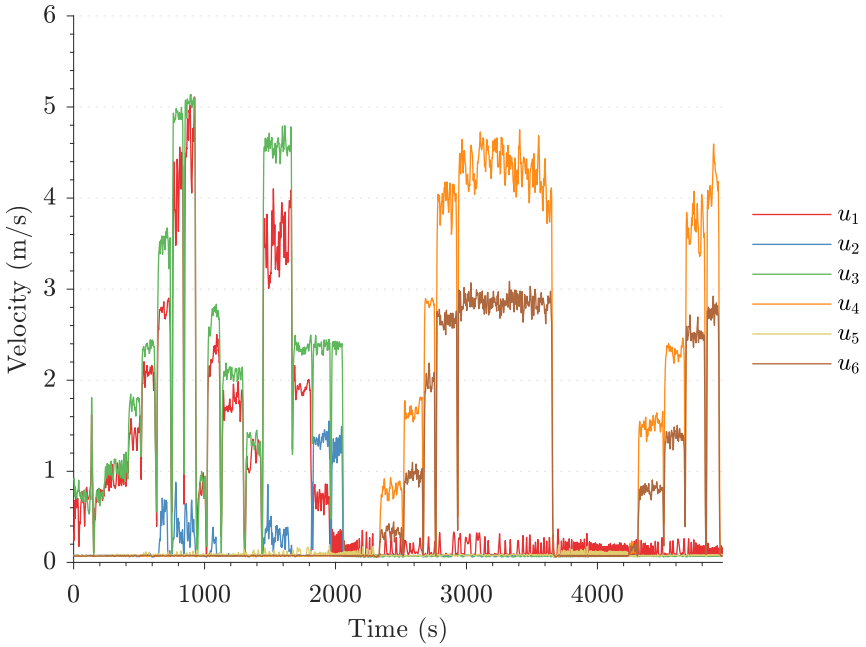

Figure 5.12: Velocity probe data from `leakage_1`. The initial 2000 s was the test of the exhaust system. The latter 3000 s was the test of the supply system.

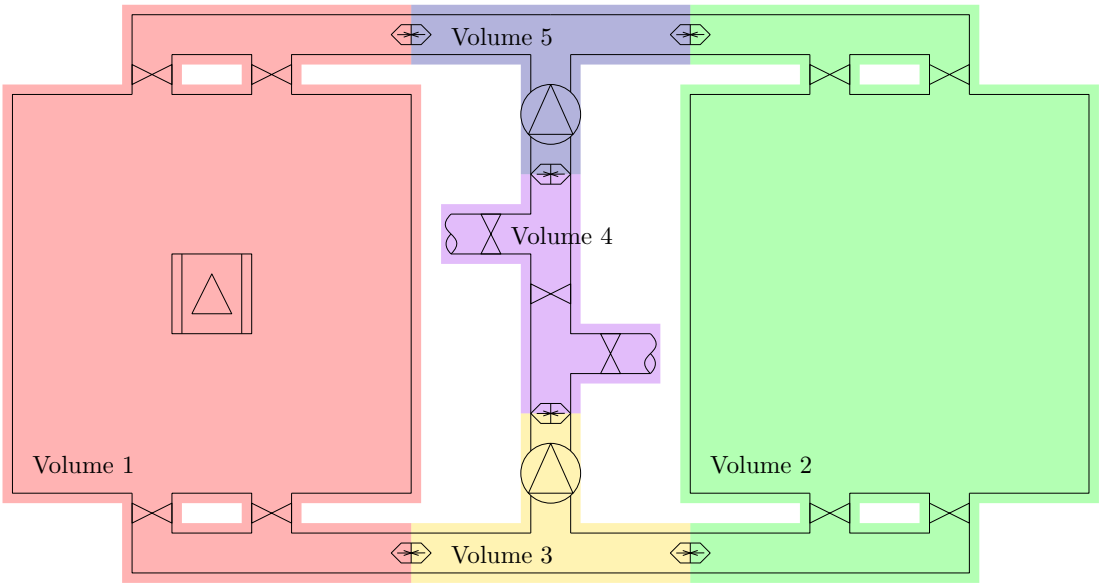

Figure 5.13: Control volumes possible based upon instrumentation of the experimental apparatus. Positive is taken as out of the control volume, negative is taken as into the control volume.

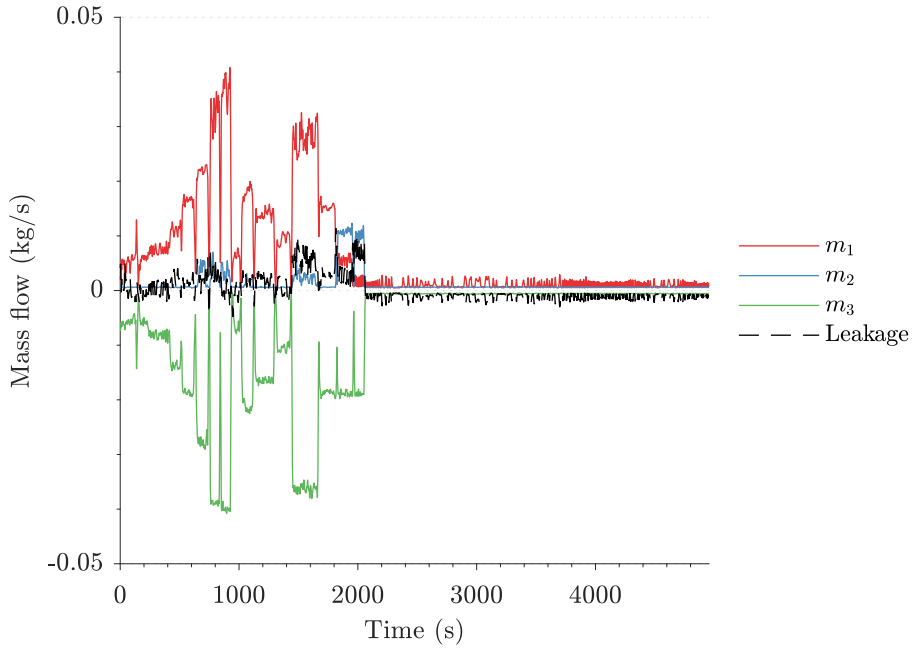

Figure 5.14: `leakage_1` mass conservation, volume 3.

5.15. The analysis quantifies the predicted leakage from the exhaust and supply side ventilation system. The analysis shows that there is more leakage into the supply system when compared to leakage out of the exhaust system.

5.8.2 Modelling and calibrating of leakage in the numerical experiment

The leakage between the computational domain and ambient within the field domain (i.e. the hot box and the cool box) was modelled using the leakage sub-model within FDS. This sub-model essentially creates HVAC ducts connecting the field domain to ambient at vents. Such vents were specified at the edges of each box and assigned a leakage area of 1.0×10^{-3} m each (i.e. a leak width of 1 mm). A loss coefficient of 0.61 was specified for these leakage paths [210].

With the leakage from the field domain specified based on geometric consideration of the simple cubes, the quantitative data generated as described in Section 5.8.1, being both the velocities and the mass conservation analysis, can be used to calibrate the leakage in the exhaust and supply system of the numerical set up across a range of potentiometer levels. Most importantly potentiometer levels equating to the fan cases.

The leakage within the network subdomain of the numerical set up is lumped together for the four sub-parts of the ventilation system and modelled a single leakage path. These sub-parts are the supply and exhaust systems for both the hot box and the cool box. Each one of these sub-parts has a single duct to connected to ambient, representing all leakage within that sub-part. There are four degrees of freedom when calibrating the duct that represents the ventilation system leakage: length, losses, roughness, and area. The properties of these leakage ducts have been calibrated to match the results from `leakage_1` and other cool flow experiments. An example of a leakage duct used to model leakage (in this case from the hot box exhaust sub-part of the network domain) is presented in the following FDS input file extract:

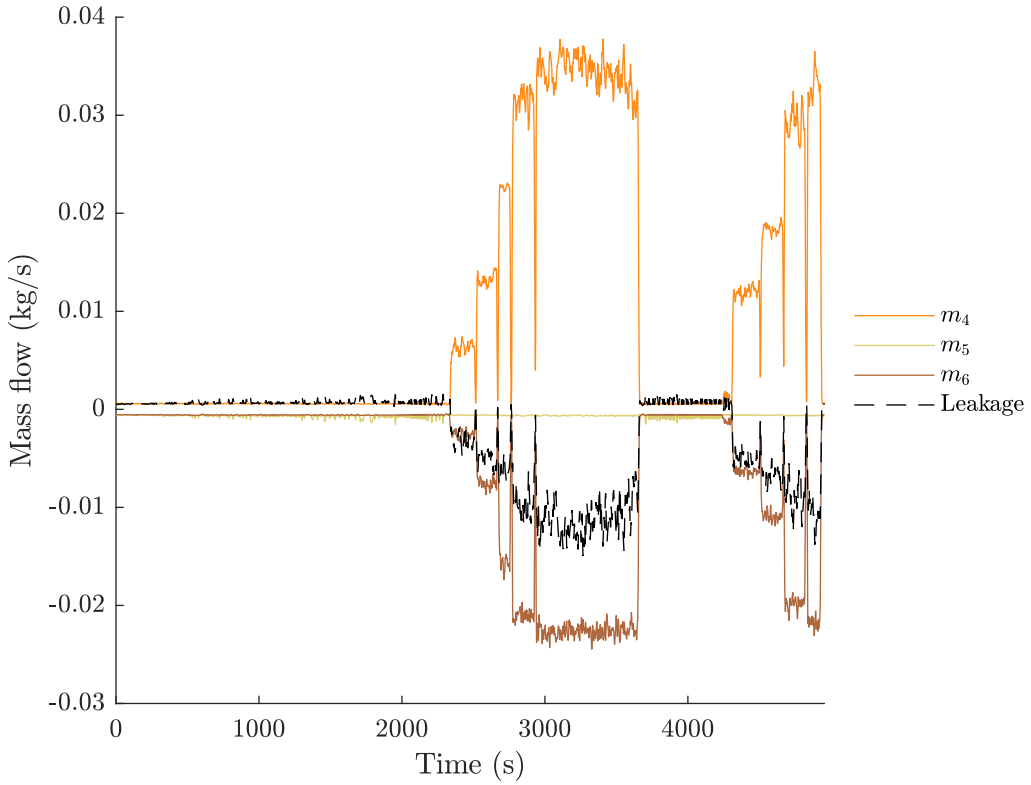

Figure 5.15: `leakage_1` mass conservation, volume 5.

```
1 &HVAC ID='u2_leak', TYPE_ID='DUCT', DIAMETER=0.03, LOSS=0.1,0.2, NODE_ID='
    b2_exh_upper_2','exh_b2_leakNode', ROUGHNESS=5.0E-4, LENGTH=4.0,
    N_CELLS=1/
```

The numerical set up leakage ducts are fixed across all calibrations and numerical experiments. Once the properties of the numerical set up leakage ducts were calibrated, they were not changed again to suit different results from the experimental apparatus.

The post-calibration output of the numerical set up compared to the experimental output from the experimental apparatus for `leakage_1` is presented in Figures 5.16 through 5.19. There is very good agreement between the output of the experimental apparatus and the numerical set up. The numerical set up predicts a slightly higher velocity in most cases (of the order of 5 %). The agreement at lower velocities is the least good. Shown in Figure 5.17, supply system fan level `F1` shows the worst agreement. The numerical set up prediction of u_6 is approximately 30 % greater than the output of the experimental apparatus. This may be attributed to the poor performance of the experimental apparatus velocity probes at very low velocities and pressure-dependent leakage not being captured by the numerical set up.

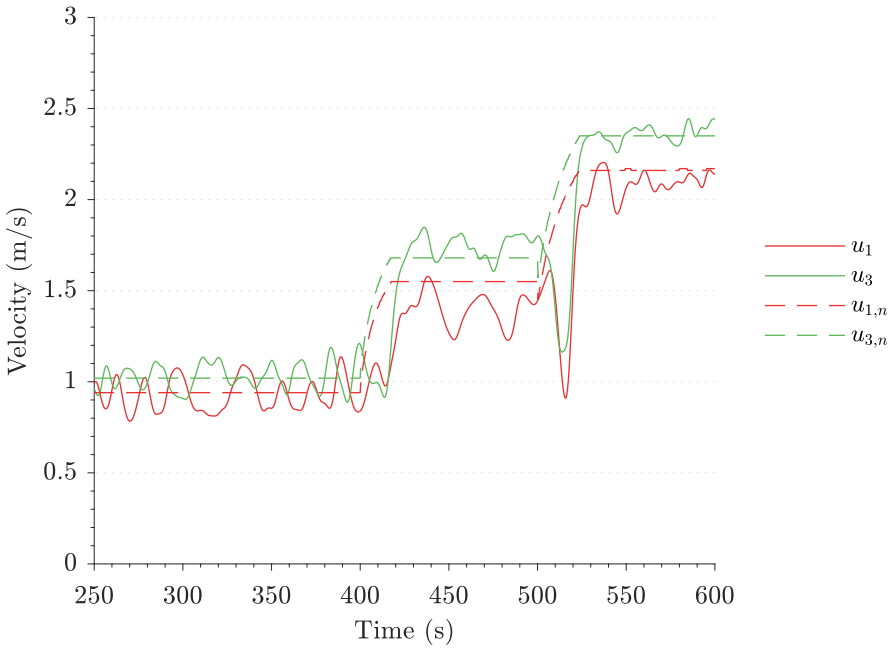

Figure 5.16: Exhaust velocities from the experimental apparatus and the numerical set up for `leakage_1`. The three stages represent three different potentiometer levels for the exhaust fan. These three potentiometer levels equate to `F1`, `F2` and `F3` cases.

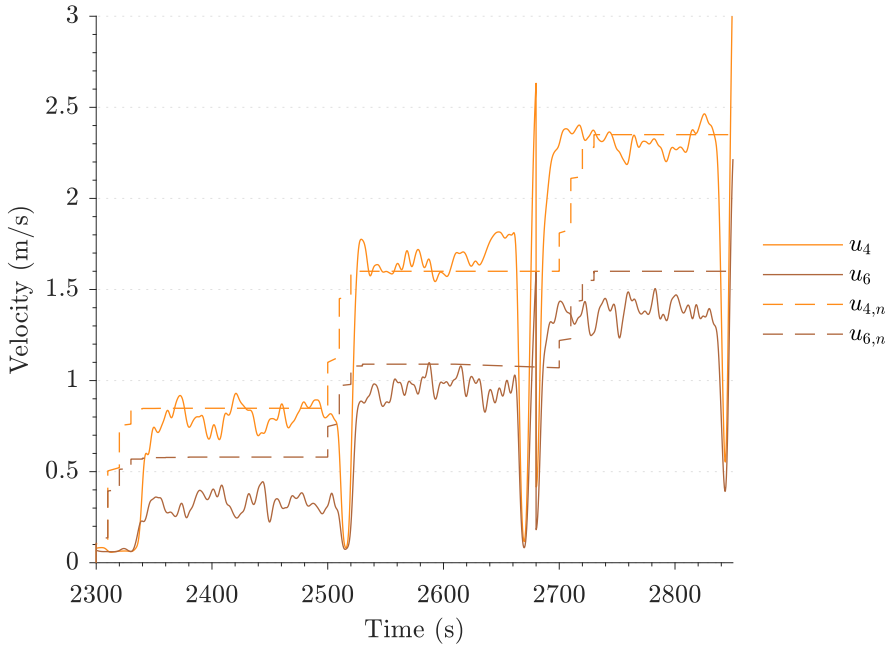

Figure 5.17: Supply velocities from the experimental apparatus and the numerical set up for `leakage_1`. The three stages represent three different potentiometer levels for the supply fan. These three potentiometer levels equate to `F1`, `F2` and `F3` cases. Real time has been manipulated such that the potentiometer levels equating to `F1`, `F2` and `F3` cases occur in succession.

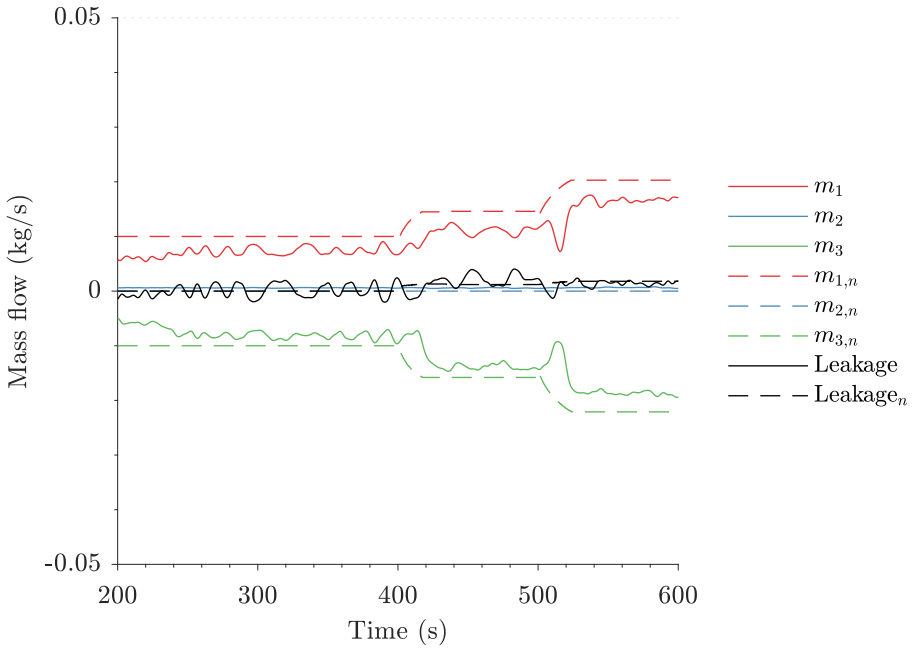

Figure 5.18: Mass conservation analysis for conversation volume 3 from the experimental apparatus and the numerical set up for `leakage_1`. The three stages represent three different potentiometer levels for the supply fan. These three potentiometer levels equate to `F1`, `F2` and `F3` cases.

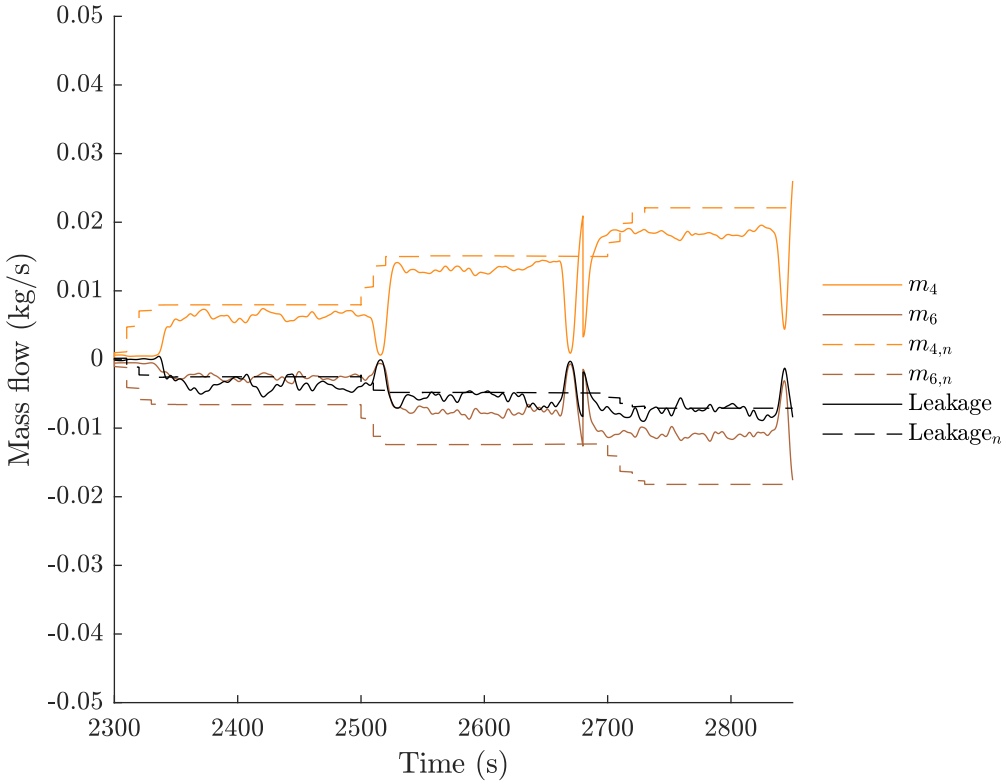

Figure 5.19: Mass conservation analysis for conversation volume 5 from the experimental apparatus and the numerical set up for `leakage_1`. The three stages represent three different potentiometer levels for the supply fan. These three potentiometer levels equate to `F1`, `F2` and `F3` cases. Real time has been manipulated such that the potentiometer levels equating to `F1`, `F2` and `F3` cases occur in succession.

5.9 Closing remarks

The general description, including numerical considerations and input parameters, of the numerical set up has been presented. Relevant geometric simplifications and assumptions have been stated. The grid sensitivity study carried out has been documented and final grid sizing adopted for the numerical campaign using the numerical set up stated. The importance of a case's location within the pertinent numerical parameter space (to enable useful validation exercises to be carried out by end users) has been put forward and the numerical parameters listed. The methodology of the calibration and design of the leakage within the numerical set up has been discussed.

Now that the experimental apparatus and its numerical counterpart have been presented, the following chapter presents a sample of experimental results.

Chapter 6

Experimental results

6.1 Box temperatures

Figure 6.1 presents a full set of box thermocouple tree measurements for `P35_F2_1`. Each subfigure is a single thermocouple tree. Trees from the hot box are presented first and then trees from the cool box.

6.1.1 Temperatures in the hot box

Figure 6.1a shows the measured temperatures in the back left thermocouple tree increase rapidly upon ignition. The upper three thermocouples (1, 2 and 3) all increase to approximately 230 °C. This demonstrates the quick formation of a homogeneous upper hot layer with a thickness of at least 400 mm. For the duration of the experiment the upper three thermocouples measure approximately the same temperature. This indicates that the formed hot layer is maintained during the course of the experiment, including the change of ventilation system mode to smoke-spill and fresh air mode at 2600 s. All temperatures steadily rise during the initial 2600 s of the experiment. Upon smoke spill the lowermost measured temperature increases in trajectory slightly.

Figure 6.1b shows the measured temperatures in the back right thermocouple tree. This is the tree adjacent to the supply air inlets. The data from this tree present a similar relationship when compared with tree 1 discussed above. That being a rapid increase in measured temperatures and a formation of a near-homogeneous hot layer.

Figure 6.1c presents the thermocouple tree directly over the propane burner. The lowermost thermocouple B1_3_5 had been damaged and therefore no data are available. The data clearly show the flame zone near the bottom of the hot box. Measured temperatures of B1_3_4 and B1_3_3 are much higher than temperatures seen else where in the box. The uppermost thermocouples, B1_3_1 and B1_3_2, are outside of the flame zone and are instead within the hot plume. The measured temperatures from these thermocouples are higher than those within the rest of the hot box measured by the corner trees. Upon spill mode the flame zone temperature drops.

Figure 6.1d presents the data from the front left tree within the hot box. This is the tree that is immediately adjacent to the exhaust inlets. Similar behaviour is witnessed upon ignition when compared to the other corner trees. Upon spill mode being activated the uppermost thermocouples measure a flattening out of temperature and the lowermost thermocouple, B1_4_5, measures an increasing temperature.

Figure 6.1e presents the data from the front right tree within the hot box. A similar behaviour is witnessed when compared to the other corner trees. Upon spill the

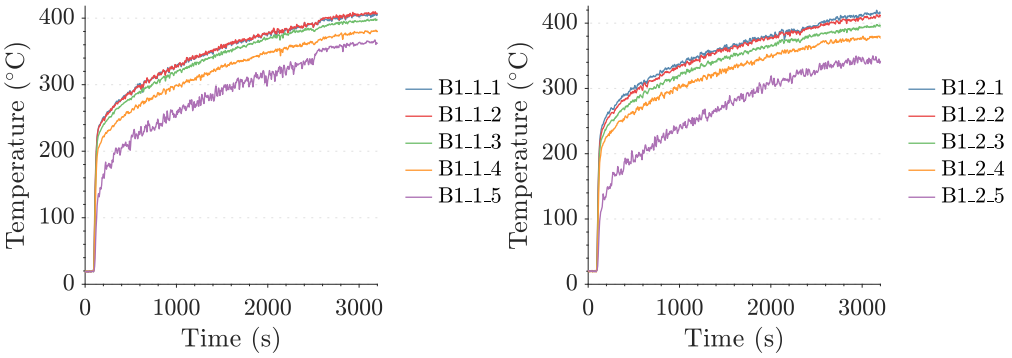

(a) Thermocouple tree 1 (back left).

(b) Thermocouple tree 2 (back right).

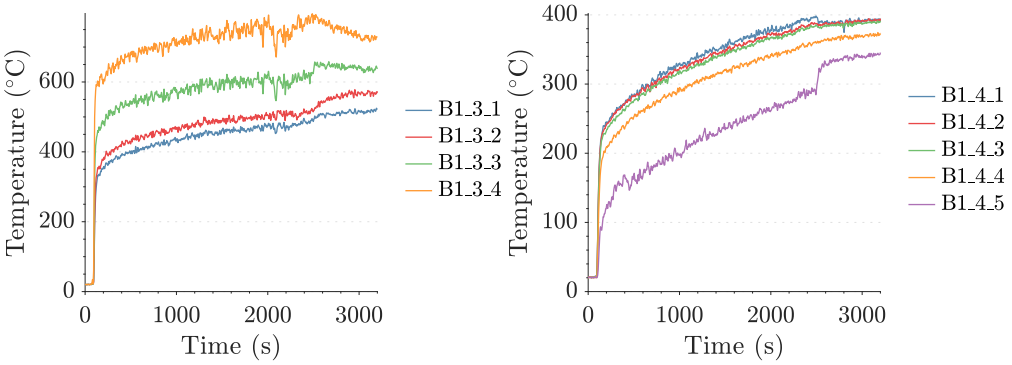

(c) Thermocouple tree 3 (central tree).

(d) Thermocouple tree 4 (front left).

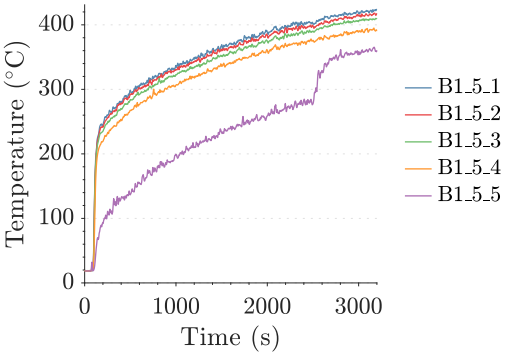

(e) Thermocouple tree 5 (front right).

Figure 6.1: Thermocouple data from hot box; experiment `P35_F2_1`. Thermocouple 1 is the highest, 5 is the lowest.

lowermost thermocouple, B1_5_5, measures a rapid increase in temperature.

6.1.2 Temperatures in the cool box

Figure 6.2 presents the cool box thermocouple tree measurements. There is much less variation from tree to tree when compared to the hot box temperature measurements. This is because there is no high energy input in the cool box. The temperature rises are due to the shared ventilation system only. The increase in temperature is much less steep when compared to the hot box and the highest temperature reached is substantially less than that experienced in the hot box. There is more of a spread between the uppermost and lower most thermocouple measurements for trees 3, 4 and 5, which are the middle and front two trees. This is due to the arrangement of supply to the rear of the cool box and exhaust from the front of the cool box. Upon spill mode the temperatures within the cool box decrease rapidly. This is because fresh air at ambient temperature is being supplied to the cool box.

6.1.3 Summary of box temperatures

The hot box experiences very rapid temperature increase, due to the heat from the propane burner, and the formation of a hot upper layer. There are local variations within the hot box due to the location of the lower supply outlet and the upper exhaust inlet. The air flow pattern induced by the mechanical exhaust system causes temperature variations within the hot box and disturbance of the typically experienced hot layer. The hot box does not experience a marked temperature decrease upon spill mode, with the exception of the lowermost thermocouples of the front two trees (which increase by approximately 40 °C).

The cool box does not have such a clearly defined upper hot layer when compared to the hot box. This is because there is no high energy input in the cool box (i.e. there is no fire within the cool box). Instead energy enters the cool box via the shared ventilation system. This leads to a much more well mixed temperature field within the cool box when compared to the hot box and a more homogeneous temperature distribution. The cool box experiences relatively rapid temperature decrease upon spill mode. This is because the ambient temperature fresh air mixes with the higher temperature recycled air and lowers the near-homogeneous temperature within the cool box.

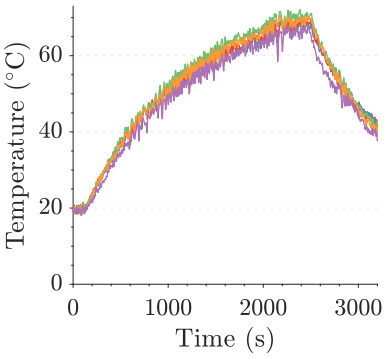

(a) Thermocouple tree 1 (back left).

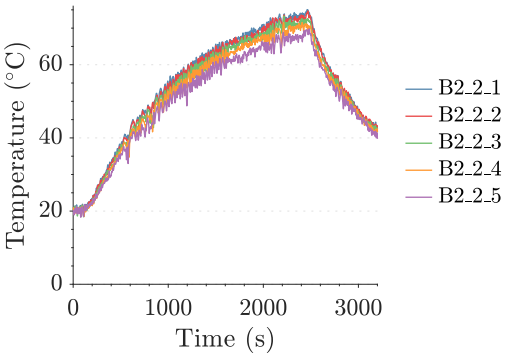

(b) Thermocouple tree 2 (back right).

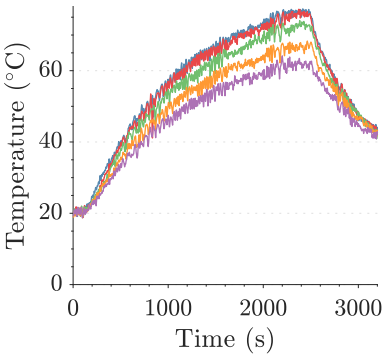

(c) Thermocouple tree 3 (central tree).

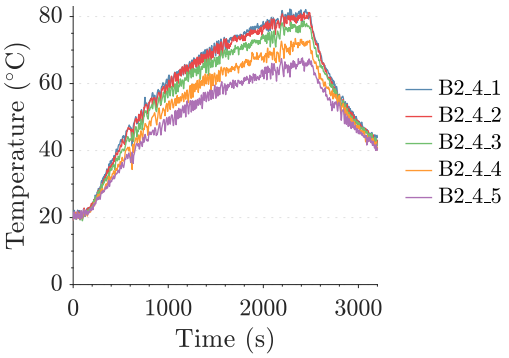

(d) Thermocouple tree 4 (front left).

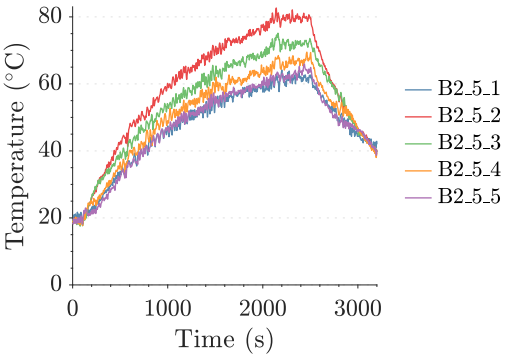

(e) Thermocouple tree 5 (front right).

Figure 6.2: Thermocouple data from cool box; experiment `P35_F2_1`. Thermocouple 1 is the highest, 5 is the lowest.

6.2 Duct temperatures

Figures 6.3 and 6.4 provide duct temperatures within the exhaust system and duct temperatures within the supply system respectively. Thermocouples 1, 6, 15 and 12 are omitted. This is because these thermocouples are in either the inlet or outlet of vents that are closed with a damper. For example, thermocouple 1 is in the lower exhaust inlet of the hot box. These data would serve to clutter the already cluttered plots.

6.2.1 Exhaust system

The highest temperatures are measured within the hot box exhaust duct (ducts 02 and 03). The lowest temperatures are measured within the cool box exhaust system (ducts 04 and 05). This indicates that hot gases from the hot box are not travelling down the cool box exhaust duct. The shared exhaust duct (duct 07) has a relatively high measured temperature but much less than the hot box exhaust duct. This is because much cooler air is being mixed into the shared duct from the cool box. The smoke-spill outlet temperature measurement (duct 08) measures a reasonably increasing temperature prior to smoke-spill mode. This is indicative of leakage of hot gases occurring at the smoke-spill damper (the temperature measurement was taken on the downstream side of the air damper). Upon smoke-spill mode the temperature at the smoke-spill outlet increases rapidly to approximately match the temperature measurement in the shared exhaust duct (duct 07).

6.2.2 Supply system

The lowest temperature is measured at the fresh air supply inlet (duct 09). There is a slight increase in temperature to 50 °C, which is indicative of hot gas leakage through the closed air damper and perhaps radiation from the hot duct surface. The shared supply duct (duct 10) measures the highest temperature in the supply system. This is as expected as the hot gas has had less opportunity to mix with ambient leakage and heat losses to the duct are less. The temperature measurements for the hot box and the cool box exhaust ducts (ducts 14 and 13 respectively) match each other almost perfectly. This indicates a very equal splitting of the shared ventilation system flow (refer to Section 6.5 for discussion of measurement of the flow in the cool box supply duct). The cool box supply duct temperature measurements (ducts 11 and 12) demonstrate a flow that is cooling as it passes through the supply duct, entraining fresh air via leakage and losing heat to the boundary. Unexpectedly the temperature measurement in the supply duct increases along the duct (i.e. duct 11 has a higher reading than that of duct 12). The hot box supply duct temperature measurements (ducts 15 and 16) are higher than the cool box supply duct temperature measurements. This implies that there is heating of the gas either via gas phase diffusion from the hot box or convection from the duct that is experiencing heat transfer via conduction along its length.

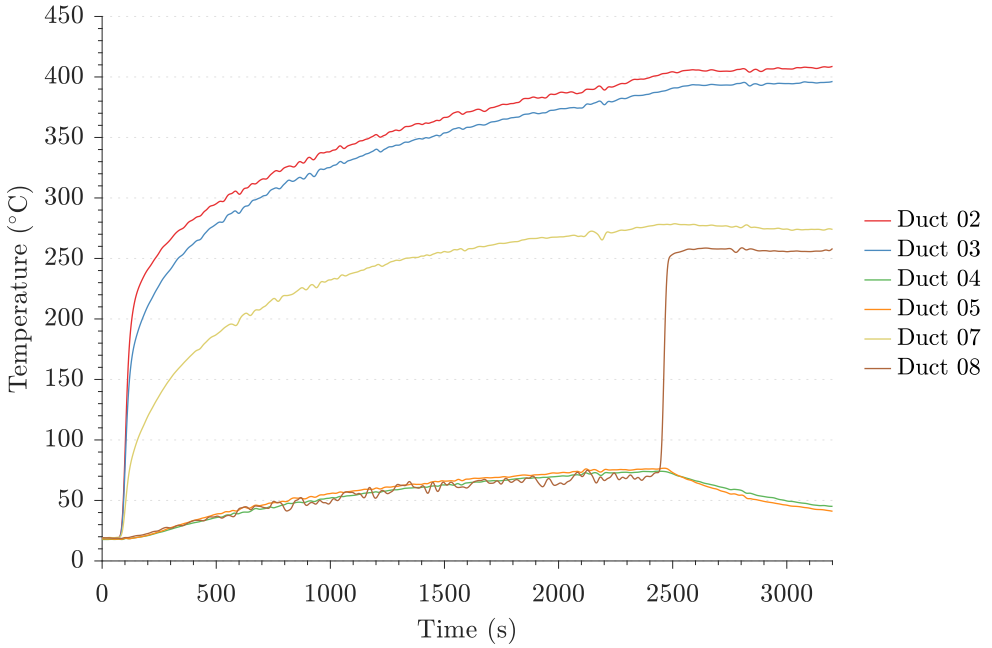

Figure 6.3: Data from in-duct thermocouples in the exhaust system; experiment `P35_F2_1`. Rapid temperature increase is witnessed by duct 02 and duct 03 (the exhaust ducts of the hot box) and, to a lesser extent, duct 07 (the shared exhaust duct). Rapid increase of duct 08 (the smoke-spill outlet) is witnessed on smoke spill.

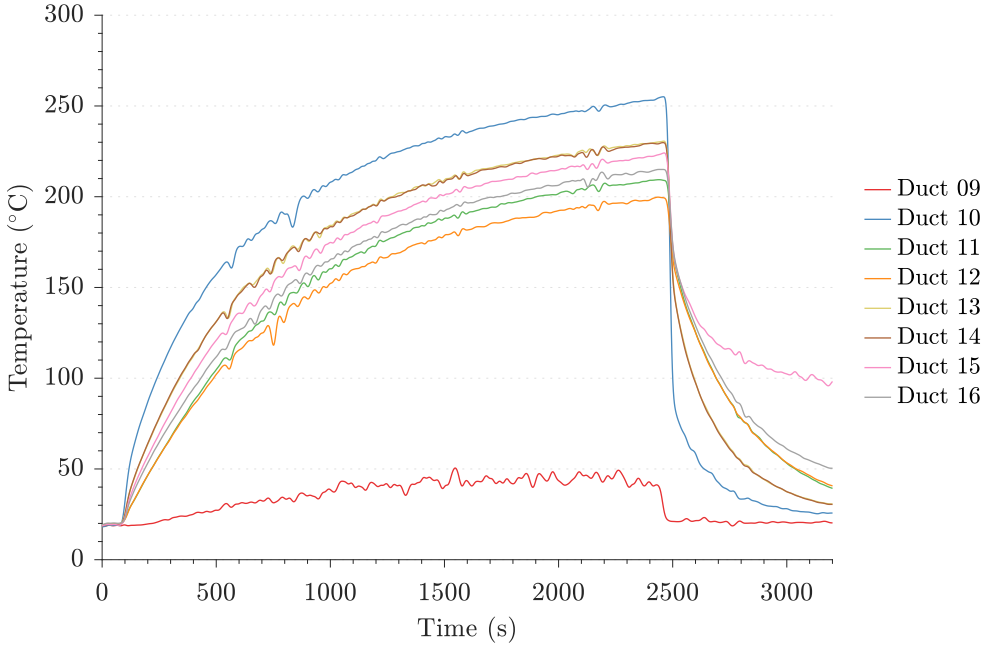

Figure 6.4: Data from in-duct thermocouples in the supply system; experiment `P35_F2_1`. Steady increase of all but duct 09 (fresh air inlet) witnessed. Highest temperature presented is duct 10 (shared supply duct). All temperatures rapidly decrease upon spill mode. Highest temperature during spill mode is duct 15 (hot box supply outlet).

6.3 Duct velocities

Velocity measurements within the ducts are presented for `P35_F2_1` in Figure 6.5. Positive measurements are taken as 'in the normal operational direction'. i.e. positive velocities for the exhaust system indicate gas flow out of the boxes and positive velocities for the supply system indicate gas flow into the boxes.

6.3.1 Pre-ignition

The initial 100 s is prior to propane ignition. At this time the fans and compressed air are on. Velocities u_1, u_2 and u_6, being the hot box exhaust, the cool box exhaust and the hot box supply respectively, are approximately equal at 0.8 m/s. Velocities u_3 and u_4, being the shared exhaust duct and the shared supply duct, are also approximately equal at 2.1 m/s. This makes intuitive sense. At this time the experimental apparatus is on recycle mode. The fans are working in series to recycle the air, relatively equally, to both the hot box and the cool box. u_5 is behaving very oddly and is measuring a velocity of 0 m/s.

6.3.2 Ignition and recycle mode

Upon ignition, u_1, the exhaust out of the hot box, increases rapidly. This is because the fire-induced flow and pressure, and dropping gas density, is forcing gas out of the hot box. u_1 sees a steep increase as this divergence of hot gas is in the same direction of the fans-induced flow. u_1 steadily climbs through the recycle mode period, appearing to reach a plateau at just below 2.5 m/s.

Upon ignition, u_2, the exhaust out of the cool box, sees a decrease in velocity to approximately 0.2 m/s. This is due to two phenomena. Firstly, the air within the cool box exhaust duct collides with the incoming air from the hot box (which now has higher momentum due to the fire-induced increase in flow and pressure) at the tee junction prior to entering the shared exhaust duct. Secondly, there is an increased upstream pressure (within the hot box). This increased pressure reduces the pressure drop down the cool box exhaust duct and hence reduces the velocity. After the initial decrease, u_2 does climb slightly during the recycle mode period. This may be due to temperature and pressure building slightly within the cool box and an increasing supply rate into the cool box.

Upon ignition of the propane burner, u_3, the shared exhaust duct, experiences an increase in velocity. This is likely for the same phenomenological reasons as for the increase in u_1. The high momentum hot gas leaving the hot box flows into the shared exhaust duct. It will likely also be leaking to ambient within the hot box itself and within the ventilation system. A recognised leak within the shared ventilation system is the smoke-spill damper when closed. This damper experienced very high temperatures (typically 600 °C) and sustained damage to its gaskets. There was reasonable leakage out of the smoke-spill damper in the closed position. u_3 steadily climbs throughout the recycle mode of the experiment; plateauing at approximately 2.9 m/s. At this stage it is slightly higher than u_1.

Upon ignition u_4, the shared supply duct, experiences a marked increase in magnitude to almost 3.8 m/s at its peak. The high momentum, low density, hot gas from the hot box exhaust system is passing through the shared ventilation system.

The unusual data from u_5 continues following ignition. The unusual behaviour of u_5 will be revisited in more detail in Section 6.5.

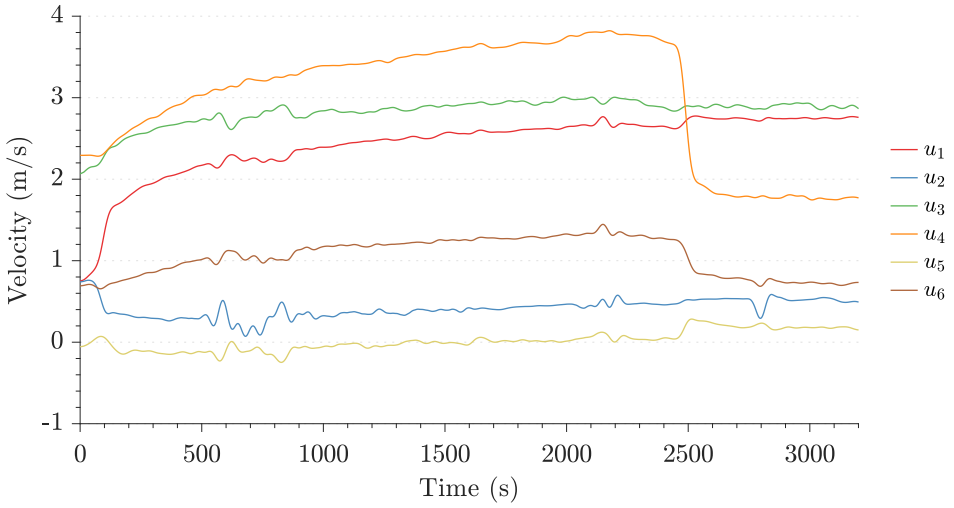

Figure 6.5: Duct velocity measurements; experiment `P35_F2_1`.

Following ignition u_6, the hot box supply increases in velocity to approximately 1.2 m/s. This follows the general trend of increasing velocities.

6.3.3 Smoke-spill and fresh air mode

At approximately 2500 s smoke-spill and fresh air mode is engaged. The return damper is closed and the smoke-spill exhaust and fresh air inlet damper are opened. At this time the fans effectively stop working in series, at least directly. They are still indirectly coupled through the boxes but they are no longer within a shared ventilation system.

Upon spill, u_1 does not vary greatly. This may seem surprising as the fans are no longer working in series within the ventilation system. This may be due to multiple mechanisms. Firstly, the friction losses that the exhaust fan is now required to overcome are greatly reduced. This means that the induced pressure increase will decrease across the fan and the volume flow will increase (refer to Figure 6.6). Secondly, the fire-induced flow may be dominating the flow within the exhaust system.

Upon spill mode, u_2 does not see a marked change. This is because the flow within the cool box exhaust duct is controlled primarily by the upstream pressure conditions at the shared exhaust meeting tee - which haven't changed.

Upon the operation of spill mode, u_3 also does not see a great change. There is a slight decrease in velocity in the shared exhaust duct. u_3 is heavily coupled to u_1 and the mechanisms dominating the value of u_1 discussed above have a controlling effect on u_3 also.

On spill mode, the shared supply duct sees the greatest change in velocity. u_4 drops rapidly from the greatest recorded velocity, approximately 3.8 m/s to below that of the exhaust system's u_1 and u_3 at approximately 1.8 m/s. When fans are arranged in series the potential pressure increase is doubled but the flow rate is constant. The opposite is true for fans connected in parallel - the pressure increase is unchanged but the flow rate is doubled. The system curve for the supply fan is heavily dominated by the downstream pressures. These have not markedly changed upon spill. This is in contrast to the downstream pressures experienced by the exhaust fan - which have fallen to ambient. Therefore, the supply fan is experiencing a similar shaped system curve but is capable of approximately half the pressure increase to overcome it. This is

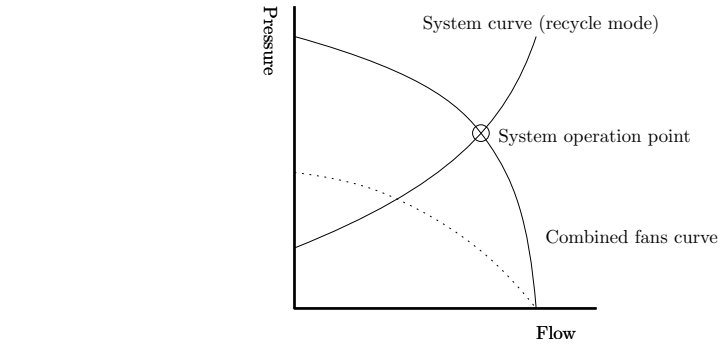

(a) Recycle mode.

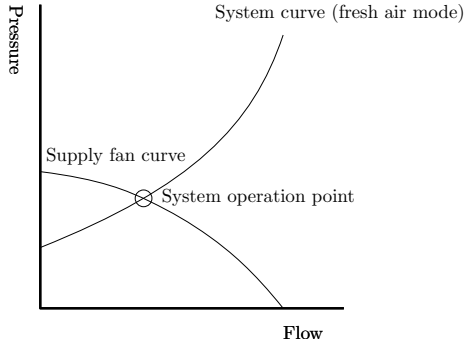

(b) Supply.

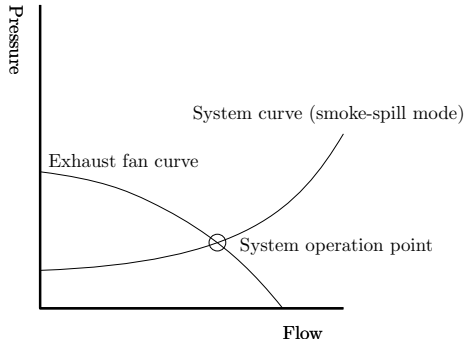

(c) Exhaust.

Figure 6.6: Fan operation points.

most likely the reason that there is a great reduction in u_4. The supply fan has sharply moved to the left of its characteristic fan curve; and is required to deliver flow at a lower pressure and a lower flow rate. This is diagrammatically described in Figure 6.6.

On spill mode, u_5 continues to act unusually. This will be examined in Section 6.5.

After spill mode is operated, u_6 decreases to approximately 1 m/s (its pre-ignition magnitude). As the flow in u_6 is coupled to the flow in u_4, the shared supply duct, the same mechanisms are causing the reduction in the velocity in the hot box supply duct.

6.4 Duct mass flow

From the available data the mass flow rate in the ducts at the locations of the velocity probes can be estimated. To do this some assumptions have to be made. First that the absolute pressure within the experimental apparatus does not change and the air is dry. This enables the output of temperature-dependent density from a form of the ideal gas law [161]:

$$\rho = \frac{p}{R_{spec}T} \tag{6.1}$$

where ρ is the density, p is the absolute pressure, R_{spec} is the specific gas constant for dry air and T is the temperature. The next assumption is that the average velocity in the ducts u_{avg} can be approximated as given in Equation 6.2 [211]. This assumption is based upon geometric consideration of the plug type flow within fully developed pipe flow.

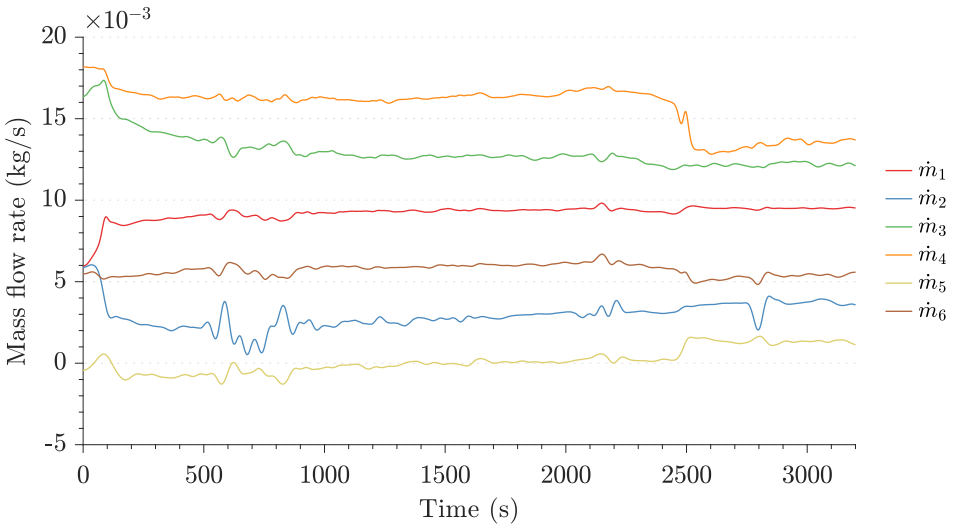

Figure 6.7: Mass flow rate estimates; experiment `P35_F2_1`.

$$u_{avg} \approx 1.2 u_{max} \tag{6.2}$$

In fully developed duct flow, as assumed to occur within the experimental apparatus, the centre line velocity is expected to be the maximum velocity [212]. Mass flow rate can be estimated as:

$$\dot{m} = \rho u_{avg} A \tag{6.3}$$

where $\dot{m}$ is the mass flow rate, ρ is the temperature-dependent density, u_{avg} is the average velocity in the duct, and A is the area of the duct. The mass flow rates for `P35_F2_1` are presented in Figure 6.7 and described in the following paragraphs.

6.4.1 Pre-ignition

Prior to the ignition of the propane burner $\dot{m}_1$, $\dot{m}_2$, and $\dot{m}_6$ are approximately at the same magnitude of 6×10^{-3} kg/s. $\dot{m}_4$ and $\dot{m}_5$ are at approximately the same magnitude of 17.5×10^{-3} kg/s. There is evidently leakage into the experimental apparatus within the ventilation system. This is explored quantitatively in Chapter 7. The measured mass flow rate in the cool box supply duct, $\dot{m}_5$, behaves unusually. At pre-ignition stage there is a negative mass flow rate. In other words there is a measured mass flow rate, against the pressure induced by the fans, from the cool box to the hot box.

6.4.2 Ignition and recycle mode

Upon ignition of the propane burner, $\dot{m}_1$ increases to just below 9×10^{-3} kg/s. The decrease in density is outweighed by the large increase in volume flow due to the flow and pressure induced by the fire. This leads to an increase in the mass flow rate in the hot box exhaust duct.

Upon ignition, $\dot{m}_2$ decreases to a value of approximately 2.5×10^{-3} kg/s. This is the effect of the downstream pressure at the shared exhaust tee. Due to the fire in the

hot box, the pressure head and the velocity head are both increased at this location. Therefore, there is a reduced flow in the cold box exhaust duct.

Upon ignition, $\dot{m}_3$ experiences a rapid decrease to a new plateau of approximately 12.5×10^{-3} kg/s. This is information that was not illuminated by the examination of duct velocities within Figure 6.5. u_3 increases but $\dot{m}_3$ decreases. This is because of the greatly reduced density of the gas at position 3. Mass conservation will be examined in Chapter 7 but it is evident that mass is leaving the experimental apparatus volume between velocity probe positions 1 and 3 via leakage.

At ignition and during recycle mode, $\dot{m}_4$ decreases to approximately 16×10^{-3} kg/s. Due to decreased gas density the mass flow rate actually decreases even as u_4 increases.

Unusual behaviour of $\dot{m}_5$ continues to be witnessed at ignition and during recycle mode.

Upon ignition and during recycle mode, $\dot{m}_6$ increases slightly. Although the measured velocity at this probe location increases, this is balanced by the decreased gas density to deliver approximately the same mass flow rate within the hot box supply duct.

6.5 The conundrum of velocity probe 5

6.5.1 Incongruity in measurements

It is clear from the above data that the measurements from velocity probe 5 are not as expected. The output of velocity probe 5 does not agree with the intuitive output expected from the experimental apparatus. The primary irregularities exhibited by measurements from velocity probe 5 are:

- If flow within the supply system was from the cool box to the hot box a lower temperature measurement would be expected at duct 13 compared to duct 14. This is not witnessed.
- The pre-ignition values of u_5 and $\dot{m}_5$ are not expected to be negative. This indicates a flow against the pressure increase induced by the fans.
- The pre-ignition values of the hot box and cool exhaust ducts' and the hot box supply duct's velocities and mass flow rates are approximately equal as expected. The values of u_5 and $\dot{m}_5$ do not match the other in and outflow ducts as expected.
- Upon ignition the pressure in the hot box is expected to increase. The pressure at the shared supply tee is expected to increase. The flow within the cool box supply duct $\dot{m}_5$ towards the cool box is expected to increase. The opposite of this is witnessed.

6.5.2 Potential causes

Different reasons for the unusual behaviour of velocity probe 5 were considered. These are:

1. The tubing to the pressure transducer was accidentally swapped. That is, what is processed as the downstream pressure was processed as the upstream pressure and vice versa. This would lead to the correct magnitude of velocity to be measured but for this velocity to be in the reverse direction.

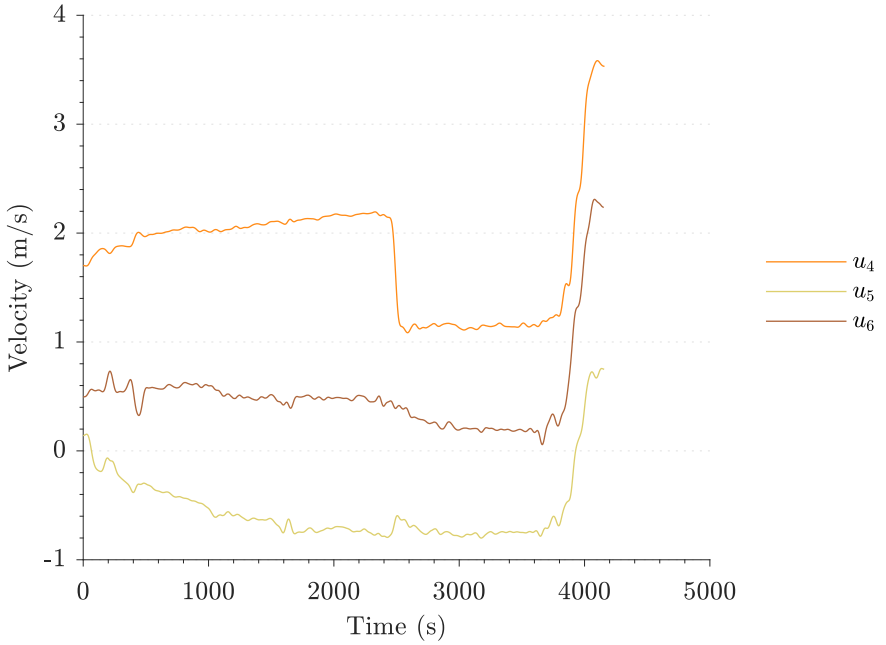

Figure 6.8: Measured supply velocities for experiment `P20_F1_1`. The plot includes the data signal after the termination of the formal experiment at 3700 s.

2. The positive and negative wiring from the pressure transducer signal output was accidentally reversed. This would have a similar effect as described above: the correct magnitude of velocity being recorded but its direction being reversed.

3. A mechanical or electrical problem with the pressure transducer. For example, a sticking of the piezoelectric diaphragm leading to incorrect differential pressures to be measured.

4. A mechanical problem with the bidirectional pressure probe. For example, incorrect orientation or partial blocking of the in or outlet.

6.5.3 Probing of the probe

Items 1 and 2 are the most 'attractive' in the sense that simply reversing the data signal about the 5 V midpoint would return a corrected measurement. The tubing and wiring was checked and double checked. It was found to be tubed and wired correctly. To validate that velocity probe 5 was not either tubed or wired incorrectly after the termination of experiments `P20_F1_1` and `P20_F1_2` the supply fan potentiometer was increased to its maximum level. The full length of the processed supply system data signals for these two experiments is presented in Figures 6.8 and 6.9.

The data from the two experiments show u_5 starting with a slightly negative value pre-ignition. Both experiments show u_5 increasing in magnitude during the experiments. That is, the flow from the cool box to the hot box via the cool flow supply duct increasing; against both the pressure increase in the hot box and the pressure increase from the fans. After the formal experiments terminate, the supply fan potentiometer level was increased to its maximum. It is expected that the shared supply duct velocity u_4, the hot box supply duct velocity u_6 and the cool box supply duct velocity u_5 all increase. This is witnessed. At this stage u_5 is positive; that is, flow is in the direction

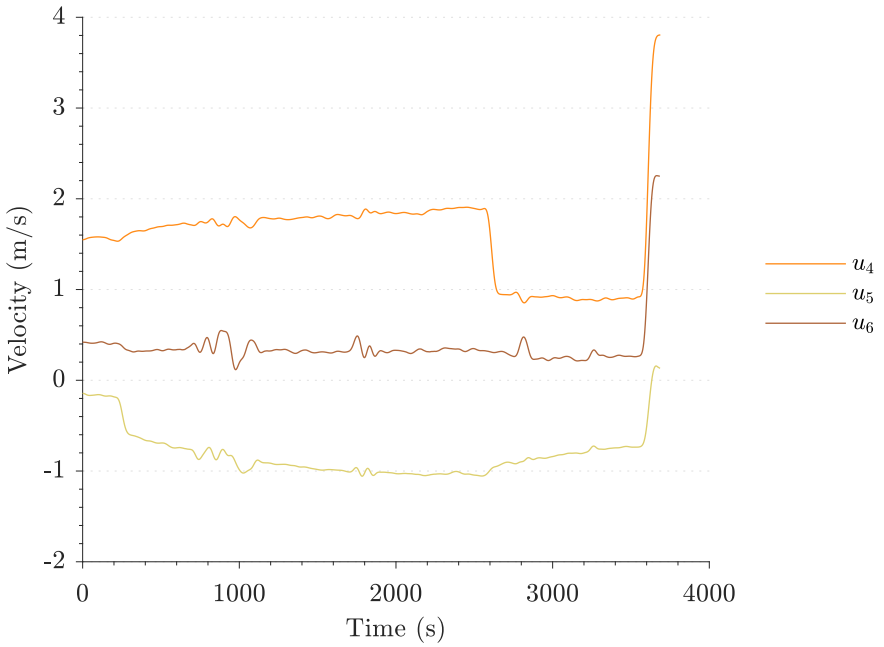

Figure 6.9: Measured supply velocities for experiment `P20_F1_2`. The plot includes the data signal after the termination of the formal experiment at 3700 s.

of the supply fan towards the cool box. It can only be concluded that both points (1) and (2) are not the reason for the unusual behaviour of velocity probe 5.

A cool flow experiment, named `fanTest_01`, was carried out on the supply systems of the hot and cool boxes with the doors both open. The procedure was:

1. All dampers closed with the exception of the fresh air supply damper and the upper supply damper to the hot box.
2. Start the supply fan.
3. Close the upper hot box supply damper and open the lower hot box supply damper.
4. Close the lower hot box supply damper and open the upper cool box supply damper.
5. Close the upper cool box supply damper and open the lower cool box supply damper.
6. End experiment.

The supply system velocity measurements are provided in Figure 6.10.

The velocity measurements from `fanTest_01` show u_5 behaving as expected. It is concluded that potential causes (1) and (2) are rejected. This experiment also double checks that velocity probes 5 and 6 were connected to the correct box; the cool box and hot box respectively.

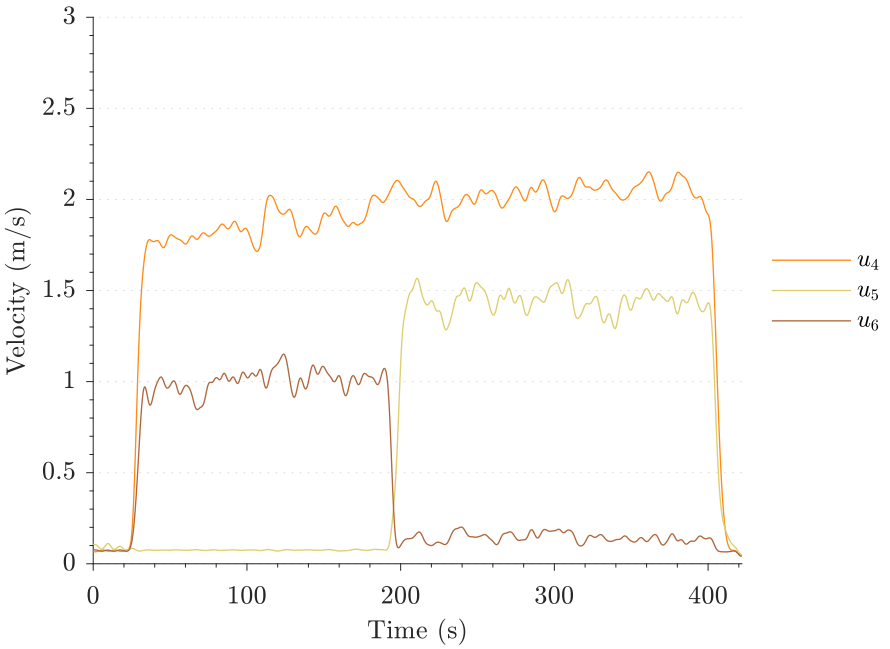

Figure 6.10: Supply system velocity measurements for experiment `fanTest_01`. From 20 s to 200 s is the study of the hot box. From 200 s to 400 s is the study of the cool box. The different amount of leakage within the hot and cool box supply system is illuminated by the different magnitudes of u_5 and u_6.

6.5.4 Conclusion of examination of probe 5

Based upon the analysis of this section it can be concluded that the unusual behaviour of u_5 is not caused by incorrect tubing or wiring direction and no simple post-processing can recover usable data. The conclusion is that the incongruous data must be caused by either a problem with the transducer or the velocity probe. These are impossible to address using data post-processing. Therefore, the sad conclusion is made to disavow the data from velocity probe 5 for the remainder of this work. This includes, in general, mass conservation analysis and benchmarking.

6.6 Discussion of leakage through the experimental campaign

The initial design of the experimental apparatus comprised sealing of the vermiculite boards of the hot box and the cool box and the damper penetrations from the outside of the experimental apparatus using high temperature fire cement. During each experiment the seals were observed to open slightly. The seals could be heard cracking and warm gas could be felt escaping the boxes, especially at the upper corners and edges of the hot box. After each experiment the joints of the vermiculite boards were resealed using high temperature fire cement. This was easily achieved for the front, back and left and rightmost faces of the experimental apparatus. The internal faces (that is, the right wall of the hot box and the left wall of the cool box) were, however, not easy to access. The gap between the two boxes was approximately 250 mm. This meant that reaching to fully externally reseal the joints of the vermiculite boards was not possible. The boxes were also sealed internally using high temperature fire cement.

It is expected that throughout the experimental campaign leakage from the experimental apparatus to ambient generally increased. This is due to burning of damper rubberised gaskets, damage to the vermiculite boards, and fatigue to the rig due to moving the experimental apparatus in and out from under the exhaust hood.

6.7 Closing remarks

Near full results (being box thermocouple data, in-duct thermocouple data, velocity measurements and mass flow rate estimates) have been presented for one example experiment `P35_F2_1`. The results were described in phenomenological terms.

Highlight has been drawn to the unusual output from velocity probe 5, which was located in the cool box supply duct. The oddities of the output of velocity probe 5 have been examined and possible reasons explored and tested. The conclusion of the analysis is that the data from velocity probe 5 will be ignored in the subsequent analysis and benchmarking exercises.

An appreciation of the basic output data from the experimental apparatus has been achieved. The stage is now set for a more in-depth analysis of the experimental apparatus data. This is documented in the following chapter.

Chapter 7

Experimental analysis

7.1 Recap: why a new experimental set up?

It is useful to return to the aims that were defined during the creation of the experimental apparatus.

1. To provide good quality data to use to benchmark the new coupled hybrid model.
2. **To investigate phenomena that may currently be being ignored or missed within the fire safety building design paradigm or model solutions.**

The first aim is dealt with specifically in Chapter 8. The second aim is examined in this chapter. It is more convenient to examine aim two initially as discoveries made on the way to fulfilling aim two can directly help define what 'good quality data' means specific to the subject parameter space.

To investigate phenomena that may be ignored or not addressed within the current fire safety design guidance and Standards, the results of the experiments, and trends seen in these results, are examined. Attention is paid to the tendency of phenomena to change with differing propane flow rates and fan settings. When highlighted, these trends, affiliated with a fire/ventilation dominance ratio change, can illuminate potential risks within the current fire safety design methodologies. For example, if typically utilised methods or model solutions break down when the effect of the ventilation system overcomes the effect of a fire (e.g. flow magnitude or direction, temperature distribution), this tendency can be extracted from the data produced by the experimental apparatus. The highlighting of the break down of typically used methodologies or the exploitation of limitations within guidance can inform the adapted use of methods and extensions to the guidance.

7.2 Expectations of experimental outcomes

A concept used within this chapter is the 'ratio of fire power to fan power' (ϕ_P). This concept is used to describe the relative influence of the heat release rate of the fire and the energy transfer potential of the ventilation system. It is convenient to utilise this concept as it helps to describe phenomenological trends and shifts in the experimental data across the experimental matrix. This ratio can be considered as:

$$\phi_P = \frac{P_{\text{fire}}}{P_{\text{fan}}} = \frac{\dot{Q}}{qc_p\rho T} \tag{7.1}$$

where $\dot{Q}$ is fire heat release rate, q is volume flow rate, c_p is specific heat, ρ is gas phase density, and T is gas phase temperature. Quantities on the denominator vary with time and space throughout the duration of an experiment. Therefore, it is not practical or useful to explicitly evaluate ϕ_P but it remains a useful concept to describe the overall location of an experimental case on the experimental matrix.

A higher nominal value of ϕ_P would entail a case where the fire may be expected to have a dominant affect on relevant quantities compared to the ventilation system. Within the real world, this may be where a fire has grown to a large size, there is a high hazard fuel load, or where the ventilation system has low duty. A lower nominal value of ϕ_P would indicate a case where the effect of the mechanical ventilation system may dominate that of the fire with respect to environment conditions. Within a practical application, this may occur in the early stages of a fire or for a design where a high duty mechanical smoke hazard management system is used.

Based upon the examination of the arrangement it is expected that, at higher nominal values of ϕ_P, a reduction of the performance of the supply ventilation system to the hot box may be experienced.

It is hypothesised that at very low nominal values of ϕ_P flow may be witnessed against the pressure increase induced by the fans within the supply side ventilation system. That is, it is hypothesised that negative velocities will be witnessed in the hot box supply duct at cases with a high propane flow rate and a low fan setting. Moreover it is expected that there will be trends in the maximum velocity data across the experimental matrix. Analysis of these data can illuminate trends that may be applicable for real world applications.

It is also expected that maximum temperatures within the hot box and the cool box will increase with increasing propane flow rate. It is hypothesised that there will be a variation in the results from the experimental apparatus and predictions of the maximum temperature from typically utilised models. This is because of the shared mechanical ventilation system. If this hypothesis is proven then the use of simple models when there is a shared mechanical ventilation system may be not valid.

Finally there is an expectation that leakage to and from the experimental apparatus will vary across the experimental matrix and also during an experiment. An examination of this change in leakage can identify trends in behaviour that can be used to inform real world designs of modern buildings.

7.3 Questions to ask of the experimental data

Based upon the previous discussion, the following questions are asked of the data:

- Section 7.5: how were leakage and over/underpressures affected by the independent variables and through an experiment?
- Section 7.6: was flow against the pressure increase induced by the fans witnessed within the supply duct to the hot box?
- Section 7.7: how did maximum temperatures in the boxes and the ducts vary with the independent variables?

– Section 7.7: did the maximum temperatures in either of the boxes or the ducts vary from what would be expected based upon simple often-used empirical models?

– Section 7.8: how did the velocities and mass flow rates in the ducts vary with the independent variables?

– Section 7.8: did the velocities and mass flow rates in the ducts vary from what would be predicted using commonly used simple models?

7.4 Experiments carried out

The experimental campaign matrix is re-presented in Table 7.1. The aim of the spread of cases was to span a range of fire to fan power ratios ϕ_P to enable the highlighting of trends in experimental output (for example, maximum temperatures or maximum velocities).

Table 7.1: Experimental programme case matrix.

Case	Propane flow rate (g/s)	Target free flow velocity (m/s)
P20_F1	0.20	1.0
P20_F2	0.20	2.0
P20_F3	0.20	3.0
P25_F1	0.25	1.0
P25_F2	0.25	2.0
P25_F3	0.25	3.0
P30_F1	0.30	1.0
P30_F2	0.30	2.0
P30_F3	0.30	3.0
P35_F1	0.35	1.0
P35_F2	0.35	2.0
P35_F3	0.35	3.0
P40_F1	0.40	1.0
P40_F2	0.40	2.0
P40_F3	0.40	3.0
P45_F1	0.45	1.0
P45_F2	0.45	2.0
P45_F3	0.45	3.0

7.5 Leakage and over/underpressures in the experiment

7.5.1 Importance of leakages

Leakage plays an important role within the spread of smoke throughout a building [213] and the development of a fire [182]. Leakage can also affect overall air movement within a building (for example stack effect [214]) and can compromise ventilation systems [215].

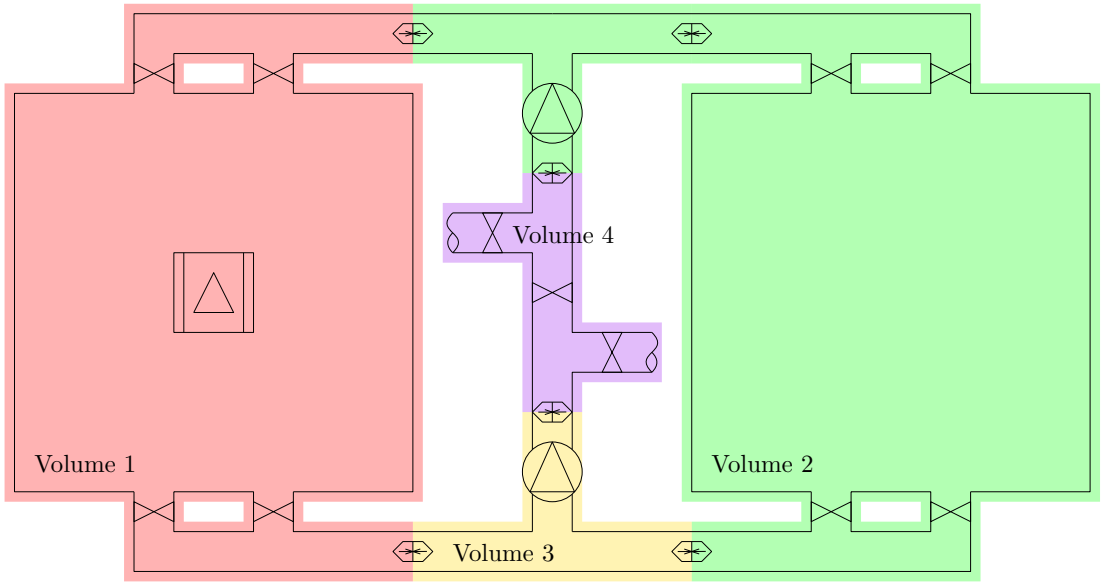

Figure 7.1: Available control volumes for mass conservation analysis. Volume 2 is expanded due to the discounting of u_5 data.

Therefore, it is important to estimate the leakage from and to the experimental apparatus and comment on its variability to illuminate potential gaps in the current understanding; hence fulfilling aim two of the experimental apparatus.

7.5.2 Description of estimation of leakage and characterisation of over/underpressure

Mass conservation analysis can be carried out based upon the available mass flow rate estimations. Mass conservation analysis can be used to estimate the leakage into and out of a number of volumes of the experimental apparatus. Unfortunately the compromise of u_5 data means that the ability to carry out mass conservation analysis is reduced. A diagram of the available control volumes is presented in Figure 7.1. Flow into the control volume is taken as a positive value.

Estimation of leakages can further be used to qualitatively characterise over/underpressure and leakage area within the control volumes. The leakage mass flow rate is related to the pressure, the leakage area, the gas density, and an empirically derived flow coefficient. The flow coefficient represents inefficiency due to friction losses and boundary layer effects in the flow paths connecting the internal enclosure and ambient. Given the dataset captured from the experiments (which does not include measurement of static pressures nor leakage area) it is impossible to separate the over/underpressure, the leakage area, the spatially variable gas density, and the flow coefficient. To make the exercise even less tractable, these four quantities vary through the duration of the experiment and within space. The pressure will vary due to the fans, the induced velocity fields, and the variable density. The leakage area will vary due to thermal expansion of the linings of the experimental set up. The gas density varies through time as the gas gains enthalpy and in space. The flow coefficient will change as the size, number, and arrangement of leakage paths varies. Therefore, only qualitative indicative discussion can be presented based upon the available data.

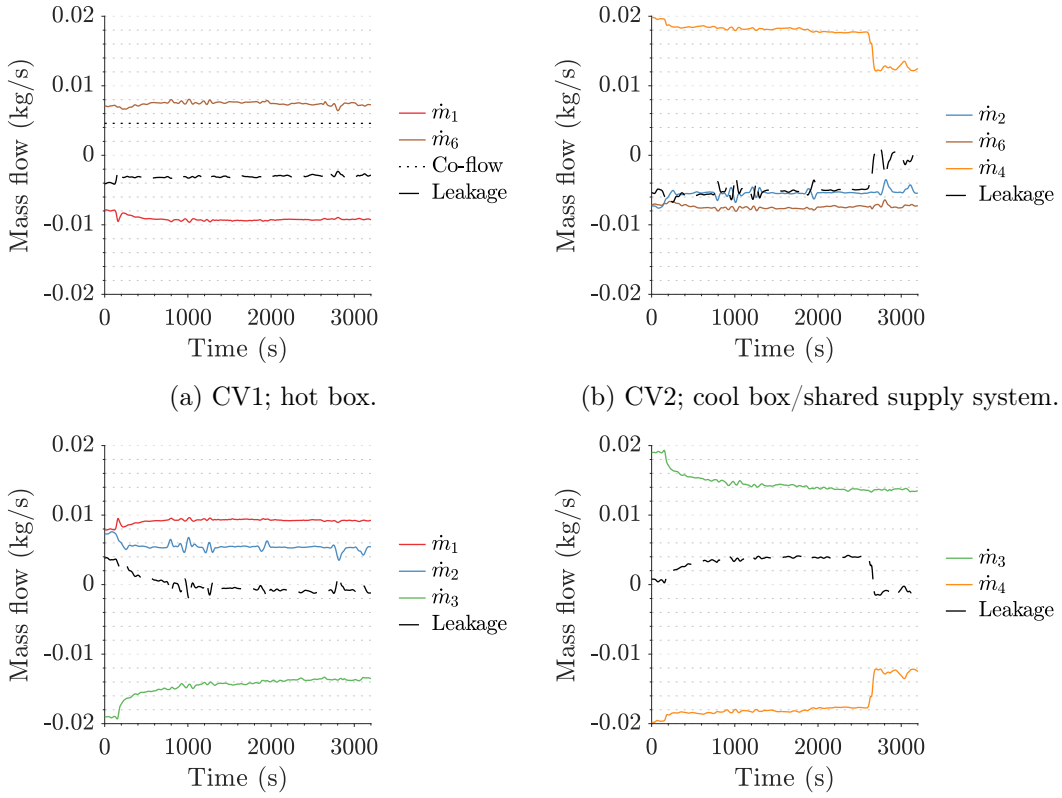

(a) CV1; hot box.

(b) CV2; cool box/shared supply system.

(c) CV3; shared exhaust system.

(d) CV4; smoke-spill, return and fresh air.

Figure 7.2: Mass conservation analysis for `P30_F2_1`. Flow into control volume is defined positive.

7.5.3 Time-dependent leakage for a specific experiment

As an example of a mass conservation analysis for `P30_F2_1` is presented in Figure 7.2.

Figure 7.2a presents the estimation of leakage for the hot box. The figure demonstrates that there is an estimated leakage out of the hot box and it is expected to be in overpressure. The leakage is broadly constant throughout both the recycle and spill mode of the experiment. This indicates that, although the joints of the vermiculite boxes were heard to crack during experiments, leakage remained approximately constant irrespective of temperature.

Figure 7.2b presents the estimation of leakage from the cool box and the shared supply system. It is unfortunate that, due to the compromise of u_5, the leakage from the cool box only cannot be estimated. The figure demonstrates that there is reasonably high leakage out of the subject volume and it is expected to be in overpressure. The leakage magnitude is approximately equal to that of mass flow into the hot box via the supply duct and out of the cool box via the exhaust duct. It is impossible to state whether this leakage is occurring within the shared supply ventilation system or the cool box. Upon spill mode being operated the leakage decreases. This is due to the reduction of overpressure within the control volume. In recycle mode, the inflow boundary condition of the control volume is above ambient pressure due to the pressure increase from the upstream exhaust fan. Upon spill mode the inflow boundary condition is no longer directly connected to the exhaust fan and instead is only a short duct section removed from ambient pressure conditions at the fresh air supply inlet. Therefore, the

pressure distribution within this control volume is expected to experience a global drop.

Figure 7.2c presents the estimated leakage from the shared exhaust system. The figure demonstrates that there is leakage into the shared exhaust system during the initial stages of the experiment. This indicates that the shared exhaust system is initially in overall underpressure. During the course of the experiment the leakage into the exhaust system steadily decreases, the mass flow out of the shared recycle system ($\dot{m}_3$) decreases, and the mass flow into the system from the cool box ($\dot{m}_2$) decreases. The overall underpressure of the control volume decreases during the experiment.

Figure 7.2d presents the estimated leakage for the shared recycle, smoke-spill, and fresh air ventilation system. Initially the control volume has approximately zero net leakage and is expected to be at approximately ambient pressure. As the experiment continues, the leakage into the control volume increases and the volume experiences underpressure. The underpressure may be caused in part by the cooling of hot gases flowing from the shared exhaust duct. Upon spill mode being operated the leakage drops substantially as the flow into and out of the experimental apparatus via the open fresh air supply inlet and smoke-spill outlet are approximately equal.

7.5.4 Comparison of leakage estimation and over/underpressure characterisation across the experimental campaign

The leakage mass flow rate into and out of the four control volumes of the experiment has been estimated using the previously described method for the entire experimental dataset. The experiments demonstrate time-dependent mechanisms and therefore the leakage analysis is carried out for three stages of the experimental procedure: (1) pre-ignition recycle mode, (2) post-ignition recycle mode, and (3) post-ignition spill mode.

The qualitative pressure distribution within the experimental set up at stages 1 and 3 are described in Figures 7.3 and 7.4. These figures can be used to illustrate not only the overall likely over or underpressure within the control volumes but also the potential distributions of pressure along the flow path. The schematics greatly simplify the arrangement and present the hot box and the cool box simply as ducts.

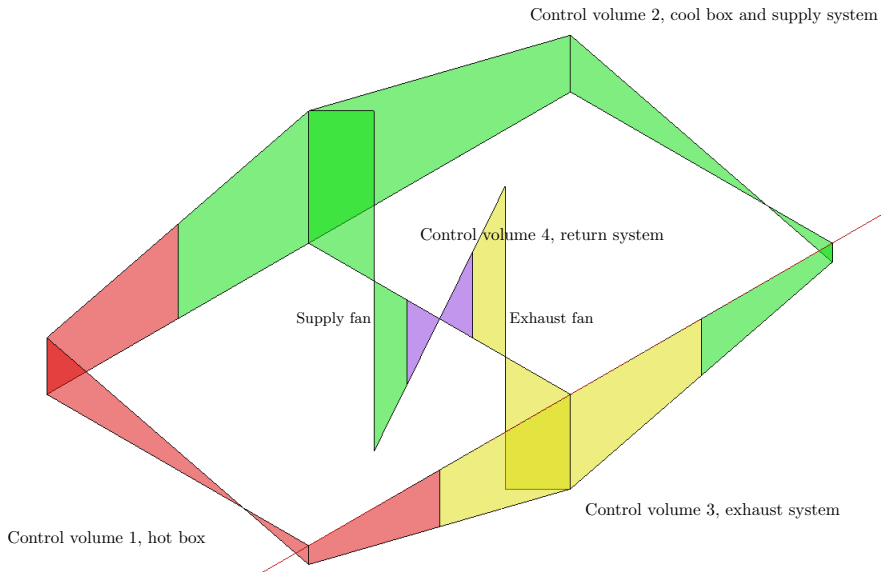

Figure 7.3: Schematic of qualitative pressure distribution at stage 1. Control volumes are described and coloured. Boxes are simplified as ducts. The schematic helps describe how a single control volume, although in net over or underpressure, will have a distribution of over or underpressure and leakage in and out of the volume.

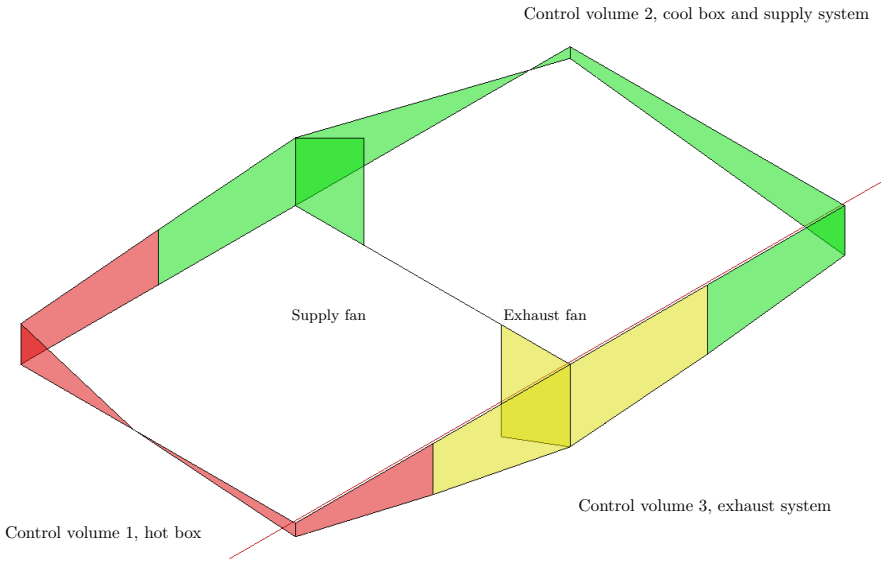

Figure 7.4: Schematic of qualitative pressure distribution at stage 3. Control volumes are described and coloured. Boxes are simplified as ducts. The schematic illustrates how, in spill mode, the fans are either supplying from ambient or discharging to ambient (fan pressure magnitudes for illustration only) and how this alteration may re-distribute pressure.

Control volume one, hot box

In stage 1, presented in Figure 7.5a, across all experiments (i.e. all propane flow rates and potentiometer settings), leakage is estimated to be out of the control volume 1. It follows that control volume 1 is likely in net overpressure during stage 1 for all experiments. As expected, there is little correlation between propane flow rate and leakage in stage 1 - as the propane has not been ignited yet. However, there is some variation witnessed and this is, at least in part, due to the differing air co-flow being provided into the control volume (which was started pre-ignition in stage 1). There is a correlation between potentiometer setting and leakage. In all cases the lowest potentiometer setting (`F1`) has the lowest leakage out of the control volume and the highest potentiometer setting (`F3`) has the highest leakage out of the control volume. This is most likely due to the increased pressure provided by the faster spinning fans and the resultant increase in net overpressure in the experimental enclosures, including control volume 1. The second (coupled) phenomenon could be the increase in leakage area due to the aforementioned overpressure.

In stage 2, presented in Figure 7.5b, there is a global shift of all data towards less leakage mass flow out of, and in three cases, leakage mass flow into the control volume. There continues to be no strong relationship between propane flow and leakage rate and a strong relationship between potentiometer setting and leakage mass flow rate. This indicates that the leakage mass flow rate within control volume 1 is not overly sensitive to propane flow rate within the studied range; although it is sensitive to the presence of combustion (witnessed by the global upwards shift on the plot). Three of the `F1` cases are now experiencing net leakage into control volume 1. This indicates that the control volume, at lower potentiometer settings and higher nominal ϕ_P values, is experiencing overall underpressure by the end of the smoke spill (stage 2). This net leakage mass flow into the volume may be due to the lower entrainment flow at low level provided by the slower spinning supply fans and hence the increase in leakage entrainment flow below the neutral plane of the volume.

In stage 3, presented in Figure 7.5c, there is no consistent global shift witnessed across all potentiometer settings as there was for stage 2. `F1` cases present a shift towards increased leakage into the control volume. This may be due to the reduced inflow from the supply outlet, as the supply fan is no longer working in series with the exhaust fan and therefore has moved to the left of its characteristic fan curve (i.e. reduced pressure increase and flow rate). `F2` cases present either no shift or a minor shift towards less leakage out of the control volume (in case `P40_F2` leakage changes to into the control volume). Conversely `F3` cases, those with the highest potentiometer setting, present a further increase in leakage out of the control volume; indicating an increased overpressure and/or leakage area.

Control volume two, cool box and supply system

In stage 1, presented in Figure 7.6a, all computed net leakage mass flows are out of control volume 2. This indicates that this volume is in net overpressure. This is intuitive as this volume contains the supply fan near to the upstream of the control volume. Therefore, the majority of the control volume is downstream from the pressure increase from the fan. There is no clear correlation between either propane flow rate, nor potentiometer setting, and estimated leakage mass flow rate.

In stage 2, presented in Figure 7.6b, the net leakage mass flow continues to be out of the control volume for all experimental cases. There continues to be no clear correlation

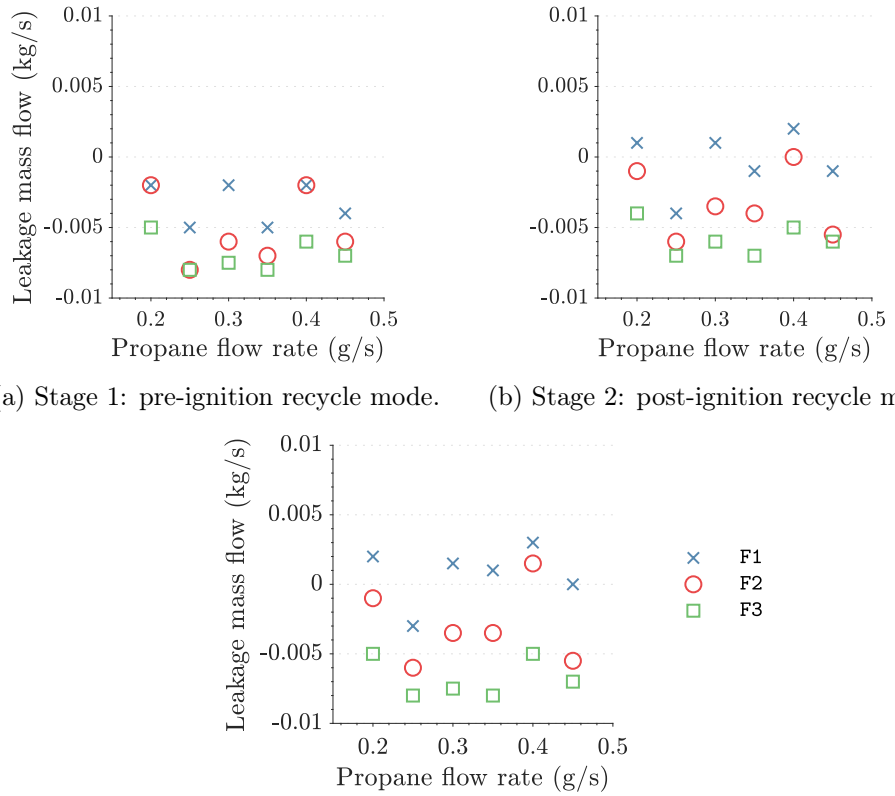

(a) Stage 1: pre-ignition recycle mode.

(b) Stage 2: post-ignition recycle mode.

(c) Stage 3: post-ignition spill mode.

Figure 7.5: Leakage estimation for control volume 1 (hot box). The plots illustrate the dependence of leakage upon potentiometer setting; with `F1` cases (higher nominal ϕ_P value) presenting the most tendency for leakage into the volume and `F3` (lower nominal ϕ_P value) presenting the most tendency for leakage out of the volume.

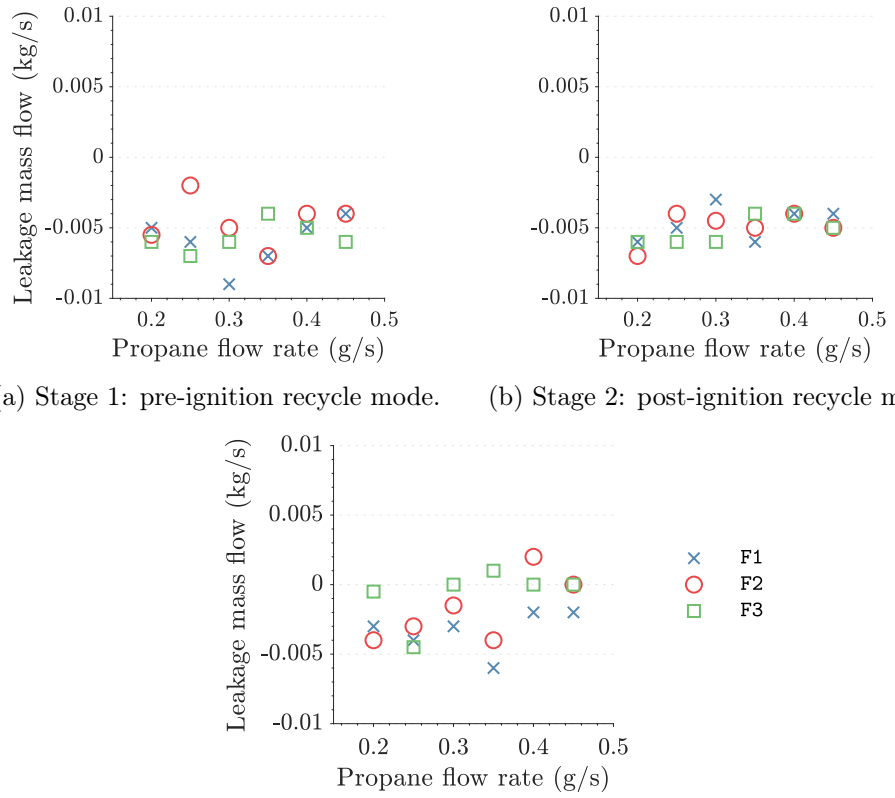

(a) Stage 1: pre-ignition recycle mode.

(b) Stage 2: post-ignition recycle mode.

(c) Stage 3: post-ignition spill mode.

Figure 7.6: Leakage estimation for control volume 2 (cool box and supply system). The plots illustrate no strong correlation between leakage mass flow rate and either propane flow rate or potentiometer setting - with the exception of a slight correlation with potentiometer setting at stage 3.

between either propane flow rate, no potentiometer setting, and estimated leakage mass flow rate.

In stage 3, presented in Figure 7.6c, all leakage mass flows out of the volume decrease (in cases `P35_F3` and `P40_F2` the leakage changes to mass flow into the volume). This global shift indicates a reduction in net overpressure and/or a decrease in leakage area. This is intuitive as the supply fan is no longer working in series with the exhaust fan and therefore would be expected to move left on its characteristic fan curve (to a lower pressure increase). There is the general trend for `F3` cases to present a larger decrease in leakage out of the volume when compared to the other fan cases, indicating the drop in effective total fan pressure from series fans to individual fans may be greater than the other fan cases.

Control volume three, exhaust system

In stage 1, presented in Figure 7.7a, all experiments present control volume 3 in net leakage out. This is intuitive as the exhaust fan within the volume is at the downstream end of the flow path. The portion of the volume upstream of the fan is most likely all in underpressure and therefore experiencing leakage mass flow into the volume. There is likely a volume of overpressure downstream from the exhaust fan; however the limited extent of this volume means that the volume is in net underpressure and experiences a net leakage mass flow into the volume.

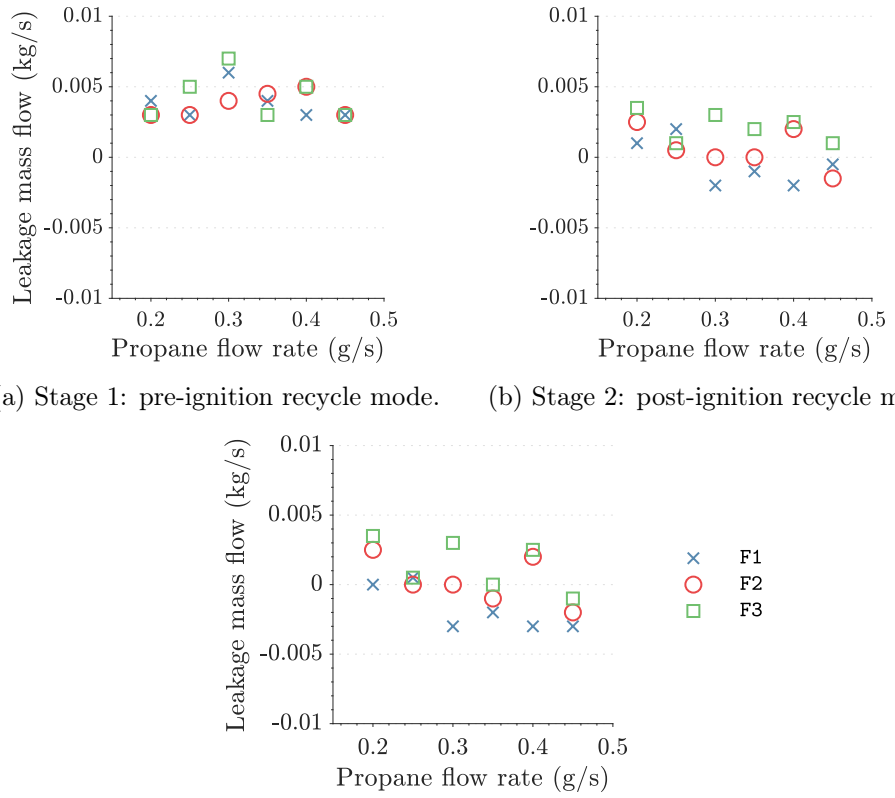

(a) Stage 1: pre-ignition recycle mode.

(b) Stage 2: post-ignition recycle mode.

(c) Stage 3: post-ignition spill mode.

Figure 7.7: Leakage estimation for control volume 3 (exhaust system). The plots illustrate the initial net flow into the volume due to the downstream exhaust fan. This net flow is reduced as the nominal ϕ_P value increases, and in the case of lower potentiometer settings reversed, at higher propane flow rates. This illustrates the dominance of upstream fire-induced pressure over fan pressure and becomes more apparent at higher propane flow rates and in stage 3.

In stage 2, presented in Figure 7.7b, all experiments exhibit a reduction in net leakage into the volume. In five cases (four of which are `F1` cases) the leakage mass flow has reversed to be out of the volume, indicating that the volume has experienced a global increase in pressure. This increase, and the affiliated decrease or reversal of leakage flow, is presented more so in the lowest potentiometer setting. This indicates that the fire-induced pressure has more dominance over leakages than fan pressure increase at these lower fan speeds. This is in agreement with the witnessed increasing leakage out of the volume at higher propane flow rates for `F1` cases.

In stage 3, presented in Figure 7.7c, the majority of cases move further down the plot, exhibiting less leakage into the volume and in some cases reversal of leakage from into to out of the volume. As the exhaust fan moves from recycle mode to spill mode the discharge pressure changes from the downstream internal pressure to ambient pressure. Figure 7.6c illustrates that the downstream control volume is in net leakage into the volume and therefore likely in underpressure. The exhaust fan discharge pressure therefore increases from an underpressure to ambient and correspondingly the upstream pressure distribution moves upwards also. This has the effect of moving the control volume towards overall underpressure and net leakage flow into the volume.

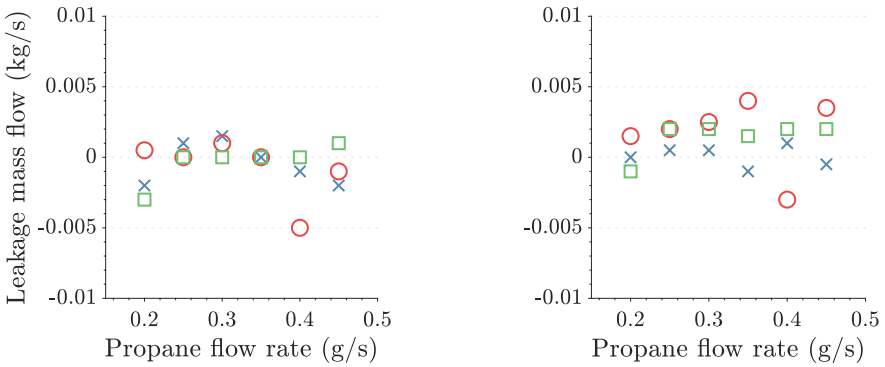

(a) Stage 1: pre-ignition recycle mode.

(b) Stage 2: post-ignition recycle mode.

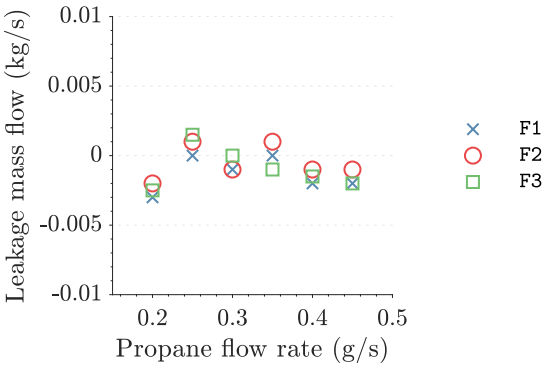

(c) Stage 3: post-ignition spill mode.

Figure 7.8: Leakage estimation for control volume 4 (recycle, supply, and spill system). The plots indicate a correlation between increasing net leakage into the volume with increasing propane flow rate during stage 2 but, conversely, a correlation between increasing net leakage out of the volume with increasing propane flow rate during stage 3.

Control volume four, recycle, supply, and spill system

In stage 1, presented in Figure 7.8a, the majority of cases across the experimental matrix present minimal net leakage into or out of the volume. This is expected as control volume 4 is located just downstream from the exhaust fan and just upstream from the supply fan. Therefore, it is expected that there is a cross over of under and overpressure within the volume. This would lead to an overall equal pressure and a minimal net leakage.

In stage 2, presented in Figure 7.8b, there is a global shift of the data from the higher two potentiometer settings towards a net leakage into the volume, indicating that this volume is in overall underpressure. Conversely, for the lowest potentiometer setting there is a shift towards net zero leakage into or out of the volume. There appears to be a weak positive correlation between net leakage into the volume and increasing propane flow rate.

In stage 3, presented in Figure 7.8c, there is a global shift down the plot towards lower net leakages into the volume and a reversal to net leakage out of the volume. There appears to be less of a correlation between net leakage flow and potentiometer setting when compared to stage 2. Contrasting with stage 2, there appears to be a weak correlation between increasing propane flow rate and increasing leakage into the volume. This indicates that at higher propane flow rates there is likely to be overpressure in the control volume.

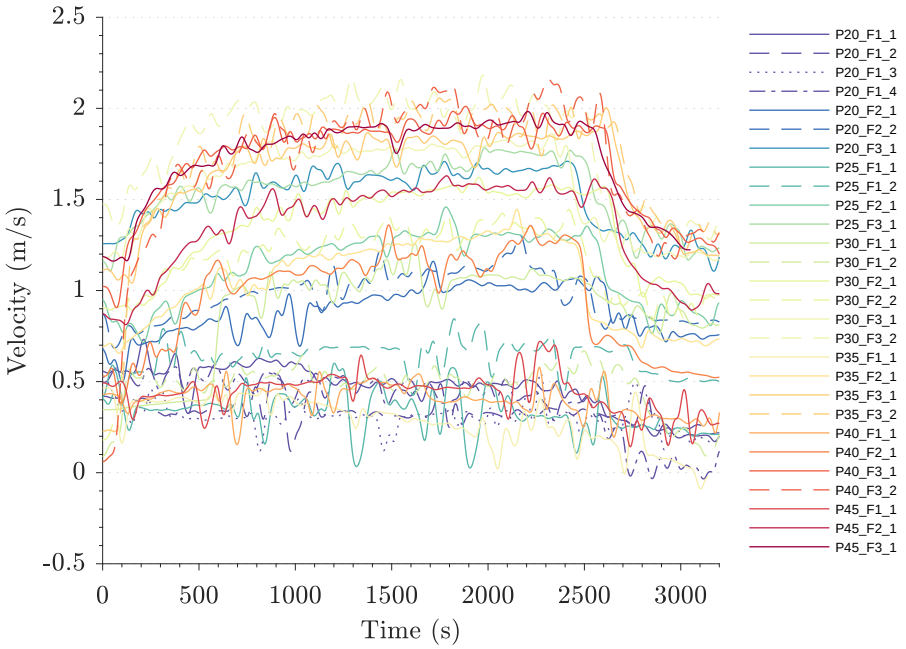

Figure 7.9: All u_6 vectors for all experiments within the campaign. The individual case data is difficult to read; but what is illustrated is that very few cases present a u_6 vector becoming negative.

7.6 Analysis of the supply ventilation system performance

7.6.1 Flow against the supply system

One part of aim two of the experimental apparatus was to investigate the potential for fire-induced pressure and flow to overcome the supply system to a fire enclosure. To quickly answer the question of whether this occurred, all u_6 data for all experiments and repeats are presented in Figure 7.9.

Obviously these data are impossible to assimilate in anything other than the broadest terms. The broadest terms do however include the conclusion that (for the range of propane flow rates and potentiometer levels covered by the experimental campaign) flow did not occur against the direction of the hot box supply system. This certainly does not mean that fire-induced flow against a supply system never occurs. Only that for the specific experimental arrangement and for the range of subject experimental campaign, this phenomenon did not occur. However, trends and tendencies can be drawn out of the available data. It is certainly more valuable to look for patterns, than simply answering 'no' and moving on.

7.6.2 Effect of potentiometer setting

To more clearly analyse the tendencies of compromise of the supply system due to the variation of fan power a set of plots is presented in Figure 7.10 for each potentiometer setting. Each plot represents u_6 data for a single propane flow rate for differing fan potentiometer settings. In this way the effect of differing fan powers can be highlighted across each fire power.

Figure 7.10a gives u_6 data for `P20` cases and shows a clear trend of increasing u_6 magnitude for increasing fan setting. As expected at higher fan settings the magnitude

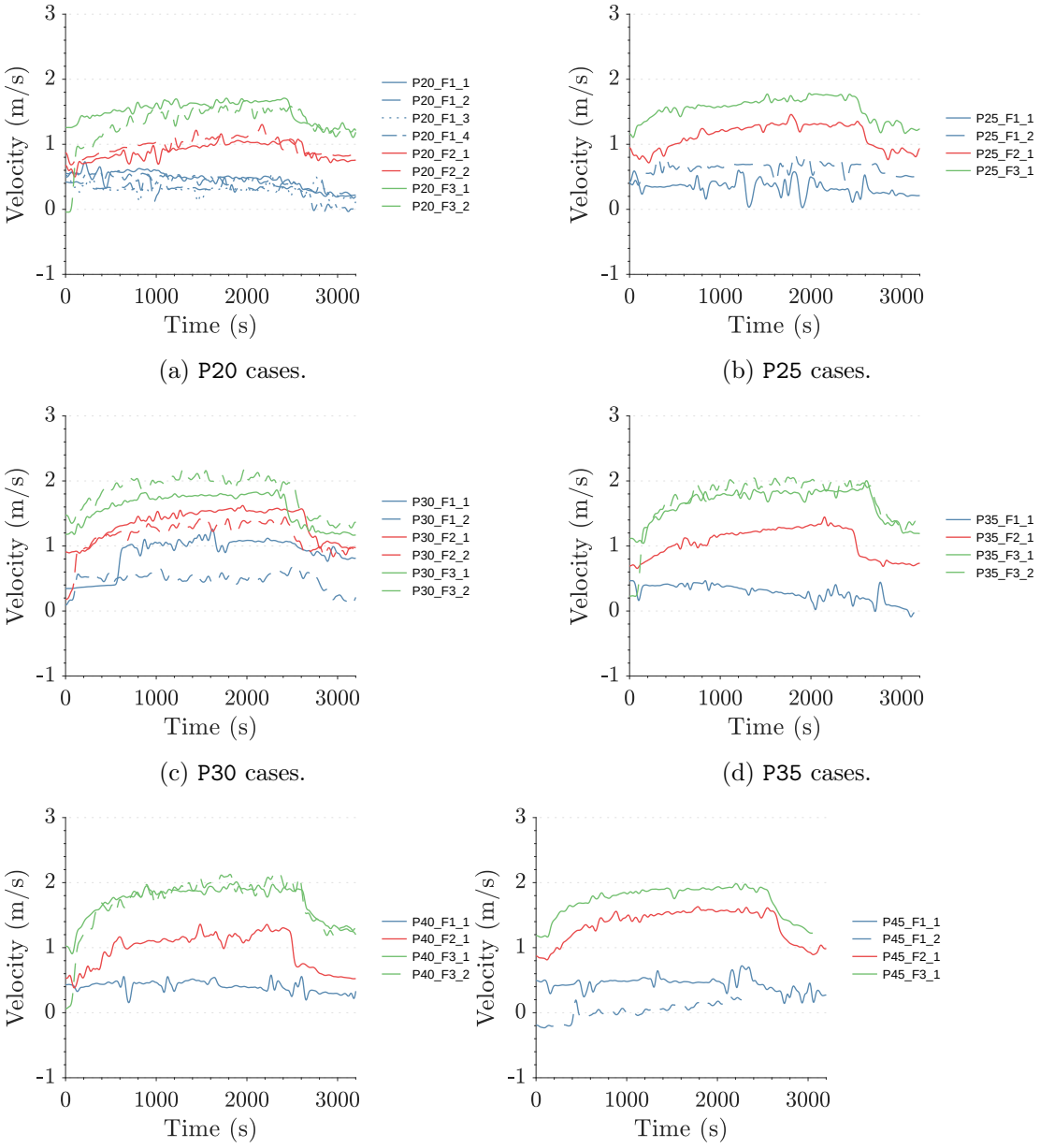

(a) P20 cases.

(b) P25 cases.

(c) P30 cases.

(d) P35 cases.

(e) P40 cases.

(f) P45 cases.

Figure 7.10: All u_6 vectors. There is some tendency for a steadily decreasing velocity in F1 cases. In all cases u_6 drops upon spill mode.

of u_6 is higher. What is interesting is that there is a greater decrease in u_6 magnitude upon spill mode for the higher fan setting. The conclusion of this is that for fire safety designs with a greater fan duty there may be more potential for fire and smoke spread against the direction of the supply side ventilation system during fresh air mode.

Another interesting phenomenon is the transient tendencies of the u_6 data through the experiments. At higher fan settings there is a positive tendency of u_6 magnitude. That is, as the boxes are heating up, the supply duct velocity into the hot box is increasing. The converse is seen for the lower fan setting of `F1`. In this case there is a negative trend through the experiment. The magnitude of u_6 is steadily decreasing as the experimental apparatus gains energy and heats up (both gas phase and condensed phase). The real world implication of this finding is that for fire safety designs incorporating lower fan duties, when exposed to smaller fires, there may be a steady compromise of the mechanical supply ventilation system as the fire event progresses.

Figure 7.10b shows the same expected trend, of increasing u_6 magnitude with increasing fan setting, for `P25` cases. Similarly to `P20` cases there is a greater reduction in u_6 upon spill mode for the higher fan settings. Interestingly, one could expect that the phenomenon of decreasing u_6 during the course of the experiment for the lower fan setting would be more pronounced at a higher fire power; however this is not the case.

Figure 7.10c presents the u_6 data for `P30` cases and illustrates a differing arrangement when compared to `P20` and `P25` cases. First looking at the higher two fan settings, `F2` and `F3`; the difference in the magnitude of u_6 is less pronounced than when compared to `P20` and `P25` cases. This reduction in difference becomes more conspicuous after spill mode when the u_6 magnitudes almost converge. The u_6 data for `F1` are less clear due to a relatively large difference between the two repeats. Therefore, it is difficult to make statements about the lower fan setting.

Figure 7.10d shows the expected increasing magnitude of u_6 for increasing fan setting, similarly to previous propane flow rates. The plot illustrates a clear reduction in the magnitude of u_6 for the `F1` case. This is as expected, but not as witnessed when increasing propane flow rate from `P20` to `P25`. The convergence of `F2` and `F3` cases seen in Figure 7.10c for `P30` cases is not seen at this higher propane flow rate. The plot also shows that there is no marked difference in the negative gradient of `F1` case data following spill mode; this is in contrast to the behaviour seen in lower propane flow rates.

Figure 7.10e shows the expected increasing u_6 magnitude for increasing fan setting; similarly to lower propane flow rates. The transient reduction in the `F1` case is witnessed, similarly to other higher propane flow rates and in contrast to lower propane flow rates.

The real world implication of this is that there may be a trend for the compromising of the supply system mechanical ventilation for larger fires. This compromise appears to increase following spill mode. This means that, in a real fire safety design, fire and smoke spread may not be occurring against the supply side ventilation system initially. But when the mechanical ventilation system changes to smoke-spill mode there is an increased risk of fire and smoke spread against the supply side system. This is a risk as this operational change often happens automatically upon double-knock (i.e. operation of two detectors) smoke detection.

The magnitude of u_6 for the highest propane flow, `P45` cases, is presented in Figure 7.10f. The familiar and expected trend of increasing u_6 magnitude with increasing fan setting is witnessed, as well as decreasing u_6 magnitude for higher fan settings upon spill mode.

7.6.3 Summary and discussion

The previous figures demonstrate that, as expected, there is a clear positive increase in u_6 magnitude with increasing fan setting across all propane flow rates. For the subject experimental matrix, no flow against the supply system was seen from the hot box.

The data illustrate that there is a much greater reduction in supply duct velocity upon spill mode for high fan duties. The real world implication of this is that for designs that incorporate a high fan duty (for example, large malls or airports) there may be an increased likelihood of the fire overcoming the pressure increase from the fans upon operation of smoke-spill and fresh air mode of the mechanical ventilation system. This is important to consider as the operation of smoke-spill mode is typically automatic. Therefore, the building may be experiencing no smoke spread against the supply side ventilation system during normal recycle mode but, upon automatic triggering of smoke-spill mode, fire and smoke spread via the supply system may suddenly become more likely. This would be difficult for building management, the fire brigade, or emergency response team to manage - as the areas to which smoke spread was occurring may change rapidly during an emergency.

There is also important transient behaviour witnessed for low fan setting cases. Based upon the data there is a tendency for the effective supply rate to decrease during the progression of a fire event for low fan duty cases. This is most likely because the gas and condensed phase are gaining energy and increasing in temperature - increasing the pressure within the hot box. The real world implications of this phenomenon is that, although initially having sufficient performance, make up air systems forming part of a mechanical smoke exhaust system may drop below target performance levels during a fire. This reduction in performance of mechanical make up air would have a consequential effect on the mechanical or natural exhaust system. Therefore, there would be an increased likelihood that the build up of smoke within an enclosure would be greater than that accounted for in the original fire safety design. This would have a negative impact upon any fire engineering solutions; for example, a reduction of passive fire protection to elements of structure (whereby the structure would be exposed to unexpectedly high temperature smoke).

7.7 Maximum temperature data

7.7.1 Importance of maximum temperatures

Maximum temperatures (more technically 'l_∞-norms of temperature vectors') are of interest for fire life safety, property protection, and fire risk assessments [216]. Maximum temperatures can be used to quantify risk to occupants [186], likelihood of component failure, and structural failure [217]. The examination of maximum likely temperatures is a key part of the ongoing international risk management of nuclear facilities [218].

It is crucial that the accuracy and validity of typical simplified models are checked for elements of the built environment that incorporate shared ventilation systems. This forms part of aim two of the experimental apparatus. If there are systematic differences between the likely maximum temperatures within a fire compartment, or a connected non-fire compartment, and the output of a widely used engineering method, there is the possibility of either inefficient engineered solutions or arrangements with unacceptably low levels of life and structural safety. Objective two of this thesis and aim two of the experimental apparatus incorporate the illumination of trends between risk and differing nominal ϕ_P values that may not be effectively captured by current analysis methods.

For this reason, the following subsections investigate the roles of the independent variables on the l_∞-norms of the temperature vectors measured in the experiments. The l_∞-norms of the temperature vectors are output as given in Equation 7.2.

$$\|\boldsymbol{T}\|_\infty = \max_t |T_t| \tag{7.2}$$

where $\boldsymbol{T}$ is the temperature vector, t is the time index of the experiment and T are the vector values.

7.7.2 In the boxes

Relating temperatures to the independent variables

The l_∞-norm is calculated for each individual experiment for both the hot box and the cool box. These data are then plotted against the propane flow rate and fan potentiometer level. A curve is fit to the data using a nonlinear least squares method. Based upon the McCaffrey, Quintiere and Harkleroad (MQH) correlation [186] it is assumed that the maximum steady state temperature within the box is in the form given in Equation 7.3.

$$\|\boldsymbol{T}\|_\infty = C\dot{m}_p^{2/3} + T_\infty \tag{7.3}$$

where $\|\boldsymbol{T}\|_\infty$ is the l_∞-norm of all temperature vectors in the box, C is a coefficient that incorporates thermophysical properties, geometric parameters, and characteristics of the ventilation, $\dot{m}_p$ is the propane release rate, and T_∞ is the ambient temperature (don't confuse those ∞s!)

It is recognised that the plume equation on which the MQH correlation is based breaks down within the structure of the flame [186]. For this reason, within the hot box, two datasets are analysed. One is the l_∞-norm of all temperature vectors and the second is the l_∞-norm of all temperature vectors except the central thermocouple tree. For each analysis case, a curve is fit to the three potentiometer level sub-datasets. The output of the analysis is presented in Figures 7.11 through 7.13.

The curve fits show reasonable solutions for Equation 7.3. R-square values are good, generally being above 0.8, though there is one notable exception of 0.212. This exception is due to the high spread of data between repeats. If the outliers are ignored, the R-square value increases to 0.851. Correlated ambient temperatures are in the range 15 °C to 25.4 °C.

The analyses for both boxes show a clear positive trend between propane flow rate and l_∞-norms of box temperatures as expected.

There is an increase in l_∞-norms of box temperature for the increasing fan levels within the cool box. This is reflected in the variable value of C. This relationship is not witnessed as strongly within the hot box, especially outside of the plume (Figure 7.12). This is because the relative effect of the mechanical ventilation system is greater for the cool box compared to the hot box. This is reflected in relatively constant values of C within the hot box analysis cases; being between 1515 to 1615 for the total hot box and 842 to 884.5 for the non-plume hot box.

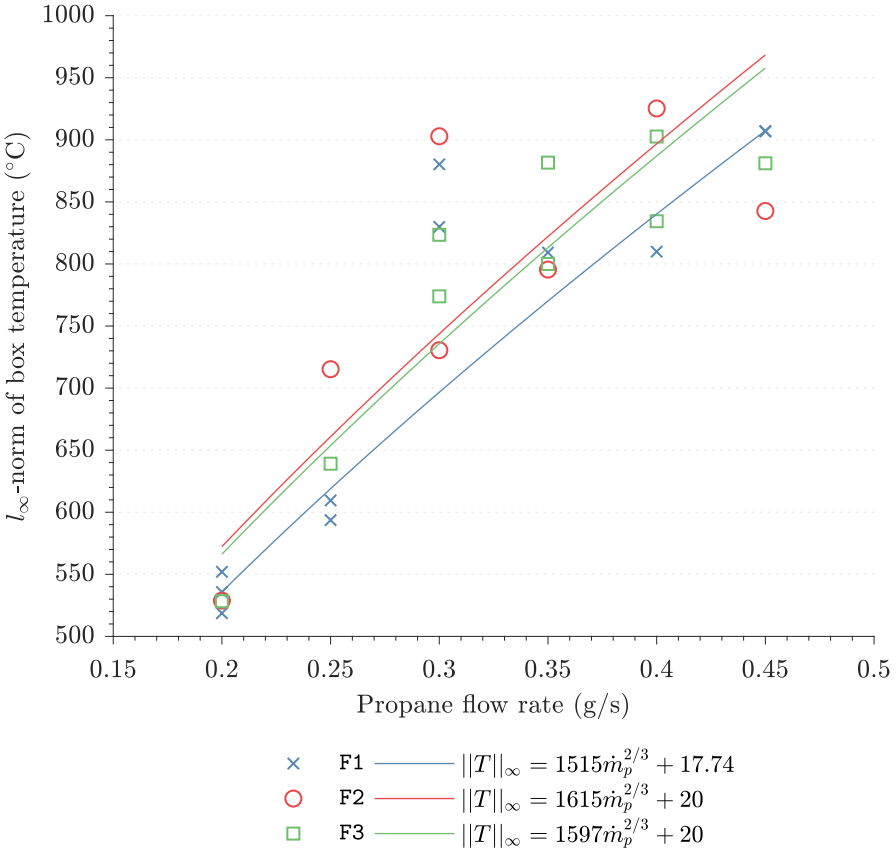

Figure 7.11: l_∞-norm of hot box temperatures. R-squares are 0.950, 0.567 and 0.802 for `F1`, `F2` and `F3` fits respectively.

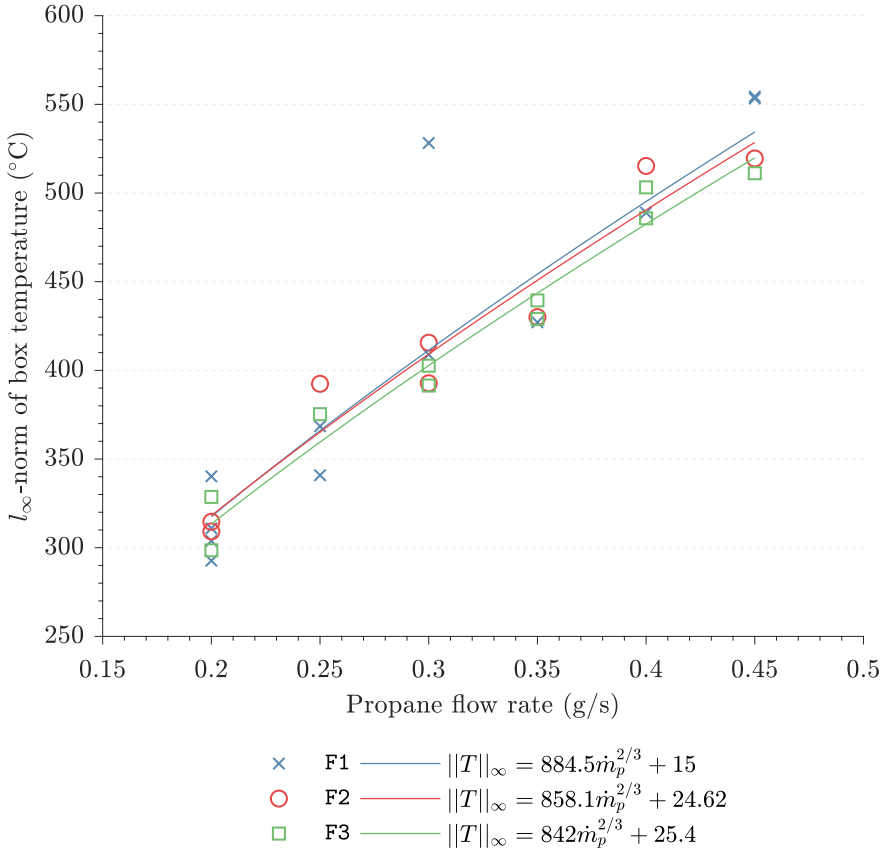

Figure 7.12: l_∞-norm of hot box temperatures, excluding the central thermocouple tree. R-squares are 0.851, 0.948 and 0.966 for `F1`, `F2` and `F3` fits respectively.

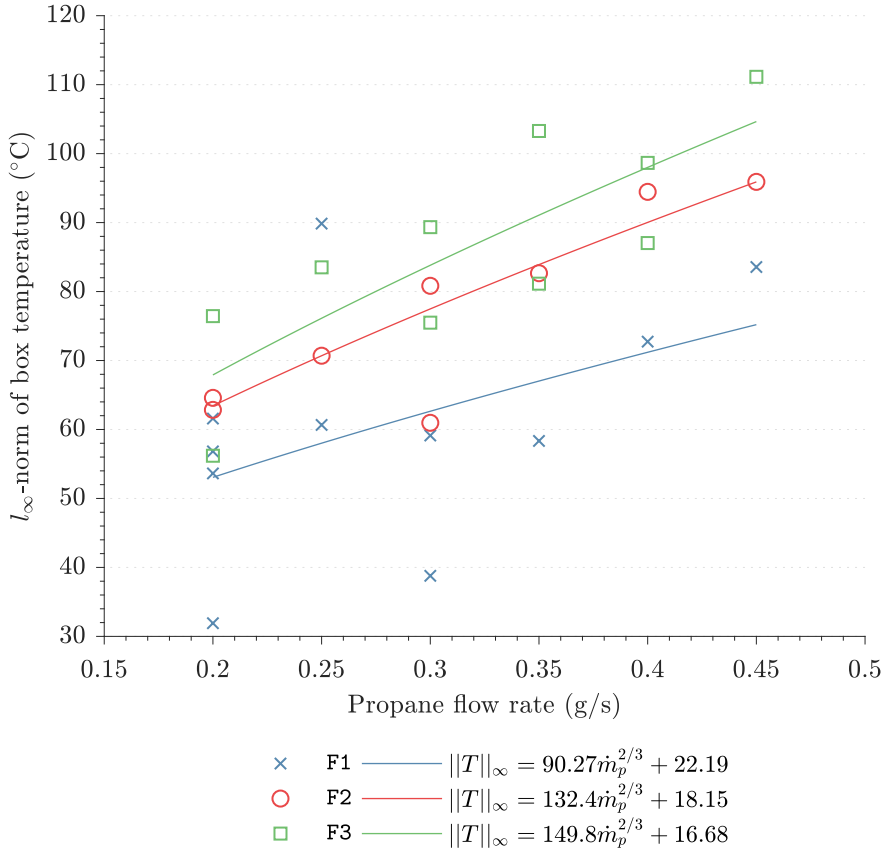

Figure 7.13: l_∞-norm of cool box temperatures. R-squares are 0.212, 0.928 and 0.651 for `F1`, `F2` and `F3` fits respectively.

Applicability of existing empirical methods

It is interesting and useful to delve further into the C of Equation 7.3. What does this parameter consist of? Can the relationship be used to make useful engineering assessment and judgements? Does the MQH correlation hold up to a case with closed enclosures and forced recycling ventilation?

This is critical to the fulfilment of aim two of the experimental apparatus; to illuminate limitations of currently widely used methods and guidance to illuminate potential unaddressed risks.

To answer these questions, the derivation of the familiar MQH correlation is examined. The MQH correlation is based upon an approximate energy balance between a hot gas layer and a cooler layer (Equation 7.4), complemented by a heat loss approximation (Equation 7.5).

$$\dot{Q} = \dot{m}_{gas} c_p (T - T_\infty) + \dot{q}_{loss} \tag{7.4}$$

$$\dot{q}_{loss} = h_k A_w (T - T_\infty) \tag{7.5}$$

$$\frac{T - T_\infty}{T_\infty} = \frac{\dot{Q}/(c_p T_\infty \dot{m}_{gas})}{1 + h_k A_w/(c_p \dot{m}_{gas})} \tag{7.6}$$

where $\dot{Q}$ is the heat release rate, $\dot{m}_{gas}$ is the gas flow rate out of the enclosure, h_k is the effective heat transfer coefficient, and A_w is the effective surface area. Combining these energy balance equations forms Equation 7.6. The original work went on to substitute an approximation for the gas flow rate based on naturally venting openings. This substitution is not appropriate for the experimental apparatus, which is based upon sealed enclosures with recycling mechanical ventilation. Instead, the gas flow out of the enclosure is temporarily maintained and the equation represented as Equation 7.7. Bearing in mind heat release rate has been substituted for propane mass flow rate via $\dot{Q} = \Delta H_c^\circ \dot{m}_p$.

$$\frac{\|\boldsymbol{T}\|_\infty - T_\infty}{T_\infty} = C_T \left(\frac{\dot{Q}}{c_p T_\infty \dot{m}_{gas}} \right)^N \left(\frac{h_k A_w}{c_p \dot{m}_{gas}} \right)^M \tag{7.7}$$

where C_T, N and M are unknown parameters. The original MQH correlation concluded that for enclosure fires venting via openings, values of C_T, N and M could be taken as 480, 2/3 and $-5/3$. C_T is recognised as being arrangement-specific. Effectively the analysis carried out in the previous paragraphs, following Equation 7.3, adopted these values of N explicitly and M implicitly. If Equation 7.7 and 7.3 are combined and solved for C, Equation 7.8 is output.

$$C = \frac{C_T T_\infty^{1/3} \Delta H_c^{\circ 2/3}}{(A_w c_p h_k \dot{m}_{gas})^{1/3}} \tag{7.8}$$

If it is assumed that gas flow out of the enclosure is related to the fan flow rate, then it is evident why the values of C were different for differing fan cases. For the subject work, instead of parameters related to natural convection (g, ρ_∞, A and H) appearing in the denominators, for this analysis there should be a parameter related to forced convection: the mechanical mass flow rate $\dot{m}_f$. The modified MQH correlation appears as given in Equation 7.9.

$$\frac{\|\boldsymbol{T}\|_{\infty} - T_{\infty}}{T_{\infty}} = C_T \left(\frac{\dot{Q}}{c_p T_{\infty} \dot{m}_f} \right)^N \left(\frac{h_k A_w}{c_p \dot{m}_f} \right)^M \tag{7.9}$$

where C_T is a constant (now equivalent to that listed in McCaffrey et al. [186], and not C of Equation 7.3), and N and M are to be determined.

In the previous analysis, values of N and M were explicitly and implicitly (respectively) assumed to be equal to the values within the original MQH correlation; that being $N = 2/3$ and $M = -5/3$ (this value of M was implicitly buried within C). The first term is a measure of the relative importance of the energy released by the fire to the energy advected away. The second term is a measure of the energy lost to the surroundings to the energy advected away.

It is reasonable to hypothesise that the values of N and M may differ for a mechanically ventilated arrangement and/or an enclosed arrangement. Therefore, on the path towards the completion of aim two of the experimental apparatus, it is key to examine the differences (if any) between the well-used MQH model and the experimental apparatus data for closed enclosures connected with a shared ventilation system.

The difficulty with formally separating in the manner presented in Equation 7.9 is that the mass flow rate of the fan is variable with time throughout the experiment. Mass flow rate of the fan depends on the characteristic fan curve, the pressure in the upstream and downstream elements of the system (the system curve), and the temperature of the gas. Both the pressures and the temperature are, in turn, dependent itself upon the heat release rate. For the purposes of this analysis, $\dot{m}_f$ is adopted as the equilibrium cool flow mass flow rate in the shared exhaust system. A multiple linear regression is carried out on the data to estimate C_T, N and M for the experiment.

It is assumed that heat losses have reached steady state and the heat transfer coefficient can be approximated by the steady state conduction equation in Equation 7.10.

$$h_k = \frac{k}{\delta} \tag{7.10}$$

where k is the conductivity of the wall materials and δ is the wall thickness. The parameters C_T, N and M may vary for the hot box and the cool box; therefore analyses of these domains are kept separated. The founding assumptions of the MQH correlation may not be valid within the flame; therefore the hot box temperature vectors minus the central thermocouple is retained as an analysis case. Changing ventilation conditions may affect the value of C_T; therefore fan cases are maintained as sub-datasets.

To summarise, three analysis cases are carried out:

1. All temperature vectors of the hot box.
2. All temperature vectors of the hot box with the exception of the central thermocouple tree.
3. All velocity vectors of the cool box.

A three-dimensional multiple linear regression analysis has been undertaken. The dataset is not very large; therefore the 95 % confidence limits on the parameters are at times quite wide. With the exception of N, which typically has a 95 % confidence bound of approximately 0.3. The output of the analysis, along with the traditional MQH parameters, is presented in Table 7.2.

Table 7.2: Temperature rise correlation parameters.

Analysis case	C_T	N	M	R-square
Hot box, complete vector set				
F1	1330	0.669	−3.06	0.916
F2	1260	0.516	−3.14	0.628
F3	588	0.582	−3.43	0.816
Hot box, edge vector set				
F1	771	0.702	−3.12	0.849
F2	1440	0.656	−3.90	0.943
F3	530	0.559	−3.70	0.949
Cool box, full vector set				
F1	530	0.649	−3.82	0.208
F2	550	0.687	−4.48	0.887
F3	450	0.479	−4.48	0.537
MQH parameters				
F1	480	0.666	−1.67	N/A

There are insufficient data to provide concrete conclusions or propose new values of C_T, N, and M, for the case of closed enclosures connected with a shared ventilation system for the experimental apparatus. However comment can be made on the trends.

The values of C_T for all analysis cases within the experimental apparatus are all above that of the MQH coefficients. There does appear to be a trend of decreasing C_T for increasing potentiometer setting; indicating a negative correlation between this parameter and the fan duty. The values of C_T are more consistent for the cool box indicating that the variation in C_T is related to the heat or co-flow air source within the hot box.

The values of N are broadly near to the MQH coefficient value; therefore the relative importance of the energy from the fire to the energy advected away are similar. This is interesting as the modes of advection are different between the MQH case (natural) and the experimental apparatus (forced). It could be supposed that the values of N are slightly lower than the MQH values (though this is hard to definitively state based on limited data). That would mean that the importance of the energy input of the fire is slightly less dominant than the energy removed by way of the mechanical ventilation system.

The values of M for the experimental apparatus are markedly and consistently different to that of MQH. The values for the experimental apparatus have a larger negative magnitude; especially the cool box. This means that the importance of forced advection of energy away against heat losses has a stronger effect on enclosure temperature when compared to the naturally ventilated MQH arrangement.

Summary of box temperatures and impact

The analysis of maximum temperatures within the experimental apparatus has shown that existing typically-used correlations may not address hazards inherent to an arrangement comprising closed enclosures connected with a shared mechanical ventilation system. New correlation parameters have been established that may better describe the

common fire safety design arrangement of a shared plant room (for example, a hospital or office building). These correlation parameters are based upon limited data and hence their validity will need to be improved with further experiments to enable uncertainties to be reduced.

The analysis has demonstrated that the importance of the ratio of forced advection phenomena to fire energy release and also to heat losses is more dominated by the advection term when compared to the same ratios for natural ventilation. Therefore, the use of the original MQH correlation for more modern fire safety design may lead to the under-accounting of forced ventilation phenomena.

7.7.3 In the ducts

Description of analysis

The l_∞-norms of certain duct temperatures can provide valuable information on hot gases passing through the shared ventilation system. The temperature of gas passing through the ventilation ducts is directly related to the hazard embodied in fire and smoke spread via a shared ventilation system. The fulfilment of thesis objective two and aim two of the experimental apparatus requires the examination of the ability of current engineering methods to quantify this fire risk. It may be that current engineering methods do not account for phenomena related to the relative influence of the fire and a shared mechanical ventilation system.

Ducts 02, 04, 07 and 11 are chosen for analysis. These are the thermocouples installed in the hot box exhaust duct inlet, the cool box exhaust duct, the shared exhaust duct, and the cool box supply outlet.

The hot box exhaust duct inlet is chosen because it quantifies the energy of the hot gases leaving the fire enclosure. The cool box exhaust duct is used as it may illuminate phenomena related to the spread of hot gases to the cool box via the shared exhaust system. The shared exhaust duct is selected as it quantifies the energy of the hot gases that will be recycled via the shared return system. The cool box supply outlet is selected as it quantifies the energy being delivered to the non-fire enclosure via the shared ventilation system. Each duct location is examined in turn in the following paragraphs.

Nonlinear least squares regression analysis is used to output a fit for each fan sub-case within each analysis case. The fit was defined in the form $y = Cx^N$ where $y = \|\boldsymbol{T}\|_\infty$ and $x = \dot{m}_p$.

Exhaust system

The l_∞-norms of the duct 02 temperature vectors are presented in Figure 7.14. The fits are more than satisfactory and have R-squares of over 0.95. The data show a very clear positive relationship between propane flow rate and l_∞-norms of temperature. The three fits almost collapse and there appears to be minimal effect on the l_∞-norms of temperature due to the fan case. It can be concluded that the fire-induced flow and advection of energy are dominant this close to the fire source. The exponent of the function, N, is approximately between 0.64 to 0.7. This is in agreement with the values determined by McCaffery et al. and Foote et al. [123] (the latter was for a standard non-recycling mechanically ventilated single enclosure).

The l_∞-norms of the cool box exhaust duct temperature vectors, duct 04, are given in Figure 7.15. The data present differently when compared to duct 02. There remains a positive relationship between the propane flow rate and the l_∞-norm temperatures.

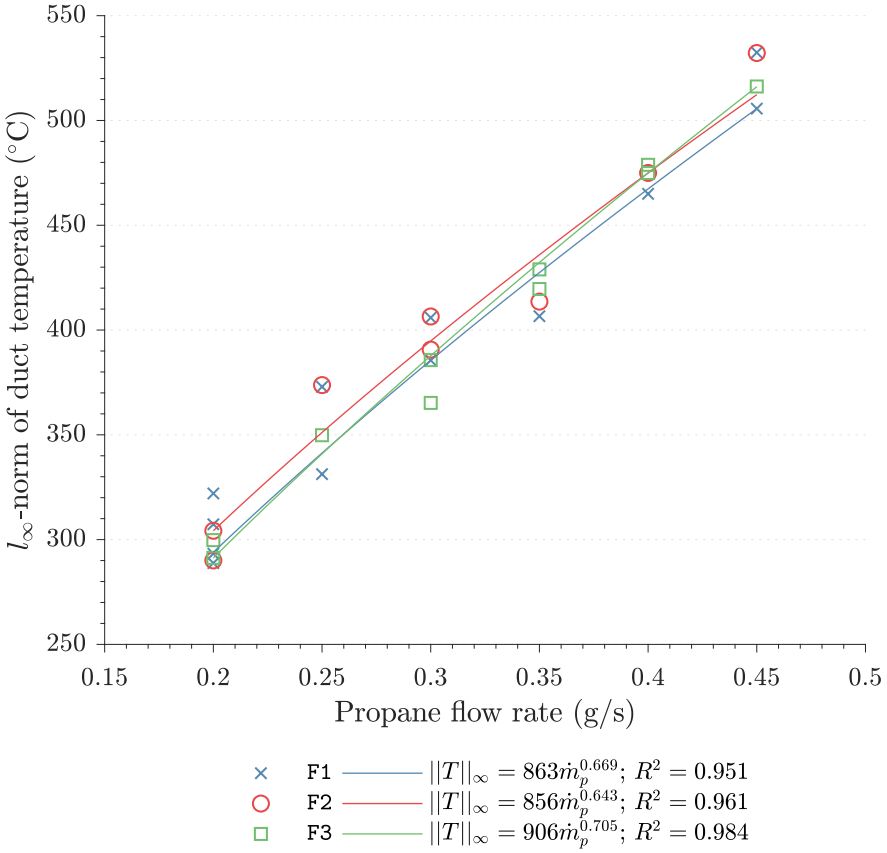

Figure 7.14: l_∞-norms of duct temperature measurements at hot box exhaust duct inlet (duct 02).

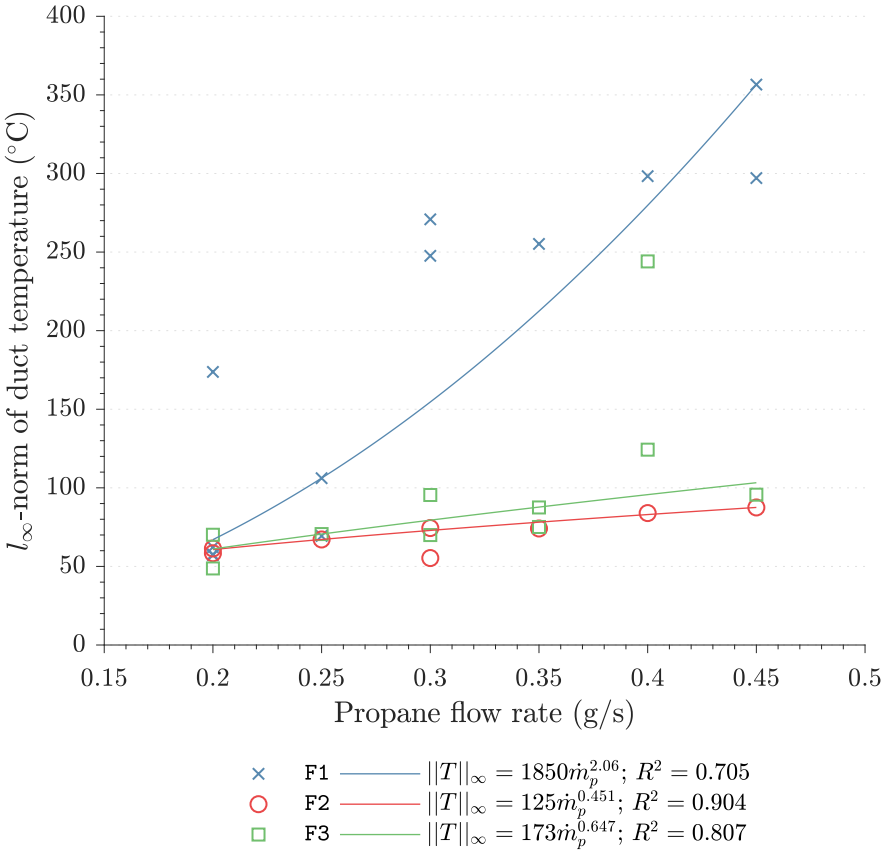

Figure 7.15: l_∞-norms of duct temperature measurements at cool box exhaust duct (duct 04).

However, for the two higher potentiometer levels (`F2` and `F3`) the coefficient C is substantially lower than that witnessed in the fits for duct 02 data. The most noticeable difference within the datasets is that of `F1`. This will be examined further.

The fit of the `F1` sub-case has a relatively low goodness and an R-squared of 0.704. The residuals for the fit are presented in Figure 7.16. The residuals describe heavy over-prediction at the lower propane flow rates and under-prediction at the higher propane flow rates. This indicates that there may be a phenomenological shift at different propane flow rates at this potentiometer level. To better describe these data an alternative fit, using a smoothing spline method, is presented in Figure 7.17.

The new two regime fit better describes the l_∞-norm temperature data at this location. So what happens between propane flow rates of 0.25 g/s and 0.3 g/s? At lower propane flow rates the pressure due to the fire, within the hot box and at the shared exhaust duct tee, and the momentum of gases in the hot box exhaust duct are both lower. This means that the exhaust flow is maintained at a higher rate within the cool box exhaust duct. This higher gas flow rate means that hot gas from the hot box migrates less against the normal direction of operation of the duct. At higher propane flow rates, the heat generated by the fire (and therefore the pressure and the gas momentum within the hot box exhaust duct) is increased. This increase in momentum and pressure is sufficient to enable a mechanistic shift to increased heat transfer against

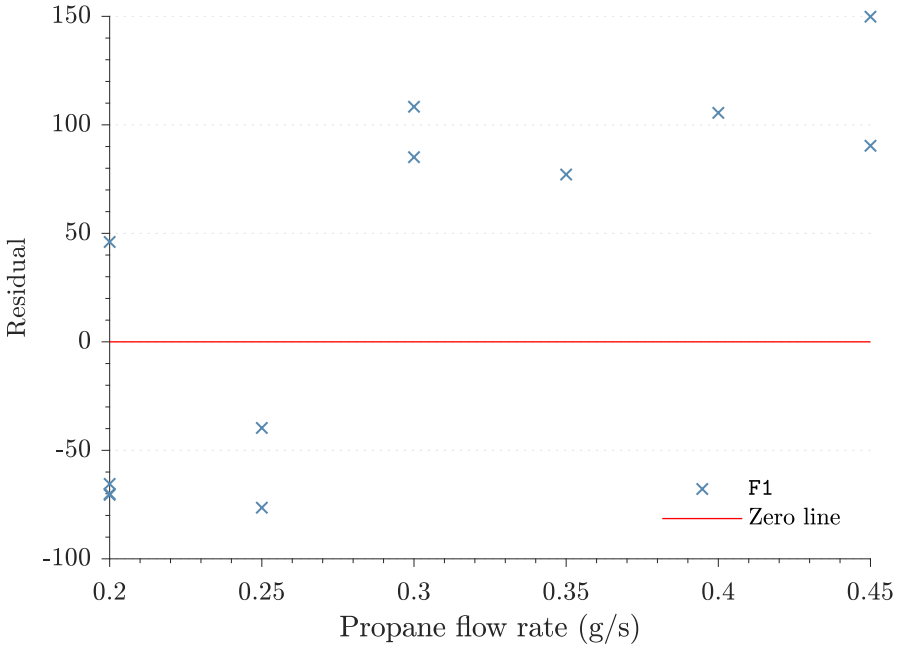

Figure 7.16: Residuals for the fit of duct temperature measurements at cool box exhaust duct (duct 04).

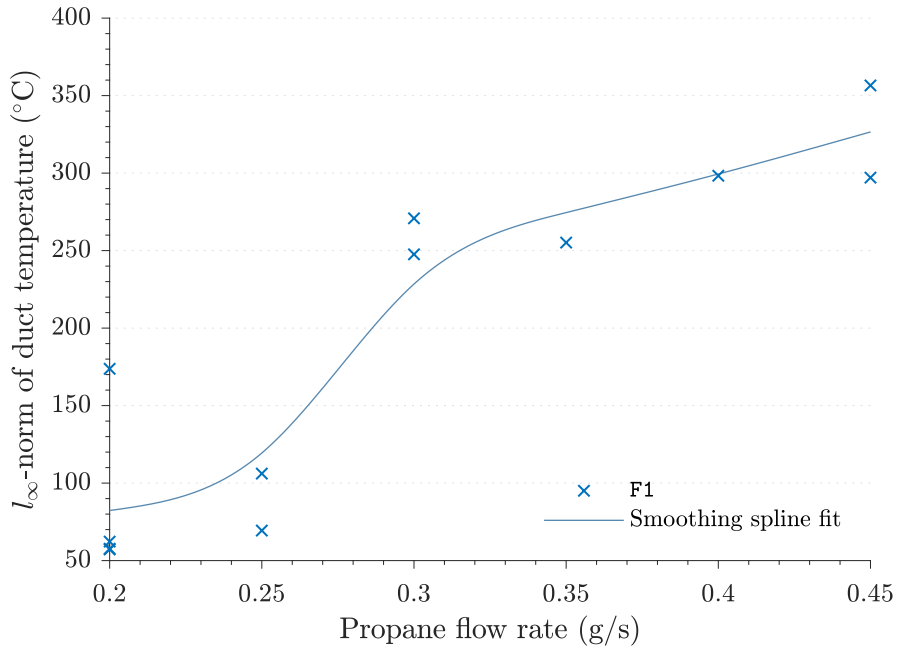

Figure 7.17: l_∞-norms of duct temperature measurements at cool box exhaust duct (duct 04) - alternative fit.

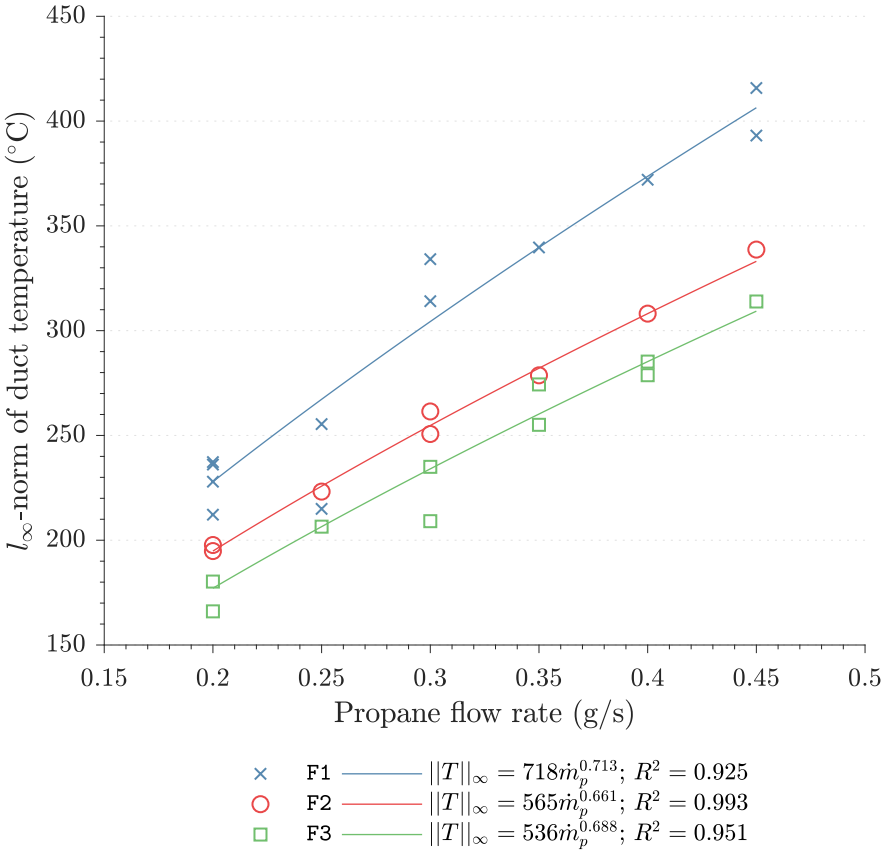

Figure 7.18: l_∞-norms of duct temperature measurements in the shared exhaust duct (duct 07).

the direction of the cool box exhaust system. Once this shift has occurred and as the propane rate is increased further, a similar increase rate to the other potentiometer levels in seen.

The l_∞-norms of the duct 07 temperature vectors is presented in Figure 7.18. The data show a clear positive relationship between increasing propane flow rate and l_∞-norm temperature at this location. The goodness of fit is high and R-square values are all above 0.92. The magnitude of C is smaller when compared to that output for duct 02. This is a quantitative indicator of the lessening effect of the fire as distance away increases. Phenomenologically other factors come into play the further away from the heat source the measurement is taken. For example, positive or negative leakage rates, fan-induced flow, and gas phase mixing. The values of N are within the typical range of approximately 0.66 to 0.71. A marked difference from the behaviour witnessed in the duct 02 data are the spread of the fan cases. There is a clear trend to increased l_∞-norms of temperature at lower potentiometer levels. This indicates that advection of energy through the system due to the fire is overpowering entrainment and mixing by the mechanical ventilation system.

Supply system

The l_∞-norms of the measured temperature at the cool box supply system outlet vent are presented in Figure 7.19. First noticeable is a number of seeming outliers in the `F1` dataset. These have been accounted for during curve fitting by the use of a least absolute residual (LAR) robust error regression method [219]. A positive relationship between the propane flow rate and l_∞-norm temperatures is witnessed. The steepness C is lower than those seen for the data from duct 02 and duct 07, indicating a lessening effect of the power of the fire source at this distal location. The exponents N are again lower but broadly in the typical range. The interesting pattern witnessed at this location is the relationship between the different fan cases. `F1` provides the lowest temperatures. This is because, at this distance from the heat source, low ventilation flow rates mean less advection of heat. Unexpectedly, the highest potentiometer level, `F3`, provides the next highest temperatures. There is not a monotonic increase in l_∞-norms of temperature at this location with increasing potentiometer level. This indicates that there is a balance point between the relative influence of the fire and the mechanical ventilation system.

There may be a 'sweet spot' in the ratio between the influence of the fire and a mechanical ventilation system (ϕ_P) with respect to spread of energy to remote parts of the building. If the fans overpower the fire more (a lower nominal ϕ_P value), there will be greater forced entrainment, mixing of cooler air and dilution of the energy field. If the fans drop more compared to the fire (an increasing nominal ϕ_P value), their ability to effectively advect energy through the system is reduced. It could well be that the data presented in Figure 7.19 demonstrates this 'sweet spot' or balance point between the influence of the fire and the fans (ϕ_P).

Summary of in-duct temperatures

Within the hot box exhaust system the relative importance of the fire energy release rate, when compared to the potential energy transfer rate of the ventilation system, is very high. Little difference is witnessed across the fan cases for the measured temperature of the exhaust gases. The real world implication of this is that the fire performance of an exhaust fan, serving the room of fire origin, may be dominated by the size of the fire and not the duty of the fans. This suggests that the specification of the exhaust fans should relate to the fuel load and ventilation of a served room and less so the duty of the fans.

For the hot box exhaust duct, the value of N output based upon the experimental apparatus data is in good agreement with that of Foote et al. [123]. This work was carried out on a non-shared, non-recycling, ventilation system. This implies that the existing empirical model, relating inter alia fire size and exhaust temperature, for a simple single enclosure with simple mechanical exhaust may show the same relative dependency on fire size and fan energy-advection potential when compared to a more complex arrangement with multiple enclosures and an interconnected, recycling, mechanical ventilation system. This is valuable as it provides some confidence to the continued use of simple engineering methods for more modern arrangements.

When examining the cool box exhaust a mechanistic shift is witnessed as the fire size increases. At lower fire sizes the fan-induced heat transfer within the cool box exhaust duct dominates over the fire-induced heat transfer. At a certain point, for the lowest potentiometer a shift is witnessed where temperatures increase greatly for a relatively small increase in fire size. This most likely represents a tipping point between

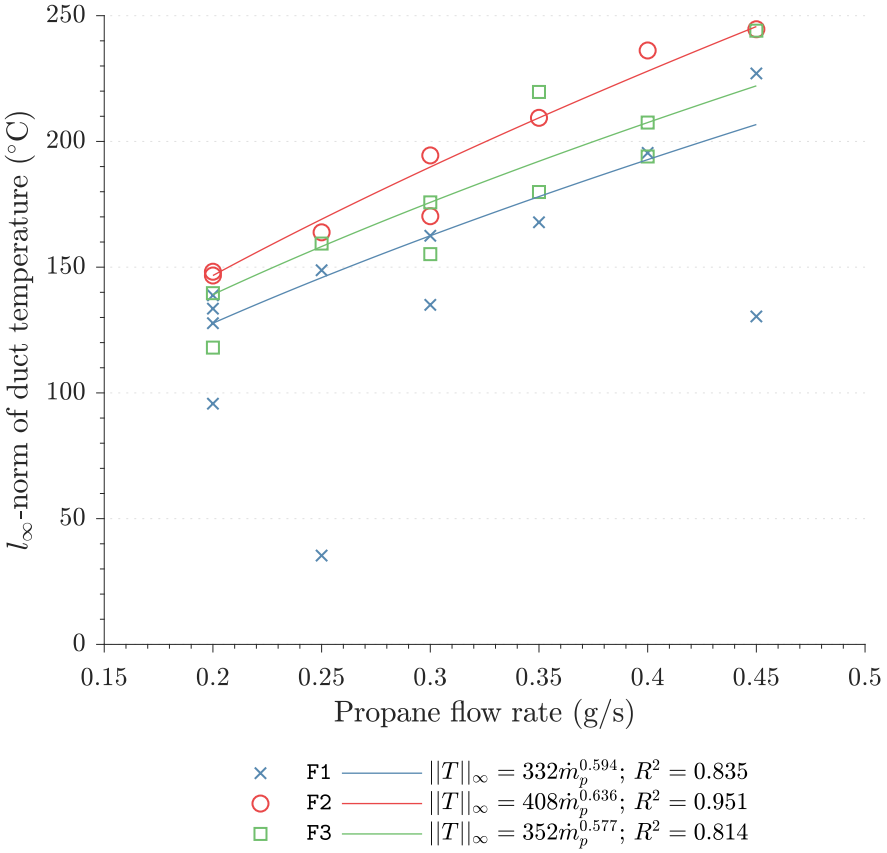

Figure 7.19: l_∞-norms of duct temperature measurements in the cool room supply system outlet (duct 11).

the dominance of the fans over the fire. This phenomenological shift is not witnessed for the higher two potentiometer settings, implying that this phenomenon only occurs at the edges of the nominal ϕ_P value range examined by the experimental campaign carried out in the experimental apparatus. The real world implication for this is that if a design is near to this tipping point then for a small change in the flow performance of an exhaust air handling unit (for example, a drop in flow rate due to an obstruction or poor maintenance) there could be a profound increase in the fire hazard within a non-fire room connected to a fire room by a shared ventilation system.

Two phenomena are witnessed as the measurement point moves further away from the fire source within the exhaust system: (1) the value of C decreases and (2) the spread of the fits for each potentiometer setting increases. (1) indicates the absolute reduction in the effect of the enthalpy transfer of the fire and the fans on temperatures; as other enthalpy transfer mechanisms (for example, heat losses to the duct walls and advection of hot gas via leakage) become more dominant. (2) demonstrates that at distances further away from the fire source the dominance of the fan-induced enthalpy transfer increases when compared to the heat release of the fire.

The real world implication of (1) is that when carrying out an engineering assessment of the fire hazard within areas more remote from a fire it may not be robust to only consider the effect of the fire load and the ventilation system; but that linings and leakage become more dominant. The design implication of (2) is that when assessing the fire hazard within rooms remote from fire origin, the correct consideration of the mechanical system may be more important than consideration of the fire size.

The final interesting item from the examination of the in-duct temperatures is the relationship between temperature in the cool box supply system outlet and fan duty. In comparison to all other examined in-duct temperature data, there is not a monotonic relationship between potentiometer setting and temperature. This suggests that there is another tipping point in the amount of energy transfer from the fire compartment to a non-fire compartment with respect to the relative dominance of the fire and the fans. The real world implication for this is that there may be a 'sweet spot' for the amount of energy transferred to areas remote from a fire event. This 'sweet spot' would correlate with an increased fire hazard within these remote spaces connected with a shared ventilation system. This therefore would require careful consideration by the designer as it is not simply a case of assuming that, for example, increasing the exhaust rate will decrease the fire hazard within distal spaces within a building.

7.8 Flow behaviour in the ducts

7.8.1 Importance of maximum duct velocities

Vent and duct velocities can strongly determine the efficacy of a mechanical smoke hazard management system [220]. This is due to the potential for plugholing and disturbance of the hot smoke layer.

Therefore, an understanding, and engineering prediction, of vent velocities is a key stage in the development of a fire safety design. It is valuable to examine the velocities within the shared ventilation system of the experimental apparatus to highlight: (1) if there are mechanisms that aren't captured in typical design methodologies or to which a solution may be very sensitive; and (2) whether established empirical engineering relationships remain valid for the case of compartments connected with a shared ventilation system.

7.8.2 l_∞-norms of velocity (and mass flow) vectors in the ducts

Description of analysis

The l_∞-norms of measured duct velocity for all u_is, with the exception of u_5, are examined and correlated with propane flow rate and potentiometer level. As discussed previously it is troublesome to plot against a function of both propane flow rate and fan mass flow rate. The latter changes through the duration of the experiment and depends, amongst other things, upon the heat release rate of the fire. For this reason, potentiometer level is again maintained as a category in the analysis.

The correlation between the l_∞-norms of duct velocity and propane are expected to be in the form $\|\boldsymbol{u}\|_\infty = C\dot{Q}^N$ where C and N are to be determined. C is expected to be a constant for each potentiometer level. C incorporates parameters related to thermophysical properties of the enclosure, geometry and the mechanical ventilation system (including the fan mass flow rate).

With reference to work carried out by Alpert [221] and Heskestad [222] on maximum plume velocity, N could be expected to be approximately 1/3. Whether this relationship holds for duct flow with mechanical ventilation is questionable. Alternatively, a relationship between pressure and velocity can be initially sought. From Drysdale [180] an estimate of velocity out of a compartment due to fire is presented in Equation 7.11.

$$u_F = \left(\frac{2(\rho_\infty - \rho_F)gy}{\rho_F} \right)^{1/2} \tag{7.11}$$

where u_F is the fire-induced velocity out of an opening, ρ_∞ is ambient density, ρ_F is fire-induced density and y is vertical height below the neutral plane. Substituting for ρ_F using Ideal Gas Law and simplifying to a proportionality with only u_F and T_F, Equation 7.12 is output. Substituting the proportionality between temperature and heat release rate (or propane flow rate) from Equation 7.3 and Equation 7.13 is output. In fact, the same exponent as hypothesised based upon the literature.

$$u_F \propto T_F^{1/2} \tag{7.12}$$

$$u_F \propto \dot{Q}^{1/3} \tag{7.13}$$

In-duct velocities (and mass flows)

The l_∞-norms of u_1 are presented in Figure 7.20. The data illustrate the expected positive correlation between propane flow rate and l_∞-norms of u_1. `F1` sub-cases have two outliers that have been successfully addressed using a robust LAR algorithm. `F2` sub-cases have high goodness of fit and consistency. `F3` sub-cases have a higher spread and a much worse goodness of fit.

The values of C are not monotonically increasing with increasing potentiometer level as expected. This may be attributed to insufficient data and inconsistent `F3` data. Broadly, and as expected, there is a positive correlation between potentiometer level and l_∞-norms of velocity.

The exponent on the propane flow rate, N, is in the range 0.315 to 0.539. Ironically the fits with the better goodness of fit, being `F1` and `F2`, have the poorer match with the expected exponent of 1/3. Also conversely to what may be expected, the `F3` sub-cases

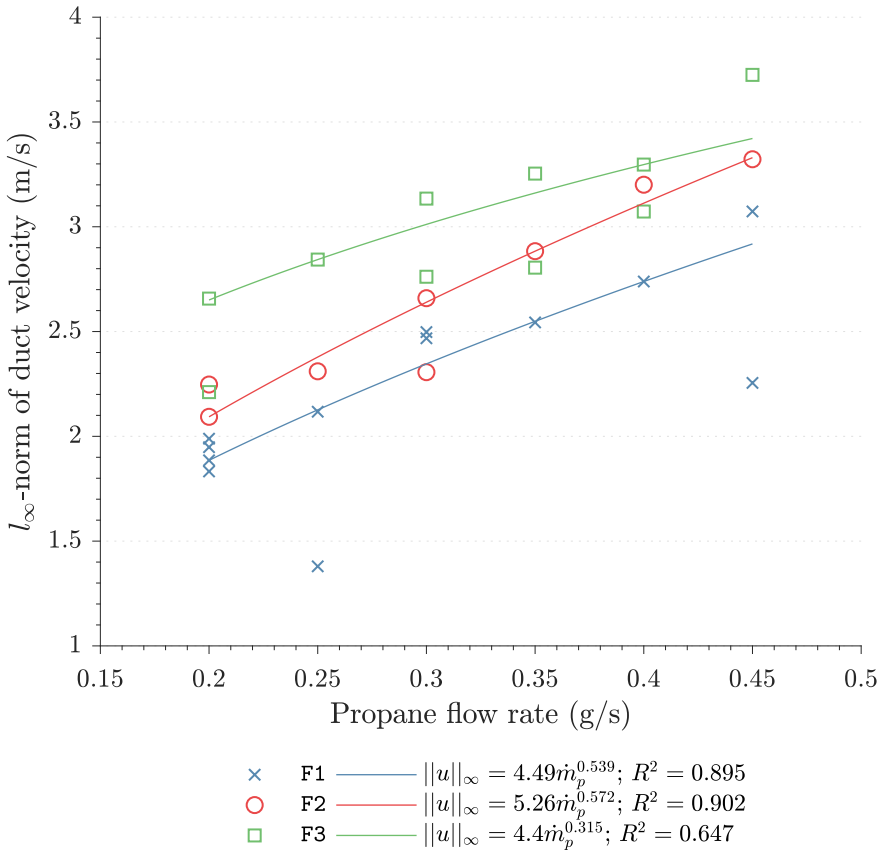

Figure 7.20: l_∞-norms of the hot box exhaust duct measured velocities (u_1).

have a N nearer to 1/3 (the value expected for a ceiling jet). It could have been hypothesised that as the fan duty increased (and hence the dominance of forced convection over heat release rate increased), the agreement with the ceiling jet correlation would decrease.

The l_∞-norms of velocities in the cool box exhaust duct, u_2, are correlated with the propane flow rate for potentiometer level categories in Figure 7.21. The data for sub-cases `F2` and `F3` present fits with very poor goodness. The velocity in the cool box exhaust duct is coupled to many interrelated parameters and mechanisms within the experimental apparatus. One may suppose that as the propane flow rate increased u_2 would monotonically decrease. However, u_2 is not only negatively correlated to the pressure in the shared exhaust system tee (which would be expected to increase with increasing propane flow rate), it is also positively correlated with the flow in the cool box supply duct (which is expected to increase with increasing propane flow rate). Therefore, there is an antagonistic relationship between u_2 and propane flow rate. That may be the reason that the fits in the form $\|\boldsymbol{u}\|_\infty = C\dot{Q}^N$ are poor. In fact, an absolute R^2 of approximately 0 to 0.2 is often considered to indicate a very weak or no correlation [223]. Therefore, it may be hypothesised that, at higher potentiometer settings, the velocity within the cool box exhaust duct is almost independent of the fire size. Whether the lack of correlation is due to antagonistic dependence or a lack of dependence is unclear from the current relatively limited dataset. More experiments are required to test these hypotheses.

To further investigate the flow behaviour in the cool box exhaust duct, the l_∞-norms of the mass flow rate vectors are presented in Figure 7.22. Regression analysis

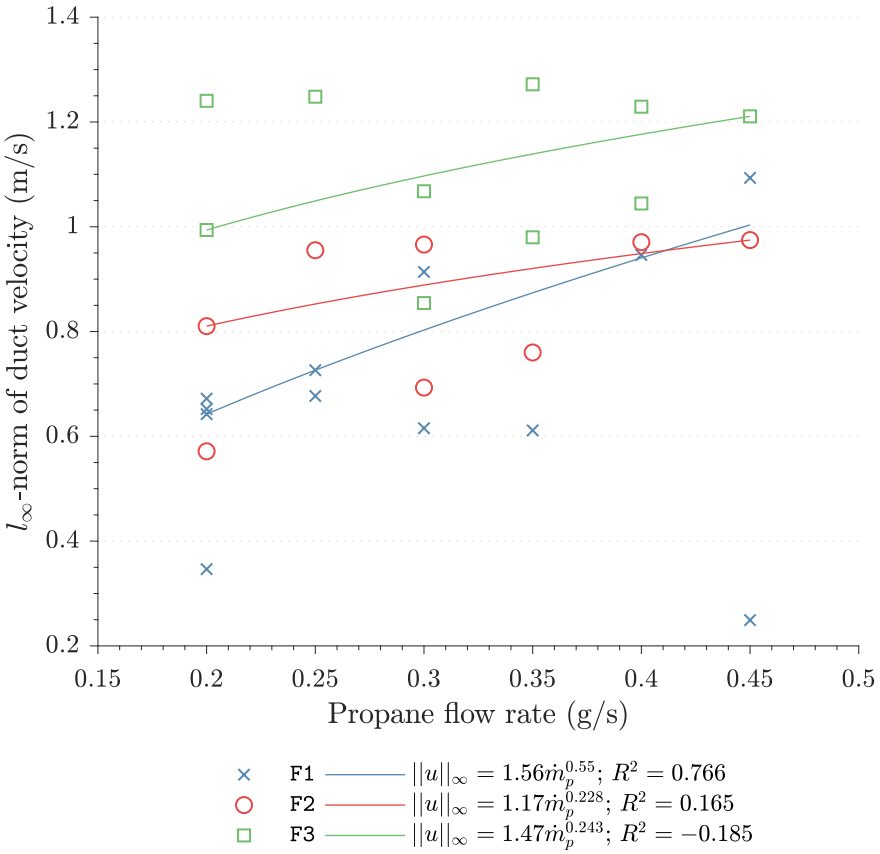

Figure 7.21: l_∞-norms of the cool box exhaust duct measured velocities (u_2).

was attempted using these data but no satisfactory fits were found. Visually also the figure presents little indication of a dependence of mass flow rate on propane flow rate. It can be concluded then that the mass flow rate within the cool box exhaust duct is more dominated by other phenomena (for example, leakage, fan duty, and heat losses; though these other phenomena are coupled to the heat release rate within the hot box - by way of pressure and temperature changes).

The l_∞-norms of measured velocities in the shared exhaust duct are presented in Figure 7.23. The data present the expected positive correlation between maximum velocities and propane flow rates and maximum velocities and potentiometer level. The data illustrate lower dependence on propane flow rate than u_1. N varies between 0.115 to 0.214. This aligns with expectations that as the measurement point moves away from the fire source, behaviour becomes less dominated by the heat release rate.

Unexpectedly the dependence upon propane flow rate is lowest within the `F1` sub-cases. It could be expected that at lower fan duties the flow within the shared exhaust duct would depend upon the heat release rate more. Instead the opposite is witnessed. In fact it could be argued that with an absolute R^2 of less than 0.1, there is no correlation between the l_∞-norms of u_3 and the propane flow rate. The phenomenon witnessed may be due to the coupling of the fan pressure and flow rate (i.e. the location on the characteristic fan curve) and the pressure in the boxes (i.e. a weak indirect coupling to heat release rate).

To further examine the relationship between the l_∞-norms of u_3 and propane flow rate, it is interesting to probe whether the dependence witnessed for `F2` and `F3` sub-cases are dominated by the induced convection from the heat source or the temperature

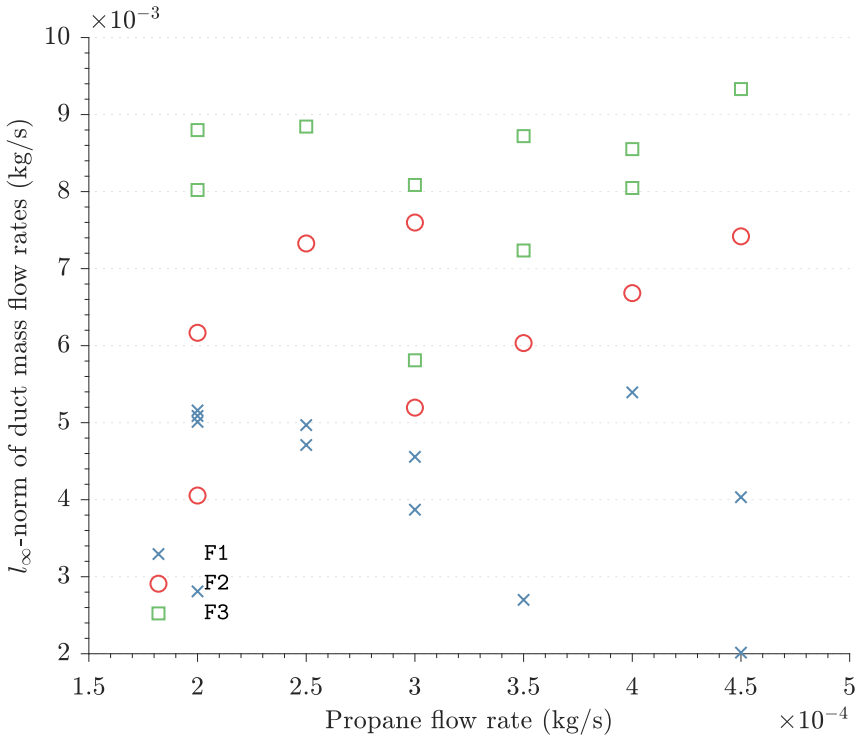

Figure 7.22: l_∞-norms of the cool box exhaust duct mass flow rate ($\dot{m}_2$).

increase due to the heat source. Therefore, the l_∞-norms of mass flow rates are presented in Figure 7.24. Regression analysis again did not output a satisfactory dependency fit for the data; therefore, it could be concluded that the mass flow rate within the shared exhaust duct is independent of the heat release rate. This may be due to the agnostic mechanisms caused by increasing propane flow rate: increasing buoyancy driven advection and decreasing gas density.

The l_∞-norms of measured velocity in the shared supply duct (u_4) correlated against propane flow rates and the potentiometer level categories are presented in Figure 7.25. The data show similar trends to the shared exhaust duct analysis. u_4 shows a very low dependency upon propane flow rate at the lowest potentiometer level (`F1`). It may be entirely possible that the velocity is so dominated by the fan duty, the effect of heat release rate tends to nil. Clear and strong dependency upon the potentiometer level is witnessed.

The l_∞-norms of measured velocity in the hot box supply duct (u_6) correlated against propane flow rates and the potentiometer level categories are presented in Figure 7.26. The expected positive correlation between potentiometer level and l_∞-norms of u_6 are witnessed. The `F1` sub-cases illustrate very little or no dependence upon the propane flow rate. This finding is counter-intuitive. It could be hypothesised that at lower fan duties the effect of heat release rate would be more pronounced when compared with higher fan duties; however this is not witnessed.

To further investigate, the full experimental data for two cases are examined; cases `P45_F1` and `P45_F3`. The leakage in the hot box for these cases is estimated (refer to Section 7.5 for a full description). Figure 7.27 presents the output of the leakage analysis. The figures clearly demonstrate that the leakage out of the hot box is much greater for the higher potentiometer level case (`F3`). Therefore, it can be concluded that a higher fan duty leads to higher leakages within the hot box. Reflecting on the initially

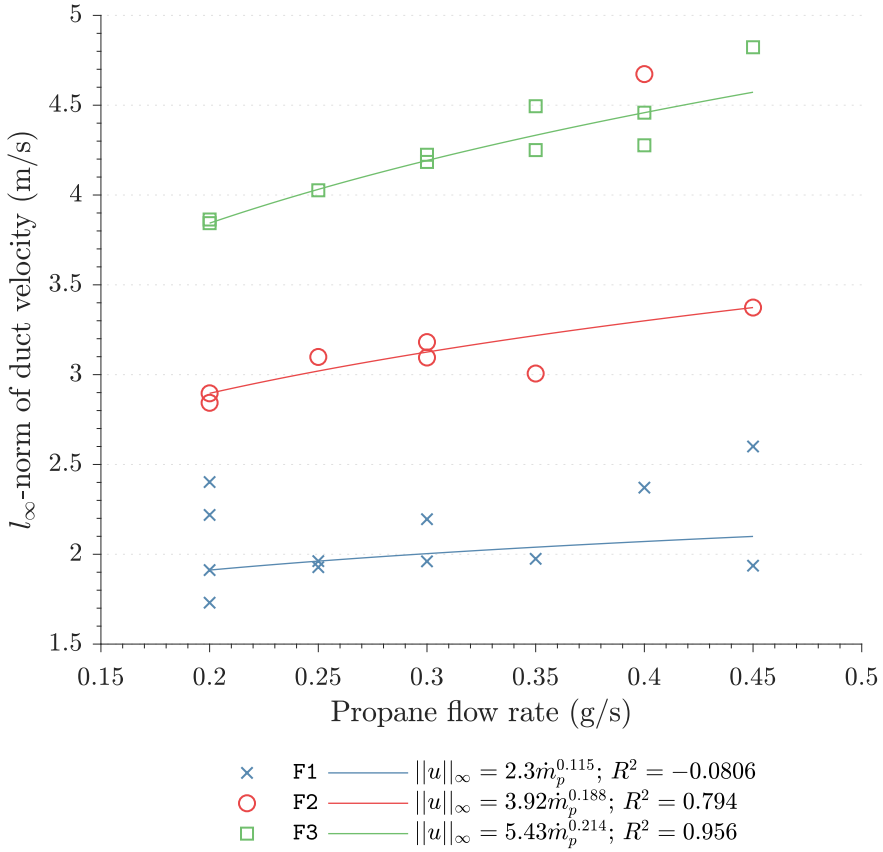

Figure 7.23: l_∞-norms of the shared exhaust duct measured velocities (u_3).

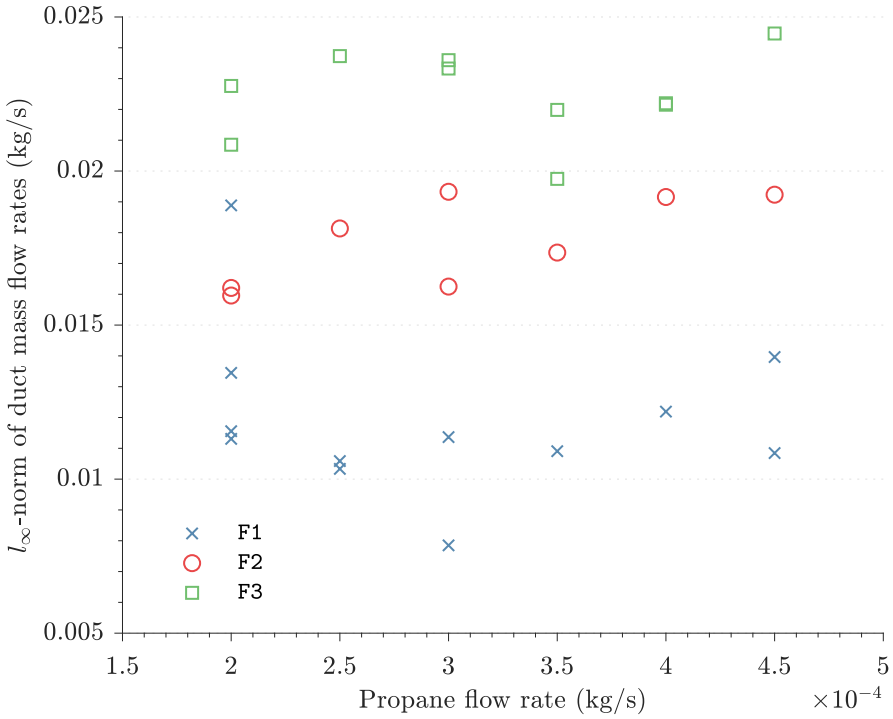

Figure 7.24: l_∞-norms of the shared exhaust duct mass flow rate ($\dot{m}_3$).

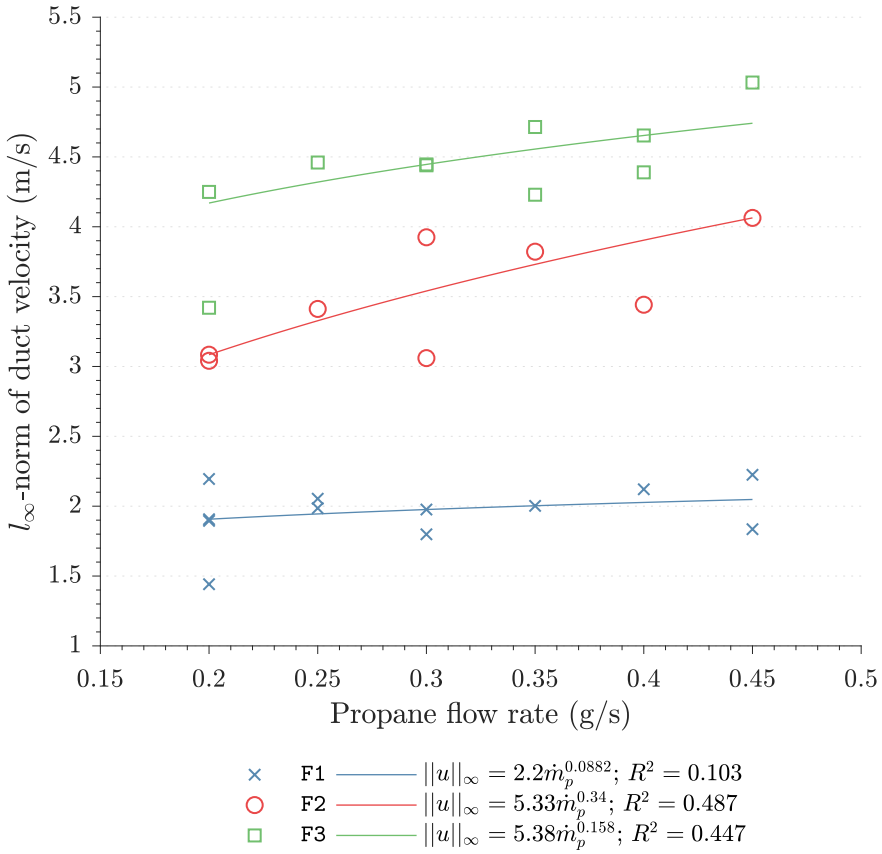

Figure 7.25: l_∞-norms of the shared supply duct measured velocities (u_4).

unexpected behaviour in Figure 7.26, the lack of correlation between propane flow rate and l_∞-norms of u_6 can now be explained as being driven by changing leakage. At lower fan duties the leakage from the hot box is lower, the downstream pressure is expected to be higher, and hence the velocity is throttled. At higher fan duties the leakage from the hot box increases, this leads to a decreased downstream pressure, and hence a higher velocity being developed in the high propane flow and high potentiometer case.

Summary of in-duct flow

With exception of ducts close to the fire, dependency of the velocity on the heat release rate is much lower than for temperatures. The potentiometer setting is much more dominant in the determination of l_∞-norms of velocity vectors. The implication of this is that typically used engineering estimations of domain-located velocity dependency upon heat release rate may not be valid for more complex modern buildings with shared ventilation systems.

In fact, at lower fan duties the velocity within ducts more remote of the fire appear near independent of the propane flow rate. This initially appears counterintuitive. However, upon examining the leakage from the hot box it is demonstrated that there is a strong dependence of leakage upon the potentiometer setting. This in turn leads to a stronger dependence of velocities upon propane flow at higher potentiometer settings. Effectively the potential increase in duct velocity due to a larger fire is being throttled by the lack of leakage from the ventilation system and the boxes.

The real world implication of this finding is that in older less well-sealed buildings duct flow could be expected to increase upon fire, when compared to more modern well-

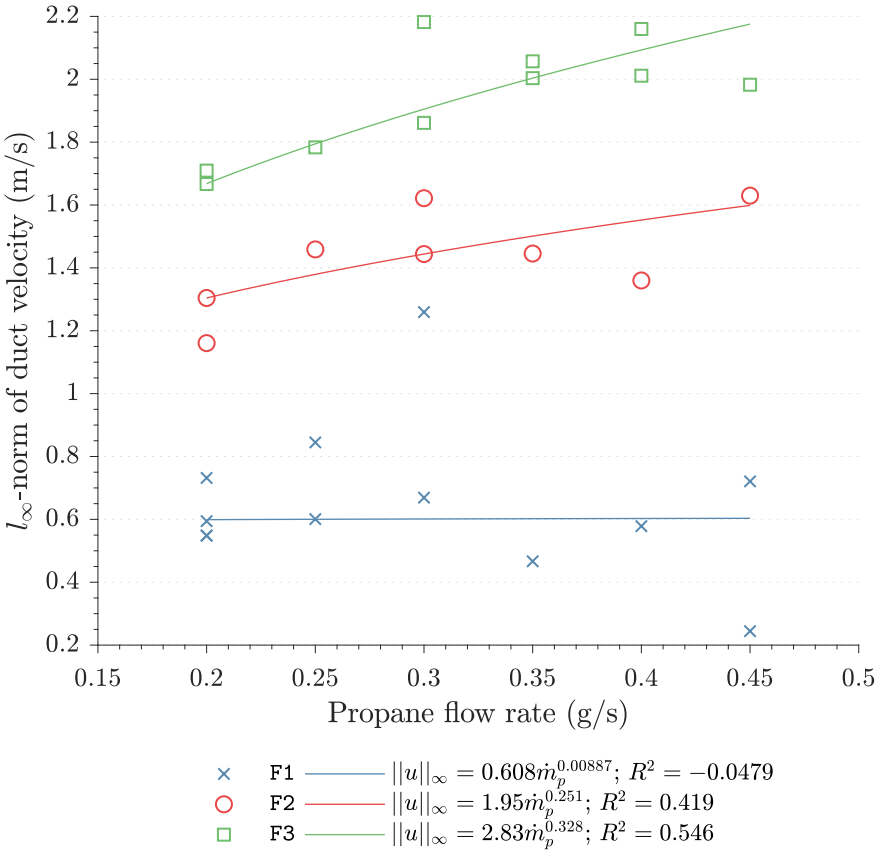

Figure 7.26: l_∞-norms of the cool box supply duct measured velocities (u_6).

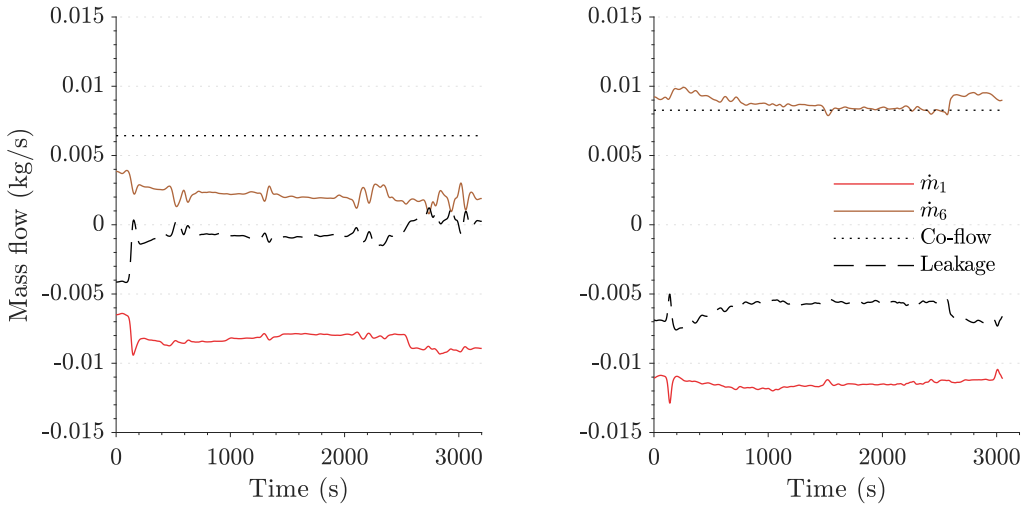

(a) Case `P45_F1`. (b) Case `P45_F3`.

Figure 7.27: Estimation of leakage in the hot box.

sealed buildings. For new build well-sealed buildings the flow within a shared ventilation system may be expected to be less dominated by the fire.

7.9 Closing remarks

This chapter has been primarily concentrated on the fulfilment of the second objective of this thesis and the second aim of the experimental apparatus. That is: to investigate phenomena that may currently be being ignored or missed within the fire safety building design paradigm. Data from individual experiments and data across the whole experimental campaign have been processed, presented, and analysed with the aim of investigating the robustness of existing design methods and the basis of guidance and Standards. Where applicable this can illuminate gaps in current engineering methods and assumptions that could embody risks to life and property. The following list presents the key conclusions of the analysis:

- Based upon the adopted experimental campaign, no flow against the hot box supply duct was witnessed - even at the highest propane flow rates and the lowest potentiometer settings (i.e. the highest nominal values of ϕ_P). However, tendencies were witnessed to the reduction of the supply rate to the compartment of fire origin for increasing ϕ_P. It may be, that if the experimental campaign was widened, flow against the supply duct would be witnessed. These experimental tendencies do imply that supply system effectiveness may be compromised and, in potentially extreme scenarios at higher nominal values of ϕ_P, hot gas spread may occur up a supply system duct during a fire. This should be examined further, using an expanded experimental matrix. The implication of this is that, for such higher ϕ_P cases, model solutions may not address this hazard as they often do not stipulate fire or smoke protection within the supply system.
- A time-dependent steady decreasing of hot box supply flow rate was witnessed at lower fan potentiometer settings. This may be due to energy transfer from the gas phase to the condensed phase (the linings of the hot box). The pressure and temperature within the hot box will be increasing as a steady thermal state is reached and heat losses to the boundary decrease. The real world implication of this is that at the start of a fire the supply system may not be experiencing a fire-induced performance compromise. However, as the fire event progresses, the building lining temperature increases, and heat losses to the boundary decrease there may an increased likelihood of the supply system being overpowered by hot gas spread from the fire. This phenomenon would be difficult for emergency response teams due to its time-dependency.
- Analysis of maximum temperatures within the experimental apparatus indicate that existing empirical engineering methods, developed for typical enclosure fires, may not be suitable for more complex scenarios featuring shared ventilation systems. The dependence upon the ratio of the heat release rate and the ventilation enthalpy flow (ϕ_P) may be approximately the same. However the dependence on the ratio of heat losses to the ventilation enthalpy flow is markedly different. The ventilation-driven enthalpy flow may dominate the boundary heat losses much more when compared to a typical naturally ventilated compartment. This means that existing empirical relationships for maximum enclosure temperature should be used with caution if attempting to apply them to a modern design scenario of enclosures connected with a shared mechanical ventilation system.

- Analysis of the exhaust duct temperatures of the cool box indicate that there is a sharp tipping point in fire hazard over a small propane flow rate change. This is likely a change in dominance from a forced convection-dominated heat transfer mode to a fire-dominated heat transfer mode (i.e. a phenomenological change at a certain value of ϕ_P). This implies that the fire hazard in rooms remote from the room of fire origin may be very sensitive to the nominal value of ϕ_P. This directly reinforces the development, validation, and use of coupled hybrid modelling to expand the analysis domain and quantify fire hazard in remote areas based upon the two-way coupling of the near and far field mechanisms. It is likely that, within the current modelling paradigm, this tipping point could be missed. To further complicate matters, this dependence of remote fire hazard on ϕ_P has been shown to not be monotonic. That is, it would be not suitable to 'err on the side of conservatism' and oversize fans by default. The maximum temperatures of the cool box supply system demonstrate that fire hazard may in fact increase at higher fan duties.

- Based upon the consideration of in-duct temperature readings at various distances away from the fire source it is apparent that the further away from the fire a measurement is taken the more dominant the effects of factors other than the fire size and the fan duty become. These may include heat losses to linings and advection of enthalpy through leakage. The implication of this is that, when carrying out an analysis of a total system careful consideration is required of input parameters that may, in the typical modelling paradigm, be resigned to 'second place'. The old adage that heat release rate is the most important variable [177] may not be *as* true when examining fire hazard in remote parts of a total building system.

The above conclusions, including potential implications for real world designs, serve to fulfil the aim to investigate phenomena that may currently be ignored within the current fire safety design paradigm. Specifically, it appears that the nil fire or smoke protection of downstream supply system within typical model solutions may present a hazard for high nominal values of ϕ_P and typically used empirical engineering methods may not accurately estimate remote fire hazard for modern building arrangements using shared ventilation systems.

So far the second aim of the experimental apparatus has been pursued with the target of fulfilling objective two of this thesis. Conclusions have been drawn that critically demonstrate that consideration of the far field within a fire engineering analysis is crucial to describing the risk within a design. Analysis has demonstrated that ignoring the far field may lead to an unsafe fire safety design being developed and delivered; that, upon a real fire event, would lead to under-predicted and unaccounted fire hazard in remote areas. Potential gaps within the current design methodology have been highlighted with respect to fire hazard within buildings with a shared ventilation system. The critical importance of the quantification of the two-way coupling between a total system and a fire, and the development of engineering tools to enable this, has been demonstrated.

Chapter 8

Experimental and numerical comparison

8.1 Aim and objective of benchmarking exercise

Providing benchmarking information for numerical models is a key stage in model evaluation. Specifically model validation. Benchmarking can provide end users with the data required to enable a validation exercise to be carried out for a specific use. At this time, the aims of the experimental apparatus are recalled:

1. **To provide good quality data to use to benchmark the new coupled hybrid model.**
2. To investigate phenomena that may currently be being ignored or missed within the fire safety building design paradigm or model solutions.

This is also directly related to objective three of the thesis: to provide relevant uncertainty metrics to enable end users to use the new model as part of a robust analysis. It is unrealistic to expect a model to be validated for all potential uses by the model developers. Instead the model developers (or other collaborators) can provide suitable benchmarking data so that a user may validate the model for their use. The benchmarking exercises should belong in the parameter space expected for the typical application. This ensures the usefulness of the benchmarking exercises.

Within the literature of numerical models for fire, there is a tendency to concentrate on a single benchmarking method. For example, the comparison of quantities through time, maximum heat release rate, or flame spread speed. In this work, a gamut of benchmarking methods are utilised to provide a fuller picture of the uncertainties between the numerical set up data and the experimental apparatus data. The more information that is provided to a model end user, the more robustly they can utilise the novel model implementation as part of a competently carried out fire engineering analysis. The benchmarking analysis documented in this chapter is:

– Section 8.2: comparison of maximum values of output quantities, across all experiments in the experimental campaign.

– Section 8.3: comparison of time-dependent output quantities for an exemplar experiment.

– Section 8.4: relative errors between experimental and numerical cases for output quantities across all experiments in the experimental campaign.

8.2 Full experimental matrix comparison

8.2.1 Description of analysis carried out

Comparison plots are generated to present every case (including repeats) on a single experimental-numerical plot. The use of more experimental benchmarking data increases the confidence in the output model uncertainty [224].

To be able to present all experimental data (within a certain data class, e.g. box temperature) on a single plot, the time-dependent data must be converted to single data points. These single data points must be representative of the end use of the model. In the case of models used to quantify fire hazard, as discussed in Chapter 7, the use of l_∞-norms are applicable and useful. Therefore, the l_∞-norms of box temperatures, in-duct temperatures, and duct velocities from all data signals for all experiments are compared on three plots.

Experimental data are given on the x axis and numerical data are given on the y axis of these $x-y$ plots. For a perfect alignment of numerical prediction and experimental data, all datapoints would sit on the line $x = y$ as described in the left diagram of Figure 8.1. This 'perfect prediction' is represented on the comparison plots as a solid blue line. However, experimental data have an affiliated uncertainty. The upper and lower bounds of this uncertainty (refer to Section 4.8.3) are represented on the plots as dashed blue lines as described in the right diagram of Figure 8.1. Finally the actual linear fit of the experimental and numerical data is represented on the plots as a solid red line.

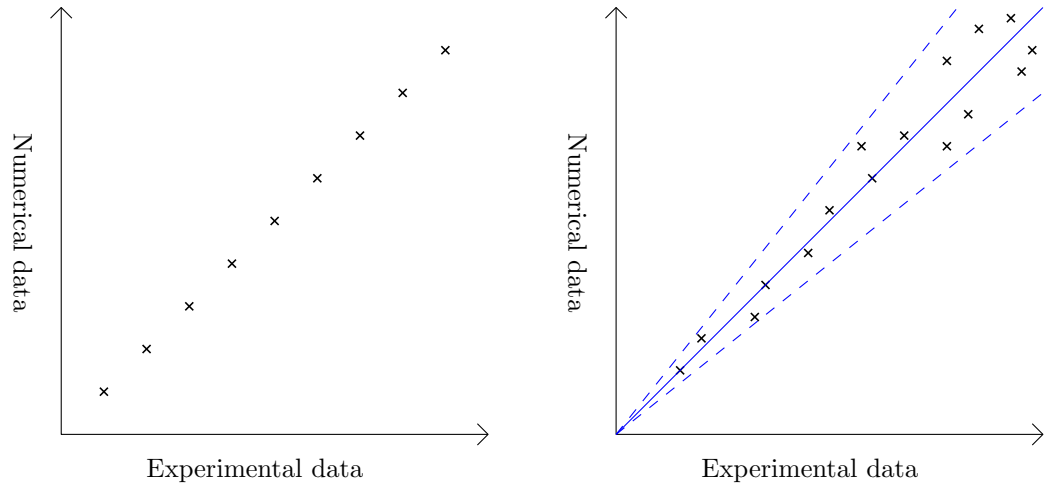

Figure 8.1: Sketch of experimental-numerical comparison plots. Perfect fit on left, fit within experimental uncertainty on right.

8.2.2 Box temperatures

The comparison of experimental and numerical box temperature data, output by the experimental apparatus and the numerical set up respectively, is presented in Figure 8.2. The figure illustrates a very good agreement between the numerical predictions and the experimental data. The $x-y$ fit to the comparison data falls within the experimental uncertainty. The numerical data tend to be higher at higher temperatures compared to the experimental data. The data to the bottom left of the plot are those within the cool box and the data to the upper right of the plot are those of the hot box. This would

generally provide a conservative fire engineering analysis as maximum temperatures would be over-predicted.

The implication for the real world use of the novel coupled hybrid model implementation is that end users should expect that, when used within a similar physical and numerical parameter space, the output of the model will slightly over-predict the temperatures within the enclosure of fire origin and enclosures connected via the network sub-model.

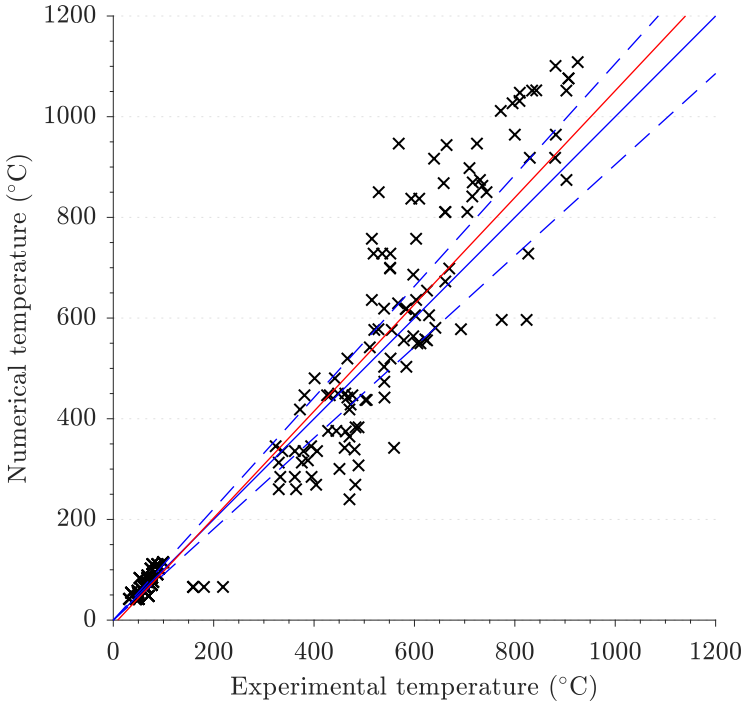

Figure 8.2: Comparison of numerical and experimental in-box temperatures.

8.2.3 In-duct temperatures

Figure 8.3 presents the comparison of experimental and numerical in-duct temperature data. The plot illustrates a reasonably good agreement between the experimental and numerical data. The plot illustrates that, especially at higher temperatures, the model under-predicts in-duct temperatures. This is unadvantageous for a fire engineering analysis as it would typically be unconservative. The likely reason for this under-prediction is the over-prediction of energy advection from the network subdomain.

The implication for end users of the novel model implementation is that a model correction factor should be applied to the analysis output to give the model user confidence that the fire hazard quantification used as part of their analysis is representative of the potential real fire hazard. A model correction factor of approximately 1.4 may be suitable for in-duct temperatures. This factor is separate to any factor of safety that is used within a deterministic event-based analysis.

8.2.4 Duct velocities

Figure 8.4 presents the comparison of experimental and numerical data for in-duct velocities. The plot illustrates an over-prediction of the in-duct velocity. The impact of

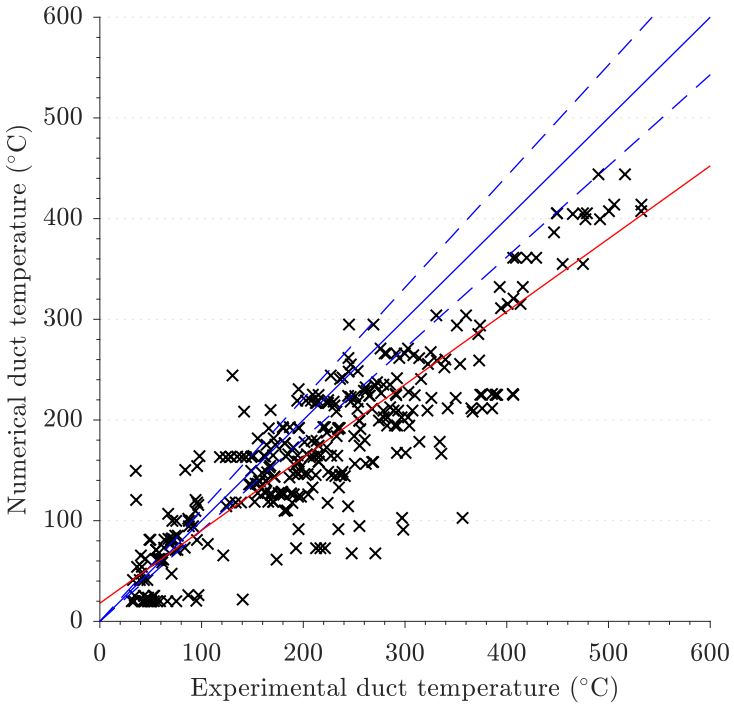

Figure 8.3: Comparison of numerical and experimental in-duct temperatures.

this model correction factor for a fire engineering analysis will depend upon the specific case. That is, this over-prediction could be conservative (for example, if assessing the likelihood of plugholing or smoke travel time) or unconservative (for example, if assessing effluent removal rates). The most likely reason for this over-prediction is the prescribed loss coefficients within the network subdomain.

The implication for end users of the novel model implementation is that a model correction factor may need to be applied to the results of their analysis. The choice to apply or not apply a correction factor will depend on the specific case and the acceptance criteria. If this over-prediction is unconservative (for example, predicting smoke detection operation time in the far field) then a model correction factor of approximately 0.7 may be suitable for in-duct velocities. Again, this factor is separate from any factor of safety applied to deterministic acceptance criterion (for example, comparison of available safe egress time to required safe egress time).

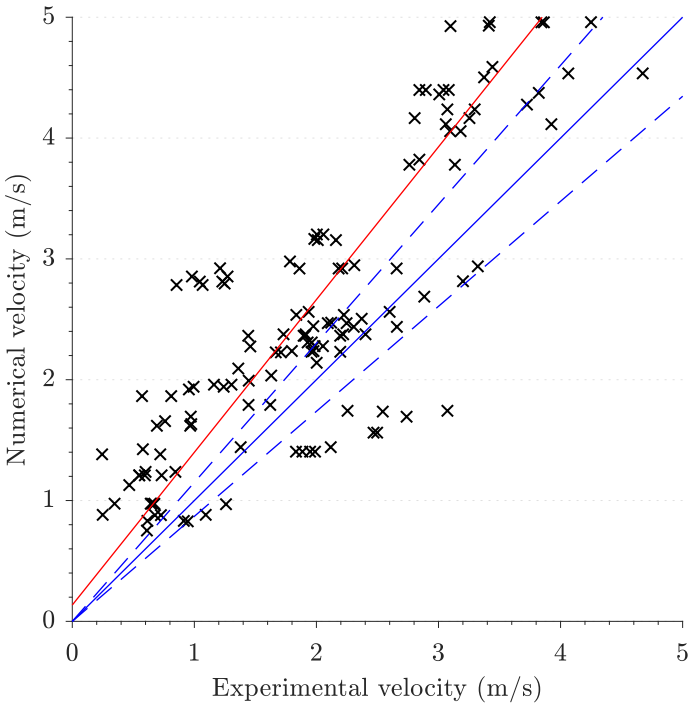

Figure 8.4: Comparison of numerical and experimental in-duct velocities.

8.3 Comparison of time-dependent output quantities

The data produced during the experimental campaign within the experimental apparatus and the numerical campaign carried out with the numerical set up can be compared. This combined dataset can be used as benchmarking data for the novel coupled hybrid model implementation.

There are eighteen cases, over thirty experiments, with each experiment having almost one hundred channels of data. It is impracticable to present the comparison of output quantities for all of these data signals. Instead `P30_F2` is picked as an example case. This sub-section provides a comparison of output quantities from the experimental apparatus and the numerical set up for this case.

8.3.1 Temperatures in the boxes

Presenting the output of all thermocouple trees for both boxes is impractical and not useful. Data from the central thermocouple tree is selected as a typical representation and presented. The temperatures measured by the central thermocouple trees within the hot box and the cool box for `P30_F2` are presented in Figures 8.5 and 8.10 respectively.

Due to the high variability of data from the lower thermocouples, especially B1_3_4 (the lower-most thermocouple), it is difficult to interpret the data in Figure 8.5. A plot for each thermocouple B1_3_1 through B1_3_4 is presented in Figures 8.6a through 8.6d. For added clarity the results from the numerical set up are now presented in black. A decreasing trend in turbulence is witnessed for the numerical set up data at increasing height. This is not witnessed in the experimental apparatus data due to signal conditioning.

The output is further examined in Figure 8.7, which gives the time-dependent (i.e. vector element-wise) relative l_1-norm error for the central hot box thermocouple tree

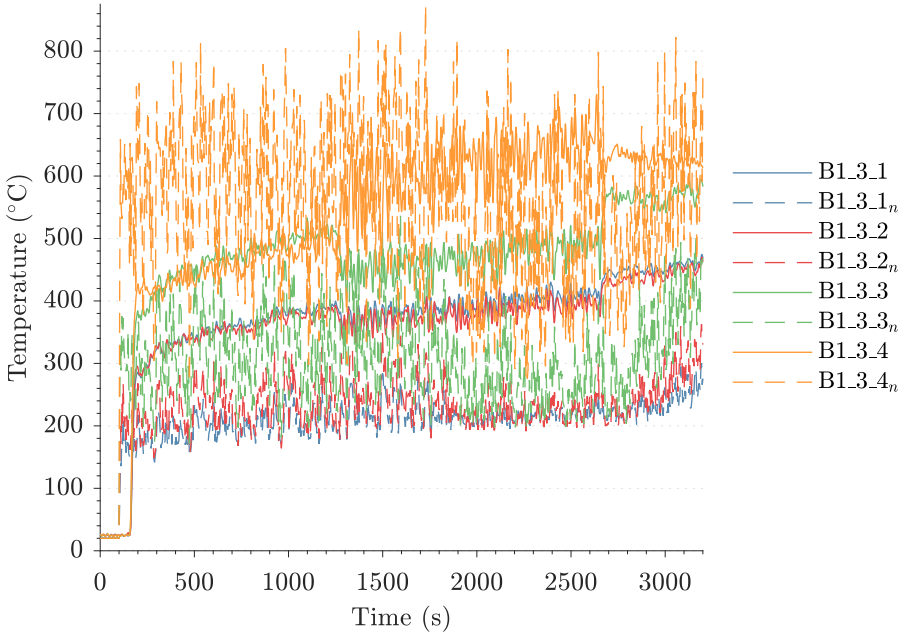

Figure 8.5: Comparison of central thermocouple tree hot box temperature data; experiment `P30_F2` (subscript n is numerical data).

data.

Temperatures in the hot box

Figures 8.6a and 8.6b illustrate that the prediction of the higher two thermocouples of the central thermocouple tree underpredict the data from the experimental apparatus by approximately 100 °C to 200 °C (broadly the same as other coupled hybrid models in the literature, maximums of 50 % as shown in Figure 8.7a and 8.7b). The trend is correctly predicted. A very rapid increase in temperature at ignition, a slowly increasing temperature during recycle mode and a steepening in $\frac{dT}{dt}$ following spill. Based upon the lower agreement at a higher elevation, the model may be entraining more cooler air into the rising buoyant plume than occurs within the experiment. This may be due in part to the uniform velocity vector field of gases flowing out of the network-field coupling boundary condition within the field domain.

In reality, the flow exiting the experimental apparatus' ventilation system at the supply outlets is expected to be turbulent and contain many eddies. This increases momentum transfer from the gas exiting the outlet to the gas within the box in proximity to the outlet. In comparison, within the numerical set up, the flow exiting the coupling boundary condition within the field domain has no turbulence and contains no eddies upon exiting. The flow structure may represent something more akin to a laminar buoyant jet. Figure 8.8 presents velocity vector slices for cases `P20_F1` and `P45_F3`. The images illustrate a jet-like flow structure of the inflow for the higher fan case but not strongly at the lower fan case. Unfortunately, this structure cannot be compared with that within the experimental apparatus as suitable experimental measurements were not taken. An unrealistic jet-like flow structure, if present, would be a direct impact of the defective boundary condition forced upon the coupling boundary condition within the field domain. A method to address this would be to utilise a synthetic-eddy-

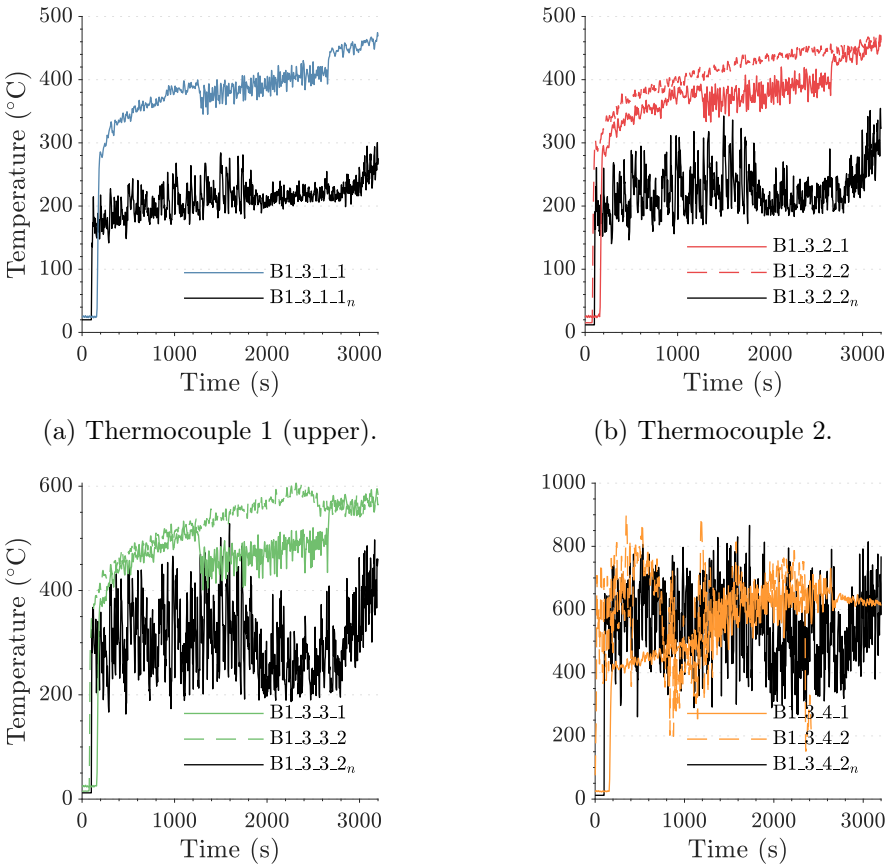

(a) Thermocouple 1 (upper).

(b) Thermocouple 2.

(c) Thermocouple 3.

(d) Thermocouple 4 (lower).

Figure 8.6: Comparison of the experimental apparatus and the numerical set up hot box central thermocouple tree data for case `P30_F2`.

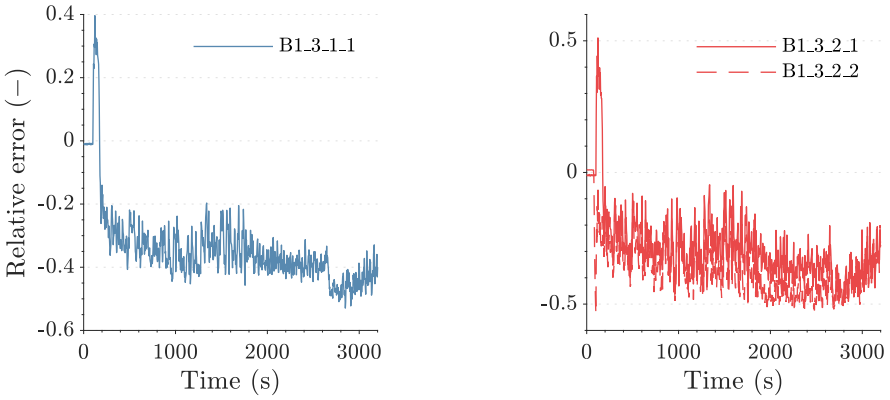

(a) Thermocouple 1 (upper).

(b) Thermocouple 2.

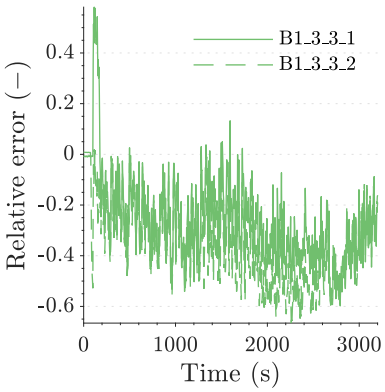

(c) Thermocouple 3.

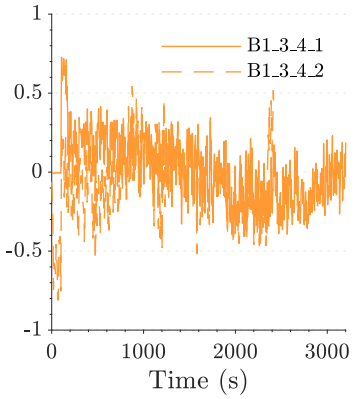

(d) Thermocouple 4 (lower).

Figure 8.7: Relative time-dependent l_1-norm error between the numerical set up and the experimental apparatus hot box central thermocouple tree data for case `P30_F2`.

method [225] to model turbulence within the inflow gas and an interpolation scheme for the velocity profile at the vent. If not representative of the experimental flow structure, the inflow laminar buoyant jet of the numerical set up may be expected to transfer less momentum in proximity to the vent as it flows into the enclosure. In turn, the jet may be expected to transfer more momentum to the buoyant rising plume, deeper into the enclosure and further away from the vent, and hence entrain more cooler air.

This can be quantitatively examined by comparing the relative errors in upper layer temperature in the hot box for three cases of increasing potentiometer setting. It would be expected that if the disagreement in upper layer temperature was related to the modelling of the flow structure of the inflow, the error would increase as fan potentiometer increases. Figure 8.9 presents these data and demonstrates that the lowest consistent relative error is witnessed in the lowest fan case, although there is not a great difference (approximately 10 % at its maximum). This would indicate that the disagreement in upper layer temperature is, at least in part, due to the treatment of the inlet boundary condition, an effect that increases as inflow velocity increases.

Figures 8.6c and 8.6d present the comparison of data from the experimental apparatus and the numerical set up for the lower two thermocouples in the central tree of the hot box. There are some peak underpredictions of approximately 200 °C (approximately 40 %) though generally predictions are within 100 °C to 150 °C (approximately 15 %). The peak temperature for the lowest thermocouple is predicted well. Maximum temperatures are reached more quickly within the numerical set up predictions when compared to the experimental apparatus data. This is most likely primarily due to the adiabatic modelling of the network domain and hence to conductive enthalpy losses from the ventilation system.

Temperatures in the cool box

The comparison of temperatures measured by thermocouple tree three in the cool box is presented in Figure 8.10. The temperature data present much lower fluctuations when compared to the temperature data from the hot box. It is still somewhat difficult to parse the data. A plot for each thermocouple is provided in Figures 8.11a through 8.11e. Relative time-dependent l_1-norm errors are presented in Figure 8.12.

The data of individual output quantities illustrate that the numerical set up prediction is much closer to the experimental apparatus data for the cool box when compared to the hot box. Maximum temperatures predicted in the numerical set up are within 2 °C to 5 °C (less than 5 %) of the experimental apparatus data. The general trends are predicted. However the time response of the temperature data is less well predicted. This is illustrated in the relative time-dependent l_1-norm error plots in Figure 8.12. The figures show a sharp increase in relative l_1-norm error, to approximately 50 %, near the start of the experiments. The second peak in relative error is due to a mismatch of timing between the numerical and experimental data.

The cool box temperatures within the numerical set up respond much more quickly than those of the experimental apparatus, for both heating and cooling. This indicates a larger magnitude ventilation flow (this is, in fact, the case; refer to Section 8.3.3) and lower thermal inertia of the enclosure lining material within the numerical set up.

The steeper $\frac{dT}{dt}$ within the heating during recycle mode and the cooling during spill-modes of the numerical set up also reflects the adiabatic assumption within the ducts. With the exception of enthalpy advecting to or from the network domain at leakage locations, heat losses or gains to the gas phase of the network subdomain are not modelled. This means that hot gas being extracted from the hot box of the numerical

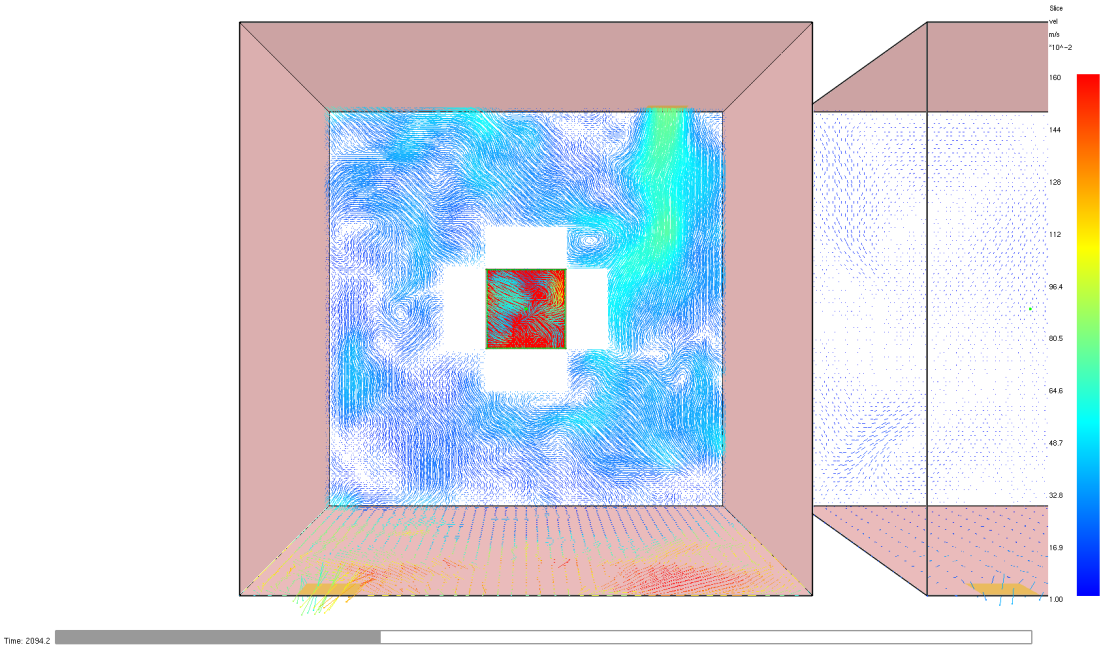

(a) Case `P20_F1`. The image illustrates that a strong laminar jet-like characteristic is not presented.

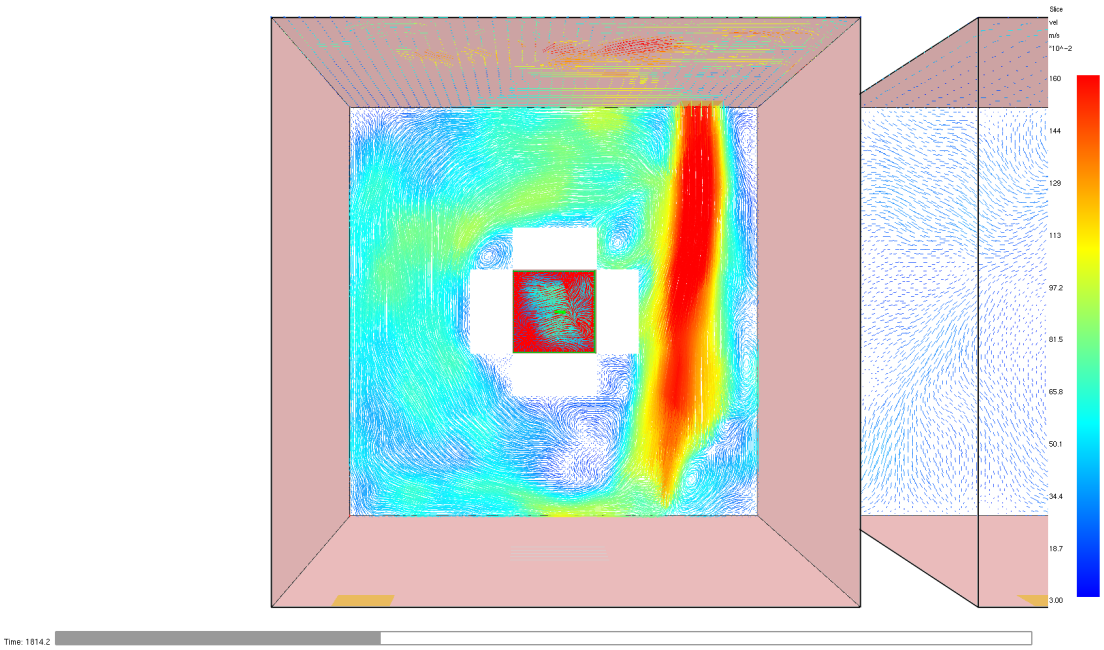

(b) Case `P45_F3`. The image illustrates the laminar jet-like characteristics induced by the inflow velocity boundary condition at this higher fan setting.

Figure 8.8: Slices of velocity vectors at z =0.1 m (i.e. mid height of the supply vent) in the hot box. Unfortunately it is not possible to validate these flow structures due to the available experimental data.

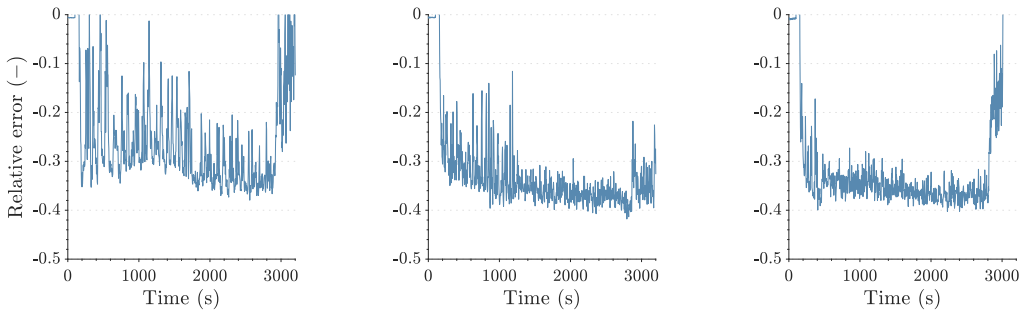

(a) F1. (b) F2. (c) F3.

Figure 8.9: Comparison of relative time-dependent l_1-norm errors between the experimental apparatus and the numerical set up hot box central upper thermocouple data for cases P45 cases.

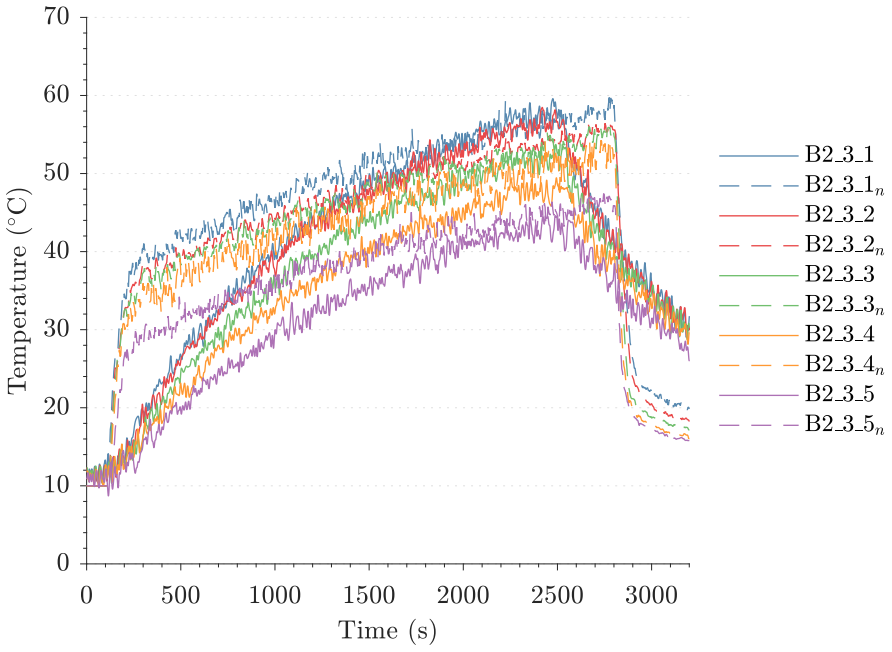

Figure 8.10: Comparison of central thermocouple tree of cool box; experiment P30_F2.

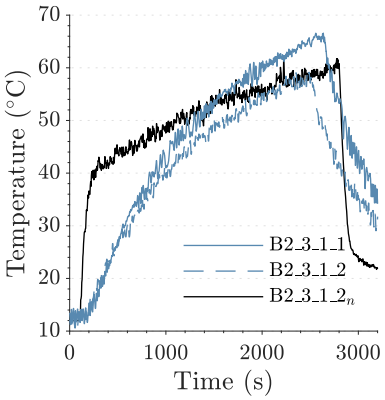

(a) Thermocouple 1 (upper).

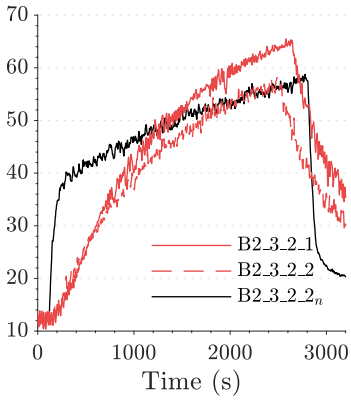

(b) Thermocouple 2.

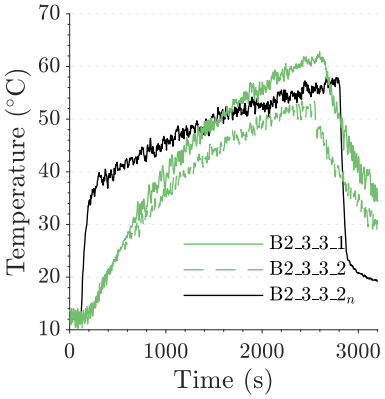

(c) Thermocouple 3.

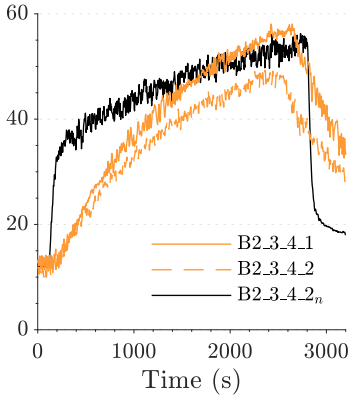

(d) Thermocouple 4.

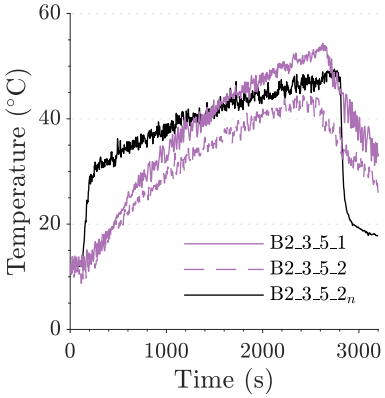

(e) Thermocouple 5 (lower).

Figure 8.11: Comparison of the experimental apparatus and the numerical set up cool box central thermocouple tree data for case `P30_F2_1`.

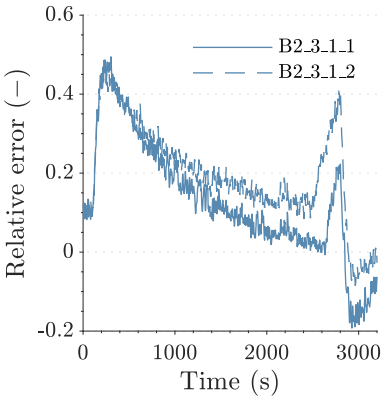

(a) Thermocouple 1 (upper).

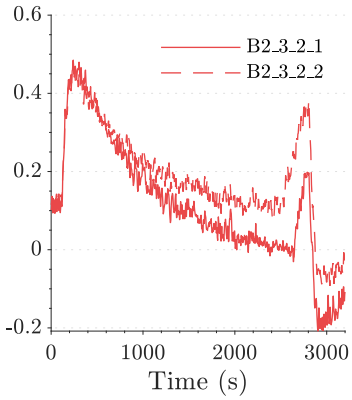

(b) Thermocouple 2.

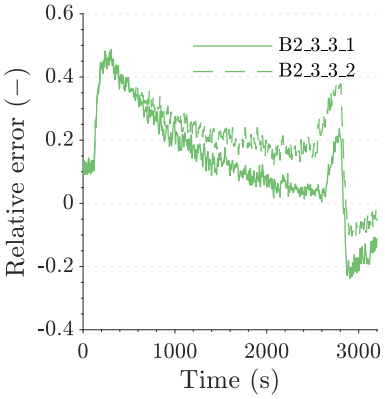

(c) Thermocouple 3.

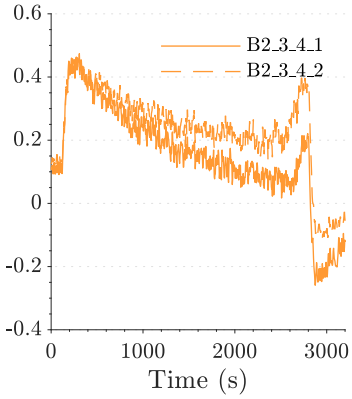

(d) Thermocouple 4.

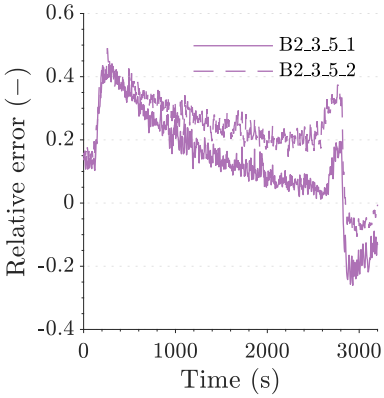

(e) Thermocouple 5 (lower).

Figure 8.12: Relative time-dependent l_1-norm error between the numerical set up and the experimental apparatus cool box central thermocouple tree data for case `P30_F2`.

set up and moving towards the cool box does not lose enthalpy to the duct walls. The flow will therefore arrive at the supply system outlets of the numerical set up at a higher temperature than that of the experimental apparatus. This accounts for the much steeper increase in temperature upon ignition within the numerical set up data.

The same phenomenon explains the steep drop in temperature upon smoke-spill and fresh air supply seen in the numerical set up data. Upon fresh air mode air at ambient temperature is drawn into the supply ventilation system. In the experimental apparatus the ducts to which the air (nominally at ambient temperature) is being drawn in at a high temperature. Air drawn in to the supply system of the experimental apparatus will experience heat transfer from the duct walls. This will increase the temperature of the ambient fresh air. This higher temperature supply air will decrease the steepness of temperature reduction in the cool box upon fresh air supply mode within the experimental apparatus. For the numerical set up, the duct walls are considered as adiabatic. As ambient air flows into the fresh air supply inlet the duct walls instantly adopt the temperature of the ambient temperature air. There is no heat transfer between the duct and the in-flowing air. In the numerical set up the ambient air does not have its temperature increased by heat transfer from the hot duct walls. This explains the much steeper drop in temperature upon fresh air mode for the numerical set up when compared to the experimental apparatus.

Summary of temperatures in the boxes

The in-box thermocouple data produced by the numerical set up is in generally good agreement with that of the experimental apparatus (approximately 15 %); especially in the cool box (approximately 5 %). General trends are well predicted. Temperatures within the flame region and in the cool box show good agreement. There are two primary disagreements between the numerical set up data and the experimental apparatus data that serve to illuminate current limitations of the new coupled hybrid model implementation:

1. The maximum temperatures in the hot layer of the hot box of the numerical set up do not show good agreement with the data from the experimental apparatus. The upper thermocouple measurements above the fire for the numerical set up are 100 °C to 200 °C (up to 50 %) lower than that measured in the experimental apparatus. Although this is not dissimilar to other coupled hybrid models in the literature, it may highlight a current limitation of the model: the simple treatment of defective boundary conditions at the network-field hybrid interface. This simple treatment, incorporating no synthetic turbulence or flow distribution, may be leading to a laminar jet-like supply inflow pattern which may be causing increased volumetric mixing throughout the field domain. However, at lower fan settings, no strong jet-like behaviour is witnessed - but underpredicted temperatures are present. Therefore, the boundary condition treatment alone is most likely not causing the temperature underpredictions.

2. The temperature change response time in the cool box is quicker for the numerical set up data when compared to the experimental apparatus data. This is most likely because of the adiabatic duct walls within the network domain in the numerical set up. This lack of accounting of heat transfer means that (1) air exhausted from the hot box does not cool prior to being transported into the cool box and (2) ambient temperature air doesn't gain enthalpy as it travels through the supply system in fresh air mode.

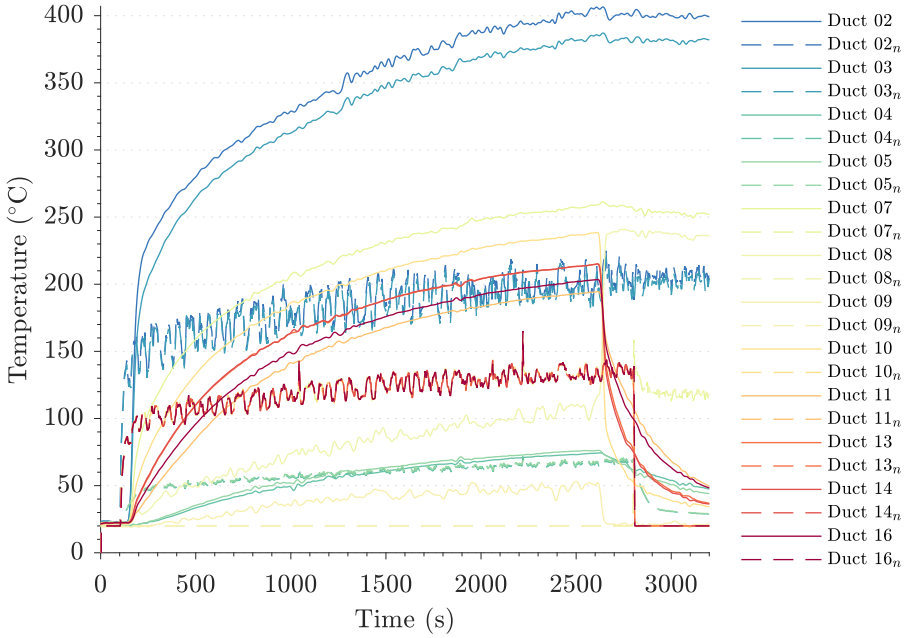

Figure 8.13: Comparison of all relevant duct temperature measurements for the experimental apparatus and the numerical set up case `P30_F2_1`.

8.3.2 Temperatures in the ducts

The measured temperatures in the ducts for an example case `P30_F2_1` are presented in Figure 8.13. Similarly as for the box thermocouples, the representation of the data in this manner is hard to read. Therefore, each thermocouple is individually presented. The data are grouped into exhaust system and supply system.

In-duct temperatures for the exhaust system

Figure 8.14 presents the in-duct temperature data for the numerical set up and the experimental apparatus for the exhaust system. Unsurprisingly, based upon the examination of hot box temperatures, Figures 8.14a and 8.14b illustrate that, although the general trend is in good agreement, the output hot box exhaust inlet and exhaust duct in-duct temperatures of the numerical set up are 100 °C to 200 °C lower than that output by the experimental apparatus. This is directly related to the lower temperatures within the hot box of the numerical set up. The same lower in-duct temperature is witnessed in the shared exhaust duct of the numerical set up presented in Figure 8.14e. This disagreement may be due, at least in part, to the undeveloped treatment of the defective boundary condition at the network-field hybrid interface and the subsequent laminar jet-like behaviour of the ventilation system outlets.

Figures 8.14c and 8.14d illustrate that the general trends and the maximum temperatures are in good agreement for the cool box of the numerical set up and the experimental apparatus (approximately 5 %). This is encouraging as one of the main aims of the coupled hybrid model is to quantify quantities in the far field (i.e. non-fire enclosures and connected infrastructure). As seen in the cool box temperatures the response rate of the numerical set up is much more rapid than that of the experimental apparatus. This is because of the lack of modelling of heat transfer within the network model of the numerical set up.

The smoke-spill outlet data, presented in Figure 8.14f does show agreed trends between the numerical set up and the experimental apparatus but the absolute values of temperature differ by approximately 100 °C (approximately 40 %). The numerical set up data shows a flat lined temperature held at ambient until spill mode is operated. This is because (1) heat transfer is not modelled within the network domain and (2) due to a limitation of the damper sub-model used, leakage of gas is not modelled at the closed air damper.

The effect of (1) is that the ducting and damper adjacent to the relevant thermocouple of the numerical case do not experience an enthalpy increase and affiliated temperature rise. This is in comparison to the experimental apparatus, whereby heat is transferred from the hot gases to the duct and damper adjacent to the smoke-spill thermocouple and hence this sensor records an increased temperature. The effect of (2) is that no hot gases leak through the air damper of the numerical set up and come into contact with the relevant thermocouple, meaning its recorded temperature does not increase. In comparison within the experimental apparatus, the air damper (as previously discussed) allows some hot gases to leak through it in the closed position. Therefore, hot air flows through the closed damper and past the thermocouple, increasing its temperature.

In-duct temperatures for the supply system

Figure 8.15a presents the fresh air inlet thermocouple outputs and shows data from the numerical set up flatlining at ambient temperature whilst that of the experimental apparatus increases. This illustrates the lack of modelling of heat transfer within the network domain of the numerical set up. The thermocouple measurement from the experimental apparatus increases by 50 °C due to the combined effect of enthalpy transfer from the hot gas to the duct and the air damper and hot gas leakage through the damper. Neither of these phenomena are modelled within the numerical set up and hence the temperature remains at ambient.

Figures 8.15b through 8.15f describe the thermocouple measurements in the shared supply system of the numerical set up and the experimental apparatus. The general trends are in good agreement. However the initial increase in temperature of the in-duct temperatures of the numerical set up is much steeper than those of the experimental apparatus. This is due to the modelling of the duct wall boundary conditions as adiabatic, meaning that no energy is transferred from the hot gas to the (in reality initially cool) ducts.

The maximum temperatures output by the numerical set up are 50 °C to 100 °C lower than that of the experimental apparatus. This may be due, at least in part, to the treatment of the defective boundary condition within the hot box as previously discussed. However, a jet-like flow structure is not witnessed at lower fan settings and hence other inaccuracies must be negatively effecting the predictions. This lower temperature may also be due to the modelling of leakage within the numerical set up. As previously discussed, leakage was modelled from the network domain of the numerical set up via the use of additional ducts connected to ambient nodes. These duct-node elements of the network subdomain allowed for gases to exit the computational domain. The definition of these duct and node parts was optimised for cool flow experiments carried out in the experimental apparatus. However, this arrangement has multiple degrees of freedom (duct length, shape, diameter, roughness, inlet and outlet flow coefficient, and node inlet and outlet flow coefficients). Therefore, it may be that the optimisation selected a set of parameters that performed well for cool flow cases but less well for

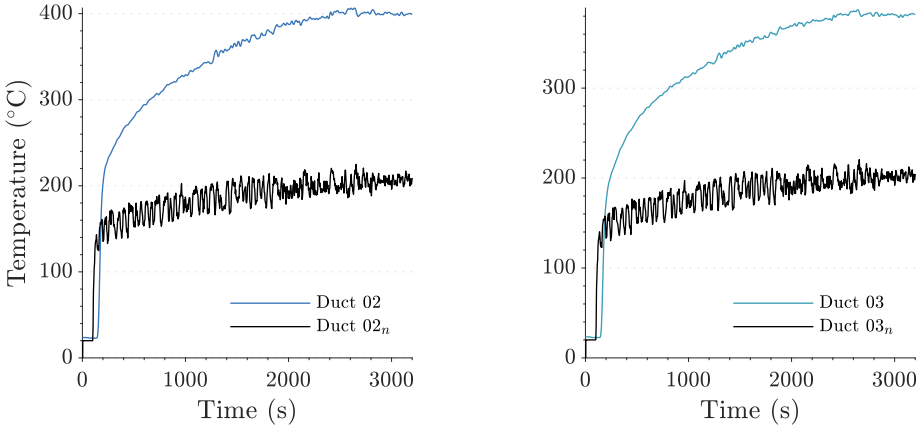

(a) Hot box exhaust inlet.

(b) Hot box exhaust duct.

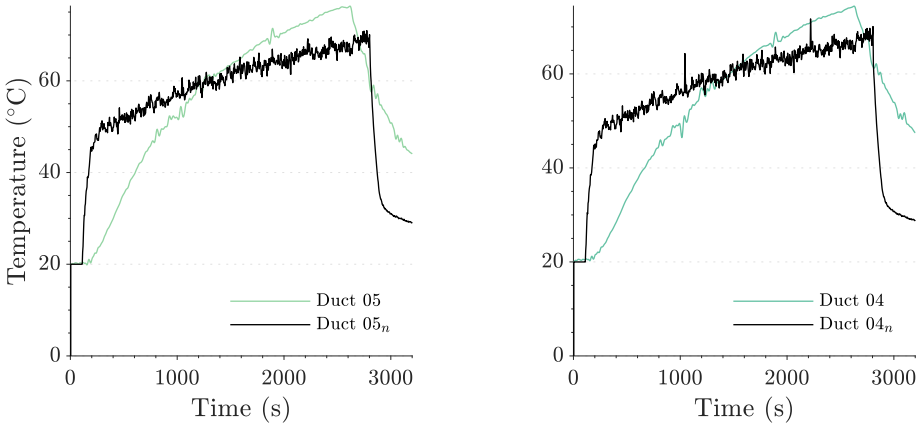

(c) Cool box exhaust inlet.

(d) Cool box exhaust duct.

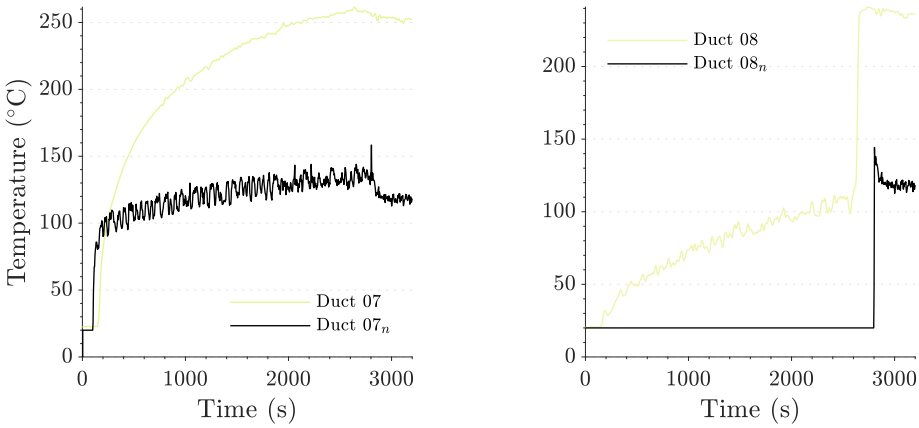

(e) Shared exhaust duct.

(f) Smoke-spill outlet.

Figure 8.14: Comparison of the experimental apparatus and the numerical set up exhaust system temperatures for case `P30_F2_1`.

hot flow cases. For example, the adopted parameters may lead to more enthalpy being advected out of the network domain of the numerical set up when compared to enthalpy leaking out of the ventilation system of the experimental apparatus. This would lead to decreased temperatures within the network domain of the numerical set up when compared to the experimental apparatus.

Summary of in-duct temperatures

The data show that overall trends for both the exhaust and supply systems of the numerical set up and the experimental apparatus agree well. The agreement between the cool box exhaust system is especially good (approximately 5 %). This is encouraging as the novel model implementation was designed to quantify output in the far field of a calculation (e.g. a non-fire room connected to a fire room with a shared ventilation system). The data also illuminate current limitations of the model as used to run the numerical set up cases:

1. The underpredicted temperatures within the hot box have consequential effects on the temperatures within the ventilation system. This consequently reduces the in-duct temperatures of the numerical set up, especially the exhaust system.

2. The modelling of the wall heat transfer boundary conditions of the network domain of the numerical set up as adiabatic increases the steepness of temperature changes within the ventilation system. As no enthalpy is transferred from the hot gas to the duct of the numerical set up the hot gas remains at a higher temperature as it passed through the network subdomain. Additionally, upon spill mode, the ambient temperature air entering the fresh air inlet of the numerical set up does not experience enthalpy increase due to heat transfer from the (in reality, hot) ducts.

3. The account taken of gas leakage from the network subdomain of the numerical set up may be leading to greater enthalpy advection from the domain when compared to the experimental apparatus. The parameters of the leakage modelling method for the numerical set up were optimised for cool flow cases. It may be that the parameters output via this optimisation are less valid for hot flow cases.

8.3.3 Velocities in the ducts

The measured velocities for all in-duct probes for the experimental apparatus cases `P30_F2_1` and the numerical set up case `P30_F2` are presented in Figures 8.16 and 8.17. u_5 data is presented for completeness. The figures demonstrate a good agreement of trends between the numerical set up and the experimental apparatus velocity data. The datasets agree with respect to greatest through lowest magnitude of velocity measurement (e.g. u_2 is the lowest and u_4 is the highest). The data for each velocity probe is presented in Figures 8.18a through 8.18e. The sharp negative spikes in the numerical set up data is temporary flow reversal within the 1D network subdomain, due to rapid pressure fluctuations within the field domain. The initial low velocities in repeat two is an experimental error.

In-duct velocities for the shared ventilation system

Figure 8.18a presents comparison of u_1 for the numerical set up and the experimental apparatus for the subject case. The figure shows very good agreement between data

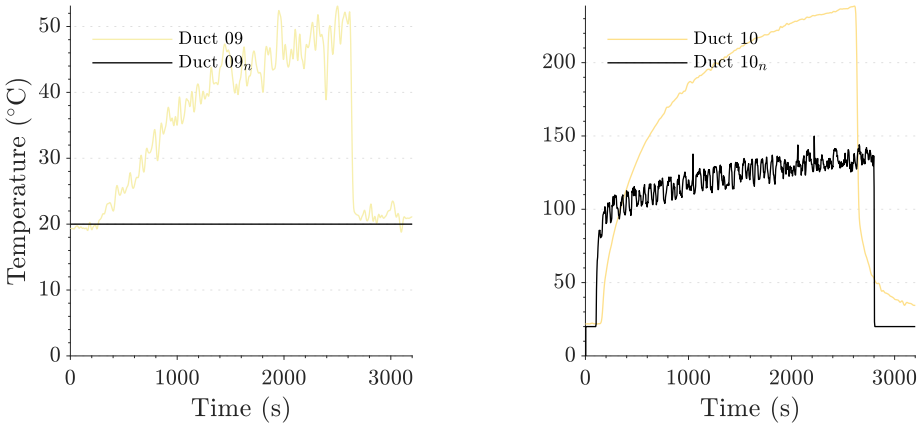

(a) Shared fresh air inlet.

(b) Shared supply duct.

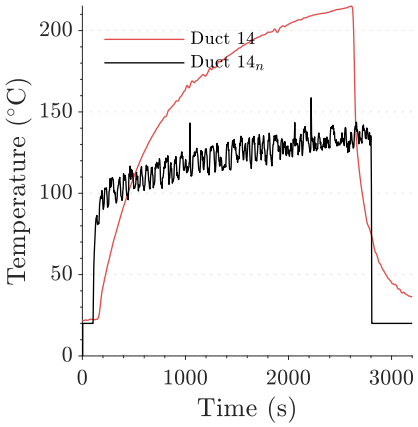

(c) Hot box supply duct.

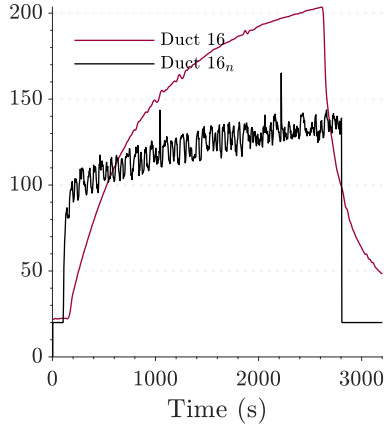

(d) Hot box supply outlet.

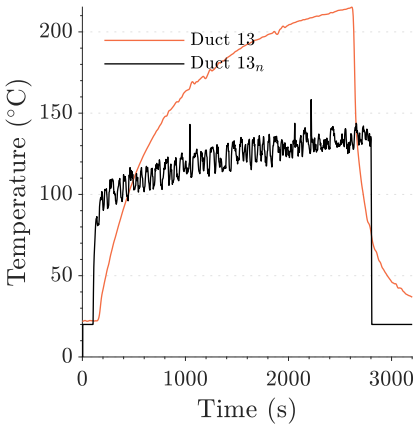

(e) Cool box supply duct.

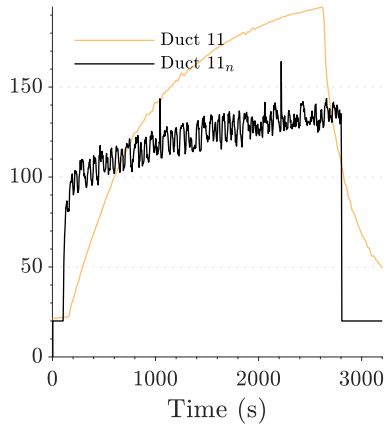

(f) Cool box supply outlet.

Figure 8.15: Comparison of the experimental apparatus and the numerical set up supply system temperatures for case `P30_F2_1`.

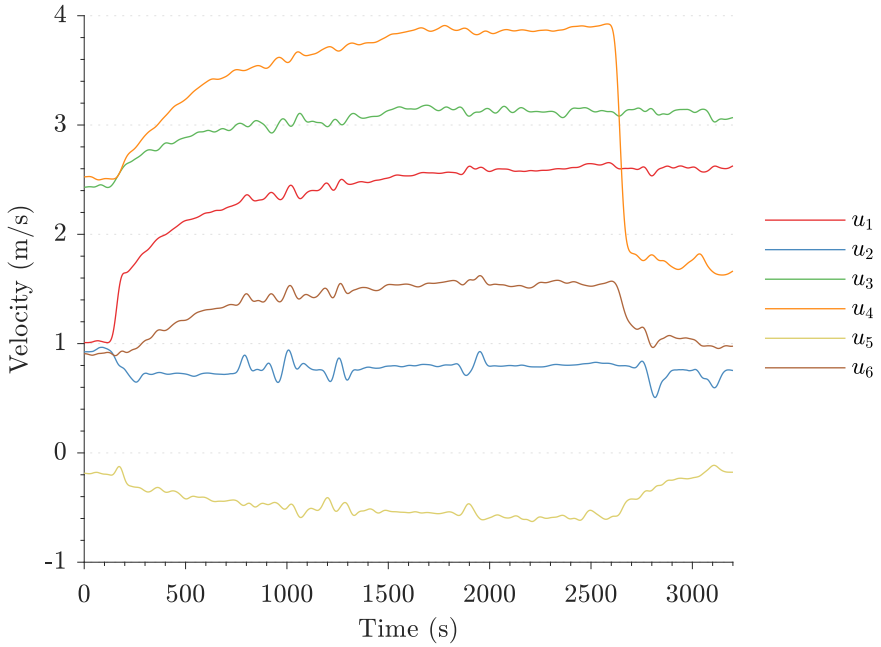

Figure 8.16: All in-duct velocity probe data for the experimental apparatus case `P30_F2` repeat one

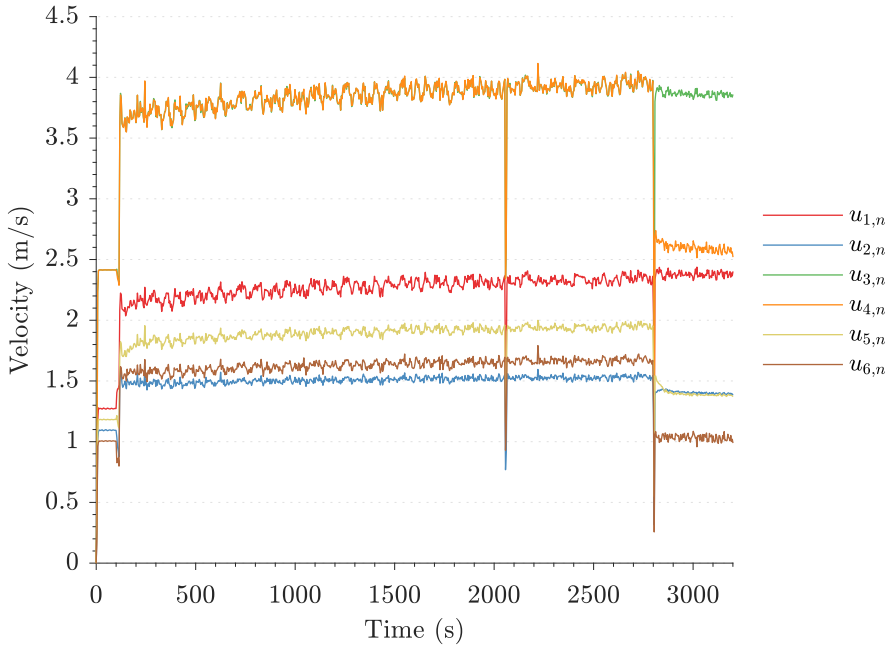

Figure 8.17: All in-duct velocity probe data for the numerical set up case `P30_F2`

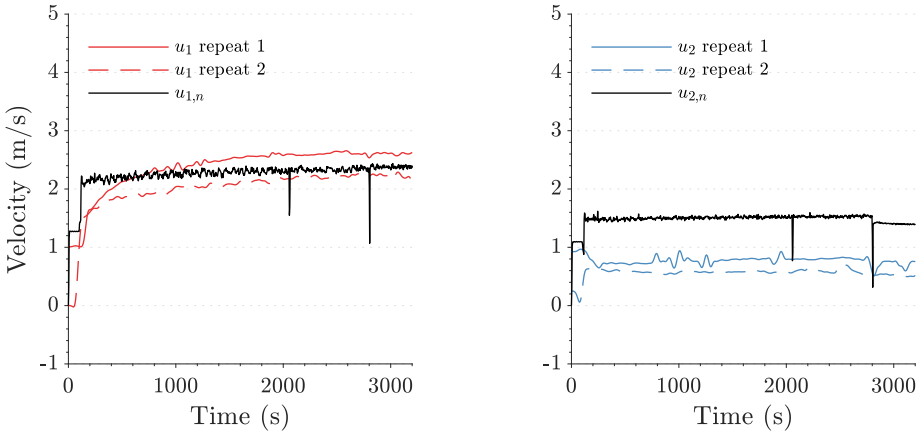

(a) Hot box exhaust duct, u_1.

(b) Cool box exhaust duct, u_2.

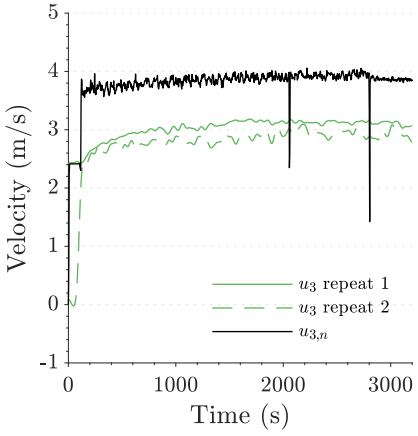

(c) Shared exhaust duct, u_3.

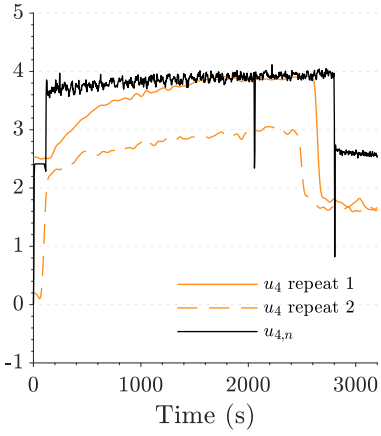

(d) Shared supply duct, u_4.

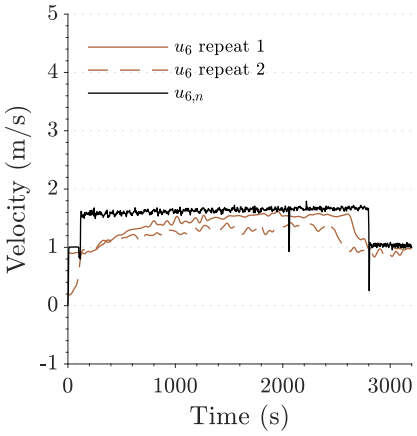

(e) Hot box supply duct, u_6.

Figure 8.18: Comparison of the experimental apparatus and the numerical set up in-duct velocities for case `P30_F2`.

from the numerical set up and the experimental apparatus, especially the maximum magnitude (less than 0.1 m/s or less than 5 %). The rate of increase is quicker for the numerical set up output compared to the experimental apparatus output. This is reflective of the much quicker increase in the hot box temperature of the numerical set up compared to the experimental apparatus. This phenomenon, related to the network-field hybrid interface, has been discussed at length in Section 8.3.1 and is not re-presented here. Another potential reason for the more rapid hot box temperature increase within the numerical set up when compared to the experimental apparatus is a lower thermal inertia within the numerical set up. As discussed in Chapter 5 values of thermophysical properties were taken from the literature. The values for the materials used in the construction of the experimental apparatus were not measured. It is possible that the thermophysical parameters of the materials used within the experimental apparatus differed from those in the literature (which are recognised to incorporate uncertainty). There is good agreement between numerical set up and the experimental apparatus u_1 data for pre and post-ignition, and pre and post-spill mode operation. The magnitude of u_1 remains steady for both datasets after spill mode is operated.

Figure 8.18b presents comparison of u_2 for the numerical set up and the experimental apparatus for the subject case. The agreement of u_2 data is less good than that from other velocity probes. The cool box exhaust duct velocity of the numerical set up is approximately 0.6 m/s (approximately 50 %) greater than that of the experimental apparatus. Phenomenologically the trend of the numerical set up does not well represent that of the experimental apparatus after ignition either. The numerical set up u_2 data show an increase in magnitude following ignition whereas the experimental apparatus u_2 data present a slight decrease in velocity. More encouragingly the post-smoke spill mode behavioural trend is in better agreement. Both the numerical set up and the experimental apparatus data present a decrease in cool box exhaust velocity following the operation of spill mode. The differences in the datasets is most likely due to the modelling of leakage within both the experimental apparatuses and the ventilation system. The leakages within the network subdomain of the numerical set up were optimised using cold flow experiments. It is likely that, in fact, leakage is dependent upon pressure within the rig. This is not captured within the numerical set up. Therefore, the leakages within the hot box, the hot box exhaust duct and the shared exhaust system of the experimental apparatus potentially increased during each experiment. This increase of leakage is likely to be caused by thermal expansion of the materials forming the experimental apparatus and pressure-induced mechanical deformation. Neither of these phenomena are captured within the numerical set up. It is therefore likely that the leakage within the hot box exhaust duct and the shared exhaust duct of the experimental apparatus differed from that within the numerical set up as temperatures in the ventilation system increased (i.e. temperature-dependent leakage area occurred within the experimental apparatus but were not captured within the numerical set up).

Figure 8.18c presents comparison of u_3 for the numerical set up and the experimental apparatus for the subject case. The data show good agreement between the pre-ignition magnitudes and trends of u_3. The absolute magnitude of u_3 output by the numerical set up is approximately 1 m/s (approximately 25 %) greater than that output by the experimental apparatus. The post-spill mode behaviour of u_3 (being a maintenance of magnitude) shows good agreement between the numerical set up data and the experimental apparatus data (though the absolute magnitude has a less good agreement). u_3 is coupled to many parameters; the leakage within the ventilation system, the minor losses at bends, junctions, and the like, and material thermophysical properties of the

boxes and the ducts. During the design of the numerical set up, data from literature and optimisation against cool cases was generally used to output leakage and minor losses. This system has multiple degrees of freedom and, due to programming constraints on the experimental campaign, suitable experiment data were limited. It is possible that the optimisation led to inaccurate values of, for example, minor loss coefficients for the numerical set up when compared to the experimental apparatus. For example, the minor loss coefficient for the arrangement of the centrifugal fans (with their housing used as the ducting) is not available in the literature. Therefore, engineering judgement had to be used based upon coefficients for similar or related arrangements. Furthermore, it is recognised that loss coefficients are poorly defined. It is possible that the mismatch in minor loss coefficients of the numerical set up and the experimental apparatus, in the relatively complex shared ventilation system arrangement, lead to lower pressures within the shared ventilation system of the numerical set up. This potentially lower upstream pressure would cause a higher u_3 magnitude within the shared exhaust duct.

Figure 8.18d presents comparison of u_4 for the numerical set up and the experimental apparatus for the subject case. The agreement between the numerical set up data and the experimental apparatus data is very good. Especially the maximum magnitude of u_4 and the pre-ignition and post-spill behaviour trend (less than 5 %). Again the rate of increase is much higher for the numerical set up data when compared to the experimental apparatus data. The numerical set up value of u_4 reaching its peak within a very short duration compared to that of the experimental apparatus which takes over 15 min. This is most likely due to the following elements of the numerical set up (which have been discussed already): the treatment of the hybrid interface within the hot box, the adiabatic boundary conditions within the network domain, the constant value leakage, and potential differences in thermophysical properties. The peak value is in good agreement for the numerical set up data and the experimental apparatus data. This is encouraging because maximum velocities typically play an important role within a fire engineering analysis. The post-smoke spill behaviour is also well captured with the magnitude of the numerical set up data dropping rapidly upon spill mode similarly to the experimental apparatus data. The numerical set up data return to the pre-ignition level once again, compared to the experimental apparatus data, for which u_4 drops below the initial pre-ignition magnitude. This is a strong indicator that the minor loss coefficients of the numerical set up do not fully represent the real losses within the ventilation system of the experimental apparatus. Evidently the losses in the fresh air supply system of the numerical set up are lower than that of the experimental apparatus.

Comparing Figure 8.18c and 8.18d illuminates an interesting occurrence. u_3 of the numerical set up is higher than that of the experimental apparatus; therefore it would be reasonable to assume that u_4 of the numerical set up would also be higher than that of the experimental apparatus. This however is not the case. The implication of this is that (1) the absolute leakage within the network domain of the numerical set up between velocity probe 3 and 4 is greater than that of the experimental apparatus and/or (2) the hot gases within the ducting of the experimental apparatus between velocity probe 3 and 4 lose substantially more enthalpy to the bounding material when compared to the numerical set up (which has a value of 0 MJ/s due to the adiabatic assumption). (1) could mean that either more hot gases escape the ventilation system of the numerical set up when compared to the experimental apparatus or more ambient temperature air leaks into the ventilation system of the experimental apparatus when compared to the numerical set up. (2) would cause reduction of the density of the hot gases within

the ventilation system of the experimental apparatus, and hence a reduction in velocity magnitude; a divergence mechanism not modelled within the numerical set up.

The final figure, Figure 8.18e gives the comparison of u_6 for the numerical set up and the experimental apparatus for case `P30_F2`. The figure shows a very good agreement between the numerical set up data and the experimental apparatus data (less than 5 %). The pre-ignition, maximum, and post-smoke spill magnitude of u_6 are similar for both the numerical set up and the experimental apparatus. The primary difference between the datasets is the speed of response upon ignition. Similarly to the box and in-duct temperature vectors and the other velocity probe data, u_6 output by the numerical set up increases in magnitude much more quickly than that of the experimental apparatus. The likely causes of this have been discussed at length in previous paragraphs and are not re-presented here.

Summary of in-duct velocities

The maximum velocities from the numerical set up and the experimental apparatus are generally in very good agreement (between 5 % to 25 %). The velocities of the numerical set up increase much more quickly when compared to the experimental apparatus. This is primarily due to the coupling of velocity to hot box temperature. The temperatures within the numerical set up increase more rapidly than those of the experimental apparatus due to: the network-field hybrid interface, uncertainties in thermophysical properties, and the modelling of the network domain as adiabatic thermal boundary conditions, and uncertainties in minor losses.

However, the agreement between u_2 for the numerical set up and the experimental apparatus is relatively poor. Although the post-spill mode trends are in good agreement, the pre-spill trends are not. This is most likely due to the modelling of leakage from both the field domain and the network subdomain within the numerical set up. The leakage of the numerical set up was designed based upon calibration against a collection of cold flow tests. This was decided to be the 'fairest' method of modelling leakage - as oppose to changing on a case-by-case basis to match the experimental apparatus data. However, it is likely that the leakage area from both the boxes and the ventilation system is dependent upon the temperature fields and pressure within the experimental apparatus. The leakage area from the numerical set up is constant. Phenomena like mechanical increases in leakage area due to thermal expansion of the ducting material are not captured within the numerical set up. This is a current limitation of the coupled hybrid model implementation and the numerical set up cases.

Another factor that may be causing differences in the velocities output by the numerical set up and the experimental apparatus is the modelling of losses within the network subdomain of the numerical set up. Minor losses, for example tees, junctions, and the fans, were specified based upon the available literature. Minor losses are widely accepted in the literature to carry wide uncertainties [72]. In some cases component minor loss coefficients were not available in the literature. Therefore, the coefficients picked, based upon similar arrangements, may not reflect those of the experimental apparatus. This will affect the pressure distribution within the network subdomain of the numerical set up and hence the output velocities.

A final point of interest is generated when comparing u_3 and u_4 output by the numerical set up. The drop between these two datasets indicates that there are large leakages from the network subdomain of the numerical set up between these two measurement points. This means that more enthalpy will advect out of the network domain to ambient (i.e. outside of the computational domain). The second factor of the numer-

ical set up that may be causing this large reduction is output velocity is the modelling of walls of the ducts as adiabatic. This model will lead to higher gas temperatures and hence lower gas density.

8.4 Relative root mean square error

The root mean square error (RMSE) is a useful method to quantify the difference or error between a prediction vector and the supposed 'real' vector. RMSE is related to the difference between the root mean squares (RMS) of the two compared vectors, which is in turn related to the l_2-norms of the two vectors. In fact, the RMS of a vector is simply the l_2-norm factored by the number of elements in the vectors. RMSE is defined as:

$$RMSE = \sqrt{\frac{1}{n}\sum_{n}\left(\hat{\phi}_i - \phi_i\right)^2} \tag{8.1}$$

where n is the number of elements in each vector, $\hat{\phi}$ is the prediction vector, ϕ is the target vector, and i is the vector index. RMSE is a method to quantify the shortest path between two vectors as a quadratic mean, and therefore quantify their agreement. It can be thought of as the 'quadratic distance' between two vectors and has the same units as the vectors.

RMSE is the generalised mean error with $p = 2$; again, it is related to the l_2-norm. Other generalised mean errors are available for use; for example, the arithmetic mean error ($p = 1$) and the cubic mean error ($p = 3$). A l_2-norm based error is however generally adopted for measurements that satisfy typical probability laws [226].

To make comparison of errors across different vector types the relative RMSE is output, by normalising the error to the span of the vector. The advantage of utilising relative RMSE as a measure of the quality of a predictive method is that the total solution vector is encapsulated within the metric.

The relative RMSE for all data signals has been computed and is presented in Figures 8.19 through 8.21. The data are grouped as box temperatures, in-duct temperatures, and in-duct velocities. Based upon distribution fitting analysis, different distributions have been applied to the data with the objective of minimising probability plot error between the data and the fit.

The figures also present the relevant means of the relative RMSE; this gives a quantitative measure of the prediction uncertainty. These data both describe how accurate the coupled hybrid model is at predicting the experimental data and also, from a practical perspective, can be used by end users to inform their use of the model as part of a fire safety design.

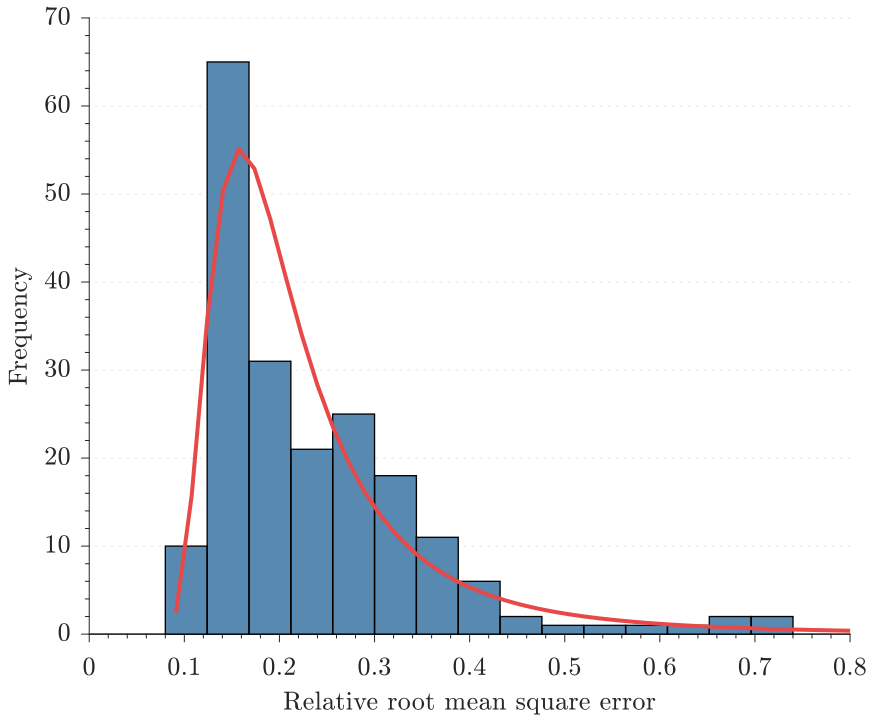

Figure 8.19: Box temperature prediction error. Generalised Extreme Value distribution fit. $\mu = 0.242$.

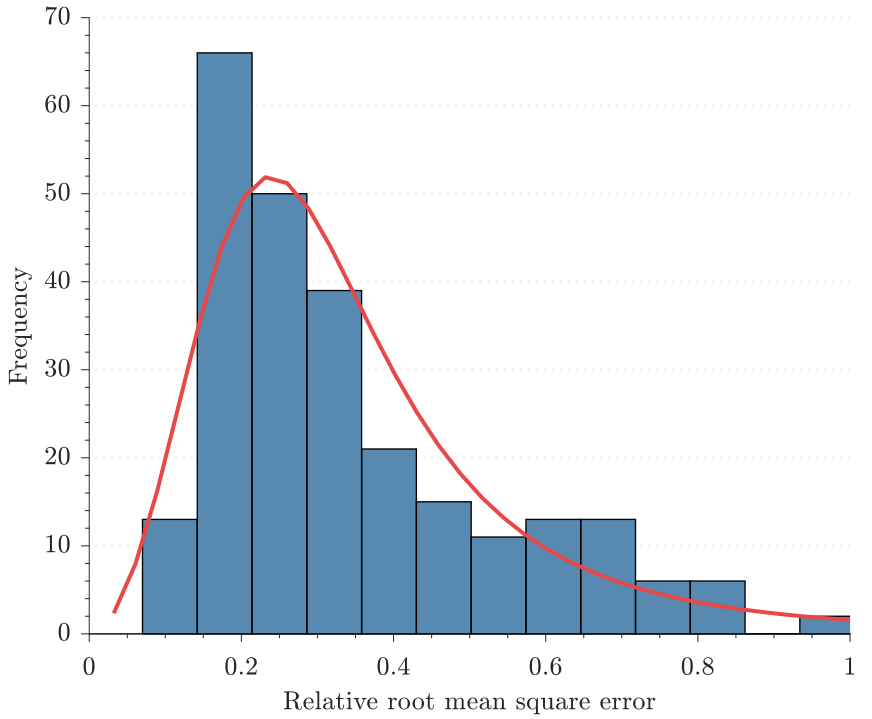

Figure 8.20: In-duct temperature prediction error. Log-logistic distribution fit. $\mu = 0.369$.

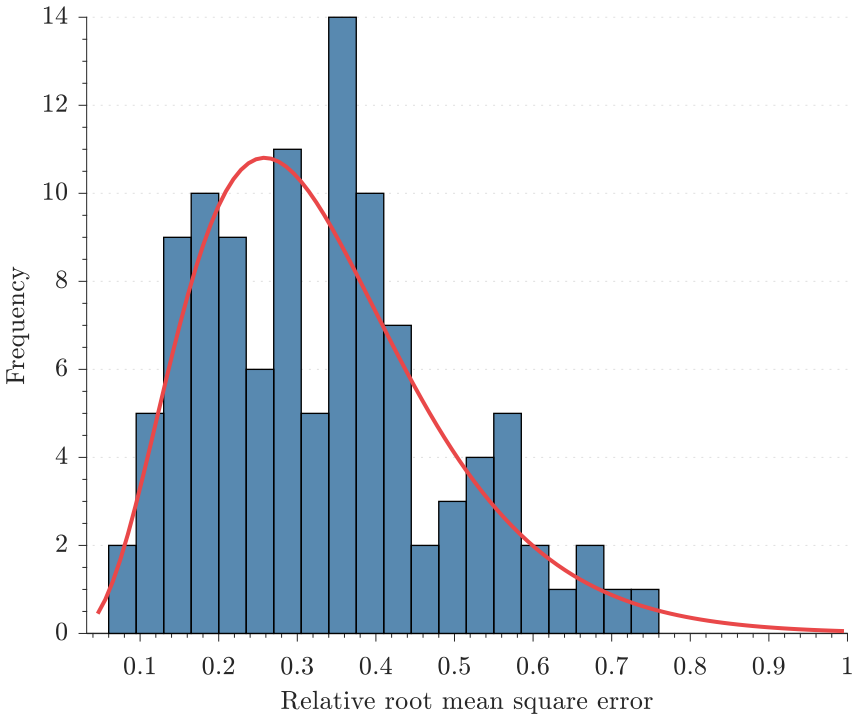

Figure 8.21: In-duct velocity prediction error. Gamma distribution fit. $\mu = 0.332$.

8.5 One final set of: closing remarks

Based upon the fulfilment of objective three of this thesis and aim one of the experimental apparatus, benchmarking of the novel coupled hybrid model implementation has been documented. This benchmarking is in the form of time-dependent output quantities for a specific case, outputting qualitative information, and also comparison of experimental and numerical data for all cases and independent variables, outputting quantitative model correction factors. The primary outcomes of the benchmarking process, which forms part of a validation exercise of the coupled hybrid model, are:

- The maximum temperatures within the non-fire enclosure are well predicted (less than 5 %). This is especially important as the coupled hybrid model implementation has been, in part, specifically scoped to quantify the fire hazard in the far field. This gives end users confidence in engineering conclusions concerning the tenability or structural performance of far field parts of the building.
- The effect of the treatment of the network-field hybrid interface, which is a defective boundary condition, may have an effect on the numerical prediction of temperature in the hot box. The inflow flow structure is laminar and presents a uniform velocity field at the field domain outlet. This is a limitation of the current coupled hybrid model. The implication of this limitation is that, when using the current code, any hybrid interface that is expected to experience flow from the network subdomain to the field domain should not be located in proximity to a fire plume. This would be especially pertinent if high vent velocities are expected or specified.
- The duct walls within the network subdomain are currently modelled as adiabatic.

Based upon the specific case, this may lead to a conservative or an unconservative fire engineering analysis. For example, if assessing tenability in the far field, temperature would be expected to rise more quickly in the prediction - this would output a lower available safe egress time and therefore be conservative. Conversely, if an analysis was being carried out to predict the time until sprinkler operation within the far field, this increased temperature would cause a quicker sprinkler operation time and therefore deliver an unconservative analysis case. The end user must make a judgement on whether this current limitation of the model will fall on the side of conservatism or unconservatism.

- Design and optimisation of the network subdomain advective losses within the numerical set up was carried out using cool flow experimental data. These losses may not be suitable for hot flow experiments. It appears that more enthalpy is being advected from the ventilation system of the numerical set up when compared to that of the experimental apparatus. This contributes to lower temperatures overall within the numerical set up.

- The difference in the advective losses between the numerical set up and the experimental apparatus may be due to pressure-induced and thermal expansion-related mechanical movement of the boxes and the ducts.

- The minor losses and leakage ducts specified within the network subdomain of the numerical set up were optimised using cool flow experimental data. The losses form part of a heavily coupled, multiple variable system with a high degree of freedom. Therefore, it is possible that the adopted arrangement of the network subdomain of the numerical set up was not fully representative of the experimental apparatus. More experimental data would have been required to reduce this uncertainty; this wasn't possible due to time constraints within the fire laboratory.

- Overall, agreement between experimental and numerical data of in-box temperatures is very good. This is very encouraging and gives end users confidence in the application of the novel model implementation as part of a robust fire engineering approach.

- The agreement between experimental and numerical data of in-duct temperature and velocity is less good but still reasonable. The numerical data tends to under-predict in-duct temperature and over-predict in-duct velocity. Model correction factors of approximately 1.4 and 0.7 for in-duct temperature and velocity respectively are put forward to be incorporated within a fire engineering analysis case.

The first stage of validation, for the subject physical and numerical parameter space, has been provided for the novel coupled hybrid implementation. Therefore, objective three of this thesis has been completed and the first aim of the experimental apparatus is met for the subject parameter space. This first stage gives end users the qualitative and quantitative means to carry out the second stage of model validation for their specific use.

Based upon the quantitative benchmarking data and model correction factors provided within this chapter, in combination with the qualitative time-dependent evaluation and observations, an end user has been given the tools to competently utilise the novel model implementation within the subject physical parameter space as part of a fire engineering analysis.

8.5.1 Qualitative example of model validation

An end user desires to carry out an analysis using the novel coupled hybrid implementation. They know that the two-way interaction of the total building system and the fire may be critical to the description of fire life safety within the building. Therefore, they will use the novel model implementation to expand the domain of the calculation whilst keeping simulation time practical.

The end user examines the qualitative benchmarking information and sees that the treatment of the network-field boundary condition (a defective boundary condition) may cause laminar jet-like velocity vectors, especially at higher vent velocities, and this may cause unrepresentative implications of the flow field within the field domain. Therefore, they build the model such that the ventilation duct and vent nearest to the fire location are captured within the field domain and not the network subdomain. The network subdomain is utilised for elements further away from the design fire.

The end user carries out a range of simulations covering a range of fire scenarios. They are interested in temperatures within the ventilation system as these affect the potential for component failure within the ducts which may cause failure of an air containment system. Based upon the quantitative benchmarking data, they are cognisant that the model is likely to under-predict temperatures within the ventilation system. Therefore, they apply a model correction to the output of the deterministic analysis.

Based upon the qualitative and quantitative benchmarking data provided, the end user has both altered the design of the analysis case and corrected the output of the analysis case to deliver a more reliable and robust fire engineering approach.

Chapter 9

Discussion

9.1 Major findings and real world implications

9.1.1 State of play

Holes within the typical fire engineering design paradigm have been uncovered; both strategically and at a granular level. Strategically, none of the examined international guidance documents recognise that hot gaseous fire products may spread via the supply system of a shared ventilation system. Specific to modelling methods, it is typical for fire engineers to greatly curtail the calculation domain to deliver output within an industry expected timeframe. This contributes to a lack of accounting for the ability of fire and smoke to spread throughout a total building system and also for the total building system to affect a fire. The implication is that a fire design may not be fully describing the life safety risk embodied within a complex building.

Existing coupled hybrid models that could potentially be used to expand the domain of the calculation have been critically reviewed. Most are not readily available and there is very little agreement as to which sub-models, what hybrid interface boundary condition, or which coupling method provides the best solution. One thing that is clear from the literature, is that the amount of robust evaluation of the existing models is not comprehensive. This lacking is especially critical for benchmarking and validation exercises.

Without this important part of model evaluation, it is impossible for fire engineers (if they could even obtain the model) to use the majority of the existing models to carry out a robust analysis, including quantification of numerical uncertainty. Where benchmarking has been carried out, the cases are not representative of how the models will typically be used in the real world. The driver behind coupled hybrid models is the analysis of not only the compartment of fire origin but connected enclosures beyond that also - and no benchmarking experiments reflected this. Therefore, use of existing coupled hybrid models would incorporate unknown life safety risk, as fire engineers could not quantify uncertainty in output due to the lack of benchmarking data.

It is also evident from the literature that the use of proprietary codes holds back collaboration and leads to dead models. At a time when international web-facilitated working is commonplace, attempt should be made to use open source models and work collaboratively. The most-used fire model (FDS) is open source and had existing coupled hybrid model capability; but the existing implementation had prohibitive limitations. Primarily, these were a lack of time-dependent mass and energy transfer through the network subdomain and the quadratic fan model.

9.1.2 Phenomena and mechanisms

For the experimental programme carried out there was no flow against the supply system of the shared ventilation system. There were however tendencies of reduced flow rate at higher nominal ϕ_P values. This was especially prevalent at lower fan duties and the reduction steadily increased during the duration of the experiments as the experimental apparatus reached thermal steady state. This behaviour indicates that, for a more fire-dominated case (higher ϕ_P) than covered within the subject experimental campaign, hot fire products may spread through a building system against the supply ventilation system. This phenomena is not addressed within current typical model solutions.

The experimental results indicate that existing empirical engineering methods for predicting fire hazard may not be applicable for more complex configurations incorporating enclosures connected with a shared mechanical ventilation system. The experimental results indicate that there is a stronger dependence upon the ratio of heat losses and enthalpy advection for such arrangements. The real world implication is that simple empirical correlations should be used with caution when designing complex buildings with recycling shared mechanical ventilation systems.

The experimental results indicate that the fire hazard in remote elements of a system with a shared ventilation system is very sensitive to the relative dominance of a fire and the mechanical ventilation system (ϕ_P). This is critical to the subject work as these phenomena would not be captured at all by the current typical fire engineering approach. To add further complications, the fire hazard within in the far field did not vary monotonically with increasing fan dominance. At both higher and lower fan duties the fire hazard was witnessed to increase in remote areas. The ramification of this is that design of mechanical systems based on curtailed domain and lack of quantification of tipping point may be leading to unforeseen fire risk. A small variation in fire size could lead to markedly increased fire hazard in remote areas in the case of a fire. Further, it would not be sufficient or conservative to oversize the fans; this could lead to another increase in fire hazard in remote areas. The use of a coupled hybrid model would allow fire engineers to quantitatively capture these very sensitive interconnected phenomena.

The experiments indicate that the relative importance of variables other than the fire size and the fan duty increases in remote areas. As the observation point moves further away from the fire source, the influence of advective enthalpy losses via leakages and heat losses become more dominant. The significance of this finding is that, when fire engineers are examining total building systems, it is important to pay close attention to variables that may, in the typical analysis paradigm, be consigned to 'second place'. These include leakages and heat losses to the building envelope.

Lastly, the experiments demonstrate that the dominance of a mechanical ventilation system over a fire decreases as leakage increases. For a building with a life safety mechanical ventilation system, commissioning prior to the opening of a building only may be insufficient. There is a likelihood that, due to increasing leakages within the building over time, the performance of the mechanical system will decrease and the dominance of fire-induced flow will increase. This suggests that re-commissioning of life safety mechanical systems should be carried out at intervals.

9.1.3 Model evaluation

A new coupled hybrid model implementation was introduced into FDS and satisfactorily numerically verified. An example test case comparing the prior version of FDS+HVAC and the improved version demonstrate that the use of the new implementation will

enable fire engineers to more realistically quantify risk within their design.

Benchmarking of the novel coupled hybrid model implementation is very promising. Temperatures within the enclosures are well predicted. Critical to the objectives of a coupled hybrid model, temperatures within the connected enclosure are well predicted by the model. Predictions of in-duct temperatures and velocities are predicted less well but still within the bounds of other coupled hybrid models in the literature. Due to a relatively large dataset reasonably robust model correction factors have been output. A model correction factor of 1.0 for enclosure temperature, 1.4 for in-duct temperatures, and 0.7 for duct velocities may be suitable.

The simple treatment of the defective boundary condition at the network-field hybrid interface is likely to be causing reductions in the agreement between the numerical predictions and the experimental data. The jet-like outlet velocity field lacks turbulence and disturbs the fire plume. This is most noticeable when the hybrid interface is located close to the fire plume. The real world inference of this is that end users of the model should test the sensitivity of the calculation output to the proximity of network-field hybrid interfaces to the fire plume. It is recommended that end users do not provide such a boundary condition where flow from the network domain will impinge directly on the rising fire plume.

Benchmarking data have been provided for the novel model implementation within the likely use parameter space. This quantitative data enables end users to confidently use the model and account for prediction uncertainties within their analysis output.

9.2 Limitations of findings and next steps

The primary qualifications and opportunities for future work embodied within the study are:

- Future investigatory work into the interaction of the near and far field of complex buildings could expand the currently documented experimental matrix to include more extreme ratios of fire to fan dominance for example. The experimental work of the project formed only part of the overall thesis and this led to the matrix being bracketed.

- On the roadmap for the model is the implementation of heat transfer between the gas phase and the condensed phase within the network subdomain. Walls within the network subdomain are currently modelled as adiabatic. This may be conservative or unconservative depending on the analysis case.

- Heat transfer between the field domain and the network subdomain where they overlap is on the development roadmap of FDS+HVAC; the proposed method is to utilise the existing Lagrangian particle capability (which incorporates solid-gas heat transfer) of FDS. For example, if a duct modelled within the network subdomain containing a flow of hot gas passes through a room modelled within the field domain, there is no transfer of energy from the hot gas flow within the duct (network subdomain) to the room (field domain).

- The ability of smoke-filling within network subdomain nodes could be added in the future to allow more adaptable use of the coupled hybrid model. Although mass storage and time-dependent transport has been added to the 1D elements of the network model, the nodes remain as 0D. It is currently possible to model

elements such as corridors or rooms using ducts as surrogates. However, currently nodes cannot be inherently used to model smoke filling times or be used as smoke reservoirs.

- Diffusion within the network subdomain could be added. Currently, the solution of the transport PDE is based upon pure advection; physical diffusion is not simulated. A potential solution for this would be to calibrate, on the fly, duct cell sizing to equate numerical diffusion to physical gas diffusion. In this way, a nuisance numerical artefact of the solution scheme could be made useful.
- The simulation of leakage area within the network subdomain could be developed. Implementation of 'continuous' or 'distributed' leakage could be investigated to enable leakage into and out of the domain in areas of under and overpressure. This is especially pertinent on either side of pressure increasing devices such as fans to be modelled more accurately. Simulation of temperature-dependent leakage areas could be added to enable leakage gaps to increase or decrease in size based upon temperature-related material expansion. Although it is recognised that defining valid input values would be liable to wide uncertainties.
- There is the opportunity for the treatment of the network-field hybrid interface to be refined. For example, the introduction of synthetic turbulence modelling within the 2D boundary condition and the use of the Lagrange method for the treatment of the defective boundary condition could be pursued.
- There is potential to introduce simple empirical correlations within the network subdomain to expand its capability and adaptability. For example, empirical models for stairs, shafts, and corridors could be implemented within either the ducts or nodes of the network subdomain.

9.3 Original contributions and the bigger picture

The specific contributions to knowledge in the field embodied in this thesis are:

- Novel coupled hybrid model implementation capable of computing time-dependant mass and enthalpy transfer through the network subdomain.
- New fan model based upon an original method of locating the operation point as the intersection of the system curve and the characteristic fan curve.
- Innovative experimental rig used to generate data of fire hazard within a multiple-compartment arrangement connected with a shared ventilation system which previously did not exist. These data have been used to benchmark the subject model but could also be used to benchmark future models.
- Illumination of the interaction of fire power and fan duty (ϕ_P) on the fire hazard of enclosures connected with a shared recycling mechanical ventilation system. Critical review of existing empirical methods, which appear not to be appropriate for such arrangements.

The model development and experimental campaign has contributed to the ongoing collaborative FDS project. The code is available for review, use, and further development by the community. It is hoped that the community continues the development of FDS and its coupled hybrid capability.

Chapter 10

Conclusion

A critical literature review was carried out on international efforts towards coupled hybrid modelling within the field of fire science and fire engineering. The review concluded that, although there have been sporadic efforts into the area, model evaluation is critically lacking. Especially benchmarking against experiments that fall within the usage parameter space of such models. The review also concluded that siloisation of workstreams has lead to wasted effort, cessation of model use and development, and abandonment of models.

Therefore, it was concluded that two key elements were required for a successful coupled hybrid model: (1) documented model evaluation, comprising of numerical verification and benchmarking against experiments within probable end user-desired parameter space; and (2) model development within an open source, well-used, and community-supported platform.

For these reasons, as part of this thesis, the following has been delivered: (1) numerical verification examination of each model sub-function and experimental benchmarking using specifically-designed and carried out experiments; and (2) model development within the open source, continuously-integrated, and collaborative FDS project.

The choice was made to develop within the FDS project. At the time of project initiation FDS had a network model, called HVAC, which enabled coupled hybrid modelling capabilities. However, the existing capability was critically lacking with respect to time-dependent transport of mass, species, and energy. Additionally the existing fan model did not perform physically for arrangement involving interconnected field enclosures. Therefore, transient transport of conserved variables and an original quadratic fan model were implemented into the model.

The transient transport routines enable time-dependent fire engineering assessments to be carried out; for example, occupant evacuation analysis. The novel fan model is based upon establishment of the unsteady operation point (the intersect of the characteristic fan curve and the system curve). This method has not been adopted previous to this work.

Satisfactory numerical verification of each constituent part of the novel coupled hybrid model implementation has been carried out. For example, mass transport, energy conservation, branching and combining ducts, and species conservation.

A novel experimental rig was specifically designed to meet the objectives of this study. The two aims of the experimental rig were: (1) to provide high quality benchmarking data and (2) to investigate risks embedded with the typical fire safety design methodology.

To meet aim (1), the experimental rig was designed to occupy the parameter space

that the model is most likely to be used within. Output quantities were picked to reflect those typically used within fire engineering analyses. The rig was designed with the mind of a modeller - ensuring that uncertainties in geometry, material properties, and boundary conditions were kept to a minimum.

In order to fulfil (2), the experimental rig was designed in cognisance of a review of international guidance documents and Standards concerned with the design of shared mechanical exhaust systems. The experiments demonstrated that there is a tendency, at high fire/fan power ratios (ϕ_P), for the fire-induced flow to compromise the supply ventilation system - potentially leading to spread of fire product against the direction of the supply system. The experiments also demonstrated that there is a very complex non-linear coupling between a fire and the mechanical ventilation system with respect to fire hazard in the far field and that simply oversizing mechanical systems may not always deliver a safer arrangement. This reinforces the importance of a "total building" type analysis, which can only currently be practicably achieved using an alternative to the typical CFD-based fire modelling paradigm (for example, coupled hybrid modelling).

Additionally, analysis of the experiments conclude that simple empirical methods may not describe fire hazard for arrangements comprising shared recycling ventilation systems. These methods may under-account for the relative affect of heat losses compared to advection losses. Furthermore, the current typical fire engineering analysis framework, of considering the near field only, does not enable the fire engineer to capture these complex interactions. It is entirely likely that conclusions are drawn and requirements defined based upon an incomplete description of the interaction between the building system and the fire (and the fire hazard embodied therein).

The coupled hybrid model described in this thesis can be used to quantitatively examine the fire hazard in both the near and far field for complex arrangements comprising a shared mechanical ventilation system. This model can explicitly account for the interaction between a total system and a fire.

The data from the novel experimental rig were used as benchmarking data for the developed coupled hybrid model implementation. The model predicted enclosure temperatures very well (between 5 % to 20 %) and ventilation temperatures and velocities slightly less well - but still reasonably (between 5 % to 50 %).

The experimental data, consisting of over thirty experiments across eighteen cases, were used to output model correction factors for output quantities used typically within fire engineering assessments. Model correction factors of 1.0 for enclosure temperatures, 1.4 for in-duct temperatures, and -0.7 for in-duct velocities are put forward. These quantitative model correction factors can be used by end users, as part of their case-specific validation exercise, to carry out a robust quantitative analysis. This analysis can form part of an overall fire engineering approach for a complex building featuring shared ventilation systems.

The overarching aim of this thesis was to facilitate the reduction of unquantified hazard within complex elements of the built environment. The reasoning being that if the hazard can be more robustly assessed then the design can be adapted and also risk can be more accurately described to stakeholders. Towards this aim, a novel coupled hybrid model implementation was developed and evaluated. Benchmarking delivered quantitative model correction factors which make it usable for engineers to carry out total building type analysis and reduce unquantified fire hazard. Furthermore, experimental data were used to critically examine typical model solutions and simplified methods used for shared ventilation systems. The conclusion was made that for higher nominal ϕ_P values there may be a tendency for supply system ventilation to be overcome by

fire-induced flow - which is not addressed within model solutions and should be examined further for a wider range of values of ϕ_P. Secondly, simplified methods may not be applicable for modern arrangements with shared ventilation systems as they do not reflected the increased dominance of boundary heat losses over advection heat transfer and they are recommended to be used with care in these scenarios.

It is the sincere hope of the author that the coupled hybrid model be used by fire engineers to help deliver safer buildings. Furthermore, that it is also developed and evaluated, both by himself and other members of the active community, as part of the ongoing development of the open source FDS project.

Bibliography

[1] H. Baum, O. Ezekoye, K. B. Mcgrattan, and R. G. Rehm, "Mathematical modeling and computer simulation of fire phenomena," *Theoretical and Computational Fluid Dynamics*, vol. 6, no. 2-3, pp. 125–139, 1994.

[2] B. J. McCaffrey and G. Heskestad, "A robust bidirectional low-velocity probe for flame and fire application," *Combustion and Flame*, vol. 26, no. C, pp. 125–127, 1976.

[3] A. Fraser and M. Cummion, *King Charles II.* London: Weidenfeld and Nicolson London, 1979.

[4] B. J. Meacham and I. J. van Straalen, "A socio-technical system framework for risk-informed performance-based building regulation," *Building Research and Information*, vol. 46, no. 4, pp. 444–462, 2018.

[5] G. C. Foliente, "Developments in performance-based building codes and standards," *Forest Products Journal*, vol. 50, pp. 12–21, 2000.

[6] W. K. Chow, "Performance-based approach to determining fire safety provisions for buildings in the Asia-Oceania regions," *Building and environment*, vol. 91, pp. 127–137, 2015.

[7] G. Yeoh, R. Yuen, S. Lo, and D. Chen, "On numerical comparison of enclosure fire in a multi-compartment building," *Fire Safety Journal*, vol. 38, pp. 85–94, 2 2003.

[8] M. Ali and K. Moon, "Structural Developments in Tall Buildings: Current Trends and Future Prospects," *Architectural Science Review*, vol. 50:3, pp. 205–223, 2007.

[9] R. Howard and B. C. Björk, "Building information modelling - Experts' views on standardisation and industry deployment," *Advanced Engineering Informatics*, vol. 22, no. 2, pp. 271–280, 2008.

[10] T. M. Williams, "The need for new paradigms for complex projects," *International Journal of Project Management*, vol. 17, no. 5, pp. 269–273, 1999.

[11] M. E. Paté-Cornell, "Organizational Aspects of Engineering System Safety: The Case of Offshore Platforms," *Science*, vol. 250, no. 4985, pp. 1210–1217, 1990.

[12] A. Afzal, Z. Ansari, A. R. Faizabadi, and M. K. Ramis, "Parallelization Strategies for Computational Fluid Dynamics Software: State of the Art Review," *Archives of Computational Methods in Engineering*, vol. 24, no. 2, pp. 337–363, 2017.

[13] E. Woźniak-Szpakiewicz and S. Zhao, "Modular construction industry growth and its impact on the built environment," *Czasopismo Techniczne*, vol. 2018, no. Volume 12, pp. 43–52, 2018.

[14] E. Galea, "On the Field Modelling Approach to the Simulation of Enclosure Fires," *Journal of Fire Protection Engineering*, vol. 1, no. 1, pp. 11–22, 1989.

[15] B. Karlsson and J. Quintiere, *Enclosure fire dynamics*, vol. 1. New York, USA: CRC Press LLC, 2000.

[16] British Standard Institution, "BS 9999: Code of practice for fire safety in the design, maintenance and use of buildings," tech. rep., BSI, London, 2008.

[17] Standards Australia Limited/Standards New Zealand, "AS/NZS 1668.1: The use of ventilation and air conditioning in buildings, Part 1: Fire and smoke control in buildings," 2015.

[18] NFPA, *Standard for Smoke Control Systems*. Quincy, MA: National Fire Protection Association, 2018.

[19] C. R. Harrel, B. K. Ghosh, and R. Bowden, "Simulation using promodel," *Simulation*, vol. 14, p. 3, 2004.

[20] K. Lewis, W. Chen, and L. Schmidt, *Decision making in engineering design*. New York, USA: ASME Press, 2006.

[21] P. Y. Papalambros and D. J. Wilde, *Principles of optimal design: modeling and computation*. Cambridge university press, 2000.

[22] American Society for Testing and Materials, "ASTM E1355-12, Standard Guide for Evaluating the Predictive Capabilities of Deterministic Fire Models," 2012.

[23] M. Ahrens, "Home Structure Fires," *National Fire Protection Association*, vol. Available, no. September, p. 139, 2016.

[24] Department for Communities and Local Government, "Fire Statistics: Great Britain April 2012 to March 2013," 2013.

[25] A. M. Hasofer and I. Thomas, "Analysis of fatalities and injuries in building fire statistics," *Fire Safety Journal*, vol. 41, no. 1, pp. 2–14, 2006.

[26] P. G. Holborn, P. F. Nolan, and J. Golt, "An analysis of fatal unintentional dwelling fires investigated by London Fire Brigade between 1996 and 2000," *Fire Safety Journal*, vol. 38, no. 1, pp. 1–42, 2003.

[27] J. G. Quintiere and C. A. Wade, "Compartment Fire Modeling," in *SFPE Handbook of Fire Protection Engineering* (M. J. Hurley, D. T. Gottuk, J. R. Hall Jr., K. Harada, E. D. Kuligowski, M. Puchovsky, J. L. Torero, J. M. Watts Jr., and C. J. Wieczorek, eds.), pp. 981–995, New York, NY: Springer New York, 2016.

[28] H. T. Z. Kodur V. K. R., *SFPE Handbook of Fire Protection Engineering*. New York: Springer, fifth edit ed., 2016.

[29] J. J. Lu, Y. Xing, C. Wang, and X. Cai, "Risk factors affecting the severity of traffic accidents at Shanghai river-crossing tunnel," *Traffic injury prevention*, vol. 17, no. 2, pp. 176–180, 2016.

[30] K. Meredith and V. Vukčević, "Towards Resolving an Idealized Fire Sprinkler Atomization Pattern with VOF Modeling and Adaptive Mesh Refinement," in *14th International Conference on Liquid Atomization and Spray Systems*, 2018.

[31] F. Liu, S. Zhao, M. Weng, and Y. Liu, "Fire risk assessment for large-scale commercial buildings based on structure entropy weight method," *Safety science*, vol. 94, pp. 26–40, 2017.

[32] G. Zigh, I. Ong, and K. Kang, "CFD application for station fires," in *Proceedings of the 10th BHR Group international symposium on aerodynamics and ventilation of vehicle tunnels, Boston, MA, USA*, 2000.

[33] M. Tabarra, D. Abi-Zadeh, N. Mawjee, and I. Kingham, "Modelling smoke migration in the redeveloped King's Cross St Pancras underground station," in *11th International Symposium on Aerodynamics & Ventilation of Vehicle Tunnels. UK: BHR GROUP*, pp. 243–255, 2003.

[34] B. Ralph and R. Carvel, "Coupled hybrid modelling in fire safety engineering; a literature review," 2018.

[35] L. Formaggia, J. F. Gerbeau, F. Nobile, and a. Quarteroni, "On the coupling of 3D and 1D Navier-Stokes equations for flow problems in compliant vessels," *Computer Methods in Applied Mechanics and Engineering*, vol. 191, pp. 561–582, 2001.

[36] S. J. Emmerich and D. Hirnikel, "Validation of multizone IAQ modeling of residential-scale buildings: A review," *ASHRAE Transactions*, vol. 107 PART 2, pp. 619–628, 2001.

[37] L. Wang and Q. Chen, "Validation of a Coupled Multizone-CFD Program for Building Airflow and Contaminant Transport Simulations," *HVAC&R Research*, vol. 13, no. 2, pp. 267–281, 2007.

[38] D. J. Burton, A. Grandison, M. Patel, E. Galea, and J. Ewer, "Development of a Hybrid Field/Zone Fire Model," in *Fire Safety Science-Proceedings Of The Tenth International Symposium*, pp. 1373–1386, International Association for Fire Safety Science, 2011.

[39] J. A. Prince, *Coupled 1D-3D simulation of flow in subway transit networks*. PhD thesis, Imperial College London, 2015.

[40] F. Colella, G. Rein, V. Verda, and R. Borchiellini, "Multiscale modeling of transient flows from fire and ventilation in long tunnels," *Computers and Fluids*, vol. 51, no. 1, pp. 16–29, 2011.

[41] G. Manca, G. Cervone, and K. C. Clarke, "Combined approach of a coupled fire model with atmospheric releases: The case of the 2003 glacier wildfires," *European Journal of Remote Sensing*, vol. 47, no. 1, pp. 181–193, 2014.

[42] C. Gordon, C. Cooper, C. A. Senior, H. Banks, J. M. Gregory, T. C. Johns, J. F. B. Mitchell, and R. A. Wood, "The simulation of SST, sea ice extents and ocean heat transports in a version of the Hadley Centre coupled model without flux adjustments," *Climate Dynamics*, vol. 16, no. 2-3, pp. 147–168, 2000.

[43] J. E. Floyd, S. P. Hunt, F. W. Williams, and P. A. Tatem, "Fire and Smoke Simulator (FSSIM) Version 1 - Theory Manual," tech. rep., Naval Research Laboratory, 3 2004.

[44] US Department of Transportation, "Subway Environmental Design Handbook Volume II: Subway Environment Simulation Computer Program, Version 4. Part 1, User's Manual," 1997.

[45] S. M. Olenick and D. J. Carpenter, "An Updated International Survey of Computer Models for Fire and Smoke," *Journal of Fire Protection Engineering*, vol. 13, pp. 87–110, 2003.

[46] R. Peacock, W. Jones, and G. Forney, "CFAST - Consolidated Model of Fire Growth and Smoke Transport (version 6) User's Guide," Tech. Rep. December, NIST, 2012.

[47] C. A. Wade, *BRANZFIRE Technical reference guide.* BRANZ, 2000.

[48] X. Zhang, S. Wang, J. Wang, and R. Giacomo, "A simplified model to predict smoke movement in vertical shafts during a high-rise structural fire," *Journal of Engineering Science and Technology Review*, vol. 7, no. 2, pp. 29–38, 2014.

[49] K. McGrattan, S. Hostikka, R. McDermott, J. Floyd, C. Weinschenk, and K. Overholt, "Sixth Edition Fire Dynamics Simulator Technical Reference Guide Volume 2: Verification," tech. rep., NIST, 2017.

[50] J. Ewer, E. Galea, M. Patel, S. Taylor, B. Knight, and M. Petridis, "Smartfire: an Intelligent Cfd Based Fire Model," *Journal of Fire Protection Engineering*, vol. 10, no. 1, pp. 13–27, 1999.

[51] FM Global Rhode Island USA, "FireFOAM," 2014.

[52] S. Welch, S. Miles, S. Kumar, T. Lemaire, and A. Chan, "FIRESTRUC - Integrating advanced three-dimensional modelling methodologies for predicting thermomechanical behaviour of steel and composite structures subjected to natural fires," *Fire Safety Science*, pp. 1315–1326, 2008.

[53] D. Duthinh, K. McGrattan, and A. Khaskia, "Recent advances in fire-structure analysis," *Fire Safety Journal*, vol. 43, no. 2, pp. 161–167, 2008.

[54] L. Formaggia, J.-F. Gerbeau, F. Nobile, and A. Quarteroni, "On the coupling of 3D and 1D Navier–Stokes equations for flow problems in compliant vessels," *Computer Methods in Applied Mechanics and Engineering*, vol. 191, no. 6, pp. 561–582, 2001.

[55] S. a. Urquiza, P. J. Blanco, M. J. Vénere, and R. a. Feijóo, "Multidimensional modelling for the carotid artery blood flow," *Computer Methods in Applied Mechanics and Engineering*, vol. 195, pp. 4002–4017, 2006.

[56] P. J. Blanco, L. A. M. Alvarez, and R. A. Feijoo, "Hybrid element-based approximation for the Navier – Stokes equations in pipe-like domains," *Computer Methods in Applied Mechanics and Engineering*, vol. 283, pp. 971–993, 2015.

[57] F. Nobile, "Coupling strategies for the numerical simulation of blood flow in deformable arteries by 3D and 1D models," *Mathematical and Computer Modelling*, vol. 49, no. 11-12, pp. 2152–2160, 2009.

[58] A. C. I. Malossi, P. J. Blanco, P. Crosetto, S. Deparis, and A. Quarteroni, "Implicit coupling of one-dimensional and three-dimensional blood flow models with compliant vessels," *Multiscale modeling simulation*, vol. 11, no. 2, pp. 474–506, 2013.

[59] T. K. Dobroserdova and M. a. Olshanskii, "A finite element solver and energy stable coupling for 3D and 1D fluid models," *Computer Methods in Applied Mechanics and Engineering*, vol. 259, pp. 166–176, 2013.

[60] E. Soudah, R. Rossi, and S. Idelsohn, "A reduced-order model based on the coupled 1D-3D finite element simulations for an efficient analysis of hemodynamics problems," *Computer mechanics*, vol. 54, pp. 1013–1022, 2014.

[61] L. Formaggia, F. Nobile, A. Quarteroni, and A. Veneziani, "Multiscale modelling of the circulatory system: a preliminary analysis," *Computing and Visualization in Science*, vol. 2, pp. 75–83, 1999.

[62] G. Montenegro, A. Onorati, and A. Della Torre, "The prediction of silencer acoustical performances by 1D, 1D-3D and quasi-3D non-linear approaches," *Computers and Fluids*, vol. 71, pp. 208–223, 2013.

[63] G. Montenegro, T. Cerri, A. D. Torre, A. Onorati, M. Fiocco, and D. Borghesi, "Fluid Dynamic Optimization of a Moto3TM Engine by Means of 1D and 1D-3D Simulations," *SAE Int. J. Engines*, vol. 9, pp. 588–600, 2016.

[64] A. D. Torre, G. Montenegro, T. Cerri, and A. Onorati, "A 1D/Quasi-3D Coupled Model for the Simulation of I.C. Engines: Development and Application of an Automatic Cell-Network Generator," *SAE Int. J. Engines*, vol. 10, pp. 471–482, 2017.

[65] G. Montenegro, A. D. Torre, T. Cerri, A. Onorati, L. Nocivelli, and M. Fiocco, "1D-3D Coupled Simulation of the Fuel Spray Propagation Inside the Air-Box of a Moto3 Motorbike: Analysis of Spray Targeting and Injection Timing," in *SAE Technical Paper*, SAE International, 2017.

[66] J. Bohbot, M. Miche, P. Pacaud, and A. Benkenida, "Multiscale Engine Simulations using a Coupling of 0-D / 1-DModel with a 3-D Combustion Code," *Oil & Gas Science and Technology*, vol. 64, no. 3, pp. 337–359, 2009.

[67] M. Mossi, "Simulation of benchmark and industrial unsteady compressible turbulent fluid flows," tech. rep., LIN, 1999.

[68] B. Rey, M. Mossi, P. Molteni, J. Vos, and M. Deville, "Coupling of CFD software for the computation of unsteady flows in tunnel networks," *13th International Symposium on Aerodynamics and Ventilation of Vehicle Tunnels*, vol. 1, no. January 2009, pp. 321–333, 2009.

[69] M. Tabarra, J. Alston, R. Potter, and D. Abi-zadeh, "Integrated ventilation system design of the Second Avenue Subway," in *12th International Symposium on Aerodynamics and Ventilation of Vehicle Tunnels*, (Portoroz, Slovenia), 2006.

[70] D. Charters, W. Gray, and A. McIntosh, "A computer model to assess fire hazards in tunnels (FASIT)," *Fire Technology*, vol. 30, pp. 134–154, 1994.

[71] J. Prince, J. Peiro, and M. Tabarra, "Design of a Multi-Dimensional Dynamic Fluid Network," in *First international conference in numerical and experimental aerodynamics of road vehicles and trains*, (Bordeaux, France), pp. 1–2, 2014.

[72] J. Prince and J. Peiro, "Application of a Lagrange multiplier approach for flow rate defective boundary conditions in a finite volume framework," in *Proceedings of the 23rd UK Conference of the Association for Computational Mechanics in Engineering*, (Swansea, Wales), pp. 207–210, 2015.

[73] L. Wang and Q. Chen, "Theoretical and numerical studies of coupling multizone and CFD models for building air distribution simulations.," *Indoor air*, vol. 17, pp. 348–61, 10 2007.

[74] C. O. R. Negriio, "Integration of computational fluid dynamics with building thermal and mass flow simulation," *Energy and Buildings*, vol. 27, pp. 155–165, 1998.

[75] L. Wang and N. H. Wong, "Coupled simulations for naturally ventilated residential buildings," *Automation in Construction*, vol. 17, pp. 386–398, 2008.

[76] J. Srebric, J. Yuan, and A. Novoselac, "On-site experimental validation of a coupled multizone and CFD model for building contaminant transport simulations," *ASHRAE Transactions*, vol. 114 PART 1, pp. 273–281, 2008.

[77] M. Bartak, I. Beausoleil-Morrison, J. a. Clarke, J. Denev, F. Drkal, M. Lain, I. a. Macdonald, a. Melikov, Z. Popiolek, and P. Stankov, "Integrating CFD and building simulation," *Building and Environment*, vol. 37, pp. 865–871, 2002.

[78] L. L. Wang, W. S. Dols, and Q. Chen, "Using CFD Capabilities of CONTAM 3.0 for Simulating Airflow and Contaminant Transport in and around Buildings," *HVAC&R Research*, vol. 16, no. February 2015, pp. 749–763, 2010.

[79] A. Schaelin, V. Dorer, J. v. d. Maas, and A. Moser, "Improvement of multizone model predictions by detailed flow path values from CFD calculations," *ASHRAE Transactions-American Society of Heating Refrigerating Airconditioning Engin*, vol. 99, no. 2, pp. 709–720, 1993.

[80] J. L. Coen and W. Schroeder, "Use of spatially refined satellite remote sensing fire detection data to initialize and evaluate coupled weather-wildfire growth model simulations," *Geophysical Research Letters*, vol. 40, no. 20, pp. 5536–5541, 2013.

[81] J. L. Coen and W. Schroeder, "The High Park fire: coupled weather-wildland fire model simulation of a windstorm-driven wildfire in Colorado's Front Range," *Journal of Geophysical Research: Atmospheres*, pp. 131–146, 2014.

[82] C. C. Simpson, J. J. Sharples, and J. P. Evans, "Resolving vorticity-driven lateral fire spread using the WRF-Fire coupled atmosphere–fire numerical model," *Natural Hazards and Earth System Science*, vol. 14, no. 9, pp. 2359–2371, 2014.

[83] T. Xu, J. Wang, and W. Fan, "A New Method of Modeling of a Fire - Combination of Field Modeling and Zone Modeling," in *Proceedings of the Symposium on Engineering Thermophysics*, (ZhenJiang, China), 1991.

[84] J. Wang and W. Fan, "Numerical simulation of fire process of multi-rooms," *Journal of China University of Science and Technology*, vol. 26, pp. 204–209, 1996.

[85] W. Fan, Z. Yan, H. Ran, Y. Chen, and H. Zhao, "A combined field-zone model for compartment fire," in *Proceedings of the first Asian Conference on Fire Science and Technology*, (Beijing, China), International Association for Fire Safety Science, 1992.

[86] W. Fan and X. Wang, "A new numerical calculation method for zone modelling to predict smoke movement in building fires," in *Fire Safety Science - Proceedngs of the Fifth International Symposium*, pp. 487–498, 1997.

[87] R. D. Peacock, G. P. Forney, and P. A. Reneke, "CFAST - Consolidated Model of Fire Growth and Smoke Transport (Version 6) Technical Reference Guide," Tech. Rep. October, NIST, 2011.

[88] J. Yao, W. Fan, S. Kohyu, and K. Daisuke, "Verification and application of field-zone-network model in building fire," *Fire safety journal*, vol. 33, pp. 35–44, 1999.

[89] W. K. Chow, "Simulation of Carbon Monoxide Level in Enclosed Car Parks Using an Air Flow Network Program," *Tunnelling and Underground Space Technology*, vol. 11, no. 2, pp. 237–240, 1996.

[90] D. J. Burton, *Development of a Novel Hybrid Field and Zone Fire Model.* PhD thesis, University of Greenwich, 2011.

[91] J. Hua, J. Wang, and K. Kumar, "Development of a hybrid field and zone model for fire smoke propagation simulation in buildings," *Fire Safety Journal*, vol. 40, pp. 99–119, 3 2005.

[92] J. I. Jie, Y. Rui, S. U. N. Zhanhui, and Y. Hongyong, "Validation and Evaluation of Large Eddy Simulation Based Field-Zone Model for Smoke Movement in Building Fires," in *2006 International Symposium on Safety Science and Technology*, vol. 2, pp. 721–725, 2006.

[93] H. Ren, Y. Jin, and K. Wang, "Study on Simulation Training System of Ship Fire," *2009 International Conference on Computational Intelligence and Software Engineering*, pp. 1–4, 2009.

[94] A. Grandison, D. J. Burton, M. Patel, E. Galea, Z. Wang, and F. Jia, "Probabilistic Framework for Onboard Fire Safety, Integrated Fire Model (WP2.2)," tech. rep., FSEG/UoG, Greenwich, UK, 2011.

[95] J. Floyd, "Coupling a network HVAC model to a computational fluid dynamics model using large eddy simulation," in *Fire and Evacuation Modeling Technical Conference 2011*, (Baltimore, Maryland), 2011.

[96] J. Wang, J. Hua, and K. Kumar, "Modeling of smoke propagation in multiple compartment using combined field and zone model," in *Progress in Safety Science and Technology Volume 4:Proceedings of the 2004 International Symposium on Safety Science and Technology*, pp. 1158–1163, 2004.

[97] Y. Jiao, J.-h. Wang, M.-j. Xiao, T. Xu, and W.-j. Chen, "Development of Field-zone-net Model for Fire Smoke Propagation Simulation in Ships," in *7th International Conference on Intelligent Computation Technology and Automation*, (Changsha, China), pp. 190–193, 2014.

[98] Z.-T. Li, Y.-X. Zhu, and Q.-S. Yan, "Smoke Movement In Tunnel Network," in *Asia-Oceania Symposium on Fire Science & Technology*, pp. 320–328, 1995.

[99] J. Jiang and X. Wang, "Field-network model for mine fire smoke movement," *Transactions of Nonferrous Metals Society of China*, vol. 7, no. 4, pp. 164–168, 1997.

[100] W. Deng, X. Li, and Y. Zhu, "Coupling Simulation on Subway Tunnel Smoke," *Proceedings: Building Simulation*, pp. 1246–1253, 2007.

[101] J. H. Jung, N. Hur, J.-p. Lee, and J. K. Kim, "The 1D-3D Simulation for Smoke Ventilation in a Rescue Station of a Railroad Tunnel under the Fire," *Korean Journal of Air-Conditioning and Refrigeration Engineering*, vol. 22, no. 10, pp. 665–671, 2010.

[102] CD-adapco, "STAR-CD," 1980.

[103] F. Colella, G. Rein, R. Borchiellini, R. Carvel, J. L. Torero, and V. Verda, "Calculation and design of tunnel ventilation systems using a two-scale modelling approach," *Building and Environment*, vol. 44, no. 12, pp. 2357–2367, 2009.

[104] F. Colella, G. Rein, R. Borchiellini, R. O. Carvel, J. L. Torero, and V. Verda, "Calculation and design of tunnel ventilation systems using a two-scale modelling approach," *Building and Environment*, vol. 44, pp. 2357–2367, 6 2009.

[105] F. Colella, G. Rein, R. O. Carvel, and J. L. Torero, "Tunnel ventilation effectiveness in fire scenarios," *FS-World Magazine*, pp. 36–40, 2010.

[106] F. Colella, *Multiscale Modelling of Tunnel Ventilation Flows and Fires.* PhD thesis, Politecnico di Torino, 5 2010.

[107] F. Colella, G. Rein, R. O. Carvel, P. Reszka, and J. L. Torero, "Analysis of the ventilation systems in the Dartford tunnels using a multiscale modelling approach," *Tunnelling and Underground Space Technology*, vol. 25, pp. 423–432, 2010.

[108] F. Colella, *Multiscale Modelling of Tunnel Ventilation Flows and Fires.* PhD thesis, Politecnico di Torino, 2010.

[109] F. Colella, G. Rein, V. Verda, R. Borchiellini, and J. L. Torero, "Time-Dependent Multiscale Simulations of Fire Emergencies in Longitudinally Ventilated Tunnels," *Fire Safety Science - Proceedings of the Tenth International Symposium*, vol. 10, pp. 359–372, 2011.

[110] F. Colella, G. Rein, R. Borchiellini, and J. L. Torero, "A Novel Multiscale Methodology for Simulating Tunnel Ventilation Flows During Fires," *Fire Technology*, vol. 47, pp. 221–253, 2011.

[111] R. O. Gauntt, R. K. Cole, C. M. Erickson, R. G. Gido, R. D. Gasser, S. B. Rodriguez, and M. F. Young, "MELCOR Computer Code Manuals, Vol. 2: Reference Manuals, Version 1.8," tech. rep., NRC, 2000.

[112] ASHRAE, *Fundamentals Handbook*. ASHRAE, 2007.

[113] I. M. Vermesi, "The Feasibility of Multiscale Modelling of Tunnel Fires Using FDS," 2013.

[114] D. U. Tao, Y. Dong, P. Shini, X. Yimin, and Z. Fan, "Longitudinal ventilation for smoke control of urban traffic link tunnel : hybrid field-network simulation," *Procedia Engineering*, vol. 84, pp. 586–594, 2014.

[115] C. D. E. Ang, G. Rein, J. Peiro, and R. Harrison, "Simulating longitudinal ventilation flows in long tunnels: Comparison of full CFD and multi-scale modelling approaches in FDS6," *Tunnelling and Underground Space Technology*, vol. 52, pp. 119–126, 2016.

[116] I. Vermesi, G. Rein, F. Colella, M. Valkvist, and G. Jomaas, "Reducing the computational requirements for simulating tunnel fires by combining multiscale modelling and multiple processor calculation," *Tunnelling and Underground Space Technology*, vol. 64, pp. 146–153, 2017.

[117] A. Vaitkevicius, F. Colella, and R. Carvel, "Investigating the throttling effect in tunnel fires," *Fire Technology*, vol. 52, no. 5, pp. 1619–1628, 2016.

[118] C. D. E. Ang, *Investigation of a Computationally Efficient Multi-Scale Modelling Method in Long Tunnels for Fire Dynamics Simulator 6*. PhD thesis, Imperial College London, 2014.

[119] C. D. E. Ang, *Investigation of computationally efficient multi-scale modelling method in long tunnels for FDS 6*. PhD thesis, Imperial College London, 2014.

[120] K. Mcgrattan, S. Hostikka, R. Mcdermott, J. Floyd, C. Weinschenk, and K. Overholt, "Fire Dynamics Simulator Technical Reference Guide Volume 2 : Verification," 2013.

[121] K. McGrattan, S. Hostikka, R. McDermott, J. Floyd, C. Weinschenk, and K. Overholt, "Sixth Edition Fire Dynamics Simulator Technical Reference Guide Volume 3 : Validation," tech. rep., NIST, 2015.

[122] L. Audouin, L. Rigollet, H. Prétrel, W. Le Saux, and M. Röwekamp, "OECD PRISME project: Fires in confined and ventilated nuclear-type multi-compartments - Overview and main experimental results," *Fire Safety Journal*, vol. 62, no. PART B, pp. 80–101, 2013.

[123] K. Foote, "1986 LLNL Enclosure Fire Tests Data Report. Technical Report UCID-21236," tech. rep., Lawrence Livermore National Laboratory, 1987.

[124] X. Zhu, *Hybrid Model for Smoke and Heat Propagation in Complex Structures*. PhD thesis, Carleton University, 2009.

[125] A. Kashef, G. Hadjisophocleous, X. Zhu, and D. E. Amundsen, "Algorithm for Smoke Modeling in Large , Multicompartmented Buildings — Development of a Hybrid Model," *ASHRAE Transactions*, vol. 117, no. 1, pp. 769–776, 2011.

[126] G. Hadjisophocleous, A. Kashef, X. Zhu, and D. Amundsen, "Algorithm for Smoke Modeling in Large, Multi-Compartmented Buildings–Implementation of the Hybrid Model.," *ASHRAE Transactions*, vol. 011, pp. 777–786, 2011.

[127] W. Chow, "Multi-Cell Concept for Simulating Fires in Big Enclosures Using a Zone Model," 1996.

[128] S. Jain, S. Kumar, S. Kumar, and T. P. Sharma, "Numerical simulation of fire in a tunnel: Comparative study of CFAST and CFX predictions," *Tunnelling and Underground Space Technology*, vol. 23, no. 2, pp. 160–170, 2008.

[129] C. Xiaojun, "Simulation of temperature and smoke distribution of a tunnel fire based on modifications of multi-layer zone model," *Tunnelling and Underground Space Technology*, vol. 23, no. 1, pp. 75–79, 2008.

[130] British Standard Institution, "BS 7974: Application of fire safety engineering principles to the design of buildings - Code of practice," tech. rep., BSI, London, 2001.

[131] K. McGrattan, S. Hostikka, R. McDermott, J. Floyd, C. Weinschenk, and K. Overholt, "Sixth Edition Fire Dynamics Simulator Technical Reference Guide Volume 3: Validation," tech. rep., NIST, 2017.

[132] S. R. Rakitin, *Software verification and validation for practitioners and managers.* Artech House, Inc., 2001.

[133] A. Veneziani and C. Vergara, "An approximate method for solving incompressible Navier-Stokes problems with flow rate conditions," *Computer Methods in Applied Mechanics and Engineering*, vol. 196, no. 9-12, pp. 1685–1700, 2007.

[134] K. Mcgrattan, R. Peacock, and K. Overholt, "Fire Model Validation – Eight Lessons Learned," in *Fire Safety Science - Proceedngs of the Eleventh International Symposium*, (Canterbury, New Zealand), International Association for Fire Safety Science, 2014.

[135] H. R. Baum, "Large eddy simulations of smoke movement in three dimensions," in *Conference Proceedings of the Seventh International Interflam Conference, 1996*, Interscience Communications, 1996.

[136] H. R. Baum, K. B. McGrattan, and R. G. Rehm, "Three dimensional simulations of fire plume dynamics," *Fire Safety Science*, vol. 5, pp. 511–522, 1997.

[137] K. B. McGrattan, H. R. Baum, and R. G. Rehm, "Large eddy simulations of smoke movement," *Fire Safety Journal*, vol. 30, no. 2, pp. 161–178, 1998.

[138] K. McGrattan, C. Bouldin, and G. Forney, "Federal Building and Fire Safety Investigation of the World Trade Center Disaster: Computer Simulation of the Fires in the WTC Towers," *NIST NCSTAR*, 2005.

[139] G. Rein and R. Carvel, *The Dalmarnock fire tests: experiments and modelling.* School of Engineering and Electronics, University of Edinburgh, 2007.

[140] P. H. Thomas and A. J. M. Heselden, "Behaviour of fully developed fire in an enclosure," *Combustion and flame*, vol. 6, pp. 133–135, 1962.

[141] A. J. M. Heselden, P. H. Thomas, and M. Law, "Burning rate of ventilation controlled fires in compartments," *Fire Technology*, vol. 6, no. 2, pp. 123–125, 1970.

[142] J. Wahlqvist and P. Van Hees, "Validation of FDS for large-scale well-confined mechanically ventilated fire scenarios with emphasis on predicting ventilation system behavior," *Fire Safety Journal*, vol. 62, no. PART B, pp. 102–114, 2013.

[143] R. K. Janardhan and S. Hostikka, "Experiments and Numerical Simulations of Pressure Effects in Apartment Fires," *Fire Technology*, vol. 53, no. 3, pp. 1353–1377, 2017.

[144] S. Hostikka, R. K. Janardhan, U. Riaz, and T. Sikanen, "Fire-induced pressure and smoke spreading in mechanically ventilated buildings with air-tight envelopes," *Fire Safety Journal*, vol. 91, no. February, pp. 380–388, 2017.

[145] T. S. Kuhn, *The Structure of Scientific Revolutions*. Chicago, IL: University of Chicago Press, fourth edi ed., 2012.

[146] N. M. A. Munassar and A. Govardhan, "A comparison between five models of software engineering," *IJCSI*, vol. 5, pp. 95–101, 2010.

[147] G. Von Krogh and E. Von Hippel, "The promise of research on open source software," *Management science*, vol. 52, no. 7, pp. 975–983, 2006.

[148] L. Formaggia, J. F. Gerbeau, F. Nobile, and a. Quarteroni, "Numerical treatment of defective boundary conditions for the Navier-Stokes Equations," *SIAM Journal on Numerical Analysis*, vol. 40, no. 1, pp. 376–401, 2003.

[149] L. Formaggia and C. Vergara, "Prescription of General Defective Boundary Conditions in Fluid-Dynamics," *Milan Journal of Mathematics*, vol. 80, no. 2, pp. 333–350, 2012.

[150] G. Rein, J. L. Torero, W. Jahn, J. Stern-Gottfried, N. L. Ryder, S. Desanghere, M. Lázaro, F. Mowrer, A. Coles, D. Joyeux, D. Alvear, J. A. Capote, A. Jowsey, C. Abecassis-Empis, and P. Reszka, "Round-robin study of a priori modelling predictions of the Dalmarnock Fire Test One," *Fire Safety Journal*, vol. 44, no. 4, pp. 590–602, 2009.

[151] W. D. Walton, D. J. Carpenter, and C. B. Wood, "Zone computer fire models for enclosures," in *SFPE handbook of fire protection engineering*, pp. 1024–1033, Springer, 2016.

[152] J. Prince, M. Tabarra, J. Alexander, and J. Peiro, "On the prediction of pressure losses in complex flow scenarios using CFD," in *16th International Symposium on Aerodynamics and Ventilation of Vehicle Tunnels*, (Seattle, USA), pp. 535–547, 2015.

[153] P. J. Blanco, R. a. Feijóo, and S. a. Urquiza, "A unified variational approach for coupling 3D-1D models and its blood flow applications," *Computer Methods in Applied Mechanics and Engineering*, vol. 196, pp. 4391–4410, 2007.

[154] M. Juntunen and R. Stenberg, "Nitsche's method for general boundary conditions," *Mathematics of Computation*, vol. 78, pp. 1353–1374, 9 2009.

[155] M. Malinen, "Boundary Conditions in the Schur Complement Preconditioning of Dissipative Acoustic Equations," *SIAM Journal on Scientific Computing*, vol. 29, pp. 1567–1592, 1 2007.

[156] C. Runge, "Ueber die numerische Auflösung von Differentialgleichungen," *Mathematische Annalen*, vol. 46, pp. 167–178, 6 1895.

[157] J. Butcher, *Numerical Methods for Oridinary Differential Equations*. Wiley Online Library, 3rd editio ed., 2016.

[158] S. Godunov, "A difference method for numerical calculation of discontinuous solutions of the equations of hydrodynamics," *Matematicheskiĭ Sbornik. Novaya Seriya*, vol. 47, no. 89, pp. 271 – 306, 1959.

[159] A. Handbook, "HVAC applications," *ASHRAE Handbook, Fundamentals*, 2007.

[160] BSRIA, "Guide to HVAC Building Services Calculations," 2007.

[161] B. Munson, D. Young, and T. Okiishi, *Fundamentals of fluid mechanics*. Hoboken, NJ: John Wiley & Sons, 8th ed., 2006.

[162] CIBSE, *CIBSE Guide B0 - Applications and activities : HVAC strategies for common building types*. CIBSE, 2016.

[163] M. Janssens and H. C. Tran, "Data Reduction of Room Tests for Zone Model Validation," *Journal of Fire Sciences*, vol. 10, no. 6, pp. 528–555, 1992.

[164] CIBSE, "Guide E: Fire engineering," *The Chartered Institution of Building Services Engineers, London, UK*, 2010.

[165] K. Mcgrattan and R. Mcdermott, "Sixth Edition Fire Dynamics Simulator User's Guide," tech. rep., NIST, 2016.

[166] G. N. Walton and W. S. Dols, "CONTAM User Guide and Program Documentation," tech. rep., NIST, 2013.

[167] Y. A. Cengel and J. M. Cimbala, *Fluid mechanics : fundamentals and applications*. McGraw-HillHigher Education, 2006.

[168] F. S. Zntemctisnul, "The causes of death in fire victims," *Forensic Science International*, vol. 24, no. 2, pp. 3–7, 1984.

[169] R. N. Pease, "Characteristics of the non-explosive oxidation of propane and the butanes 1," *Journal of the American Chemical Society*, vol. 51, pp. 1839–1856, 6 1929.

[170] Z. Hu, Y. Utiskul, J. G. Quintiere, and A. Trouve, "Towards large eddy simulations of flame extinction and carbon monoxide emission in compartment fires," *Proceedings of the Combustion Institute*, vol. 31, pp. 2537–2545, 1 2007.

[171] S. Vilfayeau, N. Ren, Y. Wang, and A. Trouvé, "Numerical simulation of underventilated liquid-fueled compartment fires with flame extinction and thermally-driven fuel evaporation," *Proceedings of the Combustion Institute*, vol. 35, pp. 2563–2571, 1 2015.

[172] S. Vilfayeau, J. White, P. Sunderland, A. Marshall, and A. Trouvé, "Large eddy simulation of flame extinction in a turbulent line fire exposed to air-nitrogen coflow," *Fire Safety Journal*, vol. 86, pp. 16–31, 11 2016.

[173] Society of Fire Protection Engineers, *SFPE Handbook of Fire Protection Engineering*, vol. 4. USA: Society of Fire Protection Engineers, 2008.

[174] T. Cleary and J. Quintiere, "A Framework For Utilizing Fire Property Tests," *Fire Safety Science*, vol. 3, pp. 647–656, 1991.

[175] Z. Popiolek, F. E. Jorgensen, A. K. Melikov, M. C. G. Silva, and W. Kierat, "Assessment of Uncertainty in Measurements with Low Velocity Thermal Anemometers," *International Journal of Ventilation*, vol. 6, no. 2, pp. 113–128, 2004.

[176] S. J. Hoff, D. S. Bundy, M. A. Nelson, B. C. Zelle, L. D. Jacobson, A. J. Heber, J. Ni, Y. Zhang, J. A. Koziel, and D. B. Beasley, "Real-time airflow rate measurements from mechanically ventilated animal buildings," *Journal of the Air and Waste Management Association*, vol. 59, no. 6, pp. 683–694, 2009.

[177] V. Babrauskas and R. D. Peacock, "Heat Release Rate: The Single Most Important Variable in Fire Hazard," *Fire Safety Journal*, vol. 18, no. 3, pp. 255–272, 1992.

[178] H. P. Morgan and J. P. Gardner, "Design principles for smoke ventilation in enclosed shopping centres," 1990.

[179] J. L. Torero, "Scaling-Up fire," *Proceedings of the Combustion Institute*, vol. 34, pp. 99–124, 1 2013.

[180] D. Drysdale, *An Introduction to Fire Dynamics*. Chichester, UK: John Wiley & Sons, 3rd ed., 2011.

[181] J. J. Alston and N. A. Dembsey, "Evaluation of dimensionless flame height parameters to account for fuel source effects," *Fire Safety Science*, pp. 569–580, 2003.

[182] C. L. Chow and W. Ki Chow, "Fire safety aspects of refuge floors in supertall buildings with computational fluid dynamics," *Journal of Civil Engineering and Management*, vol. 15, pp. 225–236, 1 2009.

[183] W. Ko, Min-Hang Bao, and Yeun-Ding Hong, "A high-sensitivity integrated-circuit capacitive pressure transducer," *IEEE Transactions on Electron Devices*, vol. 29, pp. 48–56, 1 1982.

[184] B. Taylor and C. Kuyatt, "Guidelines for evaluating and expressing the uncertainty of NIST measurement results," tech. rep., NIST, Gaithersburgh, Maryland, USA, 1994.

[185] A. Hamins, A. Maranghides, R. J. N. S. . . . , and U. 2003, "Report of experimental results for the international fire model benchmarking and validation exercise 3," tech. rep., NIST, Gaithersburgh, Maryland, USA, 2005.

[186] B. J. McCaffrey, J. G. Quintiere, and M. F. Harkleroad, "Estimating room temperatures and the likelihood of flashover using fire test data correlations," *Fire Technology*, vol. 17, pp. 98–119, 5 1981.

[187] R. B. Abernethy, R. P. Benedict, and R. B. Dowdell, "ASME Measurement Uncertainty," *Journal of Fluids Engineering*, vol. 107, p. 161, 6 2009.

[188] R. A. Bryant, "A comparison of gas velocity measurements in a full-scale enclosure fire," *Fire Safety Journal*, vol. 44, no. 5, pp. 793–800, 2009.

[189] R. L. Alpert, "Ceiling jet flows," in *SFPE Handbook of Fire Protection Engineering, Fifth Edition*, pp. 429–454, New York, NY: Springer New York, 2016.

[190] H. W. Ott, *Noise reduction techniques in electronic systems.* Wiley, 1976.

[191] J. R. Barnes, *Electronic system design : interference and noise control techniques.* Prentice-Hall, 1987.

[192] H. So, Y. Chan, Q. Ma, and P. Ching, "Comparison of various periodograms for sinusoid detection and frequency estimation," *IEEE Transactions on Aerospace and Electronic Systems*, vol. 35, pp. 945–952, 7 1999.

[193] V. M. Calo, Y. Bazilevs, T. J. R. Hughes, and R. Moser, "Turbulence modeling for large eddy simulations," *Computer Methods in Applied Mechanics and Engineering*, vol. 199, p. 779, 4 2010.

[194] M. Arora and P. L. Roe, "A well-behaved TVD limiter for high-resolution calculations of unsteady flow," *Journal of Computational Physics*, vol. 132, pp. 3–11, 3 1997.

[195] R. A. Sweet, "CRAYFISHPAK: a vectorized fortran package to solve Helmholtz equations," in *Recent Developments in Numerical Methods and Software for ODEs/DAEs/PDEs*, pp. 37–53, World Scientific, 3 1992.

[196] H. Xie and S. Chen, "Simulation of Combustion Process and Soot Yield in Propane/Air Laminar Diffusion Flame by Self-Defined Scalar Method," *International Journal of Chemical Reactor Engineering*, vol. 8, 1 2010.

[197] J. Ellzey, J. G. Berbe, E. Z. F. Tay, and D. E. Foster, "Total Soot Yield from a Propane Diffusion Flame in Cross-Flow," *Combustion Science and Technology*, vol. 71, pp. 41–52, 5 1990.

[198] O. L. Gulder, G. Intasopa, H. I. Joo, P. M. Mandatori, D. S. Bento, and M. E. Vaillancourt, "Unified behaviour of maximum soot yields of methane, ethane and propane laminar diffusion flames at high pressures," *Combustion and Flame*, vol. 158, pp. 2037–2044, 10 2011.

[199] K. Adiga, D. Ramaker, P. Tatem, and F. Williams, "Modeling pool-like gas flames of propane," *Fire Safety Journal*, vol. 14, pp. 241–250, 2 1989.

[200] L. Orloff, A. T. Modak, and G. H. Markstein, "Radiation from smoke layers," in *Symposium (International) on Combustion*, vol. 17, pp. 1029–1038, Elsevier, 1979.

[201] ASH International, "ASM Materials Solutions Information Database," 2018.

[202] C. F. Colebrook, T. Blench, H. Chatley, E. H. Essex, J. R. Finniecome, G. Lacey, J. Williamson, and G. G. Macdonald, "Correspondence. Turbulent flow in pipes, with particular reference to the transition region between the smooth and rough pipe laws. (Includes plates).," *Journal of the Institution of Civil Engineers*, vol. 12, pp. 393–422, 10 1939.

[203] D. J. Zigrang and N. D. Sylvester, "A Review of Explicit Friction Factor Equations," *Journal of Energy Resources Technology*, vol. 107, p. 280, 6 1985.

[204] M. L. Shur, P. R. Spalart, and M. K. Strelets, "LES-based evaluation of a microjet noise reduction concept in static and flight conditions," *Journal of Sound and Vibration*, vol. 330, no. 17, pp. 4083–4097, 2011.

[205] F. Bobaru, M. Yang, L. F. Alves, S. A. Silling, E. Askari, and J. Xu, "Convergence, adaptive refinement, and scaling in 1D peridynamics," *International Journal for Numerical Methods in Engineering*, vol. 77, no. 6, pp. 852–877, 2009.

[206] W. G. Habashi, J. Dompierre, Y. Bourgault, D. Ait-Ali-Yahia, M. Fortin, and M.-G. Vallet, "Anisotropic mesh adaptation: towards user-independent, mesh-independent and solver-independent CFD. Part I: general principles," *International Journal for Numerical Methods in Fluids*, vol. 32, no. 6, pp. 725–744, 2000.

[207] R. McDermott, K. Mcgrattan, and J. Floyd, "A Simple Reaction Time Scale for Under-Resolved Fire Dynamics," *Fire Safety Science*, vol. 10, pp. 809–820, 2011.

[208] P. J. Roache, "Conservatism of the Grid Convergence Index in Finite Volume Computations on Steady-State Fluid Flow and Heat Transfer," *Journal of Fluids Engineering*, vol. 125, no. 4, p. 731, 2003.

[209] P. Schlatter, S. Stolz, and L. Kleiser, "LES of transitional flows using the approximate deconvolution model," *International Journal of Heat and Fluid Flow*, vol. 25, no. 3, pp. 549–558, 2004.

[210] N. S. Lakshmana Rao and K. Sridharan, "Loss characteristics of long orifices," in *Fourth Australian Conference on Hydraulics and Fluid Mechanics*, (Melbourne, Australia), Monash University, 1971.

[211] J. Tu, G. H. Yeoh, and C. Liu, *Computational Fluid Dynamics: A Practical Approach*. Elsevier Ltd., second edi ed., 2008.

[212] S. B. Pope, "Ten questions concerning the large-eddy simulation of turbulent flows," *New Journal of Physics*, vol. 6, 2004.

[213] S. C. P. Cheung, S. M. Lo, G. H. Yeoh, and R. K. K. Yuen, "The influence of gaps of fire-resisting doors on the smoke spread in a building fire," *Fire safety journal*, vol. 41, no. 7, pp. 539–546, 2006.

[214] B. S. Kandola, "Wind effects on buildings with varying leakage characteristics—wind-tunnel investigation," *Journal of Wind Engineering and Industrial Aerodynamics*, vol. 3, no. 4, pp. 267–284, 1978.

[215] C. M. Beal, M. Fakhreddine, and O. A. Ezekoye, "Effects of leakage in simulations of positive pressure ventilation," *Fire technology*, vol. 45, no. 3, pp. 257–286, 2009.

[216] H. Takeda and D. Yung, "Simplified Fire Growth Models for Risk-Cost Assessment in Apartment Buildings," *Journal of Fire Protection Engineering*, vol. 4, pp. 53–65, 1 1992.

[217] J. Purkiss and L. Li, *Fire safety engineering design of structures*. CRC Press Book, 2013.

[218] M. Kazarians, N. O. Siu, and G. Apostolakis, "Fire Risk Analysis for Nuclear Power Plants: Methodological Developments and Applications," *Risk Analysis*, vol. 5, pp. 33–51, 3 1985.

[219] G. Bassett and R. Koenker, "Asymptotic Theory of Least Absolute Error Regression," *Journal of the American Statistical Association*, vol. 73, pp. 618–622, 9 1978.

[220] J. Jie, L. Kaiyuan, Z. Wei, and H. Ran, "Experimental investigation on influence of smoke venting velocity and vent height on mechanical smoke exhaust efficiency," *Journal of hazardous Materials*, vol. 177, no. 1-3, pp. 209–215, 2010.

[221] R. Alpert, "Ceiling jet flows," in *SFPE Handbook of Fire Protection Engineers*, Quincy, USA: National Fire Protection Association, 2002.

[222] G. Heskestad and M. A. Delichatsios, "The initial convective flow in fire," *Symposium (International) on Combustion*, vol. 17, pp. 1113–1123, 1 1979.

[223] J. Miles and M. Shevlin, *Applying regression and correlation: A guide for students and researchers*. Sage, 2001.

[224] D. L. Moody and G. G. Shanks, "What makes a good data model? Evaluating the quality of entity relationship models," in *International Conference on Conceptual Modeling*, pp. 94–111, Springer, 1994.

[225] N. Jarrin, S. Benhamadouche, D. Laurence, and R. Prosser, "A synthetic-eddy-method for generating inflow conditions for large-eddy simulations," *International Journal of Heat and Fluid Flow*, vol. 27, pp. 585–593, 8 2006.

[226] A. C. Aitken, "On least squares and linear combination of observations," *Proc. R. Soc. Edinb*, vol. 55, pp. 42–48, 1934.

[227] British Standards Institute, "BS EN 15650 - Ventilation for buildings. Fire dampers," 2010.

[228] K. Fridolf, D. Nilsson, and H. Frantzich, "Walking Speed in Smoke: Representation in Life Safety Verifications," tech. rep., WSP, 2016.

[229] S. Krishnan, B. M. Kumfer, W. Wu, J. Li, A. Nehorai, and R. L. Axelbaum, "An Approach to Thermocouple Measurements That Reduces Uncertainties in High-Temperature Environments," *Energy & Fuels*, vol. 29, pp. 3446–3455, 5 2015.

[230] G. E. Daniels and G. E. Daniels, "Measurement of Gas Temperature and the Radiation Compensating Thermocouple," *Journal of Applied Meteorology*, vol. 7, pp. 1026–1035, 12 1968.

Appendix A

Laboratory notes on experiments

A.1 Preamble

This appendix presents a discussion of the development process of the experimental apparatus. Although these observations are not required to describe the experimental methodology, there may be lessons learnt which could help future researchers and therefore they are presented here.

A.2 Photographs

Figures A.1, A.2, and A.3 present various views of the boxes. Views of the sand burner are provided in Figure A.4. The EP6 box set up and the ignitor and flame detector are presented in Figure A.5. The co-flow arrangement is presented in Figure A.6. Figure A.7 presents views of the quartz windows. Figure A.8 shows the ducting prior to the installation of the insulation. Figure A.9 presents stages of the installation of the ducting. Figure A.10 shows the adopted fans prior to install within the experimental apparatus. Figure A.11 presents the installation of the adopted fans. Installation and details of the box thermocouples are presented in Figures A.12 and A.13. Figure A.14 shows the installation of the bidirectional pressure probes within the ventilation ducts. Images of the preparation and install of the in-duct thermocouples are provided in Figures A.15 and A.16. Figure A.17 shows the data acquisition set up.

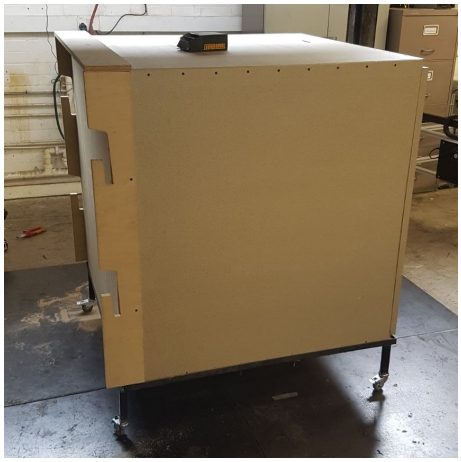

(a) Front view of one of the boxes prior to installation of ventilation system.

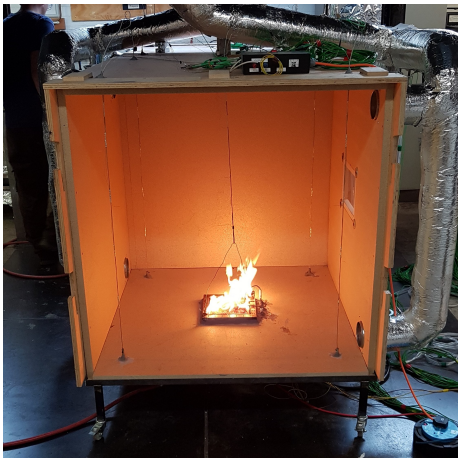

(b) Left view of hot box during initial burner testing.

Figure A.1: Views of the boxes of the experimental apparatus.

Figure A.2: Rear view of the experimental apparatus prior to installation of ventilation system.

Figure A.3: Front view of the experimental apparatus prior to installation of ventilation system.

(a) Top view of empty sand burner, prior to install.

(b) Elevation of empty sand burner, prior to install.

(c) View of sand burner, prior to install.

(d) View of sand burner, after installing meshes and filling with sand.

(e) Testing of sand burner, prior to modification of air co-flow.

(f) Sand burner viewed through viewing window, following modification of air co-flow.

Figure A.4: Sand burner of the experimental apparatus.

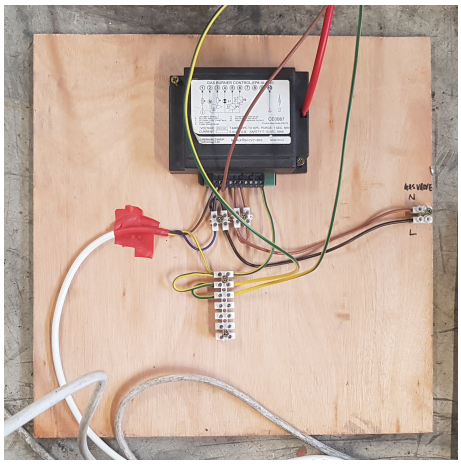

(a) EP6 control box and wiring to the high tension sparker, the gas control valves, and the flame detector.

(b) The ignitor (top) and the flame detector (middle and bottom) arrangement.

Figure A.5: Ignitor, flame detector, and gas flow control arrangement.

(a) Prior to installation of deflection baffles.

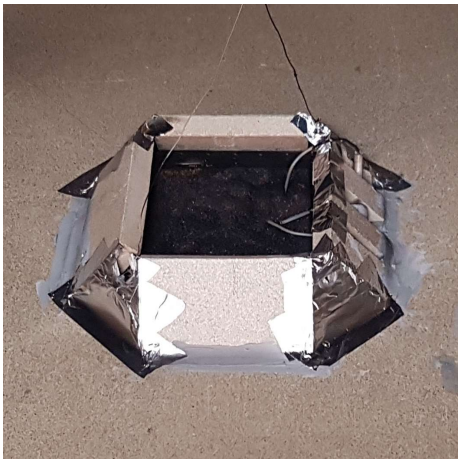

(b) With deflection baffles installed.

Figure A.6: Co-flow arrangement.

(a) Quartz viewing window, viewed from within one of the boxes.

(b) Quartz viewing window, viewed from outside one of the boxes.

Figure A.7: Quartz viewing windows provided within the front walls of both boxes of the experimental apparatus.

Figure A.8: Ventilation system prior to the installation of the insulation, fans, and return system.

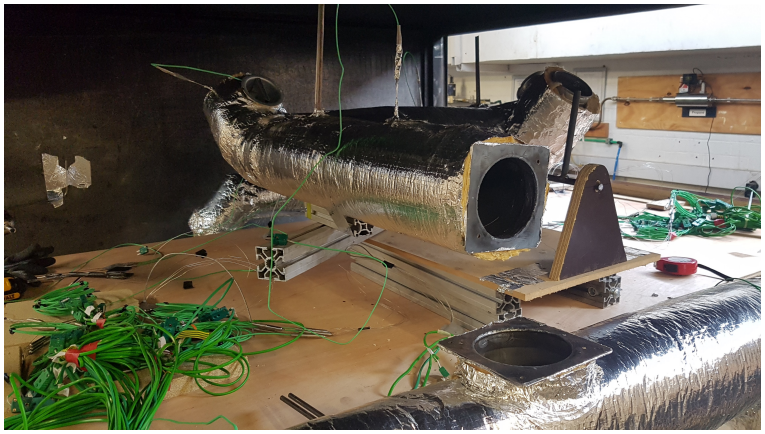

(a) Shared exhaust duct being connected to the hot and cool box exhaust system. Front view of the experimental apparatus.

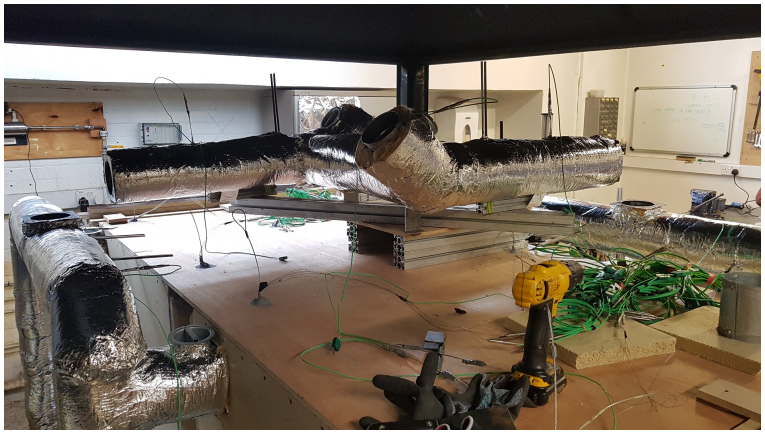

(b) Shared ventilation system being connected to the hot and cool box supply system. Rear left view of the experimental apparatus.

(c) Shared supply duct being connected to the hot and cool box supply ducts. Rear view of the experimental apparatus.

Figure A.9: Installation of the ventilation system ducting.

(a) The fan motor.

(b) The air inlet (left) and outlet (right).

Figure A.10: Centrifugal fans, prior to installation within the ventilation system of the experimental apparatus.

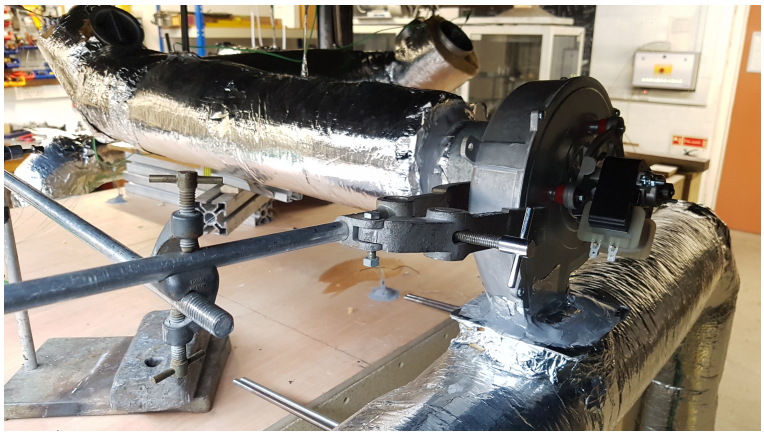

(a) Supply fan. Rear right view of the experimental apparatus.

(b) Exhaust fan. Front left view of the experimental apparatus.

Figure A.11: Installation of centrifugal fans in the shared ventilation system of the experimental apparatus.

(a) Thermocouple trees in the cool box. The trees have not been tensioned yet and have protective covers on their junctions.

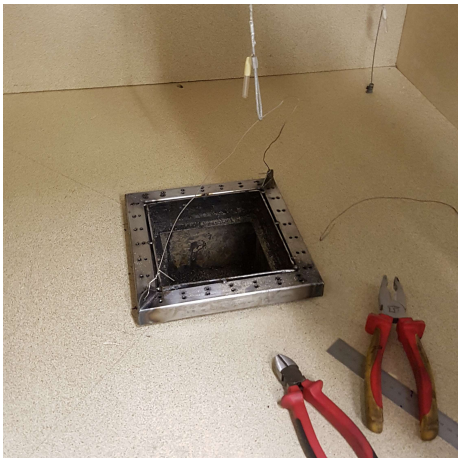

(b) Installing the thermocouple tree over the propane burner within the hot box. Inconel wire was used due to the high temperatures expected at this location.

Figure A.12: Installation of thermocouple trees within the experimental apparatus. A cable was passed through holes in the top and bottom of the boxes. The thermocouples were passed through the top hole and secured to the cable. The cable was fixed with a spring-loaded grub screw at the bottom. The cable was fixed with a screw clamp at the top. This enabled the tensioning of the cable, and the thermocouples, ensuring they didn't move during experiments.

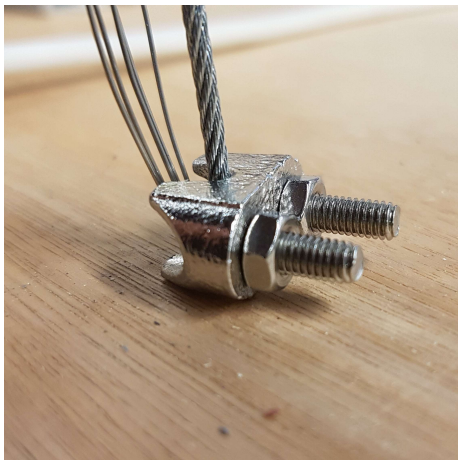

(a) Detail of the top fixing of the box thermocouples. This screw clamp enabled the cable, to which the thermocouples were attached to be tightly tensioned. The thermocouple wires, untensioned to stop damage, can be seen passing by the screw clamp to the rear of the image.

(b) The penetrations for the screw clamps (shown in this image) and the spring-loaded grub screws at the bottom of the boxes (not shown) were sealed with fire cement. This limited leakages.

Figure A.13: Details of in box thermocouple tree installation and sealing.

(a) Probe installed within duct, prior to connection to rest of ventilation system.

(b) Probe installed and connected to tubing.

Figure A.14: Bidirectional pressure probes installed within the ventilation system of the experimental apparatus.

(a) Thermocouples prepared to be installed in the ducts. To ensure that the thermocouples were mechanically protected and would remain in the same location they were threaded into stainless steel tubes. These stainless steel tubes were then slotted into steel tubes which had been welded on to the ducts.

(b) View in to the fresh air inlet of the supply system. The stainless steel tube can be seen passing through the duct wall. The thermocouple extends beyond the stainless steel tube and in to the midpoint of the duct.

Figure A.15: Preparation and installation of the in-duct thermocouples. The fine exposed thermocouples were delicate and expensive. Ensuring that they were not damaged was important.

(a) In-duct thermocouple installed within the shared supply duct.

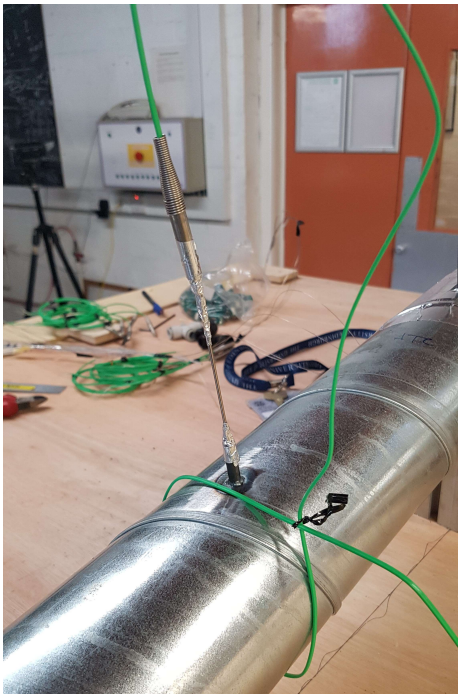

(b) In-duct thermocouple installed within the shared exhaust duct.

Figure A.16: In-duct thermocouples insitu within the ventilation system. After the thermocouples and stainless steel tube assembly was slotted into the pre-welded steel tubes the joint was taped with aluminium tape and sealed with fire cement.

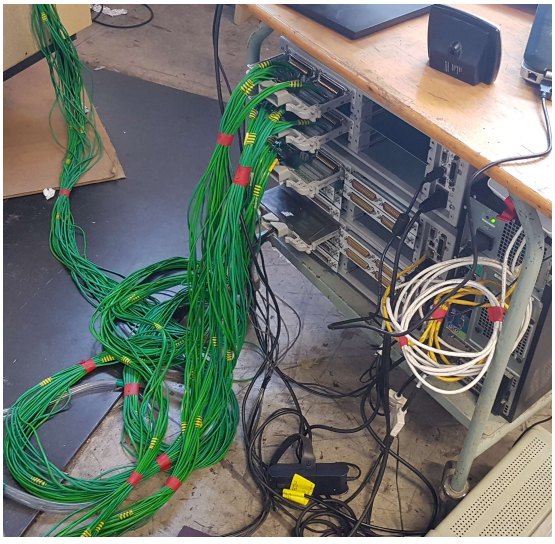

Figure A.17: Rear of 34980A data acquisition mainframes; showing four 34925A/T multiplexers and terminal blocks to sample data from the in box thermocouples (top two blocks), the in-duct thermocouples (middle block), and the pressure transducers (lowest block).

A.3 Lessons learnt

A.3.1 External timber framing

When designing and building the experimental apparatus, the priorities were, inter alia, safety, construction time, construction ease, availability of materials, and cost. For these reasons, parts of the external framing provided for torsional and lateral stability, door closing, duct affixing and wheel affixing were constructed of 20 mm thick five ply softwood plywood. The timber frame is presented in Figure A.18.

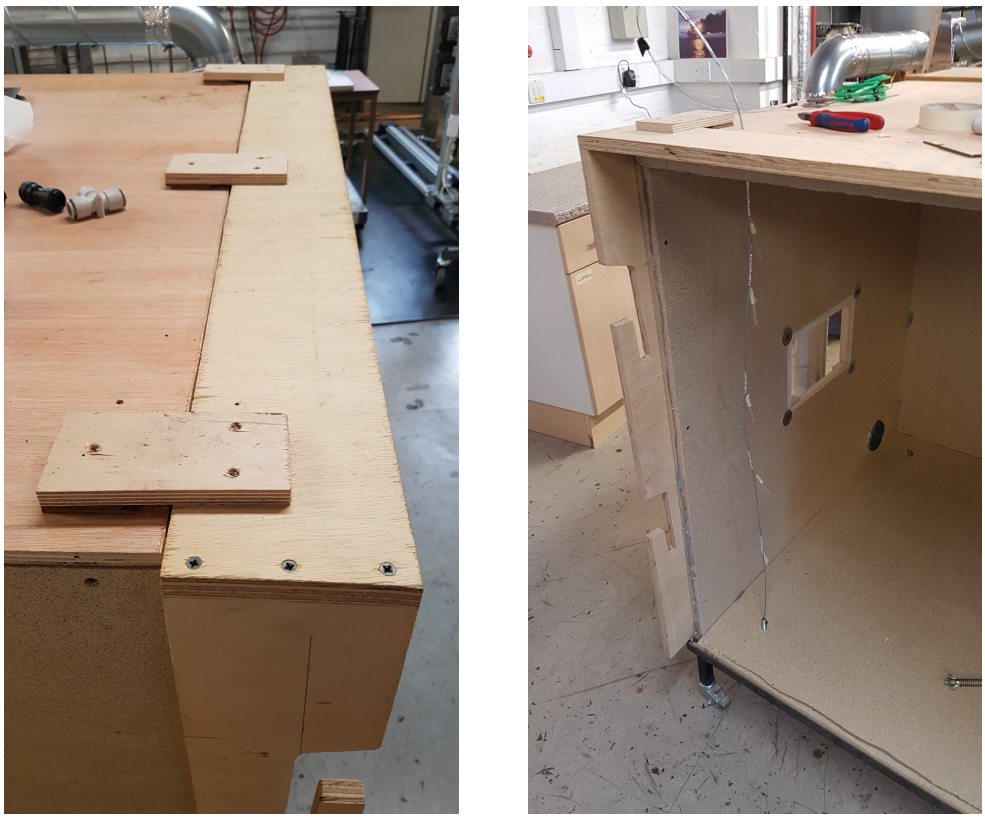

(a) Top view, showing door framing. (b) Right view of the cool box.

Figure A.18: Timber frame of the experimental apparatus.

The timber had no direct exposure to the internal envelope of the experimental apparatus. However, during early experiments at higher propane flow rates, due to leakage of hot gases at the corners of the hot box, where three sheets of vermiculite met (including the removable door), the external timber framing ignited and burnt. This ignition occurred in experiments `P40_F3_1`, `P45_F2_1` and `P45_F3_1`. Once this was observed to be a problem, from experiment `P45_F3_1` onward, the internal sealing within the hot box at the upper corners was upgraded. This was achieved by affixing ceramic paper with aluminium tape and additional high temperature fire cement. After these remedial works, no further ignition of the external timber framing occurred.

In experiments `P40_F3_1`, `P45_F2_1` and `P45_F3_1`, when the timber ignited and self-sustained burning occurred, water was applied to the external timber frame with a hand held spray bottle to extinguish the local burning. This will have changed the boundary conditions of the external envelope of the hot box and increased heat transfer through the timber and vermiculite. In an extreme case (experiment `P45_F3_1`) water from the spray bottle entered the hot box via a gap which had opened up in the vermiculite due

to the compromising of the internal sealing. This water would have evaporated within the hot box and been deposited on the internal surface of the hot box where it would have evaporated. This event, which occurred at approximately 2700 s, may have slightly reduced the gas phase temperatures of the hot box. To investigate this the data from thermocouple tree one (the rear left tree, closest to the location of potential water spray ingress) is presented in Figure A.19. The figure illustrates the measured temperatures changing at this time; however, this is also the time of smoke-spill and fresh air supply mode being operated. As the water spraying only took place for approximately 10 s, and the change in temperature continued until the termination of the experiment, it is concluded that the effect of the water spray was minimal when compared to spill mode being operated.

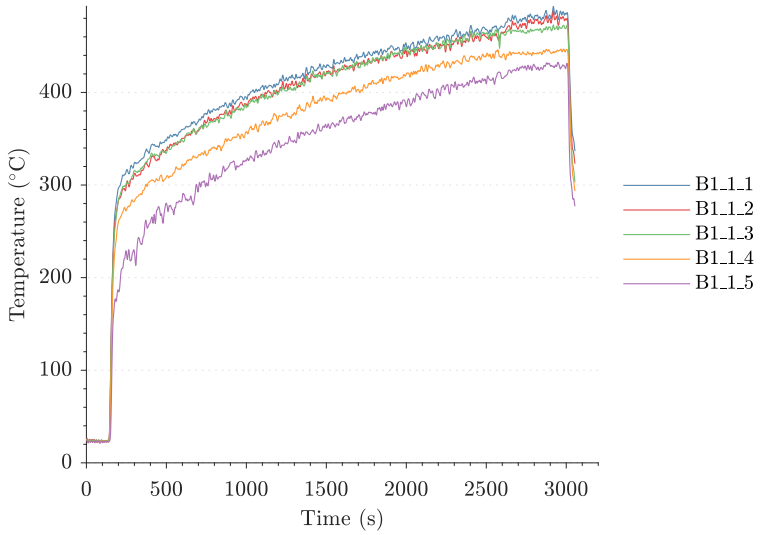

Figure A.19: Temperature measurements for thermocouple tree 1 within the hot box for experiment `P45_F3_1`. This is the rear left tree and the nearest one to the ingress of water spray used to cool the timber framing. The plot demonstrates that there was little effect on temperatures when water was used at ≈ 2700 s for ≈ 10 s. The sustained change in temperatures at this time is most likely due to the operation of spill mode at this time.

The initial design of the air co-flow was more aligned to a typical co-flow arrangement. The co-flow was directed in the positive z direction, parallel to the flow of the propane fuel. This did not achieve the objective of maintaining burning at or near the sand burner surface. During test runs, the flame was extinguished and unburnt propane smell was detected within the fire laboratory. This was unsafe. There was a risk of collection of propane in the fire laboratory and subsequent accidental ignition.

The solution was to construct baffles to re-direct the air flow into the combustion zone. There was an added benefit of these baffles. There was increased mixing and spreading of the air flow occurred. After the modification of the co-flow system, burning away from the sand burner surface was not observed. The flame did not lift from sand burner surface. One recognised omission from the experimental dataset is the characterisation of the air co-flow.

The exhaust system had two inlets in each box; one low and one high. The supply system had two outlets in each box; one low and one high. Due to time pressures within the fire laboratory, and the lack of output sensitivity during preliminary experiments, the lower exhaust and the upper supply out and inlets were not used in the

main experimental programme. Testing was carried out on the effect of varying the exhaust and supply location (high or low in and outlets open). The data output, being temperatures and velocities, were observed to be insensitive to the selection of in and outlet location and was found to be minimal - with no observed variation outside of experimental uncertainty.

A.3.2 Air control dampers

Typical fire dampers types are: folding curtain fire dampers, single blade fire dampers, multi-blade fire dampers, cone valve fire dampers, intumescent fire dampers, and spring return actuated fire dampers [227].

The first four types comprise a blade or arrangement of blades which are held in an open position with a thermal release mechanism. The thermal release mechanism is also known as a fusible link and can consist of a solder link or a frangible glass bulb [16]. Upon operation of the thermal release mechanism the blade(s) close to prevent the passage of fire. These fire damper types require the thermal release mechanism to be replaced following operation. Intumescent fire dampers are single use only, not suitable for repeating experiments. Spring return actuated can be closed and reset using an electrical signal and would be usable in an experimental type setup where the fire damper is required to be operated multiple times. Spring return actuator type fire dampers are however very expensive and require costly support infrastructure (signal controller and power unit). Especially as the experimental apparatus required eleven dampers.

The chosen alternative to a fire damper was a manually operated air control damper. The damper comprised a stainless steel housing, rotating damper plate and manually operated handle. Figure A.20 presents the typical air control dampers within the experimental apparatus.

(a) Prior to fitting of insulation. (b) Following fitting of insulation.

Figure A.20: Air control dampers installed within upper supply outlet.

The damper plate had a rubberised gasket around its perimeter to provide an air seal. The shaft attached to the operating handle was fitted with a rubberised gasket at the location of penetration through the housing of the damper. At high temperatures these synthetic elastomer polymer gaskets ignited, burnt, charred, and crumbled. For affected dampers this meant that the air seal provided around the edge of the damper plate and at the penetration of the handle shaft and the damper housing was compromised and

the damper was not hermetically sealed. This affected damper numbers 1, 2, 5, 10 and 11; as these were the dampers that were in close proximity to the heat source. Damper numbers 2, 5 and 10 were especially affected as these dampers were located either in the hot gas layer within the box or within the smoke-spill component of the ventilation system.

The negative effect of the burning, charring, and crumbling of the gaskets was that when in the closed position the dampers did not fully seal the duct. This is especially important for damper 5; which was the smoke-spill damper. This incomplete damper closing meant that when in recycle mode there would have been leakage through damper number 5 to ambient. The compromising of the rubberised gaskets within the dampers was observed to happen substantially within the first experiment carried out. A smell of burning rubber and smoking at the affected dampers was observed. Following the first experiment no further burning of the rubberised gaskets of the dampers was observed. It is concluded that the incomplete sealing of the duct at damper numbers 1, 2, 5, 10 and 11 remained constant throughout the remainder of the experimental programme.

Axial and centrifugal type fans

Axial fans are low pressure, high flow rate turbomachines. Centrifugal fans are high pressure, low flow rate turbomachines. The pressures to overcome within the experimental apparatus were predicted to be relatively low. The pressure increase from centrifugal fans could potentially be very large when compared to any pressure changes due to a fire. Furthermore, axial fans operate at more reliable blade speeds at lower potential differences (i.e. at lower free flow discharge rates). These more reliable lower flow rates would be more representative of the desired air changes per hour. Overall, axial fans were the preferred fan type.

However, there is a major drawback of axial fans: the fan motor is within the gas stream. This means that very high temperature axial fans are not possible. Components in and connected to the motor fail at higher temperatures. Based upon preliminary simulations of the experimental apparatus the predicted maximum temperature at the fans was approximately 200 °C. Therefore the initial design of the experimental apparatus was based on the use of 'high temperature axial fans'. These fans had a stated upper operational temperature of 200 °C. However, following this preliminary modelling and during the construction of the experimental apparatus the upper bound of the range of propane flows within the experimental matrix increased. By this time the axial fans had already been installed within the experimental apparatus. The temperatures within the ducts at the fans exceeded their operating temperature and during the first experiment both fans failed.

The axial fans were removed and the two centrifugal fans, which were used for all subsequent experiments, were acquired. The centrifugal fans had their motor located outside of the volute and hence outside of the gas stream. They could operate at much higher temperatures; with a stated maximum operating temperature of 450 °C. The installation of the centrifugal fans required quick turnaround adaptation of the designed duct layout.

The serendipity of this event is that centrifugal fans, due to their casing increasing in area in the direction of flow, produce a near uniform flow field distribution from the discharge outlet [161].

A.4 Limitations of experimental campaign

A.4.1 Potential independent variables

Of course there is an infinite choice of variables that could be changed to form the experimental matrix. It is one of the tasks of the experiment designers to reduce this list to the most important variables to meet the applicable objectives. Potential independent variables for the subject experiment include those selected and listed above but also fuel type, ventilation arrangement (including natural ventilation, exhausting or supplying high or low or at multiple locations), construction materials, insulation and geometry. The list goes on ad infinitum.

In fact n-heptane was trialled in the experimental rig. There were multiple problems with the use of this liquid fuel. Firstly, it was not possible to maintain burning of the pool fire for the duration of an experiment. This was due to an insufficient quantity of air being delivered in proximity to the surface of the burning fuel. At higher air co-flow rates the momentum transferred from the air flow to the pool surface caused spilling. This set an upper limit on the volume flow rate of air that was safely useable. A second problem with the use of a liquid pool fire is the complications of coupling between the volatilisation rate of fuel and the enclosure. As the enclosure increases in temperature due to heat transfer from the fire, these hot surfaces radiate back to the pool surface and increase evaporation rate. This increases burning rate. This is a complex phenomenon and investigation of it is not within the remit of the subject experiment. Therefore, a liquid fuel source was discounted.

Variation of the ventilation system was considered as an independent variable. For example, exhausting at a low level and supplying at a high level within the enclosures. The experimental rig was designed with this functionality. The effect of varying ventilation was trialled in early experiments and found to be minimal. Therefore, upon creating the experimental matrix, this independent variable was discounted as superfluous due to time and space constraints within the fire laboratory. The alternation of construction material and geometry were also discounted due to pressures of time and cost.

A.4.2 Potential dependent variables

The list of potential but unadopted dependent variables is endless. They too must be targeted to meet the stated experimental aims, be applicable to the subject application space and be bound by practicability limits. These include measurement of condensed phase temperatures, heat fluxes, visual obscuration, and species concentration.

The novel coupled hybrid model implementation is primarily concentrated on gas phase phenomena. For this reason, measurement of condensed phase quantities was not adopted. Measurement of visibility through smoke and soot is an ongoing and controversial area of research [228]. How to quantify visibility and the assumptions and basis of 'established' visibility metrics is hotly debated. To avoid this uncertainty of output metric, when choice is limited, visual obscuration measurements were not adopted. Species concentration within the experimental rig would hold interest to those within the application space. However, due to constraint on cost, availability of specialist equipment, and reliability of available equipment, this dependent variable was not adopted.

A.4.3 Limitations of instrumentation

With any experimental setup compromises have to be made. These compromises may be due to time, cost, availability of materials or products, or any other host of reasons. The experimental apparatus is no different.

The thermocouples that were used had 'reasonably small' and exposed beads. However, smaller diameter thermocouples are of course available but carry a much higher cost. The advantage of smaller diameter thermocouples is that they have lower thermal inertia and therefore can respond to gas phase temperature differences more rapidly. Additionally they are heated less by radiation from the surrounding environment [229]. The saving grace for the experimental apparatus is that when carrying out the benchmarking exercise, the modelled thermocouple temperature can be output in addition to the gas phase temperature. In this manner, although adding another layer of simulation, the benchmarking can compare (real) apples with (simulated) apples. Additionally, compensational corrections can be made to thermocouple readings to correct for irradiation from the surroundings [230]. The accessibility of the in-duct thermocouples may also cause inaccuracies with the measurements. The in-duct thermocouples may experience soot deposition and therefore experience increasing thermal lag through the course of the experimental campaign.

Velocity measurements were only made in the centre of the ducts. One assumption made when outputting volume flow, mass flow, and energy flow is that the flow in the ducts is fully developed. That is, that the inviscid core has fully disappeared as the boundary layer expands to fill the duct with flow which is dominated by viscous effects. The entrance region can be estimated using Equation A.1 for turbulent flows.

$$\frac{\ell_e}{D} = 4.4(\mathrm{Re})^{1/6} \tag{A.1}$$

where ℓ_e is the entrance length, D is the duct diameter and Re is the Reynolds number. For values typical for the experimental apparatus, the entrance length is between 4.0 m to 4.5 m. This is longer than the duct runs in the experimental apparatus. Therefore the assumption of a fully developed flow velocity profile may not be accurate. However, Equation A.1 is for a straight pipe or duct. The experimental apparatus features junctions, turns, bifurcations, unions, and fans. This will influence the expansion of the viscous boundary layer and tend the duct flow more towards fully developed flow.

Appendix B

Primary source code

This appendix presents the new source code created by the author for this project. FDS is a very large computer program spread across many source files and newly created code was dotted throughout these files. For the purpose of this appendix, only the primary code is presented. For example, new output quantities, initialisations, type definitions, declarations, and the like are not presented. The subroutine in which the new code is located is presented. Line numbering does not refer to global project source code numbering and is for local use only.

```
1 MODULE HVAC_ROUTINES
2
3 ...
4
5 SUBROUTINE HVAC_CALC(T,DT,FIRST_PASS)
6 ! Solve for flows in the HVAC networks
7 INTEGER :: NNE,NN,NR
8 REAL(EB), INTENT(IN) :: T,DT
9 LOGICAL :: CHANGE=.TRUE.
10 LOGICAL, SAVE :: INITIALIZED_HVAC_MASS_TRANSPORT
11 LOGICAL, INTENT(IN) :: FIRST_PASS
12 TYPE(NETWORK_TYPE), POINTER:: NE=>NULL()
13 TYPE(DUCTRUN_TYPE), POINTER :: DR=>NULL()
14
15 DT_HV = DT
16 DT_MT = DT
17
18 IF (CORRECTOR) THEN
19     DUCT%VEL(OLD) = DUCT%VEL(NEW)
20     DUCT%VEL(PREVIOUS) = DUCT%VEL(NEW)
21     DUCT%VEL(GUESS) = DUCT%VEL(NEW)
22     DUCT%DP_FAN(OLD) = DUCT%DP_FAN(NEW)
23     DO NN=1,N_DUCTNODES
24         IF(DUCTNODE(NN)%FILTER_INDEX > 0) DUCTNODE(NN)%FILTER_LOADING(:,OLD)
    =DUCTNODE(NN)%FILTER_LOADING(:,NEW)
25         DUCTNODE(NN)%P_OLD = DUCTNODE(NN)%P
26     ENDDO
27     RETURN
28 ENDIF
29
30 IF (FIRST_PASS) THEN
31     CALL COLLAPSE_HVAC_BC
32     IF (LEAK_DUCTS > 0) CALL ADJUST_LEAKAGE_AREA
```

```
33     CALL FIND_NETWORKS(CHANGE,T) ! calls determined fixed elements (which
       calls update fan for fixed fans)
34     IF (.NOT. INITIALIZED_HVAC_MASS_TRANSPORT) CALL FIND_DUCTRUNS ! short
       term hack to get to run once, requires changing post-BETA
35     IF (.NOT. INITIALIZED_HVAC_MASS_TRANSPORT .AND. HVAC_MASS_TRANSPORT)
       CALL SET_INIT_HVAC_MASS_TRANSPORT
36     INITIALIZED_HVAC_MASS_TRANSPORT=.TRUE.
37 ENDIF
38
39 ITER = 0
40
41 DO NNE = 1, N_NETWORKS
42     NE =>NETWORK(NNE)
43     CALL SET_GUESS(NNE,T)
44 ENDDO
45
46 IF (N_ZONE >0) ALLOCATE(DPSTAR(1:N_ZONE))
47
48 CALL DPSTARCALC
49 DUCTNODE%P = DUCTNODE%P - P_INF
50
51 ! If a ductrun has a quadratic fan(s) and requires system curve steady
       state solution: allocate, zero, populate and solve matrices
52 DO NR = 1, N_DUCTRUNS
53     DR => DUCTRUN(NR)
54     IF (DR%N_QFANS > 0) THEN
55         ALLOCATE(DR%LHS_SYSTEM_1(DR%N_MATRIX_SYSTEM,DR%N_MATRIX_SYSTEM)) !
       LHS of first point of system curve
56         ALLOCATE(DR%LHS_SYSTEM_2(DR%N_MATRIX_SYSTEM,DR%N_MATRIX_SYSTEM)) !
       LHS of second point of system curve
57         ALLOCATE(DR%RHS_SYSTEM_1(DR%N_MATRIX_SYSTEM)) ! RHS of first point
       of system curve
58         ALLOCATE(DR%RHS_SYSTEM_2(DR%N_MATRIX_SYSTEM,DR%N_QFANS)) ! RHS of
       first point of system curve
59         DR%LHS_SYSTEM_1(:,:) = 0._EB
60         DR%LHS_SYSTEM_2(:,:) = 0._EB
61         DR%RHS_SYSTEM_1(:) = 0._EB
62         DR%RHS_SYSTEM_2(:,:) = 0._EB
63         CALL RHS_SYSTEM(NR)
64         CALL LHS_SYSTEM(NR)
65         CALL MATRIX_SYSTEM_SOLVE(NR)
66         ! Deallocate matrices used for solving steady state system curve
67         DEALLOCATE(DR%LHS_SYSTEM_1)
68         DEALLOCATE(DR%LHS_SYSTEM_2)
69         DEALLOCATE(DR%RHS_SYSTEM_1)
70         DEALLOCATE(DR%RHS_SYSTEM_2)
71     ENDIF
72 ENDDO
73
74 ...
75
76 IF (HVAC_MASS_TRANSPORT) CALL UPDATE_HVAC_MASS_TRANSPORT(DT_MT)
77
78 CALL UPDATE_NODE_BC
79
80 IF (ALLOCATED(DPSTAR)) DEALLOCATE(DPSTAR)
81
82
83 END SUBROUTINE HVAC_CALC
84
85 ...
```

```
86
87 SUBROUTINE MATRIX_SYSTEM_SOLVE(RN)
88 USE MATH_FUNCTIONS,ONLY : GAUSSJ
89 INTEGER :: RN,IERR,ND,FN
90 TYPE(DUCTRUN_TYPE), POINTER :: DR=>NULL()
91 TYPE(DUCT_TYPE), POINTER :: DU=>NULL()
92
93 DR =>DUCTRUN(RN)
94 CALL GAUSSJ(DR%LHS_SYSTEM_1,DR%N_MATRIX_SYSTEM,DR%N_MATRIX_SYSTEM,DR%
       RHS_SYSTEM_1,1,1,IERR)
95
96 DO FN = 1, DR%N_QFANS
97     CALL GAUSSJ(DR%LHS_SYSTEM_2,DR%N_MATRIX_SYSTEM,DR%N_MATRIX_SYSTEM,DR%
       RHS_SYSTEM_2(:,FN),1,1,IERR)
98 ENDDO
99
100 DO ND = 1,DR%N_DUCTS
101     DU=>DUCT(DR%DUCT_INDEX(ND))
102     IF (DU%FIXED .OR. DU%AREA < TWO_EPSILON_EB) CYCLE
103     DU%VEL_SYSTEM(1,1,1) = DU%VEL_SYSTEM(1,1,2) ! vel_system(sys#,fan#,old/
       new)
104     DU%VEL_SYSTEM(1,1,2) = DR%RHS_SYSTEM_1(DR%MATRIX_SYSTEM_INDEX(ND))
105     DO FN = 1, DR%N_QFANS
106         DU%VEL_SYSTEM(2,FN,1) = DU%VEL_SYSTEM(2,FN,2)
107         DU%VEL_SYSTEM(2,FN,2) = DR%RHS_SYSTEM_2(DR%MATRIX_SYSTEM_INDEX(ND),
       FN)
108     ENDDO
109 ENDDO
110
111
112 END SUBROUTINE MATRIX_SYSTEM_SOLVE
113
114 SUBROUTINE HVAC_UPDATE(NNE,DT)
115
116 ...
117
118 ! Outputs number of substeps required to maintain CFL for mass transport
119 N_SUBSTEPS = 1
120 DO ND = 1,NE%N_DUCTS
121     DU=>DUCT(NE%DUCT_INDEX(ND))
122     IF (DU%N_CELLS > 1 .AND. ABS(DU%VEL(NEW)) > 0._EB) THEN
123         DT_CFL = DU%LENGTH/ABS(DU%VEL(NEW)) ! relevant CFL is all mass
       leaving a duct within one DT
124         N_SUBSTEPS_DUCT = MAX(1,CEILING(DT/DT_CFL))
125         IF (N_SUBSTEPS_DUCT > N_SUBSTEPS) THEN
126             N_SUBSTEPS = N_SUBSTEPS_DUCT
127         ENDIF
128     ENDIF
129 ENDDO
130 DT_MT = DT/REAL(N_SUBSTEPS,EB)
131 SUB_CYCLE_FLAG = .TRUE.
132
133 SUBSTEP_LOOP: DO NSS = 1, N_SUBSTEPS
134     ITER_LOOP: DO
135         IF (NSS == N_SUBSTEPS) SUB_CYCLE_FLAG = .FALSE. ! Stops the final
       substep call of HVAC_MASS_... and UPDATE_NODE...
136         CYCLE_FLAG = .FALSE.
137         DUCT_LOOP:DO ND = 1,NE%N_DUCTS
138             DU=>DUCT(NE%DUCT_INDEX(ND))
139             IF (DU%UPDATED) CYCLE DUCT_LOOP
140             CYCLE_FLAG = .TRUE.
```

```
141             IF (DU%VEL(NEW) > TWO_EPSILON_EB) THEN
142                 DN => DUCTNODE(DU%NODE_INDEX(1))
143             ELSEIF (DU%VEL(NEW) < -TWO_EPSILON_EB) THEN
144                 DN => DUCTNODE(DU%NODE_INDEX(2))
145             ELSE
146                 DU%UPDATED = .TRUE.
147                 DU%VEL(NEW) = 0._EB
148                 DU%RHO_D = 0.5_EB*(DUCTNODE(DU%NODE_INDEX(1))%RHO+DUCTNODE(DU%
    NODE_INDEX(2))%RHO)
149                 DU%TMP_D = 0.5_EB*(DUCTNODE(DU%NODE_INDEX(1))%TMP+DUCTNODE(DU%
    NODE_INDEX(2))%TMP)
150                 CYCLE DUCT_LOOP
151             ENDIF
152             IF (DN%UPDATED) THEN
153                 DU%RHO_D  = DN%RHO
154                 DU%TMP_D  = DN%TMP
155                 DU%CP_D   = DN%CP
156                 DU%UPDATED = .TRUE.
157                 DU%ZZ(:) = DN%ZZ(:)
158                 ZZ_GET = DU%ZZ
159             ENDIF
160         ENDDO DUCT_LOOP
161
162         NODE_LOOP:DO NN = 1,NE%N_DUCTNODES
163 ...
164
165                 MASS_TRANSPORT_IF: IF (DU%N_CELLS==1) THEN
166 ...
167                 ELSE MASS_TRANSPORT_IF
168                     ! Duct is discretized: we need to find the end of the lump
    of mass advected within a (sub)step
169                     MFLOW = ABS(DU%VEL(NEW)*DU%RHO_D)*DT_MT ! Duct mass flow
    corrected for any substepping
170                     MSUM = 0
171                     ZZSUM = 0
172                     CPTSUM = 0
173                     DU_DX = DU%LENGTH/REAL(DU%N_CELLS,EB)
174                     ! Sums cumulative mass, species and energy from the final
    cell, to locate end of advected lump of mass
175                     IF (DU%VEL(NEW) > 0._EB) THEN
176                         DO NC = DU%N_CELLS,1,-1
177                             IF (MSUM + DU%RHO_C(NC)*DU_DX > MFLOW) THEN
178                                 DU_DX = (MFLOW - MSUM)/DU%RHO_C(NC)
179                                 ZZSUM(:) = ZZSUM(:) + DU%RHO_C(NC)*DU%ZZ_C(NC,:)*
    DU_DX
180                                 CPTSUM = CPTSUM + DU%RHO_C(NC)*DU%TMP_C(NC)*DU%
    CP_C(NC)*DU_DX
181                                 EXIT
182                             ELSE
183                                 MSUM = MSUM + DU%RHO_C(NC)*DU_DX
184                                 ZZSUM(:) = ZZSUM(:) + DU%RHO_C(NC)*DU%ZZ_C(NC,:)*
    DU_DX
185                                 CPTSUM = CPTSUM + DU%RHO_C(NC)*DU%TMP_C(NC)*DU%
    CP_C(NC)*DU_DX
186                             ENDIF
187                         ENDDO
188                     ELSE
189                         DO NC = 1,DU%N_CELLS
190                             IF (MSUM + DU%RHO_C(NC)*DU_DX > MFLOW) THEN
191                                 DU_DX = (MFLOW - MSUM)/DU%RHO_C(NC)
```

```
192                             ZZSUM(:) = ZZSUM(:) + DU%RHO_C(NC)*DU%ZZ_C(NC,:)*
    DU_DX
193                             CPTSUM = CPTSUM + DU%RHO_C(NC)*DU%TMP_C(NC)*DU%
    CP_C(NC)*DU_DX
194                             EXIT
195                         ELSE
196                             MSUM = MSUM + DU%RHO_C(NC)*DU_DX
197                             ZZSUM(:) = ZZSUM(:) + DU%RHO_C(NC)*DU%ZZ_C(NC,:)*
    DU_DX
198                             CPTSUM = CPTSUM + DU%RHO_C(NC)*DU%TMP_C(NC)*DU%
    CP_C(NC)*DU_DX
199                         ENDIF
200                     ENDDO
201                 ENDIF
202                 ! Cumulative sums of energy, mass, species passing through
    duct node from ducts
203                 ETOT = ETOT + CPTSUM * DU%AREA / DT_MT
204                 MTOT = MTOT + MFLOW * DU%AREA / DT_MT
205                 ZZTOT = ZZTOT + ZZSUM * DU%AREA / DT_MT
206                 TGUESS = TGUESS + MFLOW * DU%AREA / DT_MT * DU%TMP_D
207             ENDIF MASS_TRANSPORT_IF
208             ETOT = ETOT + DU%COIL_Q
209         ENDDO
210
211 ...
212
213         DN%UPDATED = .TRUE.
214         IF (ABS(MTOT)<=TWO_EPSILON_EB) CYCLE NODE_LOOP
215         ZZ_GET = 0._EB
216         DN%ZZ(:)   = ZZTOT/MTOT
217         ZZ_GET(1:N_TRACKED_SPECIES) = DN%ZZ(1:N_TRACKED_SPECIES)
218         CALL GET_SPECIFIC_GAS_CONSTANT(ZZ_GET,DN%RSUM)
219         ETOT = ETOT/ MTOT
220         TGUESS = TGUESS/MTOT
221         ITCOUNT = 0
222         CP_LOOP: DO ! Newton method to find solution of T (and hence
    cpbar) from enthalpy
223             ITCOUNT = ITCOUNT + 1
224             CALL GET_ENTHALPY(ZZ_GET,HGAS,TGUESS)
225             CALL GET_AVERAGE_SPECIFIC_HEAT(ZZ_GET,CP,TGUESS)
226             IF (TGUESS>1._EB) THEN
227                 CALL GET_AVERAGE_SPECIFIC_HEAT(ZZ_GET,CP2,TGUESS-1._EB)
228                 DCPDT = CP - CP2
229             ELSE
230                 CALL GET_AVERAGE_SPECIFIC_HEAT(ZZ_GET,CP2,TGUESS+1._EB)
231                 DCPDT = CP2- CP
232             ENDIF
233             CP = HGAS / TGUESS
234             DN%TMP =TGUESS+(ETOT-HGAS) / (CP+TGUESS*DCPDT)
235             IF (ABS(DN%TMP - TGUESS) < TWO_EPSILON_EB) EXIT CP_LOOP
236             IF (ABS(DN%TMP - TGUESS)/DN%TMP < 0.0005_EB) EXIT CP_LOOP
237             IF (ITCOUNT > 10) THEN
238                 DN%TMP = 0.5_EB*(DN%TMP+TGUESS)
239                 EXIT CP_LOOP
240             ENDIF
241             TGUESS = MAX(0._EB,DN%TMP)
242         ENDDO CP_LOOP
243
244         CALL GET_ENTHALPY(ZZ_GET,HGAS,DN%TMP)
245         DN%CP = HGAS/DN%TMP
246         DN%RHO = (DN%P+P_INF) / (DN%RSUM*DN%TMP)
```

```
247         ENDDO NODE_LOOP
248
249         IF (.NOT. CYCLE_FLAG) EXIT ITER_LOOP
250
251       ENDDO ITER_LOOP
252
253 ! If there are substeps remaining, we must advance mass transport and
      update node BCs to ensure we're conserving mass, energy
254       IF (SUB_CYCLE_FLAG) THEN
255         CALL UPDATE_HVAC_MASS_TRANSPORT(DT_MT)
256         CALL UPDATE_NODE_BC
257       ENDIF
258
259 ENDDO SUBSTEP_LOOP
260
261 T_USED(13)=T_USED(13)+CURRENT_TIME()-TNOW
262
263 END SUBROUTINE HVAC_UPDATE
264
265
266 ...
267
268
269 SUBROUTINE RHS_SYSTEM(DUCTRUN_INDEX)
270 ! Populates right hand side of matrix for steady state solution of ductrun
      to output system curve
271 USE GLOBAL_CONSTANTS
272 INTEGER, INTENT(IN) :: DUCTRUN_INDEX
273 INTEGER :: ARRAYLOC, ND, FAN_COUNTER, IPZ
274 REAL(EB) :: HEAD,FAN_PRES,XYZ(3)
275 TYPE(DUCTRUN_TYPE), POINTER::DR=>NULL()
276 TYPE(DUCT_TYPE), POINTER::DU=>NULL()
277 TYPE(DUCTNODE_TYPE), POINTER::DN=>NULL()
278
279 DR => DUCTRUN(DUCTRUN_INDEX)
280 FAN_COUNTER = 1
281
282 DO ND = 1, DR%N_DUCTS
283     DU => DUCT(DR%DUCT_INDEX(ND))
284     IF (DU%FIXED .OR. DU%AREA < TWO_EPSILON_EB) CYCLE ! duct fixed: has a
      fixed volume, mass or fan
285     HEAD = 0._EB
286     ARRAYLOC = DR%MATRIX_SYSTEM_INDEX(DUCT_DR(DR%DUCT_INDEX(ND)))
287     DN => DUCTNODE(DU%NODE_INDEX(1)) ! point to node 1, if fixed then need
      to add p1
288     IF (DN%AMBIENT) THEN
289         HEAD = DN%P
290     ELSEIF(DN%VENT .OR. DN%LEAKAGE) THEN
291         HEAD = DN%P
292         IF (N_ZONE > 0) THEN
293             IPZ = DN%ZONE_INDEX
294             IF (IPZ > 0) HEAD = HEAD + DPSTAR(IPZ) ! adds zone pressure
295         ENDIF
296     ENDIF
297     XYZ = DN%XYZ ! get location ready for delta z
298
299     DN => DUCTNODE(DU%NODE_INDEX(2)) ! point to node 2, if fixed then need
      to subtract p2
300     IF (DN%AMBIENT) THEN
301         HEAD = HEAD - DN%P
302     ELSEIF (DN%VENT .OR. DN%LEAKAGE) THEN
```

```
303         HEAD = HEAD - DN%P
304         IF (N_ZONE > 0) THEN
305             IPZ = DN%ZONE_INDEX
306             IF (IPZ > 0) HEAD = HEAD - DPSTAR(IPZ)
307         ENDIF
308     ENDIF
309
310     XYZ = DN%XYZ - XYZ ! get delta z
311
312     ! Add hydrostatic head
313     IF(.NOT. DU%LEAKAGE) THEN
314         HEAD = HEAD + (GVEC(1)*XYZ(1)+GVEC(2)*XYZ(2)+GVEC(3)*XYZ(3))*DU%
        RHO_D
315     ENDIF
316
317     ! Populate RHS_SYSTEM for each duct equation
318     DR%RHS_SYSTEM_1(ARRAYLOC) = HEAD
319     DR%RHS_SYSTEM_2(ARRAYLOC,:) = HEAD ! same head for all fan cases
320
321     ! Add pressure from fan, if there are multiple fans, each needs a
        system curve
322     FAN_PRES = 0._EB
323     IF (DU%FAN_INDEX > 0) THEN
324         FAN_PRES = FAN(DU%FAN_INDEX)%MAX_PRES
325         DR%RHS_SYSTEM_2(ND,FAN_COUNTER) = DR%RHS_SYSTEM_2(ND,FAN_COUNTER) +
        FAN_PRES
326         FAN_COUNTER = FAN_COUNTER + 1
327     ENDIF
328 ENDDO
329
330 END SUBROUTINE RHS_SYSTEM
331
332
333 SUBROUTINE LHS_SYSTEM(DUCTRUN_INDEX)
334 ! Populates LHS matrix for steady state solution required to output system
        curve
335 USE GLOBAL_CONSTANTS
336 INTEGER, INTENT(IN)::DUCTRUN_INDEX
337 INTEGER :: NN,ND,FN, ARRAYLOC1,ARRAYLOC2
338 TYPE(DUCTRUN_TYPE), POINTER::DR=>NULL()
339 TYPE(DUCT_TYPE), POINTER::DU=>NULL()
340 TYPE(DUCTNODE_TYPE), POINTER::DN=>NULL()
341
342 DR => DUCTRUN(DUCTRUN_INDEX)
343 ! Duct energy equations
344 DUCT_LOOP: DO ND = 1, DR%N_DUCTS
345     DU => DUCT(DR%DUCT_INDEX(ND))
346     IF (DU%FIXED .OR. DU%AREA < TWO_EPSILON_EB) CYCLE DUCT_LOOP
347     ARRAYLOC1 = DR%MATRIX_SYSTEM_INDEX(DUCT_DR(DR%DUCT_INDEX(ND)))
348     ! Velocity coefficient
349     DR%LHS_SYSTEM_1(ARRAYLOC1,ARRAYLOC1) = 0.25_EB*DU%RHO_D*DU%TOTAL_LOSS*
        ABS(DU%VEL_SYSTEM(1,1,1) + DU%VEL_SYSTEM(1,1,2))
350     DO FN = 1, DR%N_QFANS
351         DR%LHS_SYSTEM_2(ARRAYLOC1,ARRAYLOC1) = 0.25_EB*DU%RHO_D*DU%
        TOTAL_LOSS*ABS(DU%VEL_SYSTEM(2,FN,1) + DU%VEL_SYSTEM(2,FN,2))
352     ENDDO
353     ! Pressure coefficients
354     ARRAYLOC2 = DR%MATRIX_SYSTEM_INDEX(DR%N_DUCTS+DUCTNODE_DR(DU%NODE_INDEX
        (1)))
355     IF (ARRAYLOC2 > 0) THEN
356         DR%LHS_SYSTEM_1(ARRAYLOC1,ARRAYLOC2) = -1._EB
```

```
357         DR%LHS_SYSTEM_2(ARRAYLOC1,ARRAYLOC2) = -1._EB
358       ENDIF
359       ARRAYLOC2 = DR%MATRIX_SYSTEM_INDEX(DR%N_DUCTS+DUCTNODE_DR(DU%NODE_INDEX
          (2)))
360       IF (ARRAYLOC2 > 0) THEN
361         DR%LHS_SYSTEM_1(ARRAYLOC1,ARRAYLOC2) = 1._EB
362         DR%LHS_SYSTEM_2(ARRAYLOC1,ARRAYLOC2) = 1._EB
363       ENDIF
364 ENDDO DUCT_LOOP
365
366 ! Node conservation
367 DO NN = 1, DR%N_DUCTNODES
368       DN => DUCTNODE(DR%NODE_INDEX(NN))
369       IF (DN%FIXED .OR. DN%VENT .OR. DN%LEAKAGE) CYCLE ! only internal nodes
370       ARRAYLOC1 = DR%MATRIX_SYSTEM_INDEX(DR%N_DUCTS+DUCTNODE_DR(DR%NODE_INDEX
          (NN)))
371       DO ND = 1,DN%N_DUCTS
372         DU => DUCT(DN%DUCT_INDEX(ND))
373         IF (DU%FIXED .OR. DU%AREA <=TWO_EPSILON_EB) CYCLE
374         ARRAYLOC2 = DR%MATRIX_SYSTEM_INDEX(DUCT_DR(DN%DUCT_INDEX(ND)))
375         DR%LHS_SYSTEM_1(ARRAYLOC1,ARRAYLOC2) = -DN%DIR(ND)*DU%RHO_D*DU%AREA
376         DR%LHS_SYSTEM_2(ARRAYLOC1,ARRAYLOC2) = -DN%DIR(ND)*DU%RHO_D*DU%AREA
377       END DO
378 ENDDO
379
380 END SUBROUTINE LHS_SYSTEM
381
382
383 SUBROUTINE UPDATE_FAN(T,DUCT_INDEX)
384 ...
385       CASE(4) ! System curve-based quadratic fan BETA
386         FLOW1 = DU%VEL_SYSTEM(1,1,2)*DU%AREA
387         FLOW2 = DU%VEL_SYSTEM(2,DU%QFAN_N,2)*DU%AREA
388         FAN_ITER = 0
389         FAN_LOOP1: DO
390           FAN_ITER = FAN_ITER + 1
391           FLOWGUESS = 0.5*(FLOW1+FLOW2)
392           IF (ABS(FLOWGUESS - FLOW1) < TWO_EPSILON_EB) EXIT FAN_LOOP1
393           FUNC = FA%MAX_PRES/((DU%VEL_SYSTEM(2,DU%QFAN_N,2)-DU%VEL_SYSTEM
          (1,1,2))*DU%AREA)**2
394           FUNC = FUNC * (FLOWGUESS-DU%VEL_SYSTEM(1,1,2)*DU%AREA)**2
395           FUNC = FUNC - FA%MAX_PRES + FA%MAX_PRES*(FLOWGUESS/FA%MAX_FLOW)
          **2 ! i think this should be a minus not a plus
396           IF (FUNC > 0) THEN
397             FLOW2 = FLOWGUESS
398           ELSE
399             FLOW1 = FLOWGUESS
400           ENDIF
401           IF (FAN_ITER > 100) THEN
402             FLOWGUESS = 0.5_EB*(FLOW1 + FLOW2)
403             EXIT FAN_LOOP1
404           ENDIF
405         ENDDO FAN_LOOP1
406         ! Output fan pressure equating to output flow rate
407         DEL_P = FA%MAX_PRES - FA%MAX_PRES*(FLOWGUESS/FA%MAX_FLOW)**2
408         DEL_P = DEL_P*EVALUATE_RAMP(TSI,FA%TAU,FA%SPIN_INDEX)
409       CASE(5) ! Local system-curve based quadratic fan BETA
410           DN1=>DUCTNODE(DU%NODE_INDEX(1))
411           DN2=>DUCTNODE(DU%NODE_INDEX(2))
412           ! Get two points on system curve
413           HEAD = DN1%P-DN2%P+DU%RHO_D*GRAV*(DN1%XYZ(3)-DN2%XYZ(3))
```

```
414             IF (DU%SYSTEM_LOSS > 0) THEN ! user input
415                 LOSS = 0.5_EB*DU%RHO_D*DU%SYSTEM_LOSS*EVALUATE_RAMP(T,0._EB,DU
        %RAMP_LOSS_INDEX)
416             ELSE
417                 LOSS = 0.5_EB*DU%RHO_D*DU%TOTAL_LOSS
418             ENDIF
419             IF (HEAD/LOSS > 0) THEN
420                 FLOW1 = SQRT(HEAD/LOSS)*DU%AREA
421             ELSE
422                 FLOW1 = SQRT(-HEAD/LOSS)*DU%AREA
423             ENDIF
424             IF ((HEAD + FA%MAX_PRES)/LOSS > 0) THEN
425                 FLOW2 = SQRT((HEAD + FA%MAX_PRES)/LOSS)*DU%AREA
426             ELSE
427                 FLOW2 = SQRT(-(HEAD + FA%MAX_PRES)/LOSS)*DU%AREA
428             ENDIF
429             DEL_P1 = FA%MAX_PRES-FA%MAX_PRES*(FLOW1/FA%MAX_FLOW)**2
430             del_p2 = FA%MAX_PRES-FA%MAX_PRES*(FLOW2/FA%MAX_FLOW)**2
431             ! Use bisect to find intersection point (operation point)
432             FAN_ITER = 0
433             guessdown = 0._EB
434             guessup = FA%MAX_FLOW
435             FAN_LOOP2: DO
436                 FAN_ITER = FAN_ITER + 1
437                 FLOWGUESS = 0.5*(GUESSDOWN+GUESSUP)
438                 IF (ABS(FLOWGUESS - GUESSDOWN) < TWO_EPSILON_EB) EXIT
        FAN_LOOP2
439                 FUNC = FLOWGUESS**2*(FLOW1-FLOW2)**2+FA%MAX_FLOW**2*(FLOWGUESS
        -FLOW1)**2-&
440                         FA%MAX_FLOW**2*(FLOW1-FLOW2)**2
441                 IF (FUNC > 0) THEN
442                     IF (ABS(FLOWGUESS - GUESSUP)/FLOWGUESS < 0.0001) EXIT
        FAN_LOOP2
443                     GUESSUP = FLOWGUESS
444                 ELSE
445                     IF (ABS(FLOWGUESS - GUESSDOWN)/FLOWGUESS < 0.0001) EXIT
        FAN_LOOP2
446                     GUESSDOWN = FLOWGUESS
447                 ENDIF
448                 IF (FAN_ITER > 100) THEN
449                     FLOWGUESS = 0.5_EB*(GUESSDOWN + GUESSUP)
450                     EXIT FAN_LOOP2
451                 ENDIF
452             ENDDO FAN_LOOP2
453             ! Output pressure at operation point
454             DEL_P = FA%MAX_PRES-FA%MAX_PRES*(FLOWGUESS/FA%MAX_FLOW)**2
455             DEL_P = DEL_P*EVALUATE_RAMP(TSI,FA%TAU,FA%SPIN_INDEX)
456 END SELECT
457
458 IF (DU%REVERSE) DEL_P=-DEL_P
459 DU%DP_FAN(NEW) = DEL_P
460
461 END SUBROUTINE UPDATE_FAN
462 ...
463
464
465 SUBROUTINE FIND_DUCTRUNS
466 ! Finds "duct runs"; being ductnodes and ducts directly (via HVAC
        components) connected to one another
467 INTEGER :: NN,NR,NN2,NN3,NN4,ND,DUCT_COUNTER(N_DUCTS),NODE_COUNTER(
        N_DUCTNODES),&
```

```
468                 NODE_CHECKED(N_DUCTNODES) ,CHKFLG,NODE_CONNECTED(N_DUCTNODES) ,
      N_QFANS,N_Q2FANS
469 INTEGER, DIMENSION(:), ALLOCATABLE :: DUCTRUN_DCOUNTER,DUCTRUN_NCOUNTER
470
471 ! Zeroing work arrays and initialising counters
472 DO NN = 1, N_DUCTNODES
473     NODE_CHECKED(NN) = 0
474     NODE_CONNECTED(NN) = 0
475     NODE_COUNTER(NN) = 0
476 END DO
477 DO ND = 1, N_DUCTS
478     DUCT_COUNTER(ND) = 0
479 END DO
480
481 NR = 1
482 NODE_COUNTER(1) = NR
483 NN = 1
484
485 ! Finds all connected ducts and nodes and hence number of ductruns
486 L1:DO
487     IF (NODE_CHECKED(NN) == 1) THEN
488         NN = NN + 1
489         CYCLE L1
490     END IF
491     NN3 = 1
492     DO ND = 1, DUCTNODE(NN)%N_DUCTS
493         DUCT_COUNTER(DUCTNODE(NN)%DUCT_INDEX(ND)) = NR
494         NODE_COUNTER(DUCT(DUCTNODE(NN)%DUCT_INDEX(ND))%NODE_INDEX(1)) = NR
495         NODE_COUNTER(DUCT(DUCTNODE(NN)%DUCT_INDEX(ND))%NODE_INDEX(2)) = NR
496         NODE_CONNECTED(DUCT(DUCTNODE(NN)%DUCT_INDEX(ND))%NODE_INDEX(1)) = 1
497         NODE_CONNECTED(DUCT(DUCTNODE(NN)%DUCT_INDEX(ND))%NODE_INDEX(2)) = 1
498     END DO
499     NODE_CHECKED(NN) = 1
500     CHKFLG = 0
501     DO NN2 = 1, N_DUCTNODES
502         CHKFLG = CHKFLG + NODE_CHECKED(NN2)
503     END DO
504     IF (CHKFLG == N_DUCTNODES) EXIT L1
505     L2:DO NN3 = 1, N_DUCTNODES
506         IF (NODE_CHECKED(NN3) == 1) THEN
507             CYCLE L2
508         ELSE IF (NODE_CHECKED(NN3) == 0 .AND. NODE_CONNECTED(NN3) == 1) THEN
509             NN = NN3
510             EXIT L2
511         ELSE IF (NN3 == N_DUCTNODES) THEN
512             NR = NR + 1
513             DO NN4 = 1, N_DUCTNODES
514                 NODE_CONNECTED(NN4) = 0
515             END DO
516             NN = 1
517             EXIT L2
518         ELSE
519             CYCLE L2
520         END IF
521     END DO L2
522 END DO L1
523
524 N_DUCTRUNS = MAXVAL(NODE_COUNTER)
525 ALLOCATE(DUCTRUN(N_DUCTRUNS))
526
527 ! Zeros and then sums up number of ducts and ductnodes for DUCTRUN array
```

```
528 DO NR=1, N_DUCTRUNS
529     DUCTRUN(NR)%N_DUCTS=0
530     DUCTRUN(NR)%N_DUCTNODES=0
531 ENDDO
532 DO ND = 1, N_DUCTS
533     DUCTRUN(DUCT_COUNTER(ND))%N_DUCTS = DUCTRUN(DUCT_COUNTER(ND))%N_DUCTS +
          1
534 ENDDO
535 DO NN = 1, N_DUCTNODES
536     DUCTRUN(NODE_COUNTER(NN))%N_DUCTNODES = DUCTRUN(NODE_COUNTER(NN))%
        N_DUCTNODES + 1
537 ENDDO
538
539 ! Allocates work arrays for duct, node and fan indexing
540 ALLOCATE(DUCTRUN_DCOUNTER(N_DUCTRUNS))
541 DUCTRUN_DCOUNTER=0
542 ALLOCATE(DUCTRUN_NCOUNTER(N_DUCTRUNS))
543 DUCTRUN_NCOUNTER=0
544
545 ! Allocates and populates DUCTRUN duct and node indexes
546 DO NR = 1, N_DUCTRUNS
547     ALLOCATE(DUCTRUN(NR)%DUCT_INDEX(DUCTRUN(NR)%N_DUCTS))
548     ALLOCATE(DUCTRUN(NR)%NODE_INDEX(DUCTRUN(NR)%N_DUCTNODES))
549 ENDDO
550 DO ND = 1, N_DUCTS
551     DUCTRUN_DCOUNTER(DUCT_COUNTER(ND)) = DUCTRUN_DCOUNTER(DUCT_COUNTER(ND))
          + 1
552     DUCTRUN(DUCT_COUNTER(ND))%DUCT_INDEX(DUCTRUN_DCOUNTER(DUCT_COUNTER(ND))
        ) = ND
553     DUCT_DR(ND) = DUCTRUN_DCOUNTER(DUCT_COUNTER(ND))
554 ENDDO
555 DO NN = 1, N_DUCTNODES
556     DUCTRUN_NCOUNTER(NODE_COUNTER(NN)) = DUCTRUN_NCOUNTER(NODE_COUNTER(NN))
          + 1
557     DUCTRUN(NODE_COUNTER(NN))%NODE_INDEX(DUCTRUN_NCOUNTER(NODE_COUNTER(NN))
        ) = NN
558     DUCTNODE_DR(NN) = DUCTRUN_NCOUNTER(NODE_COUNTER(NN))
559 ENDDO
560
561 ! Populates number of quadratic fans and indexes them within DUCT
562 DO NR = 1, N_DUCTRUNS
563     N_QFANS = 0
564     DO ND = 1, DUCTRUN(NR)%N_DUCTS
565         IF (DUCT(DUCTRUN(NR)%DUCT_INDEX(ND))%FAN_INDEX > 0) THEN
566             IF (FAN(DUCT(DUCTRUN(NR)%DUCT_INDEX(ND))%FAN_INDEX)%FAN_TYPE ==
        4) THEN
567                 N_QFANS = N_QFANS + 1
568                 DUCT(DUCTRUN(NR)%DUCT_INDEX(ND))%QFAN_N = N_QFANS
569             ENDIF
570         ENDIF
571     ENDDO
572     DUCTRUN(NR)%N_QFANS = N_QFANS
573 ENDDO
574
575 ! Allocate and zero solution matrix indices and system curve velocities
576 DO NR = 1, N_DUCTRUNS
577     ALLOCATE(DUCTRUN(NR)%MATRIX_SYSTEM_INDEX(DUCTRUN(NR)%N_DUCTS+DUCTRUN(NR
        )%N_DUCTNODES))
578     DUCTRUN(NR)%MATRIX_SYSTEM_INDEX = 0
579     DO ND = 1, DUCTRUN(NR)%N_DUCTS
```

```
580         ALLOCATE(DUCT(DUCTRUN(NR)%DUCT_INDEX(ND))%VEL_SYSTEM(2,DUCTRUN(NR)%
        N_QFANS,2)) ! vel_system(sys#,fan#,old/new)
581         DUCT(DUCTRUN(NR)%DUCT_INDEX(ND))%VEL_SYSTEM(1,:,:) = 0._EB
582         DUCT(DUCTRUN(NR)%DUCT_INDEX(ND))%VEL_SYSTEM(2,:,:) = TWO_EPSILON_EB
583      ENDDO
584 ENDDO
585
586 CALL SETUP_SOLUTION_SYSTEM_POINTERS
587
588 DEALLOCATE(DUCTRUN_DCOUNTER)
589 DEALLOCATE(DUCTRUN_NCOUNTER)
590
591 END SUBROUTINE FIND_DUCTRUNS
592
593 ...
594
595
596 SUBROUTINE SETUP_SOLUTION_SYSTEM_POINTERS
597 INTEGER:: NR,NN,ND,COUNTER
598 TYPE(DUCT_TYPE), POINTER :: DU=>NULL()
599 TYPE(DUCTNODE_TYPE), POINTER :: DN=>NULL()
600 TYPE(DUCTRUN_TYPE), POINTER :: DR=>NULL()
601
602 DO NR = 1,N_DUCTRUNS
603    COUNTER = 0
604    DR => DUCTRUN(NR)
605    DO ND=1,DR%N_DUCTS
606       DU=>DUCT(DR%DUCT_INDEX(ND))
607       IF (DU%FIXED .OR. DU%AREA<=TWO_EPSILON_EB) CYCLE
608       COUNTER = COUNTER + 1
609       DR%MATRIX_SYSTEM_INDEX(ND)=COUNTER
610    ENDDO
611    DO NN=1,DR%N_DUCTNODES
612       DN=>DUCTNODE(DR%NODE_INDEX(NN))
613       IF (DN%FIXED .OR. DN%VENT) CYCLE
614       COUNTER = COUNTER + 1
615       DR%MATRIX_SYSTEM_INDEX(DR%N_DUCTS+NN)=COUNTER
616    ENDDO
617    DR%N_MATRIX_SYSTEM = COUNTER
618 ENDDO
619
620 END SUBROUTINE SETUP_SOLUTION_SYSTEM_POINTERS
621
622 ...
623
624
625 SUBROUTINE SET_INIT_HVAC_MASS_TRANSPORT
626 ! Initialises cell densities, temperatures, specific heats and species'
       for discretised ducts
627 USE PHYSICAL_FUNCTIONS, ONLY: GET_ENTHALPY
628 USE COMP_FUNCTIONS, ONLY: CURRENT_TIME
629 INTEGER :: ND,NN,NR
630 REAL(EB) :: DRHO,DTMP,DZZ(1:N_TRACKED_SPECIES), ZZ_GET(1:N_TRACKED_SPECIES
       ),HGAS
631 TYPE(DUCT_TYPE), POINTER :: DU=>NULL()
632 TYPE(DUCTRUN_TYPE), POINTER :: DR=>NULL()
633
634 ! Propagates duct interpolation method through the ductruns, checking for
       errors in input
635 DO NR = 1, N_DUCTRUNS
636    DR => DUCTRUN(NR)
```

```
637     DO ND = 1, DR%N_DUCTS
638         DU => DUCT(DR%DUCT_INDEX(ND))
639         IF (DU%DUCT_INTERP_TYPE_INDEX /= DUCT(DR%DUCT_INDEX(1))%
        DUCT_INTERP_TYPE_INDEX) THEN
640             WRITE(MESSAGE,'(A,A,A,I5)') 'ERROR: DUCT_INTERP_TYPE must be
        consistent through ductruns. Duct ID: ',TRIM(DU%ID)
641             CALL SHUTDOWN(MESSAGE); RETURN
642         END IF
643         DU%DUCT_INTERP_TYPE_INDEX = DUCT(DR%DUCT_INDEX(1))%
        DUCT_INTERP_TYPE_INDEX
644     END DO
645 END DO
646
647 ! Initialize ductnode values and duct cell arrays for duct mass transport
648 DUCTRUN_LOOP:DO NR = 1, N_DUCTRUNS
649     DR => DUCTRUN(NR)
650     DUCT_LOOP:DO ND = 1, DR%N_DUCTS
651         DU => DUCT(DR%DUCT_INDEX(ND))
652         IF (DU%LEAKAGE) CYCLE
653         IF (DU%N_CELLS==1) CYCLE
654         SELECT CASE (DU%DUCT_INTERP_TYPE_INDEX)
655             CASE (NODE1) ! duct cells and ductnodes adopt values from node 1
        of lowest duct_index duct in ductrun
656                 DU%RHO_C(:) = DUCTNODE(DUCT(DR%DUCT_INDEX(1))%NODE_INDEX(1))%
        RHO_V
657                 DU%TMP_C(:) = DUCTNODE(DUCT(DR%DUCT_INDEX(1))%NODE_INDEX(1))%
        TMP
658                 DU%CP_C(:) = DUCTNODE(DUCT(DR%DUCT_INDEX(1))%NODE_INDEX(1))%CP
659                 DO NN = 1, DU%N_CELLS
660                     DU%ZZ_C(NN,1:N_TRACKED_SPECIES) = DUCTNODE(DUCT(DR%
        DUCT_INDEX(1))%NODE_INDEX(1))%ZZ
661                 ENDDO
662                 DO NN = 1, 2
663                     DUCTNODE(DU%NODE_INDEX(NN))%RHO = DUCTNODE(DUCT(DR%
        DUCT_INDEX(1))%NODE_INDEX(1))%RHO_V
664                     DUCTNODE(DU%NODE_INDEX(NN))%TMP = DUCTNODE(DUCT(DR%
        DUCT_INDEX(1))%NODE_INDEX(1))%TMP
665                     DUCTNODE(DU%NODE_INDEX(NN))%CP = DUCTNODE(DUCT(DR%
        DUCT_INDEX(1))%NODE_INDEX(1))%CP
666                     DUCTNODE(DU%NODE_INDEX(NN))%ZZ = DUCTNODE(DUCT(DR%
        DUCT_INDEX(1))%NODE_INDEX(1))%ZZ
667                 END DO
668             CASE (NODE2) ! duct cells and ductnodes adopt values from node 2
        of highest duct_index duct in ductrun
669                 DU%RHO_C = DUCTNODE(DUCT(DR%DUCT_INDEX(DR%N_DUCTS))%NODE_INDEX
        (2))%RHO_V
670                 DU%TMP_C = DUCTNODE(DUCT(DR%DUCT_INDEX(DR%N_DUCTS))%NODE_INDEX
        (2))%TMP
671                 DU%CP_C = DUCTNODE(DUCT(DR%DUCT_INDEX(DR%N_DUCTS))%NODE_INDEX
        (2))%CP
672                 DO NN = 1, DU%N_CELLS
673                     DU%ZZ_C(NN,1:N_TRACKED_SPECIES) = DUCTNODE(DUCT(DR%
        DUCT_INDEX(DR%N_DUCTS))%NODE_INDEX(2))%ZZ
674                 ENDDO
675                 DO NN = 1, 2
676                     DUCTNODE(DU%NODE_INDEX(NN))%RHO = DUCTNODE(DUCT(DR%
        DUCT_INDEX(DR%N_DUCTS))%NODE_INDEX(2))%RHO_V
677                     DUCTNODE(DU%NODE_INDEX(NN))%TMP = DUCTNODE(DUCT(DR%
        DUCT_INDEX(DR%N_DUCTS))%NODE_INDEX(2))%TMP
678                     DUCTNODE(DU%NODE_INDEX(NN))%CP = DUCTNODE(DUCT(DR%
        DUCT_INDEX(DR%N_DUCTS))%NODE_INDEX(2))%CP
```

```
679                     DUCTNODE(DU%NODE_INDEX(NN))%ZZ = DUCTNODE(DUCT(DR%
      DUCT_INDEX(DR%N_DUCTS))%NODE_INDEX(2))%ZZ
680                 END DO
681               CASE (LINEAR_INTERPOLATION) ! linear interp' between node 1 and 2
       (for verification case, has problem w/ complex networks)
682                 DRHO = (DUCTNODE(DU%NODE_INDEX(2))%RHO - DUCTNODE(DU%
      NODE_INDEX(1))%RHO) / DU%N_CELLS
683                 DTMP = (DUCTNODE(DU%NODE_INDEX(2))%TMP - DUCTNODE(DU%
      NODE_INDEX(1))%TMP) / DU%N_CELLS
684                 DZZ(1:N_TRACKED_SPECIES) = (DUCTNODE(DU%NODE_INDEX(2))%ZZ -
      DUCTNODE(DU%NODE_INDEX(1))%ZZ) / DU%N_CELLS
685                 DO NN = 1, DU%N_CELLS
686                   DU%RHO_C(NN) = DUCTNODE(DU%NODE_INDEX(1))%RHO + DRHO*(REAL(
      NN,EB) - 0.5_EB)
687                   DU%TMP_C(NN) = DUCTNODE(DU%NODE_INDEX(1))%TMP + DTMP*(REAL(
      NN,EB) - 0.5_EB)
688                   DU%ZZ_C(NN,1:N_TRACKED_SPECIES) = DUCTNODE(DU%NODE_INDEX(1)
      )%ZZ + DZZ(:)*(REAL(NN,EB) - 0.5_EB)
689                   ZZ_GET = DU%ZZ_C(NN,1:N_TRACKED_SPECIES)
690                   CALL GET_ENTHALPY(ZZ_GET,HGAS,DU%TMP_C(NN))
691                   DU%CP_C(NN) = HGAS / DU%TMP_C(NN)
692                 ENDDO
693               CASE DEFAULT
694                 WRITE(MESSAGE,'(A,A,A,I5)') 'ERROR: DUCT_INTERP_TYPE is not
      correctly specified. Duct ID: ',TRIM(DU%ID)
695                 CALL SHUTDOWN(MESSAGE); RETURN
696             END SELECT
697           ENDDO DUCT_LOOP
698         ENDDO DUCTRUN_LOOP
699
700         END SUBROUTINE SET_INIT_HVAC_MASS_TRANSPORT
701
702         ...
703
704
705         SUBROUTINE UPDATE_HVAC_MASS_TRANSPORT(DT)
706         USE PHYSICAL_FUNCTIONS,ONLY: GET_AVERAGE_SPECIFIC_HEAT, GET_ENTHALPY
707         REAL(EB), INTENT(IN) :: DT
708         INTEGER :: N_SUBSTEPS,ND,NS,NC,ITCOUNT
709         TYPE(DUCT_TYPE),POINTER :: DU=>NULL()
710         REAL(EB) :: CP,CP2,DCPDT,DT_CFL,DT_DUCT,MASS_FLUX,TGUESS,ZZ_GET(
      N_TRACKED_SPECIES),HGAS
711         REAL(EB), ALLOCATABLE, DIMENSION(:) :: CPT_C,CPT_F,RHOCPT_C
712         REAL(EB), ALLOCATABLE, DIMENSION(:,:) :: RHOZZ_C,ZZ_F
713
714         DUCT_LOOP: DO ND = 1,N_DUCTS
715           DU => DUCT(ND)
716           IF (DU%N_CELLS == 1 ) CYCLE DUCT_LOOP
717
718           ! Check for zero flow and zero area
719           IF (ABS(DU%VEL(NEW))<=TWO_EPSILON_EB .OR. DU%AREA<=TWO_EPSILON_EB)
      CYCLE DUCT_LOOP
720
721           MASS_FLUX = DU%RHO_D * DU%VEL(NEW)
722
723           ! Set up of CFL and sub time step
724           DT_CFL = DU%DX/(2*DU%VEL(NEW)) ! CFL for Godunov pure upwinding scheme
725           N_SUBSTEPS = MAX(1,CEILING(DT/DT_CFL))
726           DT_DUCT = DT/REAL(N_SUBSTEPS,EB)
727
728           SUBSTEP_LOOP: DO NS = 1,N_SUBSTEPS
```

```
729         ! Set upwind face indices and allocate flux arrays
730         ALLOCATE(ZZ_F(0:DU%N_CELLS,N_TRACKED_SPECIES))
731         ALLOCATE(CPT_F(0:DU%N_CELLS))
732         ALLOCATE(CPT_C(DU%N_CELLS))
733         ALLOCATE(RHOCPT_C(DU%N_CELLS))
734         ALLOCATE(RHOZZ_C(DU%N_CELLS,N_TRACKED_SPECIES))
735
736         ! Populates upwind face variables, accounting for direction of flow
        (i.e. includes relevant node value as first/last face)
737         IF (DU%VEL(NEW)>0._EB) THEN
738             ZZ_F(0,:) = DUCTNODE(DU%NODE_INDEX(1))%ZZ(:)
739             CPT_F(0) = DUCTNODE(DU%NODE_INDEX(1))%CP*DUCTNODE(DU%NODE_INDEX
        (1))%TMP
740             DO NC = 1,DU%N_CELLS
741                 ZZ_F(NC,:) = DU%ZZ_C(NC,:) ! Godunov upwinding
742                 CPT_F(NC) = DU%TMP_C(NC)*DU%CP_C(NC) ! Godunov upwinding
743             ENDDO
744         ELSE
745             ZZ_F(DU%N_CELLS,:) = DUCTNODE(DU%NODE_INDEX(2))%ZZ(:)
746             CPT_F(DU%N_CELLS) = DUCTNODE(DU%NODE_INDEX(2))%TMP*DUCTNODE(DU%
        NODE_INDEX(2))%CP
747             DO NC = 0,DU%N_CELLS-1
748                 ZZ_F(NC,:) = DU%ZZ_C(NC+1,:)
749                 CPT_F(NC) = DU%TMP_C(NC+1)*DU%CP_C(NC+1)
750             ENDDO
751         ENDIF
752
753         ! Compute discretized conservation equations using explicit Euler
        method with Godunov upwinding profile
754         DO NC = 1,DU%N_CELLS
755             RHOZZ_C(NC,:) = DU%RHO_C(NC)*DU%ZZ_C(NC,:)                - DT_DUCT /
        DU%DX * MASS_FLUX * ( ZZ_F(NC,:) - ZZ_F(NC-1,:) )
756             RHOCPT_C(NC) =  DU%RHO_C(NC)*DU%TMP_C(NC)*DU%CP_C(NC) - DT_DUCT /
         DU%DX * MASS_FLUX * ( CPT_F(NC) - CPT_F(NC-1) )
757         ENDDO
758
759         ! Update cell centre variables
760         DU_UPDATE_LOOP: DO NC = 1,DU%N_CELLS
761             DU%RHO_C(NC) = SUM(RHOZZ_C(NC,1:N_TRACKED_SPECIES))
762             DU%ZZ_C(NC,:) = RHOZZ_C(NC,:)/DU%RHO_C(NC)
763             CPT_C(NC) = RHOCPT_C(NC)/DU%RHO_C(NC)
764             ZZ_GET = DU%ZZ_C(NC,:) ! Single dimension to be used with
        GET_AVERAGE_...
765             TGUESS = DU%TMP_C(NC)
766             ITCOUNT = 0
767             CP_LOOP: DO ! Uses Newton method to iterate to find solution of
        TMP_C from enthalpy
768                 ITCOUNT = ITCOUNT + 1
769                 CALL GET_ENTHALPY(ZZ_GET,HGAS,TGUESS)
770                 CALL GET_AVERAGE_SPECIFIC_HEAT(ZZ_GET,CP,TGUESS)
771                 IF (TGUESS>1._EB) THEN
772                     CALL GET_AVERAGE_SPECIFIC_HEAT(ZZ_GET,CP2,TGUESS-1._EB)
773                     DCPDT = CP - CP2
774                 ELSE
775                     CALL GET_AVERAGE_SPECIFIC_HEAT(ZZ_GET,CP2,TGUESS+1._EB)
776                     DCPDT = CP2 - CP
777                 ENDIF
778                 CP = HGAS/TGUESS
779                 DU%TMP_C(NC) = TGUESS + ( CPT_C(NC) - HGAS ) / ( CP + TGUESS *
         DCPDT )
780                 IF (ABS(DU%TMP_C(NC) - TGUESS) < TWO_EPSILON_EB) EXIT CP_LOOP
```

```
781                 IF ((DU%IMP_C(NC) - TGUESS)/DU%IMP_C(NC) < 0.0005_EB) EXIT
        CP_LOOP
782                 IF (ITCOUNT > 10) THEN
783                     DU%IMP_C(NC) = 0.5_EB*(DU%IMP_C(NC)+TGUESS)
784                     EXIT CP_LOOP
785                 ENDIF
786                 TGUESS = DU%IMP_C(NC)
787               ENDDO CP_LOOP
788               CALL GET_ENTHALPY(ZZ_GET,HGAS,DU%IMP_C(NC))
789               DU%CP_C(NC) = HGAS / DU%IMP_C(NC)
790           ENDDO DU_UPDATE_LOOP
791
792           DEALLOCATE(RHOZZ_C)
793           DEALLOCATE(ZZ_F)
794           DEALLOCATE(CPT_F)
795           DEALLOCATE(CPT_C)
796           DEALLOCATE(RHOCPT_C)
797
798       ENDDO SUBSTEP_LOOP
799
800 ENDDO DUCT_LOOP
801
802
803 END SUBROUTINE UPDATE_HVAC_MASS_TRANSPORT
804
805 END MODULE HVAC_ROUTINES
```

Appendix C

Numerical case input file template

This appendix provides the base input file used for the numerical cases. The input file has been provided with additional comments where input parameters would be entered (for example, fan performance, propane flow rate, and the like).

```
1 &HEAD CHID='___'/ ! name of case goes here
2 &TIME T_END=3700.0/
3 &MISC HVAC_MASS_TRANSPORT=.TRUE., HVAC_LOCAL_PRESSURE=.TRUE.,
      STRATIFICATION=.TRUE./
4
5 ! Fans
6 &HVAC ID='exh', TYPE_ID='FAN', LOSS=15.0, TAU_FAN=-10.0, MAX_FLOW=___,
      MAX_PRESSURE=___/ ! fan performance goes here
7 &HVAC ID='sup', TYPE_ID='FAN', LOSS=15.0, TAU_FAN=-10.0, MAX_FLOW=___,
      MAX_PRESSURE=___/ ! alternative fan model choices here
8
9 ! Surfaces
10 &SURF ID='sandBurner___',
11       COLOR='RED',
12       MLRPUA=___,
13       ADIABATIC=.TRUE./ ! propane flow rate input here
14 &SURF ID='coFlow___',
15       RGB=26,204,26,
16       ADIABATIC=.TRUE.,
17       VOLUME_FLOW=___/ ! flow rate of co-flow input here
18
19 ! Various outputs
20 ! Flow rates
21 &DEVC DUCT_ID='u1_1', ID='u1_1', QUANTITY='DUCT VELOCITY' /
22 &DEVC DUCT_ID='u2_1', ID='u2_1', QUANTITY='DUCT VELOCITY' /
23 &DEVC DUCT_ID='u3', ID='u3', QUANTITY='DUCT VELOCITY' /
24 &DEVC DUCT_ID='u4', ID='u4', QUANTITY='DUCT VELOCITY' /
25 &DEVC DUCT_ID='u5_1', ID='u5_1', QUANTITY='DUCT VELOCITY' /
26 &DEVC DUCT_ID='u6_1', ID='u6_1', QUANTITY='DUCT VELOCITY' /
27
28 &DEVC DUCT_ID='u1_2', ID='u1_2', QUANTITY='DUCT VELOCITY' /
29 &DEVC DUCT_ID='u2_2', ID='u2_2', QUANTITY='DUCT VELOCITY' /
30 &DEVC DUCT_ID='u3', ID='u3', QUANTITY='DUCT VELOCITY' /
31 &DEVC DUCT_ID='u4', ID='u4', QUANTITY='DUCT VELOCITY' /
32 &DEVC DUCT_ID='u5_2', ID='u5_2', QUANTITY='DUCT VELOCITY' /
33 &DEVC DUCT_ID='u6_2', ID='u6_2', QUANTITY='DUCT VELOCITY' /
34
35 &DEVC DUCT_ID='u1_leak', ID='leak_u1', QUANTITY='DUCT VELOCITY' /
36 &DEVC DUCT_ID='u2_leak', ID='leak_u2', QUANTITY='DUCT VELOCITY' /
```

```
37
38 &DEVC DUCT_ID='u5_leak', ID='leak_u5', QUANTITY='DUCT VELOCITY' /
39 &DEVC DUCT_ID='u6_leak', ID='leak_u6', QUANTITY='DUCT VELOCITY' /
40
41 ! Mass flows
42 &DEVC DUCT_ID='u1_1', ID='m1_1', QUANTITY='DUCT MASS FLOW' /
43 &DEVC DUCT_ID='u2_1', ID='m2_1', QUANTITY='DUCT MASS FLOW' /
44 &DEVC DUCT_ID='u3', ID='m3', QUANTITY='DUCT MASS FLOW' /
45 &DEVC DUCT_ID='u4', ID='m4', QUANTITY='DUCT MASS FLOW' /
46 &DEVC DUCT_ID='u5_1', ID='m5_1', QUANTITY='DUCT MASS FLOW' /
47 &DEVC DUCT_ID='u6_1', ID='m6_1', QUANTITY='DUCT MASS FLOW' /
48
49 &DEVC DUCT_ID='u1_2', ID='m1_2', QUANTITY='DUCT MASS FLOW' /
50 &DEVC DUCT_ID='u2_2', ID='m2_2', QUANTITY='DUCT MASS FLOW' /
51 &DEVC DUCT_ID='u5_2', ID='m5_2', QUANTITY='DUCT MASS FLOW' /
52 &DEVC DUCT_ID='u6_2', ID='m6_2', QUANTITY='DUCT MASS FLOW' /
53
54 &DEVC DUCT_ID='u3',ID='exhPressure',QUANTITY='FAN PRESSURE' /
55 &DEVC DUCT_ID='u4',ID='supPressure',QUANTITY='FAN PRESSURE' /
56
57 &DEVC NODE_ID='b1_exh_upper', ID='D02', QUANTITY='NODE TEMPERATURE' /
58 &DEVC DUCT_ID='u1_1', ID='D03', QUANTITY='DUCT TEMPERATURE' /
59 &DEVC DUCT_ID='u2_1', ID='D04', QUANTITY='DUCT TEMPERATURE' /
60 &DEVC NODE_ID='b2_exh_upper', ID='D05', QUANTITY='NODE TEMPERATURE' /
61 &DEVC DUCT_ID='u3', ID='D07', QUANTITY='DUCT TEMPERATURE' /
62 &DEVC NODE_ID='exh_spill', ID='D08', QUANTITY='NODE TEMPERATURE' /
63 &DEVC NODE_ID='sup_fresh', ID='D09', QUANTITY='NODE TEMPERATURE' /
64 &DEVC DUCT_ID='u4', ID='D10', QUANTITY='DUCT TEMPERATURE' /
65 &DEVC NODE_ID='b2_sup_lower', ID='D11', QUANTITY='NODE TEMPERATURE' /
66 &DEVC DUCT_ID='u5_2', ID='D13', QUANTITY='DUCT TEMPERATURE' /
67 &DEVC DUCT_ID='u6_2', ID='D14', QUANTITY='DUCT TEMPERATURE' /
68 &DEVC NODE_ID='b1_sup_lower', ID='D16', QUANTITY='NODE TEMPERATURE' /
69
70 &DEVC DUCT_ID='u1_1', CELL_L = 0.1, ID='D02_', QUANTITY='DUCT CELL
       TEMPERATURE' /
71 &DEVC DUCT_ID='u1_1', CELL_L = 0.3, ID='D03_1', QUANTITY='DUCT CELL
       TEMPERATURE' /
72 &DEVC DUCT_ID='u1_2', CELL_L = 0.1, ID='D03_2', QUANTITY='DUCT CELL
       TEMPERATURE' /
73 &DEVC DUCT_ID='u2_1', CELL_L = 0.3, ID='D04_1', QUANTITY='DUCT CELL
       TEMPERATURE' /
74 &DEVC DUCT_ID='u2_2', CELL_L = 0.1, ID='D04_2', QUANTITY='DUCT CELL
       TEMPERATURE' /
75 &DEVC DUCT_ID='u2_1', CELL_L = 0.1, ID='D05_', QUANTITY='DUCT CELL
       TEMPERATURE' /
76 &DEVC DUCT_ID='u3', CELL_L = 0.5, ID='D07_', QUANTITY='DUCT CELL
       TEMPERATURE' /
77 &DEVC DUCT_ID='u4', CELL_L = 0.4, ID='D10_', QUANTITY='DUCT CELL
       TEMPERATURE' /
78 &DEVC DUCT_ID='u5_2', CELL_L = 0.65, ID='D11_', QUANTITY='DUCT CELL
       TEMPERATURE' /
79 &DEVC DUCT_ID='u5_1', CELL_L = 0.65, ID='D13_1', QUANTITY='DUCT CELL
       TEMPERATURE' /
80 &DEVC DUCT_ID='u5_2', CELL_L = 0.1, ID='D13_2', QUANTITY='DUCT CELL
       TEMPERATURE' /
81 &DEVC DUCT_ID='u6_1', CELL_L = 0.65, ID='D14_1', QUANTITY='DUCT CELL
       TEMPERATURE' /
82 &DEVC DUCT_ID='u6_2', CELL_L = 0.1, ID='D14_2', QUANTITY='DUCT CELL
       TEMPERATURE' /
83 &DEVC DUCT_ID='u6_2', CELL_L = 0.65, ID='D16_', QUANTITY='DUCT CELL
       TEMPERATURE' /
```

```
84
85 ! Geometry etc.
86
87 &DUMP COLUMN_DUMP_LIMIT=.TRUE., DT_RESTART=300.0/
88
89 &MESH ID='MESH-a', IJK=___,___,___, XB=-1.1,-0.1,-0.5,0.5,0,1.0/ ! cell
       count choices made here
90 &MESH ID='MESH-b', IJK=___,___,___, XB=0.1,1.1,-0.5,0.5,0,1.0/
91
92 &ZONE ID='ZONE1', XB=-1.0,-0.9,0.2,0.3,0.0,0.1/
93 &ZONE ID='ZONE2', XB=0.2,0.3,0.2,0.3,0.0,0.1/
94
95 &REAC ID='PROPANE',
96       FUEL='PROPANE',
97       CO_YIELD=0.012,
98       SOOT_YIELD=0.01/
99
100 &PROP ID='TC_1_3_1 props', BEAD_DIAMETER=5.0E-4/
101 &PROP ID='TC_1_3_2 props', BEAD_DIAMETER=5.0E-4/
102 &PROP ID='TC_1_3_3 props', BEAD_DIAMETER=5.0E-4/
103 &PROP ID='TC_1_3_4 props', BEAD_DIAMETER=5.0E-4/
104 &PROP ID='TC_1_3_5 props', BEAD_DIAMETER=5.0E-4/
105 &PROP ID='TC_2_3_1 props', BEAD_DIAMETER=5.0E-4/
106 &PROP ID='TC_2_3_2 props', BEAD_DIAMETER=5.0E-4/
107 &PROP ID='TC_2_3_3 props', BEAD_DIAMETER=5.0E-4/
108 &PROP ID='TC_2_3_4 props', BEAD_DIAMETER=5.0E-4/
109 &PROP ID='TC_2_3_5 props', BEAD_DIAMETER=5.0E-4/
110 &DEVC ID='TC_1_3_1', PROP_ID='TC_1_3_1 props', QUANTITY='THERMOCOUPLE',
       XYZ=-0.6,0.0,0.9/
111 &DEVC ID='TC_1_3_2', PROP_ID='TC_1_3_2 props', QUANTITY='THERMOCOUPLE',
       XYZ=-0.6,0.0,0.6/
112 &DEVC ID='TC_1_3_3', PROP_ID='TC_1_3_3 props', QUANTITY='THERMOCOUPLE',
       XYZ=-0.6,0.0,0.8/
113 &DEVC ID='TC_1_3_4', PROP_ID='TC_1_3_4 props', QUANTITY='THERMOCOUPLE',
       XYZ=-0.6,0.0,0.4/
114 &DEVC ID='TC_1_3_5', PROP_ID='TC_1_3_5 props', QUANTITY='THERMOCOUPLE',
       XYZ=-0.6,0.0,0.2/
115 &DEVC ID='TC_2_3_1', PROP_ID='TC_2_3_1 props', QUANTITY='THERMOCOUPLE',
       XYZ=0.6,0.0,0.9/
116 &DEVC ID='TC_2_3_2', PROP_ID='TC_2_3_2 props', QUANTITY='THERMOCOUPLE',
       XYZ=0.6,0.0,0.6/
117 &DEVC ID='TC_2_3_3', PROP_ID='TC_2_3_3 props', QUANTITY='THERMOCOUPLE',
       XYZ=0.6,0.0,0.8/
118 &DEVC ID='TC_2_3_4', PROP_ID='TC_2_3_4 props', QUANTITY='THERMOCOUPLE',
       XYZ=0.6,0.0,0.4/
119 &DEVC ID='TC_2_3_5', PROP_ID='TC_2_3_5 props', QUANTITY='THERMOCOUPLE',
       XYZ=0.6,0.0,0.2/
120 &DEVC ID='fire', QUANTITY='TIME', XYZ=-1.1,-0.5,0, SETPOINT=100.0/
121 &DEVC ID='startClosed', QUANTITY='TIME', XYZ=-1.1,-0.5,0, SETPOINT=2800.0/
       Spill, closed first
122 &DEVC ID='startOpened', QUANTITY='TIME', XYZ=-1.1,-0.5,0, SETPOINT=2800.0,
       INITIAL_STATE=.TRUE./ Return, open first
123
124 &MATL ID='vermiculite',
125       SPECIFIC_HEAT=1.15,
126       CONDUCTIVITY=0.2,
127       DENSITY=700.0/
128 &MATL ID='quartz',
129       SPECIFIC_HEAT=0.7,
130       CONDUCTIVITY=1.25,
131       DENSITY=2200.0/
```

```
132 &MATL ID='timberPly',
133       SPECIFIC_HEAT=1.215,
134       CONDUCTIVITY=0.12,
135       DENSITY=650.0/
136
137 &SURF ID='boxWall',
138       RGB=255,204,204,
139       DEFAULT=.TRUE.,
140       BACKING='VOID',
141       MATL_ID(1,1)='vermiculite',
142       MATL_MASS_FRACTION(1,1)=1.0,
143       THICKNESS(1)=0.025/
144 &SURF ID='quartz',
145       RGB=203,255,255,
146       TRANSPARENCY=0.494,
147       BACKING='VOID',
148       MATL_ID(1,1)='quartz',
149       MATL_MASS_FRACTION(1,1)=1.0,
150       THICKNESS(1)=3.0E-3/
151 &SURF ID='boxLid',
152       RGB=255,204,204,
153       BACKING='VOID',
154       MATL_ID(1,1)='vermiculite',
155       MATL_ID(2,1)='timberPly',
156       MATL_MASS_FRACTION(1,1)=1.0,
157       MATL_MASS_FRACTION(2,1)=1.0,
158       THICKNESS(1:2)=0.025,0.01/
159
160 &OBST ID='hotQuartz', XB=-0.7,-0.5,-0.5,-0.5,0.4,0.6, PERMIT_HOLE=.FALSE.,
        SURF_ID='quartz'/
161 &OBST ID='coolQuartz', XB=0.5,0.7,-0.5,-0.5,0.4,0.6, PERMIT_HOLE=.FALSE.,
      SURF_ID='quartz'/
162 &OBST ID='coFlowWall', XB=-0.8,-0.7,-0.1,0.1,0.0,0.1, SURF_ID='boxWall'/
163 &OBST ID='coFlowWall', XB=-0.5,-0.4,-0.1,0.1,0.0,0.1, SURF_ID='boxWall'/
164 &OBST ID='coFlowWall', XB=-0.7,-0.5,0.1,0.2,0.0,0.1, SURF_ID='boxWall'/
165 &OBST ID='coFlowWall', XB=-0.7,-0.5,-0.2,-0.1,0.0,0.1, SURF_ID='boxWall'/
166
167 &VENT ID='sandBurner', SURF_ID='sandBurnerP20', XB=-0.7,-0.5,-0.1,0.1,0,0,
       IOR=3, DEVC_ID='fire'/
168 &VENT ID='coFlowW', SURF_ID='coFlowP20', XB=-0.7,-0.7,-0.1,0.1,0.0,0.1,
      IOR=1/
169 &VENT ID='coFlowE', SURF_ID='coFlowP20', XB=-0.5,-0.5,-0.1,0.1,0.0,0.1,
      IOR=-1/
170 &VENT ID='coFlowS', SURF_ID='coFlowP20', XB=-0.7,-0.5,-0.1,-0.1,0.0,0.1,
      IOR=2/
171 &VENT ID='coFlowN', SURF_ID='coFlowP20', XB=-0.7,-0.5,0.1,0.1,0.0,0.1, IOR
      =-2/
172 &VENT ID='leak_b1_t_n', SURF_ID='boxLid', XB=-1.1,-0.1,0.4,0.5,1.0,1.0,
      IOR=-3, COLOR='INVISIBLE'/
173 &VENT ID='leak_b1_t_s', SURF_ID='boxLid', XB=-1.1,-0.1,-0.5,-0.4,1.0,1.0,
      IOR=-3, COLOR='INVISIBLE'/
174 &VENT ID='leak_b1_t_e', SURF_ID='boxLid', XB=-0.2,-0.1,-0.4,0.4,1.0,1.0,
      IOR=-3, COLOR='INVISIBLE'/
175 &VENT ID='leak_b1_t_w', SURF_ID='boxLid', XB=-1.1,-1.0,-0.4,0.4,1.0,1.0,
      IOR=-3, COLOR='INVISIBLE'/
176 &VENT ID='leak_b2_t_n', SURF_ID='boxLid', XB=0.1,1.1,0.4,0.5,1.0,1.0, IOR
      =-3, COLOR='INVISIBLE'/
177 &VENT ID='leak_b2_t_s', SURF_ID='boxLid', XB=0.1,1.1,-0.5,-0.4,1.0,1.0,
      IOR=-3, COLOR='INVISIBLE'/
178 &VENT ID='leak_b2_t_e', SURF_ID='boxLid', XB=1.0,1.1,-0.4,0.4,1.0,1.0, IOR
      =-3, COLOR='INVISIBLE'/
```

```
179 &VENT ID='leak_b2_t_w', SURF_ID='boxLid', XB=0.1,0.2,-0.4,0.4,1.0,1.0, IOR
    =-3, COLOR='INVISIBLE'/
180 &VENT ID='b1_exh_upper', SURF_ID='HVAC', XB=-1.0,-0.9,-0.5,-0.5,0.9,1.0/
181 &VENT ID='b2_exh_upper', SURF_ID='HVAC', XB=0.2,0.3,-0.5,-0.5,0.9,1.0/
182 &VENT ID='b1_sup_lower', SURF_ID='HVAC', XB=-0.3,-0.2,0.5,0.5,0.0,0.1/
183 &VENT ID='b2_sup_lower', SURF_ID='HVAC', XB=0.9,1.0,0.5,0.5,0.0,0.1/
184
185 &HVAC ID='b1_exh_upper', TYPE_ID='NODE', DUCT_ID='u1_1', VENT_ID='
    b1_exh_upper', LOSS=3.5,4.0/
186 &HVAC ID='u1_1', TYPE_ID='DUCT', DIAMETER=0.1, LOSS=1.3,1.3, NODE_ID='
    b1_exh_upper','b1_exh_upper_2', ROUGHNESS=0.1E-3, LENGTH=0.4, N_CELLS
    =10/
187 &HVAC ID='b1_exh_upper_2', TYPE_ID='NODE', DUCT_ID='u1_1','u1_2','u1_leak
    ', XYZ=-0.65,-0.5,0.95, LOSS(1,2:3)=0.2,1.0, LOSS(2,1:3)=0.2,,1.0,
    LOSS(3,1:2)=1.0,1.0/
188 &HVAC ID='u1_2', TYPE_ID='DUCT', DIAMETER=0.1, LOSS=0.1,0.1, NODE_ID='
    b1_exh_upper_2','exh_tee', ROUGHNESS=0.1E-3, LENGTH=0.4, N_CELLS=10/
189 &HVAC ID='u1_leak', TYPE_ID='DUCT', DIAMETER=0.03, LOSS=0.1,0.2, NODE_ID='
    b1_exh_upper_2','exh_b1_leakNode', ROUGHNESS=5.0E-4, LENGTH=4.0,
    N_CELLS=1/
190 &HVAC ID='exh_b1_leakNode', TYPE_ID='NODE', DUCT_ID='u1_leak', AMBIENT=.
    TRUE., XYZ=-0.65,-0.6,0.95, LOSS=15.0,10.0/
191 &HVAC ID='b2_exh_upper', TYPE_ID='NODE', DUCT_ID='u2_1', VENT_ID='
    b2_exh_upper', LOSS=3.5,4.0/
192 &HVAC ID='u2_1', TYPE_ID='DUCT', DIAMETER=0.1, LOSS=1.3,1.3, NODE_ID='
    b2_exh_upper','b2_exh_upper_2', ROUGHNESS=0.1E-3, LENGTH=0.4, N_CELLS
    =10/
193 &HVAC ID='b2_exh_upper_2', TYPE_ID='NODE', DUCT_ID='u2_1','u2_2','u2_leak
    ', XYZ=-0.05,-0.5,0.95, LOSS(1,2:3)=0.2,1.0, LOSS(2,1:3)=0.2,,1.0,
    LOSS(3,1:2)=1.0,1.0/
194 &HVAC ID='u2_2', TYPE_ID='DUCT', DIAMETER=0.1, LOSS=0.1,0.1, NODE_ID='
    b2_exh_upper_2','exh_tee', ROUGHNESS=0.1E-3, LENGTH=0.4, N_CELLS=10/
195 &HVAC ID='u2_leak', TYPE_ID='DUCT', DIAMETER=0.03, LOSS=0.1,0.2, NODE_ID='
    b2_exh_upper_2','exh_b2_leakNode', ROUGHNESS=5.0E-4, LENGTH=4.0,
    N_CELLS=1/
196 &HVAC ID='exh_b2_leakNode', TYPE_ID='NODE', DUCT_ID='u2_leak', AMBIENT=.
    TRUE., XYZ=-0.05,-0.6,0.95, LOSS=15.0,10.0/
197 &HVAC ID='b1_sup_lower', TYPE_ID='NODE', DUCT_ID='u6_2', VENT_ID='
    b1_sup_lower', LOSS=3.5,4.0/
198 &HVAC ID='u6_2', TYPE_ID='DUCT', DIAMETER=0.1, LOSS=0.8,0.8, NODE_ID='
    b1_sup_lower_2','b1_sup_lower', ROUGHNESS=0.1E-3, LENGTH=0.75, N_CELLS
    =10/
199 &HVAC ID='b1_sup_lower_2', TYPE_ID='NODE', DUCT_ID='u6_2','u6_1','u6_leak
    ', XYZ=0.05,0.5,0.05, LOSS(1,2:3)=0.2,1.0, LOSS(2,1:3)=0.2,,1.0, LOSS
    (3,1:2)=1.0,1.0/
200 &HVAC ID='u6_1', TYPE_ID='DUCT', DIAMETER=0.1, LOSS=0.1,0.1, NODE_ID='
    sup_tee','b1_sup_lower_2', ROUGHNESS=0.1E-3, LENGTH=0.75, N_CELLS=10/
201 &HVAC ID='u6_leak', TYPE_ID='DUCT', DIAMETER=0.06, LOSS=0.1,0.2, NODE_ID='
    b1_sup_lower_2','sup_b1_leakNode', ROUGHNESS=5.0E-4, LENGTH=4.0,
    N_CELLS=1/
202 &HVAC ID='sup_b1_leakNode', TYPE_ID='NODE', DUCT_ID='u6_leak', AMBIENT=.
    TRUE., XYZ=0.05,0.6,0.05, LOSS=15.0,10.0/
203 &HVAC ID='b2_sup_lower', TYPE_ID='NODE', DUCT_ID='u5_2', VENT_ID='
    b2_sup_lower', LOSS=3.5,4.0/
204 &HVAC ID='u5_2', TYPE_ID='DUCT', DIAMETER=0.1, LOSS=0.8,0.8, NODE_ID='
    b2_sup_lower_2','b2_sup_lower', ROUGHNESS=0.1E-3, LENGTH=0.75, N_CELLS
    =10/
205 &HVAC ID='b2_sup_lower_2', TYPE_ID='NODE', DUCT_ID='u5_2','u5_1','u5_leak
    ', XYZ=0.65,0.5,0.05, LOSS(1,2:3)=0.2,1.0, LOSS(2,1:3)=0.2,,1.0, LOSS
    (3,1:2)=1.0,1.0/
```

```
206 &HVAC ID='u5_1', TYPE_ID='DUCT', DIAMETER=0.1, LOSS=0.1,0.1, NODE_ID='
      sup_tee','b2_sup_lower_2', ROUGHNESS=0.1E-3, LENGTH=0.75, N_CELLS=10/
207 &HVAC ID='u5_leak', TYPE_ID='DUCT', DIAMETER=0.06, LOSS=0.1,0.2, NODE_ID='
      b2_sup_lower_2','sup_b2_leakNode', ROUGHNESS=5.0E-4, LENGTH=4.0,
      N_CELLS=1/
208 &HVAC ID='sup_b2_leakNode', TYPE_ID='NODE', DUCT_ID='u5_leak', AMBIENT=.
      TRUE., XYZ=0.65,0.6,0.05, LOSS=15.0,10.0/
209 &HVAC ID='exh_tee', TYPE_ID='NODE', DUCT_ID='u1_2','u2_2','u3', XYZ
      =-0.35,-0.5,1.05/
210 &HVAC ID='exh_branch', TYPE_ID='NODE', DUCT_ID='u3','u3_spill','return',
      XYZ=-0.35,0.0,1.3, LOSS(1,2:3)=0.2,1.0, LOSS(2,1:3)=0.2,,1.0, LOSS
      (3,1:2)=1.0,1.0/
211 &HVAC ID='exh_spill', TYPE_ID='NODE', DUCT_ID='u3_spill', AMBIENT=.TRUE.,
      XYZ=-0.35,0.2,1.3, LOSS=3.5,4.0/
212 &HVAC ID='u3', TYPE_ID='DUCT', DIAMETER=0.1, FAN_ID='exh', LOSS=0.3,0.3,
      NODE_ID='exh_tee','exh_branch', ROUGHNESS=0.1E-3, LENGTH=0.9,
      SYSTEM_LOSS=15./
213 &HVAC ID='u3_spill', TYPE_ID='DUCT', DIAMETER=0.1, DAMPER=.TRUE., LOSS
      =0.1,0.1, NODE_ID='exh_branch','exh_spill', ROUGHNESS=0.1E-3, LENGTH
      =0.2, DEVC_ID='startClosed'/
214 &HVAC ID='sup_branch', TYPE_ID='NODE', DUCT_ID='return','u4_fresh','u4',
      XYZ=0.35,0.0,1.3, LOSS(1,2:3)=1.0,1.0, LOSS(2,1:3)=1.0,,0.2, LOSS
      (3,1:2)=1.0,0.2/
215 &HVAC ID='sup_fresh', TYPE_ID='NODE', DUCT_ID='u4_fresh', AMBIENT=.TRUE.,
      XYZ=0.35,-0.2,1.3, LOSS=3.5,4.0/
216 &HVAC ID='sup_tee', TYPE_ID='NODE', DUCT_ID='u6_1','u5_1','u4', XYZ
      =0.35,0.5,1.05, LOSS(1,2:3)=0.2,1.0, LOSS(2,1:3)=0.2,,1.0, LOSS(3,1:2)
      =1.0,1.0/
217 &HVAC ID='return', TYPE_ID='DUCT', DIAMETER=0.1, LOSS=3.0,3.0, NODE_ID='
      exh_branch','sup_branch', ROUGHNESS=0.1E-3, LENGTH=0.7, DAMPER=.TRUE.,
       DEVC_ID='startOpened'/
218 &HVAC ID='u4_fresh', TYPE_ID='DUCT', DIAMETER=0.1, LOSS=0.1,0.1, NODE_ID='
      sup_fresh','sup_branch', ROUGHNESS=0.1E-3, LENGTH=0.2, DAMPER=.TRUE.,
      DEVC_ID='startClosed'/
219 &HVAC ID='u4', TYPE_ID='DUCT', DIAMETER=0.1, LOSS=0.3,0.3, FAN_ID='sup',
      NODE_ID='sup_branch','sup_tee', ROUGHNESS=0.1E-3, LENGTH=0.9,
      SYSTEM_LOSS=15./
220
221 &HVAC ID='b1_t_n', TYPE_ID='LEAK', VENT_ID='leak_b1_t_n', VENT2_ID='
      AMBIENT', AREA=1.0E-3, LEAK_ENTHALPY=.TRUE., LOSS=0.61/
222 &HVAC ID='b1_t_e', TYPE_ID='LEAK', VENT_ID='leak_b1_t_e', VENT2_ID='
      AMBIENT', AREA=1.0E-3, LEAK_ENTHALPY=.TRUE., LOSS=0.61/
223 &HVAC ID='b1_t_s', TYPE_ID='LEAK', VENT_ID='leak_b1_t_s', VENT2_ID='
      AMBIENT', AREA=1.0E-3, LEAK_ENTHALPY=.TRUE., LOSS=0.61/
224 &HVAC ID='b1_t_w', TYPE_ID='LEAK', VENT_ID='leak_b1_t_w', VENT2_ID='
      AMBIENT', AREA=1.0E-3, LEAK_ENTHALPY=.TRUE., LOSS=0.61/
225 &HVAC ID='b2_t_n', TYPE_ID='LEAK', VENT_ID='leak_b2_t_n', VENT2_ID='
      AMBIENT', AREA=1.0E-5, LEAK_ENTHALPY=.TRUE., LOSS=0.61/
226 &HVAC ID='b2_t_e', TYPE_ID='LEAK', VENT_ID='leak_b2_t_e', VENT2_ID='
      AMBIENT', AREA=1.0E-5, LEAK_ENTHALPY=.TRUE., LOSS=0.61/
227 &HVAC ID='b2_t_s', TYPE_ID='LEAK', VENT_ID='leak_b2_t_s', VENT2_ID='
      AMBIENT', AREA=1.0E-5, LEAK_ENTHALPY=.TRUE., LOSS=0.61/
228 &HVAC ID='b2_t_w', TYPE_ID='LEAK', VENT_ID='leak_b2_t_w', VENT2_ID='
      AMBIENT', AREA=1.0E-5, LEAK_ENTHALPY=.TRUE., LOSS=0.61/
229
230 &TAIL /
```